Fundamental Studies of Heterostructured Oxide Thin Film Electrocatalysts for Oxygen Reduction at High Temperatures

By

Ethan Jon Crumlin

Bachelor of Science, Mechanical Engineering
Massachusetts Institute of Technology, 2005

Master of Science, Mechanical Engineering
Massachusetts Institute of Technology, 2007

SUBMITTED TO THE DEPARTMENT OF MECHANICAL ENGINEERING IN PARTIAL FULLFILMENT OF THE REQUIREMENTS FOR THE DEGREE OF

DOCTOR OF PHILOSOPHY IN MECHANICAL ENGINEERING

AT THE

MASSACHUSETTS INSTITUTE OF TECHNOLOGY

JUNE 2012

Authored by _____
Ethan Jon Crumlin
Department of Mechanical Engineering
April 25, 2012

Certified by _____
Yang Shao-Horn
Gail E. Kendall Chair of Mechanical Engineering
Thesis Supervisor

Accepted by _____
David E. Hardt
Cross Professor of Mechanical Engineering
Chairman, Department Committee of Graduate Students

Fundamental Studies of Heterostructured Oxide Thin Film Electrocatalysts for Oxygen Reduction at High Temperatures

by

Ethan Jon Crumlin

Submitted to the Department of Mechanical Engineering
on May 4, 2012, in partial fulfillment of the
requirements for the degree of
Doctor of Philosophy in Mechanical Engineering

Abstract

Searching for active and cost-effective catalysts for oxygen electrocatalysis is essential for the development of efficient clean electrochemical energy technologies. Perovskite oxides are active for surface oxygen exchange at evaluated temperatures and they are used commonly in solid oxide fuel cells (SOFC) or electrolyzers. However, the oxide surface chemistry at high temperatures and near ambient oxygen pressure is poorly understood, which limits the design of highly active catalysts. This work investigates heterostructured interfaces between $(La_{1-x}Sr_x)CoO_{3-\delta}$ (where x = 0.2 and 0.4, $LSC80\text{-}20_{113}$ and $LSC60\text{-}40_{113}$ respectively) and $(La_{0.5}Sr_{0.5})_2CoO_{4\pm\delta}$ (LSC_{214}) enhanced ORR catalytic activity 1) via electrochemical impedance spectroscopy, atomic force microscopy, scanning electron microscopy, scanning transmission electron microscopy, and high resolution X-ray diffraction (HRXRD) and 2) using *in situ* ambient pressure X-ray photoelectron spectroscopy (APXPS) and *in situ* HRXRD.

Here we show that the ORR of epitaxial $LSC80\text{-}20_{113}$ and $LSC60\text{-}40_{113}$ is dramatically enhanced (~3-4 orders of magnitude above bulk LSC_{113}) by surface decorations of LSC_{214} ($LSC_{113/214}$) with coverage in the range from ~0.1 to ~15 nm. Such high surface oxygen kinetics ($\sim 1\cdot10^{-5}$ cm·s^{-1} at 550 °C) are among the most active SOFC cathode materials reported to date. Although the mechanism for ORR enhancement is not yet fully understood, our results to date show that the observed ORR enhancement can be attributed to highly active interfacial LSC_{113}/LSC_{214} regions, which were shown to be atomically sharp.

Using *in situ* HRXRD and APXPS we show that epitaxial $LSC80\text{-}20_{113}$ thin films have lower coverage of surface secondary phases and higher Strontium enrichment in the perovskite structure, which is attributed to its markedly enhanced activity relative to $LSC80\text{-}20_{113}$ powder. APXPS temperature cycling of epitaxial $LSC80\text{-}20_{113}$ APXPS reveled upon heating to 520 °C the initial Sr enrichment which is irreversible, however subsequent temperature cycling demonstrates a small amount of reversible Sr enrichment. With applied potentials $LSC80\text{-}20_{113/214}$ shows significant Sr enrichment greater then $LSC80\text{-}20_{113}$, and the ability to stabilize high concentrations of both lattice and surface Sr which we hypothesize is a very important factor governing $LSC80\text{-}20_{113/214}$ enhanced ORR activity.

Thesis Supervisor: Yang Shao-Horn
Title: Gail E. Kendall Chair of Mechanical Engineering

LIST OF PUBLICATIONS

Crumlin, E.J.; Ahn, S.-J.; Lee, D.-K.; Mutoro, E.; Biegalski, M.; Christen, H.; Shao-Horn, Y., "Enhanced Oxygen Reduction Activity on Epitaxial $La_{0.6}Sr_{0.4}CoO_{3-d}$ Perovskite Thin Films for Solid Oxide Fuel Cells", J. Electrochemical Society, Accepted (2012).

Crumlin, E.J.; Mutoro, E.; Liu, Z.; Grass, M.E.; Biegalski, M.D.; Lee, Y.-L.; Morgan, D.; Christen, H.M.; Bluhm, H.; Shao-Horn, Y., "Surface Strontium Enrichment on Highly Active Perovskites for Oxgyen Electrocatalysis in Solid Oxide Fuel Cells", Energy & Environmental Science, 5, 6081-6088 (2012).

Kumar, A.; Leonard, D.; Jesse, S.; Biegalski, M.; Morozovska, A.; Eliseev, E.; Mutoro, E.; ***Crumlin, E.J.***; Shao-Horn, Y.; Borisevich, A.; Kalinin, S.V., "Spatially Resolved Mapping of Oxygen Reduction/Evolution Reaction on Solid-Oxide Fuel Cell Cathodes with Sub-10 nm Resolution", Submitted (2011).

Mutoro, E.; ***Crumlin, E.J.***; Pöpke, H.; Luerssen, B.; Amati, M.; Abyaneh, M.K.; Biegalski, M.D.; Christen, H.M.; Gregoratti, L.; Janek, J.; Shao-Horn, Y., "Reversible Compositional Control of Oxide Surfaces by Electrochemical Potentials", The Journal of Physical Chemistry Letters, 3, 40-44 (2012).

Byon, H.R.; Suntivich, J.; ***Crumlin, E.J.***; Shao-Horn, Y.; "Fe-N-Modified Multi-Walled Carbon Nanotubes for Oxygen Reduction Reaction in Acid", Pysical Chemistry Chemical Physics, 13(48), 21437-21445 (2011).

Sheng, W.; Lee, S.-W.; ***Crumlin, E.J.***; Chen, S.; Shao-Horn, Y., "Synthesis, Activity and Durability of Pt Nanoparticles Supported on Multi-walled Carbon Nanotubes for Oxygen Reduction", J. Electrochemical Society, 158(11), B1398-B1404 (2011).

Mutoro, E.; ***Crumlin, E.J.***; Biegalski, M.D.; Christen, H.M.; Shao-Horn, Y., "Enhanced oxygen reduction activity on surface-decorated perovskite thin films for solid oxdie fuel cells", Energy & Environmental Science, 4(9), 3689-3696 (2011).

Crumlin, E.J.; Mutoro, E.; Ahn, S.J.; la O', G.J.; Leonard, D.; Borisevich, A.; Biegalski, M.; Christen, H.; Shao-Horn, Y., "Oxygen Reduction Kinetics Enhancement on a Heterostructured Oxide Surface for Solid Oxide Fuel Cells", The Journal of Physical Chemistry Letters, 1, 3149-3155 (2010).

Lu, Y.C.; Gasteiger, H.A.; ***Crumlin, E.***; McGuire, R.; Shao-Horn, Y., "Electrocatalytic activity studies of select metal surfaces and implications in Li-Air Batteries", J. Electrochemical Society, 157(9), A1016-A1025 (2010).

la O', G.J.; Ahn, S.J.; ***Crumli,n E.;*** Orikasa, Y.; Biegalski, M.D.; Christen, H.M.; Shao-Horn, Y., "Catalytic Activity Enhancement for Oxygen Reduction on Epitaxial Perovskite Thin Films for Solid-Oxide Fuel Cells", Angewandte Chemie-International Edition, 49(31), 5344-5347 (2010).

Crumlin, E. J.; la O', G.J.; and Shao-Horn, Y., "Architectures and Performance of High-Voltage, Microscale Single-Chamber Solid Oxide Fuel Cell Stacks", Solid Oxide Fuel Cells 10, the Electrochemical Society Transactions, 7, 981-986 (2007).

la O', G.J.; In, H.J.; ***Crumlin, E.***, Barbastathis, G.; and Shao-Horn, Y., "Recent Advances in Microdevices for Electrochemical Conversion and Storage", invited review paper, International Journal of Energy Research, 31(6-7), 548-575 (2007).

ACKNOWLEDGEMENTS

Ever since I was a little child, I was always captivated by "energy" of all forms so I am grateful for the opportunities and support of my advisor, Professor Yang Shao-Horn. Up to this point, I have been at MIT longer then Yang; however, not by much since she has been a part of my life since my sophomore year, which happened to be her first year. We have both gone through rather transformative years together providing challenging and enriching experiences, many of which I certainly could never have predicted but am grateful to have. I would also like to thank my thesis committee members: Professors Mary C. Boyce, Ahmed F. Ghoniem, and Harry L. Tuller for their constructive and insightful comments. Together, they have provided balance and vision and have been role models for the kind of scientist I hope to become. I would be honored to generate even a fraction of the impact they have had on our world.

Since money makes the world go round, it is also needed to support the work discussed within this thesis. Therefore, I would like to acknowledge the generous support given by the Department of Energy (SISGR DE- SC0002633) and the King Abdullah University of Science and Technology, King Fahd University of Petroleum and Minerals in Dharam, Saudi Arabia for funding this research via the Center for Clean Water and Clean Energy at MIT and KFUPM. All of my research conducted at the Advanced Light Source is supported by the Director at the Office of Science, Office of Basic Energy Sciences, U.S. Department of Energy under contract no. DE-AC02-05CH11231. Lastly, the sample preparation and characterization conducted at the Center for Nanophase Materials Sciences is sponsored at Oak Ridge National Laboratory by the Scientific User Facilities Division, Office of Basic Energy Sciences, U.S. Department of Energy.

This work is in large part successful thanks to the wonderful dedication and support of various research collaborators I have had the pleasure of interacting with over my years including (in no particular order) Dr. Sung-Jin Ahn, Dongkyu Lee, Wesley Hong, Dr. Yueh-Lin Lee, Prof. Dane Morgan, Dr. Donovan Leonard (STEM), Dr. Albina Borisevich (STEM), Dr. Michael Biegalski (PLD/XRD), Dr. Hans Christen (PLD/XRD), Dr. Zhi Liu (*in situ* APXPS), Dr. Hendrik Bluhm (*in situ* APXPS), Dr. Sergei Kalinin, Dr Amit Kumar, Dr. Gabriel Vieth, Dr. Nancy Dudney, Libby Shaw (MIT XPS), Dr. Scott Speakman (MIT XRD), Kurt Broderick (MTL), Dr. Cortney Kreller, TJ McDonald, and Prof. Stu Adler. I would especially like to thank Dr. Gerardo Jose la O' (G.J.) who was my early mentor for SOFCs and provided pivotal guidance and mentorship in the begining of my graduate studies, and who has progressed to becoming a close friend and great supporter. Dr. Seung Woo Lee has been my office mate and friend from the beginning and I am thankful for his calm demeanor, constant support, and continued friendship. With regards to Yi-Chun Lu (soon to be Dr.!) and Dr. Eva Mutoro, words cannot describe the roles they have played within my life, as well as within my research. Their compassion, companionship, intellectual brilliance, and infinite energy provided the fuel necessary to work so hard and the light to help guide me to reach my full potential. More than collaborators and friends, I feel they are sisters who I am very lucky to have. I am additionally grateful to Dr. Eva Mutoro, who is an equal contributor to the work presented in Chapters 3 and 5, and for her contribution, inspiration, and comments towards the figures presented in this thesis. I would also like to express my appreciation for Dr. Hubert Gasteiger for his infinite energy, lifelong friendship, continuous support, and inspiration for how to live and love life as well as research. Finally, to all past and current EEL members, thank you for sharing this experience with me and I hope I have provided

you with as much support and encouragement as you have all provided me with throughout my years.

The amount of friends who have been a part of my life during this experience is truly unimaginable and to them, I am forever grateful. Since writing about each of them individually would require several thousands of pages, I must thank you all together. However, I would like to dedicate this work to all of you and will share my appreciation with each of you personally. To my family: Dr. Irving J. Crumlin (father), Linda J. Crumlin (mother), and Alex J. Crumlin (identical twin brother), you have been my mountains, oceans, and sky. Mom and dad - you created my foundation to be as strong as the mountains, taught me that with my work ethic I can reach the sky, and supported my creativity so that I can be as infinite and fluid as the oceans. Alex - being my twin brother created strength that I could not have found alone. Having someone as great as you, who was better than myself, generated the fight and determination to never give up (which I needed to have in order to compete with you!). Dad - you have always been a fierce advocate for my education and a cheerleader every step of the way. You are the best role model for being both an intellectual and a gentleman by putting others before oneself. You paved the way for me to use the power of knowledge to help others, which I will continue to do for the rest of my life. Mom - you are amazing in every way and I hope to be as strong and fearless as you are. I also know now that you were most concerned about one of my greatest weaknesses, perseverance. I hope that through your immense love, incredible sacrifice, and ultimate commitment to making me the best person I can be, I have shown you that I not only have strength and wisdom, but the perseverance to continue to reach a goal despite the challenges in front of me. Your love is always in my heart and your final lesson is with me forever. My love and gratitude extends to the end of the world for all of you so this work is dedicated to you, my loving and devoted family.

Table of Contents

Chapter 8. Conclusions and Perspectives

List of Figures

List of Tables

Chapter 1. Introduction

1.1 Motivation

The human race has developed a lifestyle surrounded and dependent upon energy consuming devices. The energy demands of the world have only been increasing as our standard of living improves. Two critical energy challenges that we face with the increasing energy demands are the finite supply of fossil fuels[1] (**Figure 1-1**) and how inefficiently this limited supply is consumed[2] (**Figure 1-2a**). As over 80% of our current energy is provided by fossil fuels,[2] significant efforts need to be taken to more efficiently utilize and conserve one of our most precious natural resources as a bridge to other more renewable energy sources such as solar, wind, hydro, and biofuels. One of the proposed solutions to aid in improving the energy conversion efficiencies of our fossil fuels are fuel cells.

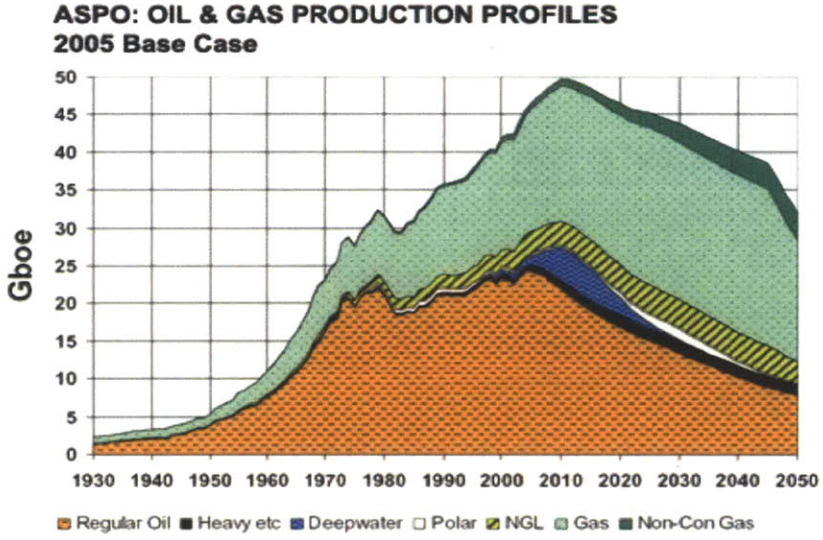

Figure 1-1. A graph provided by the Association for the Study of Peak Oil and Gas (ASPO) depicting the production of various oils and gas natural resources in billions of barrels of oil equivalent (Gboe) since the 1930's and projected to 2050, suggesting a peak in production in the 2010 decade.[1]

Fuel cells are electrochemical devices capable of directly converting fuel into electricity,[3, 4] and they are not limited by the conventional Carnot efficiency governing thermal-mechanical conversion systems. The theoretical conversion efficiencies for a fuel cell operating on oxygen and hydrogen are between >80% - 70% at 30 °C to 600 °C, respectively while the Carnot

efficiency is <65% - 30% at 200 °C to 600 °C respectively (**Figure 1-3**).[4] This increase in efficiency can aid in reducing the energy currently being wasted using conventional power plants, which will in turn help bridge the growing energy demands using the same and ultimately less fossil fuels (**Figure 1-2b**).[2] Another benefit of high temperature fuel cells is that they can easily accommodate biofuels, which are becoming more mainstream fuel sources.[5-12] Of particular interest are solid oxide fuel cells (SOFC), which has the highest,[13, 14] reported power densities and are viable energy conversion systems for both small micro-scale devices[15-23] to large power plant conversion systems.[24, 25]

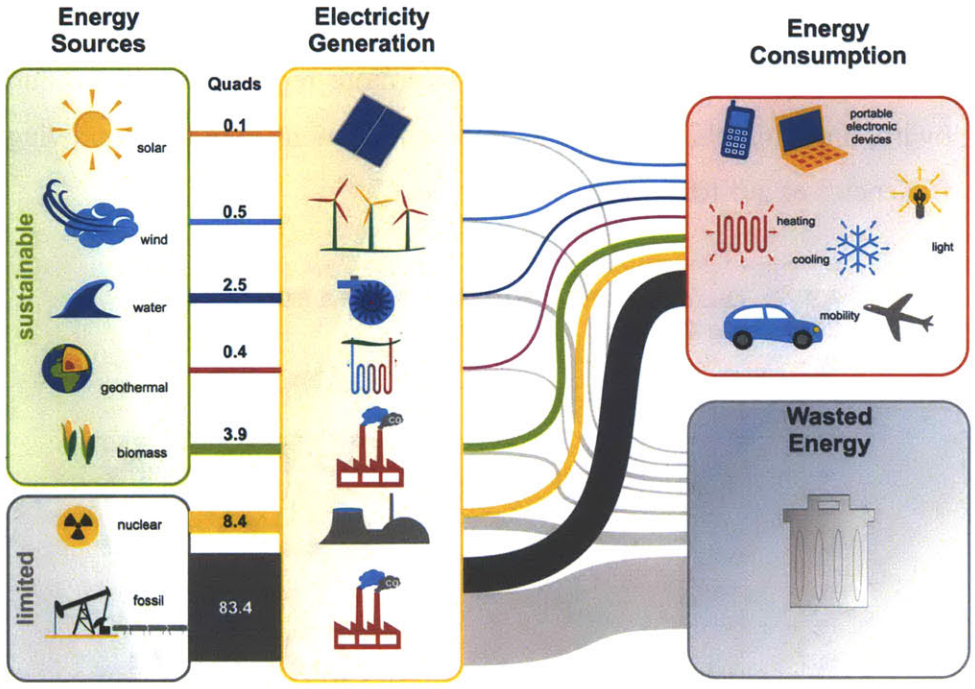

Figure 1-2a. Schematic representing the estimated U.S. Energy usage in 2008.[2]

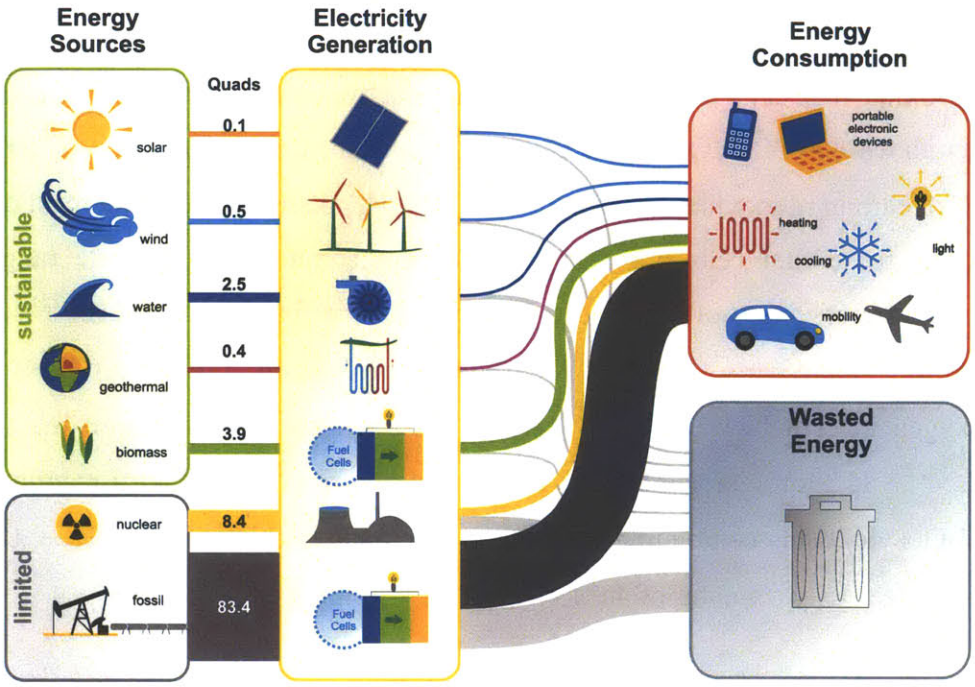

Figure 1-2b. Schematic depicting the potential increase in energy available for energy consumption by implementing fuel cells to more efficiently convert biomass and fossil fuels into electricity.[2]

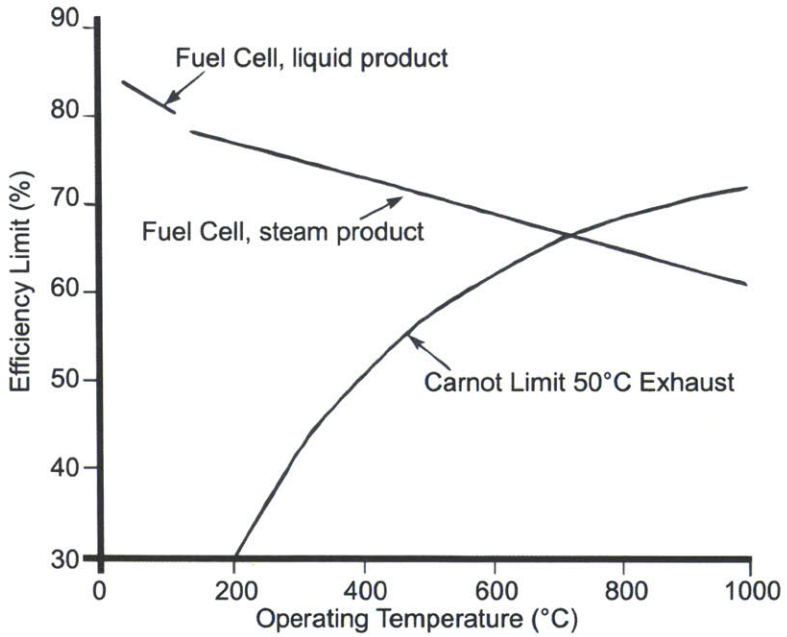

Figure 1-3. The thermodynamic efficiency limits of fuel cells and Carnot limited energy conversion systems as a function of the operating temperature.[4]

1.2 Solid Oxide Fuel Cell

Solid oxide fuel cells are high temperature electrochemical systems often operating at temperatures above 800 °C.[3] Oxygen serves as the oxidant for a wide range of fuels, such as hydrogen (H_2), carbon monoxide (CO), and methane (CH_4) being amongst the most common.[3, 4, 26, 27] However, these fuel cells are also capable of accommodating a wide range of other (hydro)carbon species, many of which can be derived from fossil or biofuels.[5-12] SOFCs are comprised of three main parts, a cathode electrode oxygen reduction reaction (ORR) $O_2 + 4e^- \rightarrow 2O^{2-}$, an oxygen ion conducting electrolyte, and an anode for fuel oxidation reaction (FOR), **Figure 1-4**.[3, 4, 27] If hydrogen gas is used as the fuel, the resulting half-cell reaction is $2\ H_2 + 2O^{2-} \rightarrow 2\ H_2O + 4e^-$, thus completing the overall electrochemical reaction ($2H_2 + O_2 \rightarrow 2H_2O$) and producing electricity (transfer of $4e^-$ for every 2 H_2O produced).

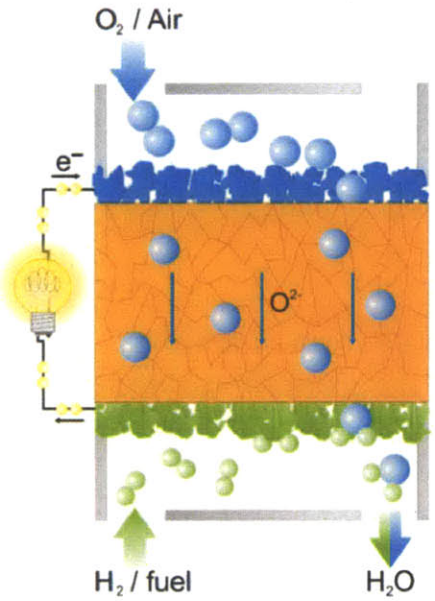

Figure 1-4. Schematic of a fuel cell operating on oxygen at the cathode (in blue), and hydrogen at the anode (in green) separated by the oxygen ion-conducting electrolyte (in orange).

Conventional SOFC materials include $(La,Sr)MnO_{3-\delta}$ (LSM) in a ABO_3 perovskite structure for the cathode, yttria-stabilized zirconia (YSZ) electrolyte, and a composite Ni-YSZ anode.[3, 4, 27] **Figure 1-5** demonstrates the area specific resistance (ASR) for a typical LSM / YSZ / Ni-YSZ fuel cell[27] where we observe that a significant amount of the fuel cells overall resistance is attributed to the sluggish ORR activity of the LSM cathode. As the fuel cell

operating temperature is increased the cathodic resistances decrease contributing to the reduction in the overall fuel cell resistance, however the slow ORR still constitutes a vast majority of the overall resistances (**Figure 1-5**).[27] Unfortunately, at these higher temperatures where the overall resistances are lower, expensive materials to construct the fuel cell that are chemically and mechanically stable in such harsh operating conditions are expensive and increase the overall cost for this technology. By reducing the fuel cells operating temperatures, less expensive materials such as steel become viable options;[25] additionally the theoretical fuel cell efficiencies are improved (**Figure 1-3**).[4] However despite the increase in theoretical efficiencies,[4] practically, the oxygen reaction kinetics becomes slower at the lower operating temperatures causing the cathode resistances to increase exponentially (**Figure 1-5**).[27] Therefore, significant efforts need to be taken to further understand the processes governing the oxygen reduction reaction as well as enhance the cathodes ORR activity as temperatures are reduced.

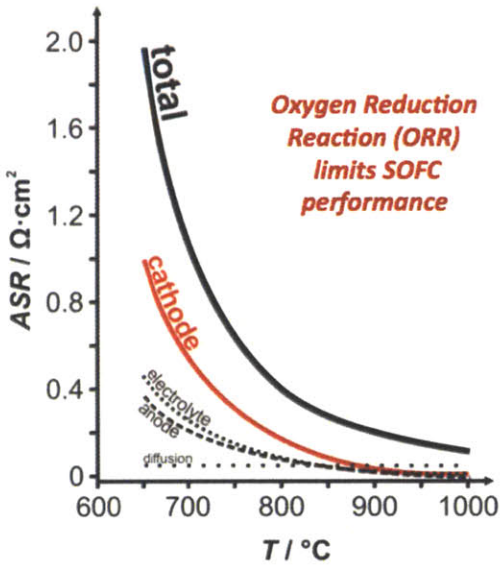

Figure 1-5. The area specific resistance (ASR) as a function of temperature for an LSM / YSZ / Ni-YSZ SOFC operating on hydrogen and oxygen. Our desired goal is to reduce the ASR at lower operating conditions.[27]

This work aims to enhance our understanding and develop highly active oxide cathode materials for ORR at an intermediate temperature of less than 600 °C.[28-31] The foundation for these experiments are epitaxially grown $La_{0.8}Sr_{0.2}CoO_{3-\delta}$ ($LSC80\text{-}20_{113}$) thin films which have previously been shown to have enhanced oxygen surface exchange activity greater then bulk $LSC80\text{-}20_{113}$ at 520 °C.[32] To further enhance epitaxial $LSC80\text{-}20_{113}$'s activity, heterostructured

interfaces between the perovskite $LSC80\text{-}20_{113}$ and the A_2BO_4 Ruddlesden-Popper $(La_{0.5}Sr_{0.5})_2CoO_{4\pm\delta}$ (LSC_{214}) were investigated using patterned micro-electrodes and electrochemical impedance spectroscopy (EIS).[29] To probe the influence of strontium substitution on the catalytic activity of an epitaxial LSC thin film and at the heterostructured interface of LSC_{214}, epitaxial base films with the Sr content of 40% ($LSC60\text{-}40_{113}$) were grown both bare and decorated with LSC_{214}.[28] To explore the properties of bare $LSC80\text{-}20_{113}$ and LSC_{214}-decorated epitaxial $LSC80\text{-}20_{113}$ thin films, *in situ* high resolution X-ray Diffraction (HRXRD) and ambient pressure X-ray photoelectron spectroscopy (APXPS) as a function of temperature, oxygen partial pressure,[31] and/or applied potentials.[30]

1.3 Heterostructured Oxides

The reason for studying oxide interfaces is their potential to have very unique transport properties.[33-39] Therefore, leveraging these properties to help improve catalytic activity and obtain a deeper understanding for what role interfaces can play in kinetic reactions can be invaluable.[29, 40-42] Heterostructured interfaces have previously been applied to explore oxygen reduction reactions[40-42] (**Figure 1-6**) and shown a significant increase in the reactants reaction rates. Unfortunately, it is very challenging to investigate and isolate what about these interfaces is unique, thus increasing the difficulty to systematically improve their performance. Some of the factors that may contribute to enhanced performance for both conventional bulk materials or heterostructured interfaces are lattice mismatch,[37] space charge effects,[36] an increase in oxygen vacancy concentration,[43] or a change in electronic structure.[44] This work explores the LSC_{113}/LSC_{214} interfaces using electrochemical impedance spectroscopy (EIS)[28, 29] and *in situ* ambient pressure XPS (APXPS) to gain additional insight into the properties that may be responsible for the enhanced ORR activity.[30]

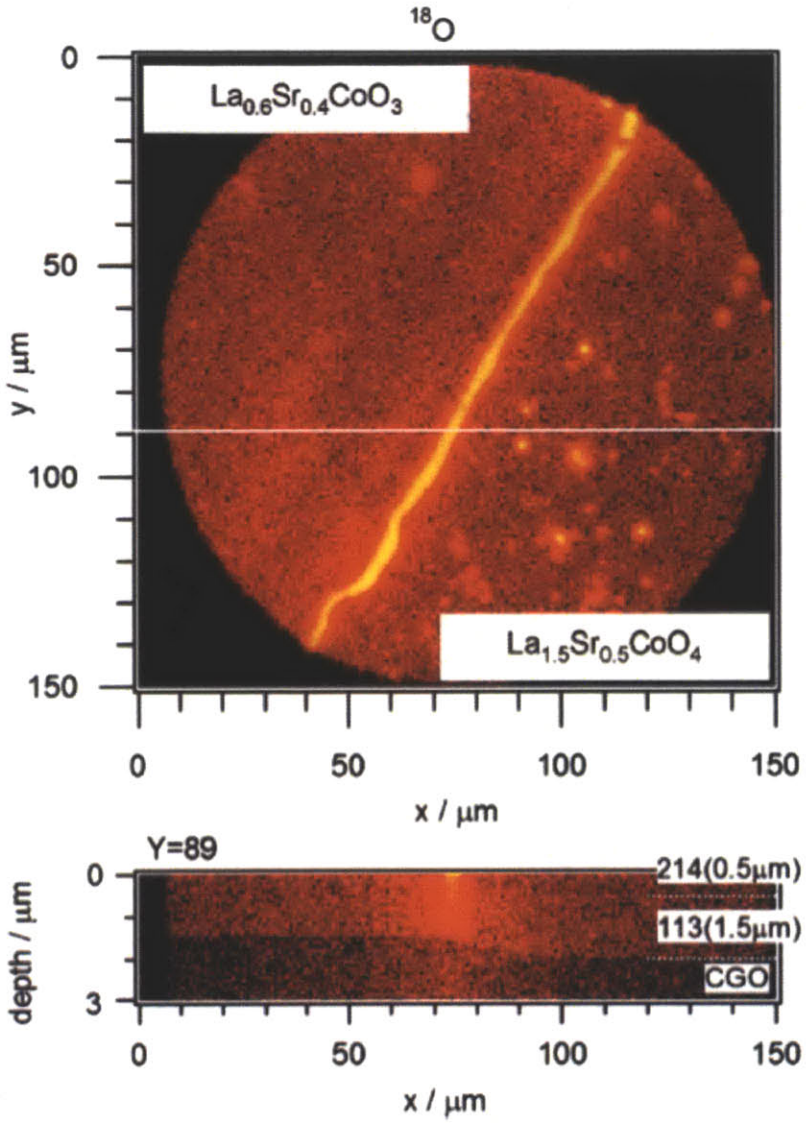

Figure 1-6. Reproduction of Sase et al[40] secondary ion mass spectroscopy (SIMS) images of ^{18}O intensity at the surface (above) and the cross-sectional images (below) of $La_{1.5}Sr_{0.5}CoO_4/La_{0.6}Sr_{0.4}CoO_3$ on a $Ce_{0.9}Gd_{0.1}O_{1.95}$substrate after the diffusion annealing at 773 K for 180 s in 0.2 bar $^{18}O_2$ gas. The bright line indicates the enhanced oxygen exchange at the heterointerface of $La_{1.5}Sr_{0.5}CoO_4/La_{0.6}Sr_{0.4}CoO_3$.

1.4 *In Situ* Characterization

To truly capture the behavior epitaxial LSC80-20_{113} and LSC_{214}-decorated LSC80-20_{113} and understand what may be responsible for the enhanced reaction mechanisms observed, we need to utilize tools that are capable of characterizing the reactions *in situ*. Moving beyond using EIS to solely observe the enhanced ORR activity, this work will discuss the progress and insight gained

from in situ high resolution XRD (HRXRD) and ambient pressure XPS (APXPS).[30, 31] *In situ* XRD will be utilized to understand how LSC80-20_{113} crystal structure is influenced by increased temperature and applied cathodic bias, while *in situ* APXPS provided the changes to various LSC80-20_{113}, LSC_{214}, and LSC_{214}-decorated LSC80-20_{113} films surface composition as a function of temperature and applied cathodic biases.[30]

1.5 Technical Overview

Chapter 2. will provide a brief overview of the experimental procedures taken to synthesis and study the various LSC thin films.[28-31] Specific details for each study will be provided within their respective **Chapters 3-6**.[28-31]

Chapter 3. is the foundation and inspiration for this thesis. This chapter will detail the unique method for studying the ORR activity of the heterostructured interface between LSC80-20_{113} and LSC_{214}. *Ex situ* XRD, atomic force microscopy (AFM), and scanning electron microscopy (SEM) is used to fully characterize the various degrees of LSC_{214}-decoraged LSC80-20_{113} ranging from a partial to complete coverage (~0.1 nm to 15 nm of LSC_{214} decoration). Using photolithography to turn the dense thin film into microelectrodes for electrochemical impedance spectroscopy (EIS) a 3-orders of magnitude enhancement in ORR activity was observed on the partially decorated films compared to bare LSC80-20_{113}. Scanning transmission electron microscopy (STEM) and conducting EIS on various sized microelectrodes we learn more about the interface and what could be contributing to the enhanced ORR activity.[29]

Chapter 4. is a continuation of **Chapter 3**,[29] attempting to learn more about what may be responsible for the enhanced activity of epitaxial LSC80-20_{113} films compared to bulk and the additional enhancements when decorated with LSC_{214} by increasing the Sr substitution to 40%. In bulk LSC_{113}, it has been shown that an increased Sr concentration leads to enhanced ORR activity. Therefore, this work continues the efforts to understand what role an increase in Sr substitution can ORR activity and whether it can further enhance ORR activity when grown as an epitaxial thin-film both bare and decorated with LSC_{214}. Using the aforementioned *ex situ* characterization techniques and micropatterned electrodes for EIS its discovered that the increase

in Sr within the epitaxial base film possessed significantly greater oxygen vacancy concentrations than LSC80-20_{113} epitaxial films, they had a lower vacancy concentration then what has been previously reported for bulk LSC60-40_{113}. Interestingly unlike bulk LSC80-20_{113} and LSC60-40_{113}, which show different ORR activity, the epitaxially grown LSC60-40_{113} did not lead to any clear increases in ORR activity for both the bare and LSC_{214}-decorated samples.[28] These results suggest that the properties of the film bulk may be less important then the surface properties at high temperatures, pressures and under applied potentials, all of which lead well into **Chapters 5**[31] **and 6**[30] which utilize *in situ* characterization to better understand how these materials behave near operating conditions.

Chapter 5. as an initial starting point for *in situ* characterization it was important to try to identify some of the key differences between LSC80-20_{113} as a bulk pellet and epitaxial thin film. Previous work established epitaxial LSC80-20_{113} having enhanced ORR activity over bulk pellet sample, *in situ* characterization is used to help understand why. To confirm the epitaxial thin films phase stability and strain state as temperature is increased from 30 °C to 550 °C in $p(O_2)$ of 1 atm, *in situ* HRXRD was conducted and reveled the LSC80-20_{113}'s strain transitioning between compression to tension at ~300 °C out-of-plane and tension to compression in-plane. The surface elemental composition was probed using *in situ* APXPS was conducted on both LSC80-20_{113} epitaxial thin film and bulk pellet at temperatures between 30 °C and 520 °C in $p(O_2)$ of $1 \cdot 10^{-3}$ atm. One of the most striking observations was the significant increase in Sr enrichment within the epitaxial LSC80-20_{113} lattice structure and reduction in surface Sr-(hydr)oxide phases while the bulk pellet remained unchanged, which may play a key role governing the epitaxial thin films enhanced ORR activity.

Chapter 6. leveraging the insight gained from the previous study, they were applied to further the understanding of bare and LSC_{214}-decorated LSC80-20_{113} under applied cathodic potentials. In this study, *in situ* HRXRD of LSC80-20_{113} was conducted to understand the structure changes that occur when under applied cathodic potentials (0 V to –0.8 V) at 550 °C and $p(O_2)$ of 1 atm. Together with *in situ* APXPS of LSC80-20_{113}, LSC_{214} and LSC_{214}-decorated LSC80-20_{113} films at various temperatures (220 °C to 520 °C) at a $p(O_2)$ of $1 \cdot 10^{-3}$ atm and under applied cathodic

potentials (0 V to –0.8 V, –1.2 V for LSC80-20_{113}) to understand how the surface elemental composition changes. Interestingly one observes that the LSC80-$20_{113/214}$ film is capable of stabilizing a much larger concentration of Sr enrichment within the lattice as well as an increase in surface Sr species while possessing low concentrations of other surface (hydr)oxide species, which combined may provide an explanation for the enhanced ORR activity.[30]

Chapter 7. will provide a brief discussion into the mechanism governing the oxygen reduction reaction and the possible reason behind the activity enhancement of $LSC_{113/214}$ compared to LSC_{113}.

Chapter 8. will provide my conclusion and perspectives of heterostructured LSC_{113} and $LSC_{113/214}$ electrode materials, and *in situ* characterization.

References

1. *Association for the Study of Peak Oil and Gas,* http://www.usehalf.com/peakoil/PeakOil.html, 2005.
2. *U.S. Energy Use,* http://www.usehalf.com/peakoil/PeakOil.html, 2008.
3. S. B. Adler, *Chem. Rev.*, 2004, **104**, 4791-4843.
4. J. Larminie and A. Dicks, *Fuel Cell Systems Explained*, John Wiley & Sons Inc, NJ, USA, 2003.
5. M. Andersson, H. Paradis, J. L. Yuan and B. Sunden, *Journal of Fuel Cell Science and Technology*, 2011, **8**.
6. S. Cordiner, M. Feola, V. Mulone and F. Romanelli, *Applied Thermal Engineering*, 2007, **27**, 738-747.
7. R. U. Dietrich, A. Lindermeir, J. Oelze, C. Spieker, C. Spitta and M. Steffen, in *Solid Oxide Fuel Cells 12*, eds. S. C. Singhal and K. Eguchi, 2011, vol. 35, pp. 2669-2683.
8. J. Mermelstein, M. Milian and N. P. Brandon, *Journal of Power Sources*, 2011, **196**, 5027-5034.
9. Y. Shiratori, T. Ijichi, T. Oshima and K. Sasaki, *International Journal of Hydrogen Energy*, 2010, **35**, 7905-7912.
10. E. Vakouftsi, G. E. Marnellos, C. Athanasiou and F. Coutelieris, *Solid State Ionics*, 2011, **192**, 458-463.
11. J. Van herle, F. Marechal, S. Leuenberger and D. Favrat, *Journal of Power Sources*, 2003, **118**, 375-383.
12. J. Van herle, Y. Membrez and O. Bucheli, *Journal of Power Sources*, 2004, **127**, 300-312.
13. Z. P. Shao and S. M. Haile, *Nature*, 2004, **431**, 170-173.
14. E. D. Wachsman and K. T. Lee, *Science*, 2011, **334**, 935-939.
15. D. Beckel, A. Bieberle-Huetter, A. Harvey, A. Infortuna, U. P. Muecke, M. Prestat, J. L. M. Rupp and L. J. Gauckler, *Journal of Power Sources*, 2007, **173**, 325-345.
16. E. J. Crumlin, G. J. la O and Y. Shao-Horn, in *Solid Oxide Fuel Cells 10*, ed. K. S. S. C. Y. H. M. H. Eguchi, 2007, vol. 7, pp. 981-986.
17. J. Fleig, H. L. Tuller and J. Maier, *Solid State Ionics*, 2004, **174**, 261-270.

18. V. Lawlor, S. Griesser, G. Buchinger, A. G. Olabi, S. Cordiner and D. Meissner, *Journal of Power Sources*, 2009, **193**, 387-399.

19. S. J. Litzelman, J. L. Hertz, W. Jung and H. L. Tuller, *Fuel Cells*, 2008, **8**, 294-302.

20. Y. Liu, S.-I. Hashimoto, H. Nishino, K. Takei, M. Mori, T. Suzuki and Y. Funahashi, *Journal of Power Sources*, 2007, **174**, 95-102.

21. N. M. Sammes, Y. Du and R. Bove, *Journal of Power Sources*, 2005, **145**, 428-434.

22. Z. P. Shao, S. M. Haile, J. Ahn, P. D. Ronney, Z. L. Zhan and S. A. Barnett, *Nature*, 2005, **435**, 795-798.

23. T. Suzuki, T. Yamaguchi, Y. Fujishiro and M. Awano, *Journal of Power Sources*, 2006, **160**, 73-77.

24. F. Mueller, B. Tarroja, J. Maclay, F. Jabbari, J. Brouwer, S. Samuelsen and Asme, *Design, Simulation and Control of a 100 Megawatt-Class Solid Oxide Fuel Cell Gas Turbine Hybrid System*, 2008.

25. M. C. Williams, J. P. Strakey and S. C. Singhal, *Journal of Power Sources*, 2004, **131**, 79-85.

26. S. McIntosh and R. J. Gorte, *Chem. Rev.*, 2004, **104**, 4845-4865.

27. S. C. Singhal and K. Kendall, *High Temperature Solid Oxide Fuel Cells - Fundamentals, Design, and Applications*, Elsevier, 2003.

28. E. J. Crumlin, S.-J. Ahn, D. Lee, E. Mutoro, M. D. Biegalski, H. M. Christen and Y. Shao-Horn, *Journal of the Electrochemical Society*, 2012, (Accepted).

29. E. J. Crumlin, E. Mutoro, S.-J. Ahn, G. J. la O', D. N. Leonard, A. Borisevich, M. D. Biegalski, H. M. Christen and Y. Shao-Horn, *The Journal of Physical Chemistry Letters*, 2010, **1**, 3149 - 3155.

30. E. J. Crumlin, E. Mutoro, Z. Liu, M. D. Biegalski, W. T. Hong, H. M. Christen, H. Bluhm and Y. Shao-Horn, *(In Preparation)*, 2012.

31. E. J. Crumlin, E. Mutoro, Z. Liu, M. E. Grass, M. D. Biegalski, Y.-L. Lee, D. Morgan, H. M. Christen, H. Bluhm and Y. Shao-Horn, *Energy & Environmental Science*, 2012, **5**, 6081-6088.

32. G. J. la O, A. Sung-Jin, C. Ethan, O. Yuki, D. B. Michael, M. C. Hans and S.-H. Yang, *Angewandte Chemie International Edition*, 2010, **49**, 3.

33. J. Garcia-Barriocanal, A. Rivera-Calzada, M. Varela, Z. Sefrioui, E. Iborra, C. Leon, S. J. Pennycook and J. Santamaria, *Science*, 2008, **321**, 676-680.
34. J. Garcia-Barriocanal, A. Rivera-Calzada, M. Varela, Z. Sefrioui, E. Iborra, C. Leon, S. J. Pennycook and J. Santamaria, *Science*, 2009, **324**.
35. X. Guo, *Science*, 2009, **324**.
36. X. X. Guo and J. Maier, *Adv. Mater.*, 2009, **21**, 2619-2631.
37. C. Korte, N. Schichtel, D. Hesse and J. Janek, *Mon. Chem.*, 2009, **140**, 1069-1080.
38. A. Cavallaro, M. Burriel, J. Roqueta, A. Apostolidis, A. Bernardi, A. Tarancon, R. Srinivasan, S. N. Cook, H. L. Fraser, J. A. Kilner, D. W. McComb and J. Santiso, *Solid State Ionics*, 2010, **181**, 592-601.
39. N. Schichtel, C. Korte, D. Hesse and J. Janek, *Physical Chemistry Chemical Physics*, 2009, **11**, 3043-3048.
40. M. Sase, F. Hermes, K. Yashiro, K. Sato, J. Mizusaki, T. Kawada, N. Sakai and H. Yokokawa, *Journal of the Electrochemical Society*, 2008, **155**, B793-B797.
41. M. Sase, K. Yashiro, K. Sato, J. Mizusaki, T. Kawada, N. Sakai, K. Yamaji, T. Horita and H. Yokokawa, *Solid State Ionics*, 2008, **178**, 1843-1852.
42. K. Yashiro, T. Nakamura, M. Sase, F. Hermes, K. Sato, T. Kawada and J. Mizusaki, *Electrochemical and Solid State Letters*, 2009, **12**, B135-B137.
43. B. A. Fan and X. L. Liu, *Solid State Ionics*, 2009, **180**, 973-977.
44. E. Dagotto, *Science*, 2007, **318**, 1076-1077.

Chapter 2. Experimental Approach

2.1 Sample Preparation

For all ORR studies the primary thin-films investigated are LSC80-20_{113}, LSC60-40_{113}, LSC_{214}, and LSC_{214}-decorated LSC_{113} which were epitaxial grown using pulsed laser deposition (PLD, as shown in **Figure 2-1**) on a single crystal yttria-stabilized zirconia (YSZ) (100) oriented substrate with an interlayer of epitaxially grown gadolinium doped ceria (GDC).[1-4]

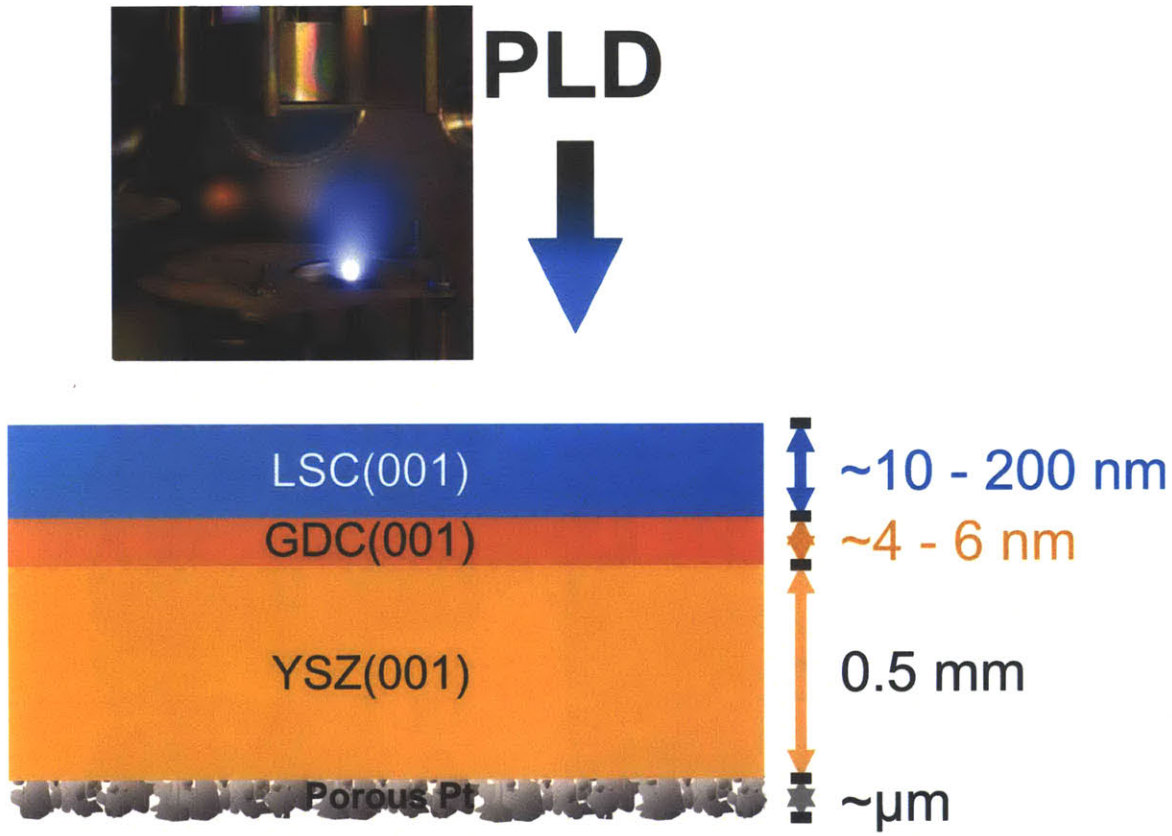

Figure 2-1. A photo of pulsed laser deposition (PLD) for the growth of an LSC thin film on YSZ with an interlayer of GDC. Below is a cross-section schematic detailing approximate thicknesses for each oxide layer.[1-4]

2.2 *Ex Situ* Characterization

Benefits for these dense thin-film electrodes are the comprehensive characterization that can be applied. The micro-patterning allows for easy tabulation for the electrodes surface area, and perimeter using an optical microscope. The high resolution X-ray diffraction (XRD) can help to confirm that the films are single phase and determine the orientation(s) of the films (**Figure 2-2a**).[1, 2] Scanning electron microscopy (SEM) and atomic force microscopy (AFM) can be utilized to evaluate the surface morphology and roughness of the films, respectively (**Figure 2-2b,c**).[1, 2] AFM can also be used to measure the height of the patterned electrodes.[1, 2] Lastly, high resolution scanning transmission electron microscopy (STEM) can be utilized to obtain atomic resolution information to help us understand what the films look like and the atomic arrangement at the interface of the various oxide layers (**Figure 2-2d**).[2] Applying all of these characterization techniques to these model systems allows for detailed understanding of electrodes initial condition.

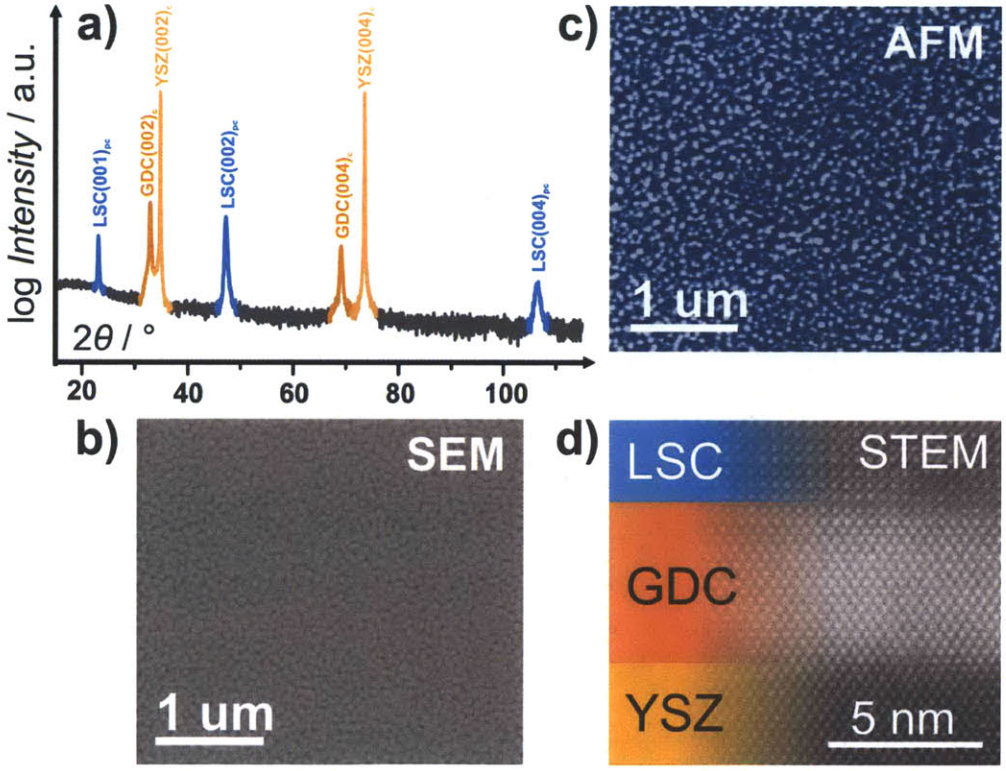

Figure 2-2. Various types of data that can be collected from *ex situ* characterization, (**a**) X-ray diffraction (XRD), (**b**) scanning electron microscopy (SEM), (**c**) atomic force microscopy (AFM), (**d**) scanning transmission electron microscopy (STEM).[1, 2]

2.3 Oxygen Reduction Reaction Activity Measurements

Electrochemical impedance spectroscopy (EIS) is a common *in situ* high temperature and high pressure electrochemical technique that can provide great insight into how an electrode is performing. This technique has been utilized for many cathodic ORR[1, 2, 5-13] studies. EIS possesses the ability to evaluate how sensitive each electrode is to temperature, pressure and when combined with reaction models can be utilized to elicit various reaction mechanisms.

For ORR studies utilizing an oxygen conducting electrolyte such as YSZ, both working and counter electrodes can be placed within a single chamber and be exposed to the same oxygen partial pressure. Since both working and counter electrodes are active catalysts for ORR and oxygen evolution reaction (OER), oxygen can essentially be oscillated between the working electrode and counter electrode, thus allowing both electrodes to be in the same oxygen environment.

To prepare the samples for electrochemical impedance spectroscopy (EIS), traditional photolithography techniques (as depicted in **Figure 2-3**) were utilized to create microelectrodes ranging in size from ~25 μm to ~200 μm (**Figure 2-4**).[1, 2]

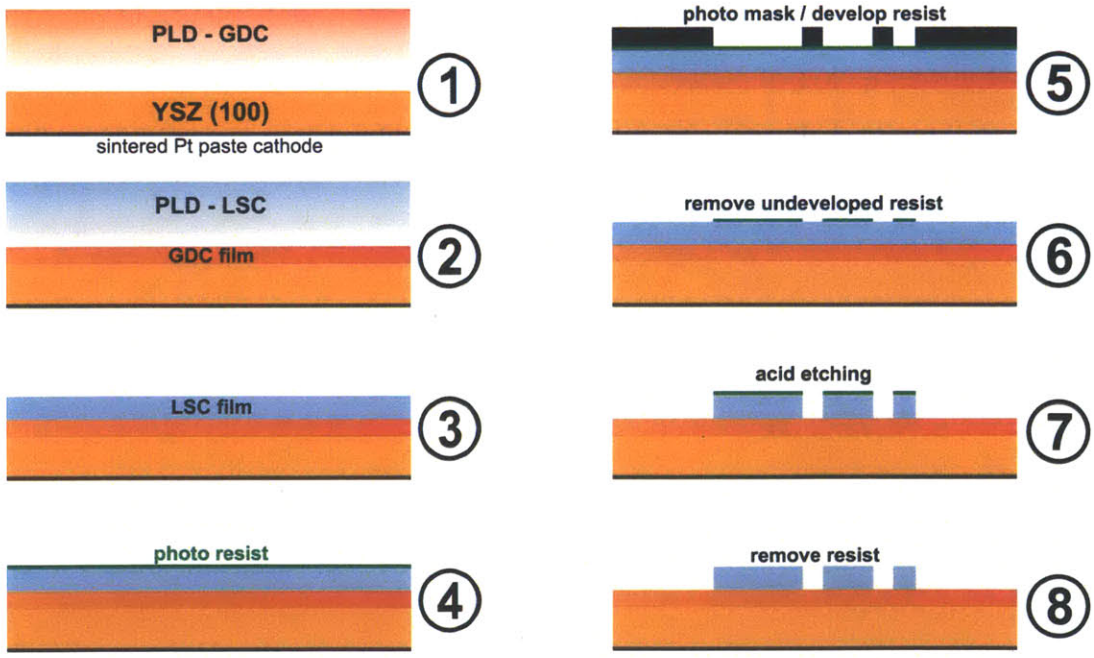

Figure 2-3. LSC microelectrode photolithography process. 1,2,3-Deposit of all desired oxide films, 4-coat with photoresist, 5-mask and UV light exposure, 6-chemical development to create features in resist, 7-acid etch, creating features within oxide film, 8-rinse in solvent to remove resist.[1, 2]

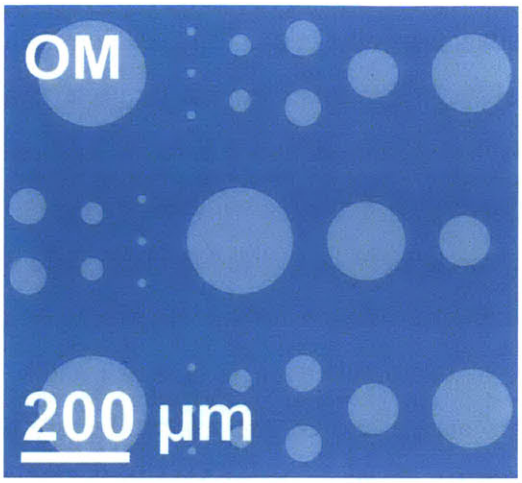

Figure 2-4. Optical microscopy image of patterned LSC80-20_{113} film.

A schematic detailing electrochemical impedance spectroscopy (EIS) is shown in **Figure 2-5** providing a representative Nyquist plot of the real and imaginary impedances accompanied with an equivalent circuit utilized to analyze the collected data. Of particular interest is the large low frequency semi-circle feature (blue) which corresponds to the oxygen reduction reaction. EIS measurements were collected on a large variety of LSC_{113} and LSC_{214}-decorated LSC_{113} samples under different oxygen partial pressures (1 atm to $1 \cdot 10^{-4}$ atm) and microelectrode sizes (~50 µm to ~200 µm in diameter). Specific EIS experimental details are provided within each respective chapter.[1, 2]

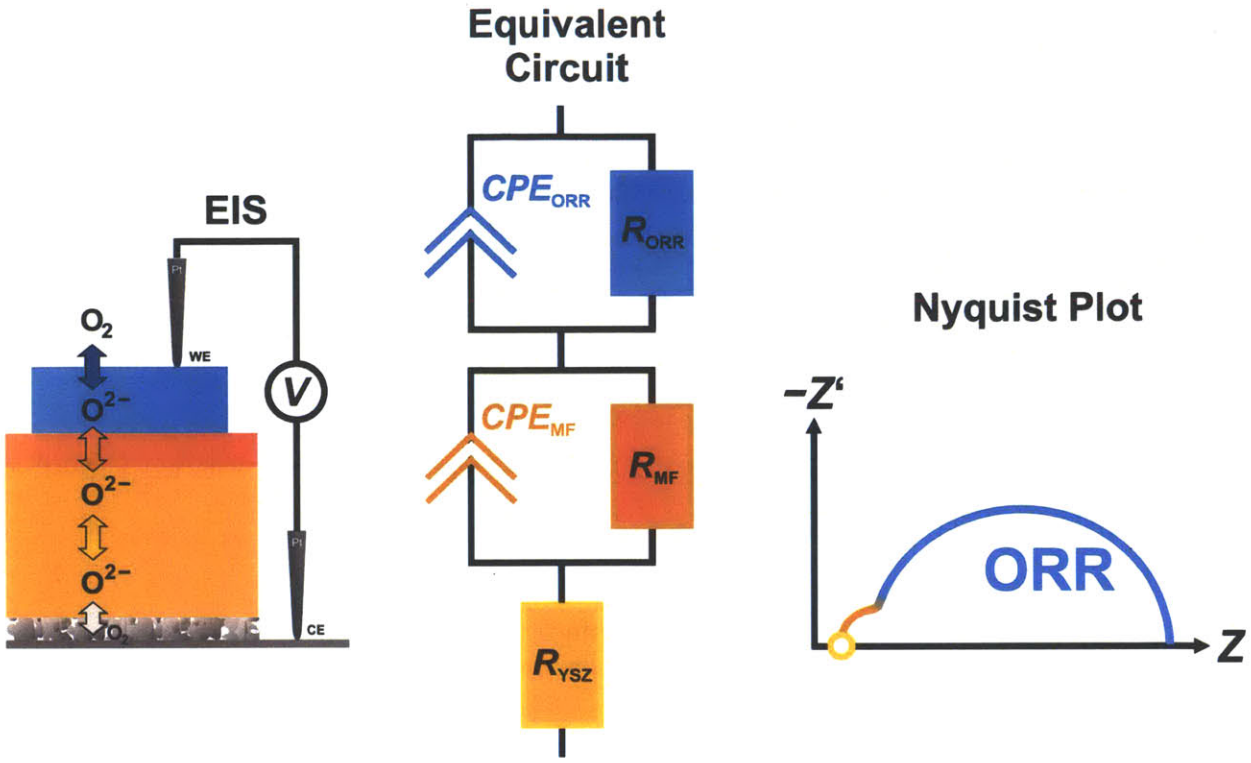

Figure 2-5. (Left) cross-section schematic depicting EIS of a microelectrode LSC thin-film, (middle) an equivalent circuit utilized to analyze the collected impedance spectra, (right) schematic of a characteristic features in Nyquist plot of the real and imaginary impedances collected during EIS. *R* = resistance, *CPE* = constant phase element (a non-ideal capacitor), *ORR* = oxygen reduction reaction (blue), *MF* = middle frequency (red) which is believed to represent resistance and capacitance associated to the interface between oxide layers, and R_{YSZ} = resistance from the oxygen ion transport within the YSZ electrolyte.[1, 2]

2.4 *In Situ* HRXRD and APXPS

EIS is a powerful tool for providing insight into the reaction processes at the electrode and to determine reaction rates. However, it is very challenging to obtain direct insight into how the material is behaving structurally, elemental compositionally. In order to determine if/what role the crystal structure or elemental composition may have in these reactions, it would be most ideal to study these properties *in situ*.[3, 4]

In Situ HRXRD

A high resolution XRD instrument equipped with a high temperature and atmosphere controlled sample holder with electrical leads was utilized to observe how the electrodes' phase,

orientation, lattice parameter, and film strain may change in constant $p(O_2)$ 1 atm at different temperatures (30 °C to 600 °C)[4] and applied potentials (0 V to –0.8 V)[3] at 550 °C. A schematic of the sample configuration for this experiment is shown in **Figure 2-6**.[3] Since larger samples can be utilized several wires can be connected to the sample, thus supporting a 3-electrode configuration with the LSC80-20_{113} thin film as the working electrode and porous Pt as the counter and reference electrodes. The film was fabricated using similar conditions previously discussed, however when sintering the Pt counter electrode on the bottom face of the YSZ substrate, a small corner on the top face was also coated with Pt paste for the sintering of the Pt reference electrode. Prior to LSC80-20_{113} PLD the Pt reference electrode was masked off to prevent physical contact to the film growth.[3]

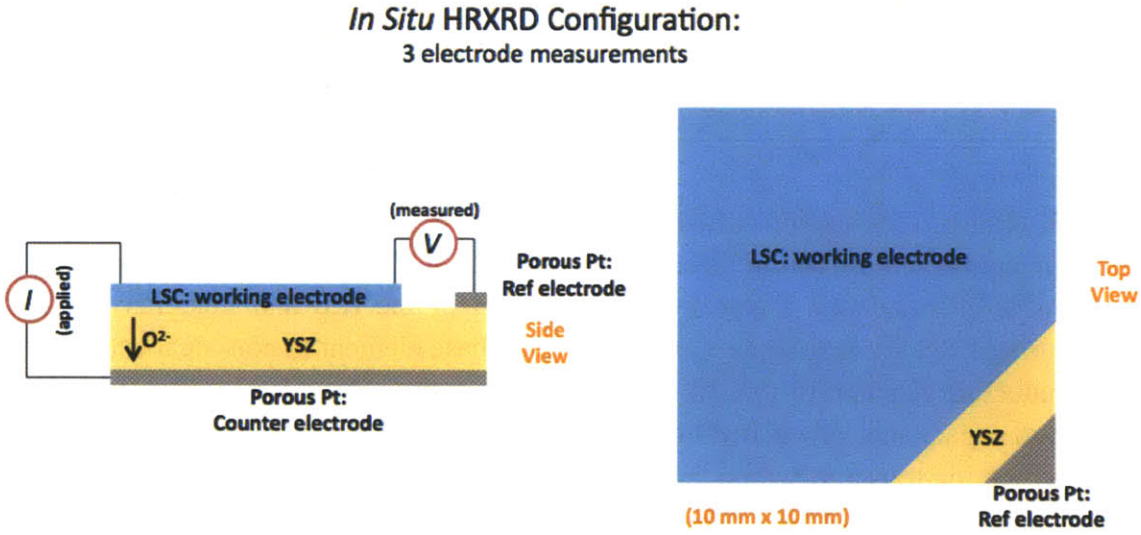

Figure 2-6. Side and top view for *in situ* HRXRD 3-electrode (LSC80-20_{113}-working, porous Pt-counter and reference electrodes) sample for high temperature and applied potential studies.[3]

In Situ APXPS

With the advent of *in situ* ambient pressure XPS surface information of these electrodes can be investigated at near operating conditions. The primary samples investigated were epitaxial thin-film of LSC80-20_{113} and a fractured bulk LSC80-20_{113} pellet for reference and comparison.[4] Primary temperature range for investigations include ~30 °C to ~520 °C at $p(O_2)$ of $1{\cdot}10^{-3}$ atm and a pressure range of $1{\cdot}10^{-3}$ atm to $1{\cdot}10^{-9}$ atm at ~520 °C. In addition, epitaxial thin-film of LSC80-20_{113}, LSC_{214}, and LSC_{214}-decorated LSC80-20_{113} films were investigated in a $p(O_2)$ of $1{\cdot}10^{-3}$ atm as a function of temperature ranging from ~220 °C to ~520 °C and applied

cathodic potentials 0 V to –0.8 V at 520 °C.[3] These experiments were conducted at Lawrence Berkeley National Laboratory's (LBL) Advanced Light Source (ALS) synchrotron facility beamlines 9.3.2 and 11.0.2. A schematic of the sample configuration for this experiment is shown in **Figure 2-7** and a picture of the sample inside the chamber at elevated temperatures is shown in **Figure 2-8**.[3]

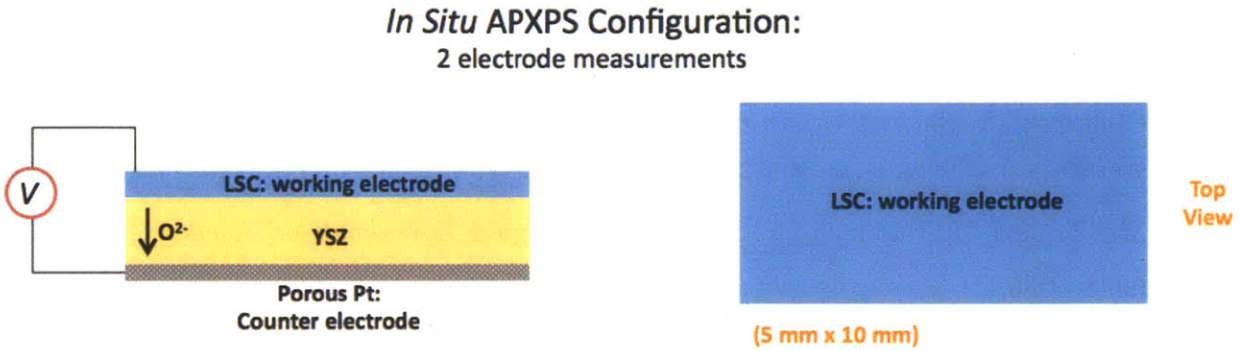

Figure 2-7. Side and top view for *in situ* APXPS due to the limited electrical inputs these studies can only facilitated a 2-electrode ($LSC80\text{-}20_{113}$-working, porous Pt-counter) sample configuration for high temperature and applied potential studies.[3]

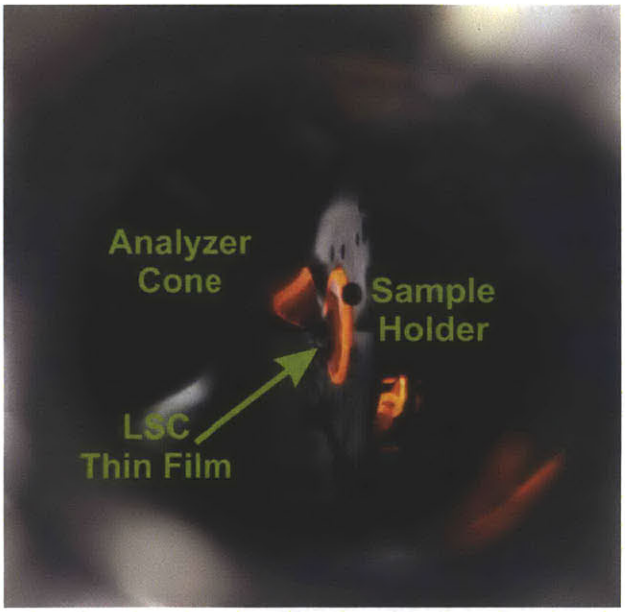

Figure 2-8. A photograph of the $LSC80\text{-}20_{113}$ sample within the *in situ* APXPS chamber at high temperatures and with applied potentials.[3]

2.5 References

1. E. J. Crumlin, S.-J. Ahn, D. Lee, E. Mutoro, M. D. Biegalski, H. M. Christen and Y. Shao-Horn, *Journal of the Electrochemical Society*, 2012, (Accepted).
2. E. J. Crumlin, E. Mutoro, S.-J. Ahn, G. J. la O', D. N. Leonard, A. Borisevich, M. D. Biegalski, H. M. Christen and Y. Shao-Horn, *The Journal of Physical Chemistry Letters*, 2010, **1**, 3149 - 3155.
3. E. J. Crumlin, E. Mutoro, Z. Liu, M. D. Biegalski, W. T. Hong, H. M. Christen, H. Bluhm and Y. Shao-Horn, *(In Preparation)*, 2012.
4. E. J. Crumlin, E. Mutoro, Z. Liu, M. E. Grass, M. D. Biegalski, Y.-L. Lee, D. Morgan, H. M. Christen, H. Bluhm and Y. Shao-Horn, *Energy & Environmental Science*, 2012, **5**, 6081-6088.
5. S. B. Adler, *Chem. Rev.*, 2004, **104**, 4791-4843.
6. F. S. Baumann, J. Fleig, G. Cristiani, B. Stuhlhofer, H. U. Habermeier and J. Maier, *Journal of the Electrochemical Society*, 2007, **154**, B931-B941.
7. V. Brichzin, J. Fleig, H. U. Habermeier, G. Cristiani and J. Maier, *Solid State Ionics*, 2002, **152-153**, 499 - 507.
8. V. Brichzin, J. Fleig, H. U. Habermeier and J. Maier, *Electrochemical and Solid State Letters*, 2000, **3**, 403-406.
9. J. Fleig, F. S. Baumann, V. Brichzin, H. R. Kim, J. Jamnik, G. Cristiani, H. U. Habermeier and J. Maier, *Fuel Cells*, 2006, **6**, 284-292.
10. G. J. la O and Y. Shao-Horn, *Electrochemical and Solid State Letters*, 2009, **12**, B82-B85.
11. G. J. la O, A. Sung-Jin, C. Ethan, O. Yuki, D. B. Michael, M. C. Hans and S.-H. Yang, *Angewandte Chemie International Edition*, 2010, **49**, 3.
12. G. J. la O, B. Yildiz, S. McEuen and Y. Shao-Horn, *Journal of the Electrochemical Society*, 2007, **154**, B427-B438.
13. G. J. la O', R. F. Savinell and Y. Shao-Horn, *J. Electrochem. Soc.* , 2009, **156**, B771 - B781.

Chapter 3. Oxygen Reduction Kinetics Enhancement on a Hetero-Structured Oxide Surface for Solid Oxide Fuel Cells

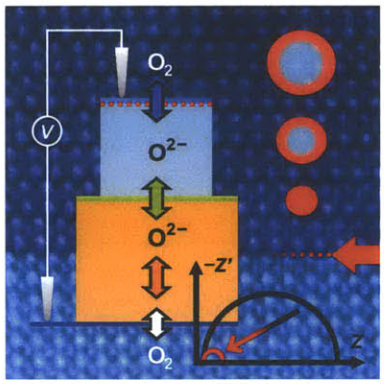

3.1 Introduction

The efficiency of solid oxide fuel cells (SOFCs) is limited primarily by the oxygen reduction reaction (ORR) at the cathode, and there is a need to search for electrode materials with enhanced ORR activity, particularly for SOFCs operated at intermediate temperatures. Mixed electronic and ionic conductors, such as ABO_3 perovskites[1-3] and A_2BO_4 Ruddelson-Popper materials,[4] are promising cathode materials due to their high oxygen ion diffusivity and surface exchange properties. Recently, hetero-structured oxide interfaces have shown surprisingly high transport or oxygen surface exchange properties.[5-14] In particular, Sase et al.[13] have reported

enhanced ORR kinetics ~3 orders of magnitude confined to an interfacial region of ~20 μm in width between $La_{0.6}Sr_{0.4}CoO_{3-\delta}$ and $(La_{0.5}Sr_{0.5})_2CoO_{4+\delta}$ films of ~1 μm in thickness relative to their bulk values. Subsequently these authors demonstrated ~1 order of magnitude enhancement in activity for the composite cathode screen-printed with these two oxide materials.[14] More recently, we have reported that epitaxial $La_{0.8}Sr_{0.2}CoO_{3-\delta}$ thin films grown on YSZ exhibit enhanced ORR kinetics up to ~2 orders of magnitude relative to bulk.[15]

In this study, we examine if $(La_{0.5}Sr_{0.5})_2CoO_{4+\delta}$ (LSC_{214}) surface decoration on epitaxial $La_{0.8}Sr_{0.2}CoO_{3-\delta}$ (LSC_{113}) thin films would lead to any further enhancement in ORR kinetics. We here report that LSC_{214}-surface decoration on the LSC_{113} thin films provides at least one additional order of magnitude of enhancement in ORR kinetics, achieving ~3-4 orders of magnitude enhancement over the entire electrode surface relative to bulk LSC_{113}.[16] Using geometrically well-defined thin film microelectrodes, particularly helpful to provide insights into ORR mechanisms,[17-24] we show that the active regions responsible for the ORR enhancement are the interfacial regions between LSC_{113} and LSC_{214}, which is good agreement with enhanced ORR activity observed at the interface of $La_{0.6}Sr_{0.4}CoO_{3-\delta}/(La_{0.5}Sr_{0.5})_2CoO_{4+\delta}$.[13]

3.2 Experimental Methods

Pt ink (#6082, BASF) counter electrodes were painted on one side of YSZ(001) single crystals (9.5 mol% Y_2O_3, Princeton Scientific) with dimensions of 10 x 10 x 0.5 mm and sintered for 1 hours at 800 °C in air. PLD deposition of GDC (500 laser pulses, ~5 nm thickness), LSC_{113} (15,000 pulses, (~85 nm; determined by AFM) and the surface coverages (either 25 pulses LSC_{113} (reference sample), 25 (~0.1 nm), 150 (~0.8 nm), 900 (~5 nm), or 2700 (~15 nm; determined by TEM cross section) pulses of LSC_{214}) were performed using self-synthesized stoichiometric targets under the following PLD conditions: KrF excimer laser, $\lambda = 248$ nm, 10 Hz pulse rate, ~50 mJ pulse energy, $p(O_2)_{PLD\ and\ cooling} = 10$ mTorr, growth temperatures: $T_{GDC} =$ 450 °C, $T_{LSC113,LSC214} = 675$ °C, $t_{cooling} = 1$ hour). Thin film high resolution XRD was performed in normal and off-normal configuration with a four-circle diffractometer (Panalytical and Bruker D8). Surface morphology was examined by optical microscopy (Carl Zeiss), AFM (Veeco), and SEM (Carl Zeiss). Microelectrodes (diameters ~50, ~100, ~150, and ~200 μm, exact diameter determined by optical microscopy) were prepared using photolithography. EIS measurements (electrodes contacted by Pt-coated tungsten carbide probes) were carried out using a microprobe

station (Karl Süss) connected to a frequency response analyzer (Solartron 1260) and dielectric interface (Solartron 1296). Data were collected between 1 MHz and 1 mHz using a voltage amplitude of 10 mV under Ar / O_2 mixtures in the $p(O_2)$ range of 10^{-4} to 1 atm. The temperature of 550 °C was measured on the sample surface and controlled with a heating stage (Linkam TS1500). ZView software (Scribner Associates) was used to analyze the EIS data. STEM (VG501UX or Nion UltraSTEM100) was utilized to examine thin film cross-sections and atomic resolution interface of LSC_{113}/LSC_{214}. Additional experimental details can be found in the Supporting Information.

3.3 Results and Discussion

Epitaxial thin films of LSC_{113} of ~85 nm in thickness were prepared by pulsed laser deposition (PLD) on yttria-stabilized zirconia (YSZ(001)) single crystals with gadolinium-doped ceria (GDC) as the buffer layer (**Figure 3-1a**) using conditions similar to those reported previously.[15] A surface decoration with LSC_{214} having different thicknesses, from partial to full coverage (~0.1 nm, ~0.8 nm, ~5 nm, ~15 nm), was deposited subsequently on top of LSC_{113}/GDC/YSZ(001) while a reference sample with surface decoration of ~0.1 nm LSC_{113} (LSC_{113}-reference) was made for comparison. Scanning electron microscopy (SEM) and atomic force microscopy (AFM) images showed that the LSC_{113}-reference and LSC_{214} surface decorated films were dense having low surface roughness of ~1 nm (**Figures 3-1b**, **S3-1**). Electrochemical impedance spectroscopy (EIS) measurements were used to probe ORR kinetics on geometrically well-defined LSC_{113} and LSC_{113}/LSC_{214} microelectrodes (**Figure 3-1b**) created by photolithography and acid etching, where sintered porous Pt served as the counter electrode. EIS data were analyzed using an equivalent circuit depicted in **Figure 3-1c,** from which the ORR resistance (R_{ORR}) and surface oxygen exchange rate were obtained.

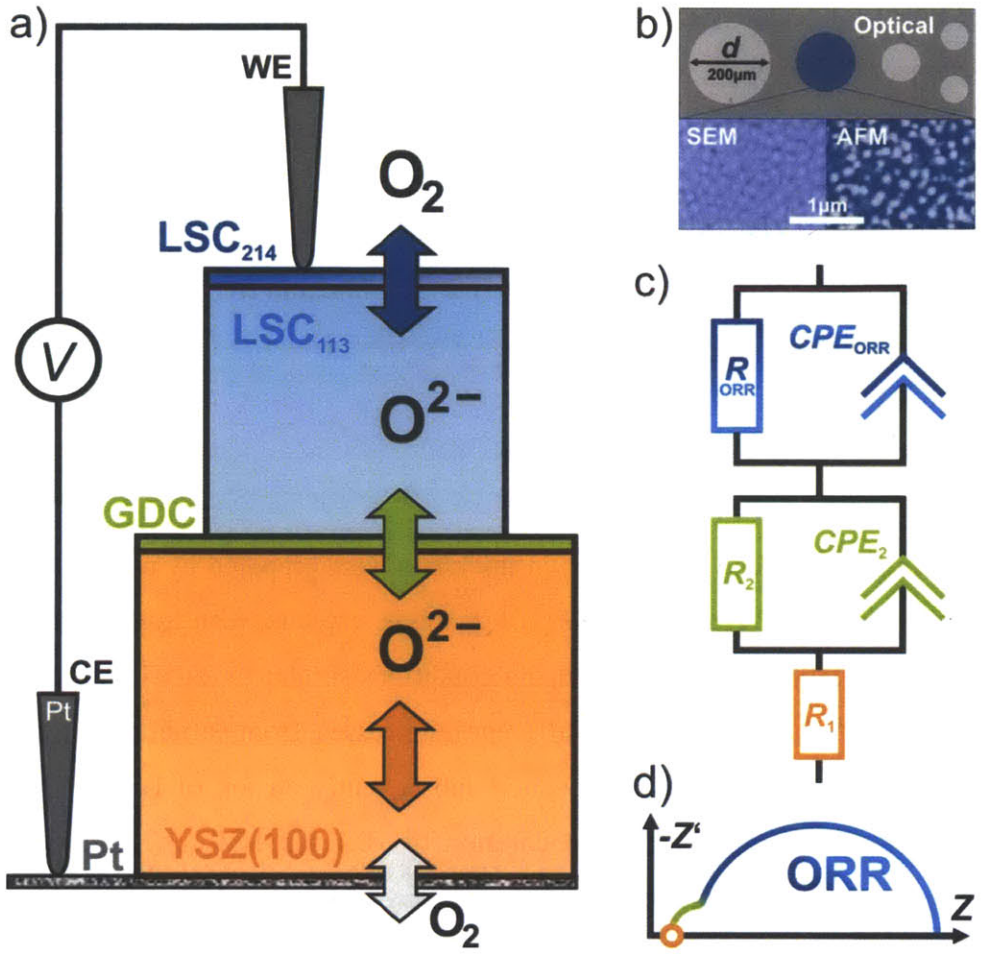

Figure 3-1. a) Schematic of an LSC_{214}/LSC_{113}/GDC/YSZ(001)/porous Pt sample and electrochemical testing configuration (not drawn to scale, dimensions provided in the **Experimental Methods §3.2**), b) optical image of a micro-patterned LSC_{113}-reference sample and magnified surface topography (SEM/AFM) with full height range of ~6 nm in the AFM image, c) equivalent circuit (R_1 = YSZ electrolyte resistance, R_2 = electrode/electrolyte interface resistance,[15] R_{ORR} = ORR resistance, CPE = constant phase element) used to extract ORR kinetics, and d) characteristic Nyquist plot schematic (color key: orange = YSZ/bulk transport, green = GDC/interface, blue = LSC/ORR).

Similar to our previous studies,[15] normal X-ray diffraction (XRD) data (**Figure 3-2a**) clearly show the presence of the $(00l)_{pc}$ (l is integer) or $(00l)_{cubic}$ (l is even) peaks of LSC_{113}, GDC, and YSZ, which indicates $(001)_{pc}LSC_{113}$ // $(001)_{cubic}$GDC // $(001)_{cubic}$YSZ. The subscript "pc" denotes the pseudocubic notation. With increasing LSC_{214} coverage to ~5 nm and ~15 nm in thickness, the $(00l)_{tetragonal}$ peaks (l is even) of LSC_{214} become visible, corresponding to $c_{tetragonal}$ = 12.5 Å, comparable to published values.[25,26] Off-normal phi-scan analysis of a similarly prepared sample with a thicker (~45 nm) LSC_{214} coverage (**Figure 3-2b**) allowed us to identify the in-plane

crystallographic relationships between GDC and YSZ (a cube-on-cube alignment), LSC_{113} and GDC (a 45° rotation having $[100]_{pc}LSC_{113}$ // $[110]_{cubic}GDC$ // $[110]_{cubic}YSZ$), and LSC_{113} and LSC_{214} (no rotation having $[100]_{pc}LSC_{113}$ // $[100]_{tetragonal}LSC_{214}$), shown in **Figure 3-2c and Figure S3-2**. The relaxed lattice parameters of the LSC_{113} films with and without LSC_{214} surface decoration in this study were found to be in the range of 3.84 -3.85 Å, having in-plane tensile strains and compressive strains in the direction normal to the film surface at room temperature (**Table S3-1**), which are in reasonably good agreement with those reported previously.[15] The origin of these strains is not understood fully but might be a consequence of different thermal expansion coefficients between YSZ (~11×10^{-6} °C^{-1} [27]) and LSC films (~17×10^{-6} °C^{-1} for bulk[28]). Experiments are ongoing to examine how these strains change upon heating to high temperatures.

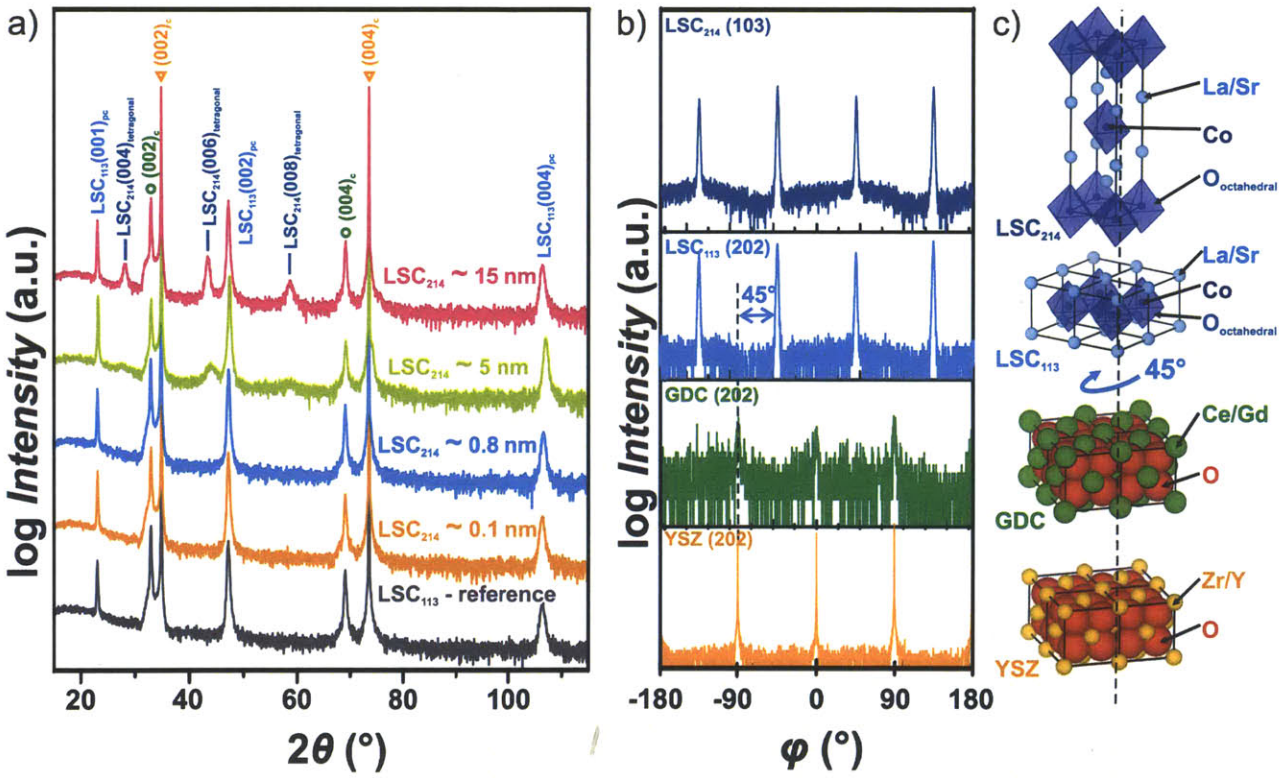

Figure 3-2. X-Ray diffraction analysis: a) normal XRD of the LSC_{113}-reference and the LSC_{214}-covered LSC_{113} films; LSC_{113} peaks are labeled in the pseudocubic (pc) notation,[15] GDC and YSZ peaks were marked by open circles (○) and open triangles (∇), respectively, b) off-normal XRD of a similarly prepared sample with a thicker (~45 nm) LSC_{214} coverage, c) schematic of the crystallographic rotational relationships among the $LSC_{214}(001)_{tetragonal}$, $LSC_{113}(001)_{pc}$, $GDC(001)_{cubic}$, and $YSZ(001)_{cubic}$.

EIS data of all samples used in this study were found to be very similar in shape, and typical features in the Nyquist plots are shown in the schematic in **Figure 3-1d**. The predominant semicircle (assigned to ORR impedance) was found to increase with decreasing $p(O_2)$. Representative EIS data collected at 550 °C in 1% $p(O_2)$ are shown in **Figures 3-3a, b**. All films with LSC_{214} surface decoration were found to have markedly smaller real impedance relative to the LSC_{113} films reported previously[15] and the LSC_{113}-reference film of this study. The ORR area specific resistance ($ASR_{ORR} = R_{ORR} \cdot Area_{electrode}$) was used to calculate the electrical surface exchange coefficient, k^q [29, 30] (**Figure S3-3**). As shown in **Figures 3-3c, d,** all the LSC_{214}-decorated films showed enhanced k^q values compared to the LSC_{113}-reference, electrodes with low coverage demonstrating the highest surface exchange. It is interesting to note that the surfaces with low coverage exhibit up to an order of magnitude higher conductance at high $p(O_2)$ than that observed for a screen-printed electrode composed of porous LSC_{214} on top of porous $La_{0.6}Sr_{0.4}CoO_{3-\delta}$ reported previously[14] (**Figure S3-4**). Assuming k^q can be approximated as k^*,[31] it is noted that the highest k^q values of LSC_{214}-decorated LSC_{113} films (0.1 nm) obtained from this study is 3-4 orders of magnitude higher than that of bulk LSC_{113}[16] at 1 atm, and is comparable to those of the most active cathode materials such as thin film $Ba_{0.5}Sr_{0.5}Co_{0.8}Fe_{0.2}Co_{3-\delta}$ [$k^* = \sim 1 \cdot 10^{-6}$ cm s^{-1} at 500 °C and 0.5 bar of $p(O_2)$[32]] and bulk La_2CoO_4 [$k^* = \sim 3 \cdot 10^{-6}$ cm s^{-1} at 500 °C and 0.2 bar of $p(O_2)$[33]].

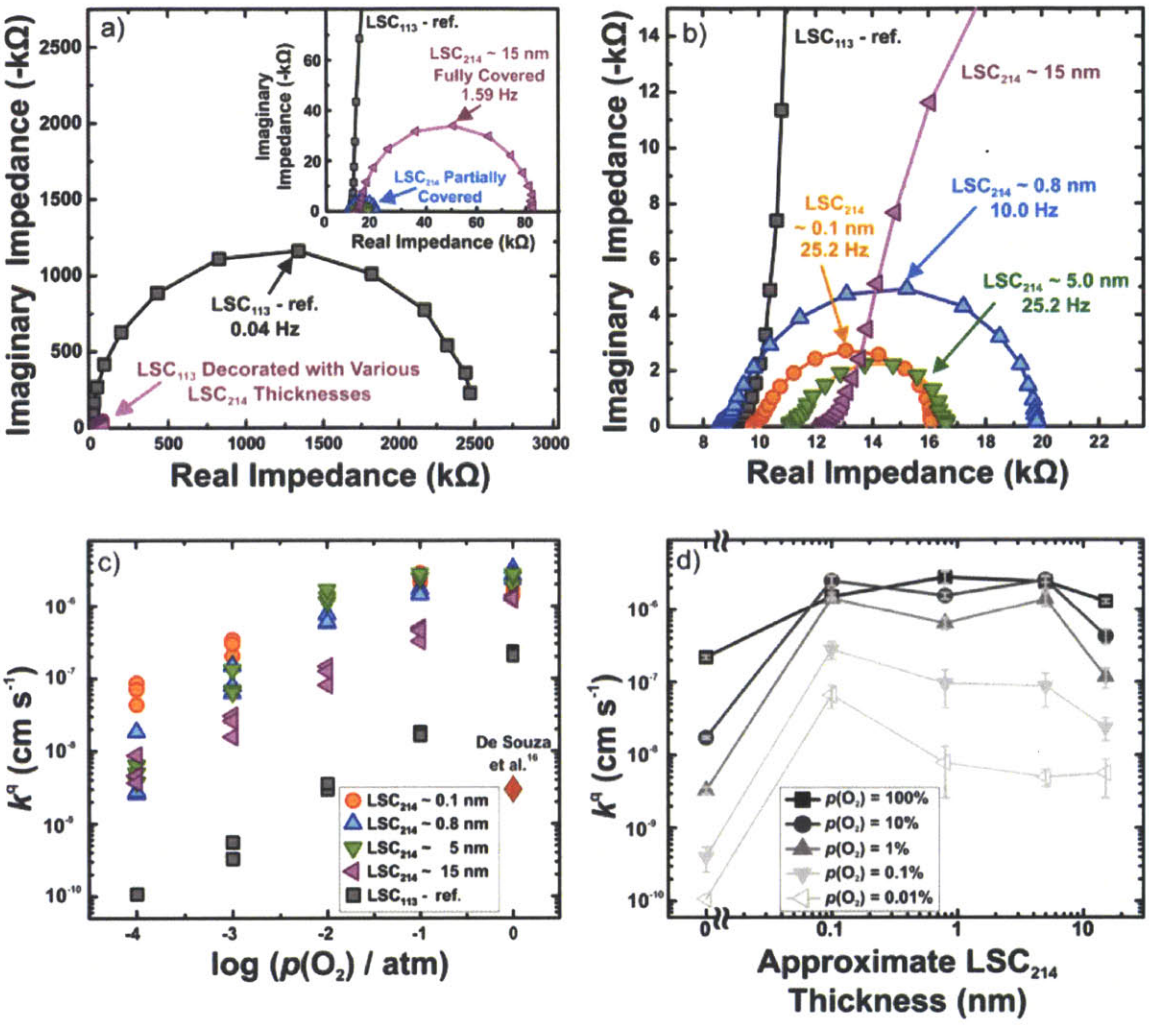

Figure 3-3. Electrochemical impedance spectroscopy (EIS) results of microelectrodes (~200 μm) for the LSC_{113}-reference and the LSC_{113} films with ~0.1 nm, ~0.8 nm, ~5 nm, and ~15 nm LSC_{214} surface coverage at 550 °C; a) Nyquist plot at 1% $p(O_2)$, the inset and b) show a magnification; c) oxygen partial pressure dependency of the surface exchange coefficients k^q of LSC_{113}/LSC_{214} films and bulk LSC extrapolated from the data reported by De Souza et al.[16] (red ♦), and d) average k^q values versus thicknesses of LSC_{214} surface coverage. Error bars represent the maximum and minimum from three independently measured electrodes.

To evaluate what is responsible for the observed ORR enhancement, we here discuss factors that may influence the ORR kinetics. We note that there is no change in the oxygen vacancy concentration of the entire film with increasing LSC_{214} surface coverage. The oxygen nonstoichiometry (δ) was estimated from the volume specific capacitance (*VSC*) of EIS data using a method published previously[15, 34] (**Figures S3-5a and S3-5b**), from which

thermodynamic parameters of the thin film samples were extracted from *VSC* dependence on $p(O_2)$ (**Table S3-2**). Therefore, the enhanced ORR activity of LSC_{214}-covered LSC_{113} films cannot result from increased oxygen vacancy in the bulk of the films. Moreover, the origin of enhanced ORR activity of LSC_{214}-covered LSC_{113} films is not apparent as the LSC_{214}-reference film composed of LSC_{214}(~15 nm)/GDC/YSZ(001)/porous Pt has comparable activity to the LSC_{113}-reference film (**Figure S3-6**). These results suggest that the presence of LSC_{113} and LSC_{214} interfaces on the surface of LSC_{214}-covered LSC_{113} films are critical to the observed ORR enhancement.

To obtain further insights into the ORR kinetics of LSC_{214}-covered LSC_{113} films, scanning transmission electron microscopy (STEM) cross sections of three samples, LSC_{113}-reference, a partially (~0.8 nm) and a fully (~15 nm) LSC_{214} covered film were compared, from which active regions for surface oxygen exchanges are proposed (**Figure 3-4**). Cross-sectional STEM imaging (**Figure 3-4a**) demonstrated that the LSC_{113}-reference film had no second-phase inclusions. By the first approximation, the ORR kinetics on these films of ~85 nm in thickness are oxygen surface exchange limited having the entire electrode surface ORR active (highlighted in red in **Figure 3-4a** right panel) as the film thickness is much lower than the critical thickness estimated from extrapolated bulk LSC_{113} values (using $t_{crit} = D_{bulk}/k_{bulk}$ at 550 °C ≈ 1 μm).[35] This is further supported by the fact that the $p(O_2)$ dependency of k^q ($k^q \propto p(O_2)^m$, having m = ~0.93) is similar to those reported previously for bulk LSC,[36] particularly in the $p(O_2)$ range from 10^{-4} atm to 10^{-2} atm. Partial LSC_{214} coverage on the LSC_{113} film led to the formation of nano-islands distributed on top of the LSC_{113} film, which is supported by the STEM cross-sectional imaging in **Figure 3-4b,** showing uneven contrast at the film surface (compared with **Figure 3-4a**). Nano-islands result in a large number of interfacial LSC_{113}/LSC_{214} boundaries on the film surface, which are correlated with the highest ORR activity values observed for partial coverage of LSC_{214} on the LSC_{113} film. Increased k^q values can decrease the critical thickness (t_{crit}) assuming a constant diffusion coefficient, D, which can lead to ORR impedance to be influenced by bulk diffusion in addition to surface oxygen exchange. The much decreased $p(O_2)$ dependency of the partially covered samples at high $p(O_2)$ (**Figure 3-3c**) may suggest that the surface oxygen exchange kinetics of these thin films are so large that they are limited by bulk diffusion in the thin films, where bulk diffusion coefficients typically have a weak dependence on $p(O_2)$.

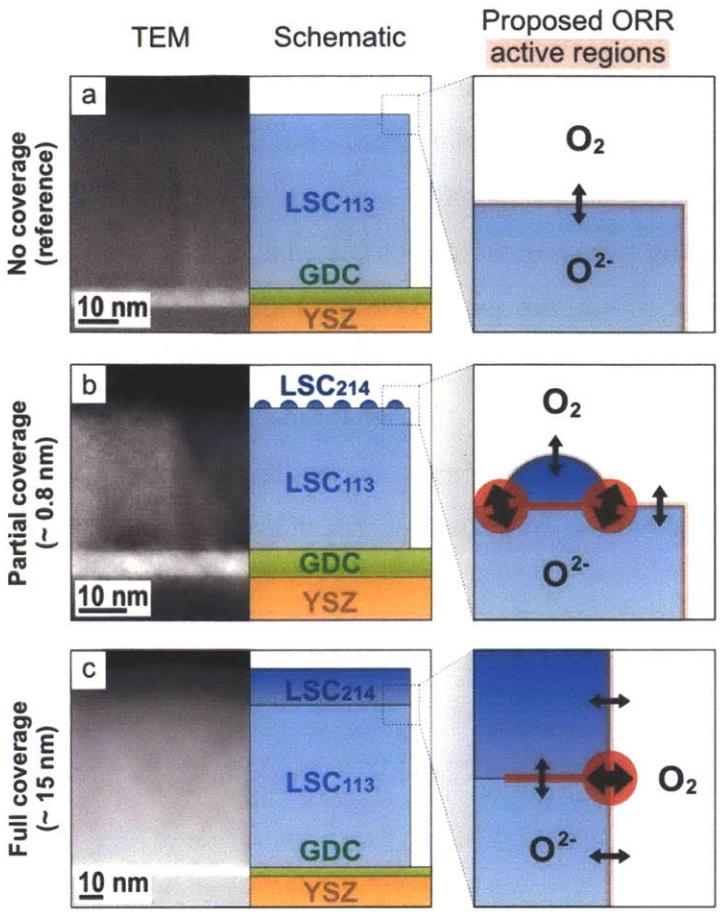

Figure 3-4. Proposed ORR active regions (red) for a) LSC_{113}-reference sample, b) partially LSC_{214}-covered samples, c) fully LSC_{214}-covered sample (STEM reveals ~15 nm LSC_{214} coverage).

With increasing LSC_{214} coverage to ~15 nm, a fully dense surface layer of LSC_{214} was developed, as shown in the cross-sectional STEM image in **Figure 3-4c**, where the LSC_{214} layer appears darker due to a lower physical density of the structure than LSC_{113}.[25,37] This reduced the triple phase boundary (LSC_{113}/LSC_{214}/gas phase), which is correlated with lower activity of fully LSC_{214}-covered films compared to the partially covered films. Even assuming that the edge of the LSC_{214} thin layer had ORR activity comparable to the boundaries of LSC_{214} nano-islands on the LSC_{113} film, a large active area at the interface between LSC_{214} and LSC_{113} extending from the microelectrode edge toward the microelectrode center would be needed to explain the ORR enhancement of these films relative to the LSC_{113} and LSC_{214} reference samples (**Figures 3-4c, 3-5, S3-6**). Evidence to support this hypothesis is provided by evaluating how the ASR_{ORR} changes with the microelectrode diameter, d. As shown in **Figure 3-5a**, all partial LSC_{214}-covered

electrodes show no apparent ASR_{ORR} dependency on the electrode diameter, which indicates that the enhanced ORR kinetics are comparable for all electrodes of different sizes. In contrast, the ASR_{ORR} of the fully LSC_{214}-covered film decreases (i.e. k^q increases) with reducing electrode size, approaching a similar value to partially covered electrodes. This result suggests that an interfacial area extending from the microelectrode edge to the electrode center with a finite radial distance, r, on the order of ~20 μm (as depicted in **Figure 3-5b**) can contribute to enhance ORR kinetics. By decreasing the electrode diameter from ~160 μm to ~35 μm, the area of the highly active circular ring becomes greater than the remaining non-ORR-enhanced area near the electrode center (**Figure 3-5b**), and finally the entire electrode is highly activated. This can explain why the ASR_{ORR} of this sample approaches those of partially LSC_{214}-covered samples.

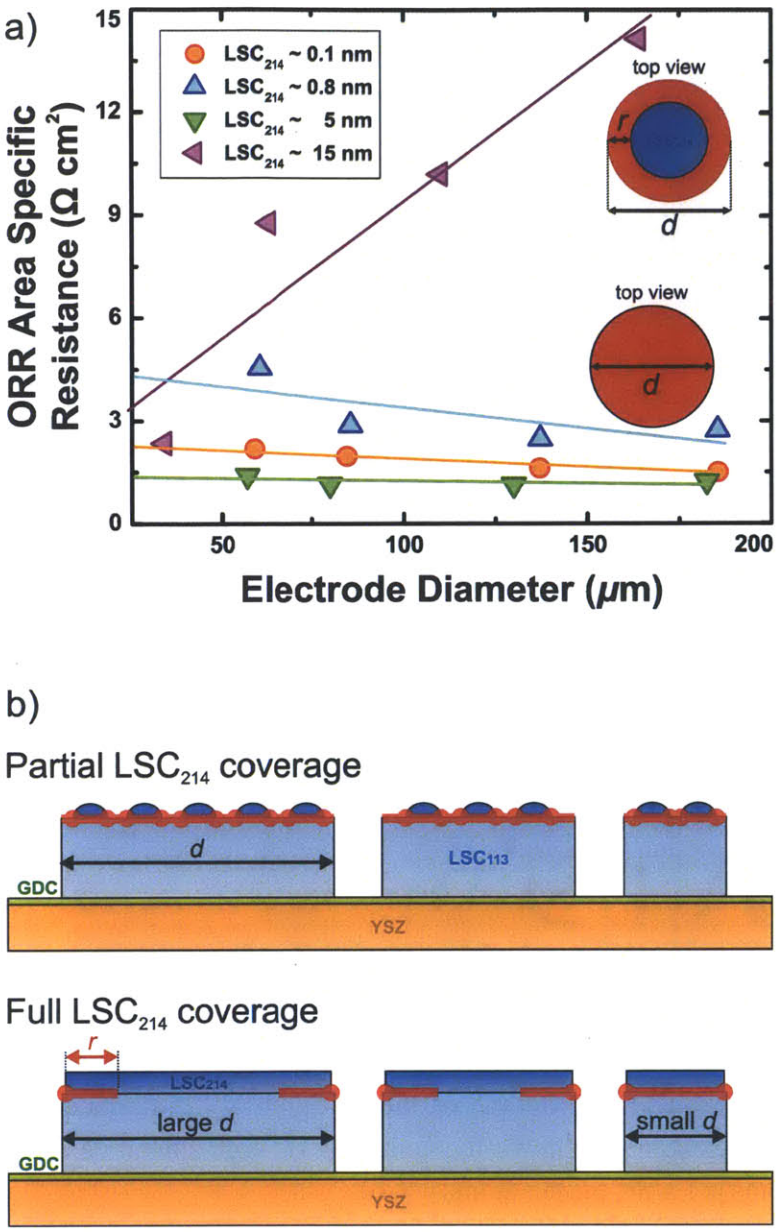

Figure 3-5. a) ORR area specific resistance (ASR_{ORR}) versus electrode diameter, d, at 550 °C in 1% $p(O_2)$. b) Schematic of proposed enhanced active regions (red) for different electrode sizes and different amounts of LSC_{214} surface coverage, r = radial distance of active area.

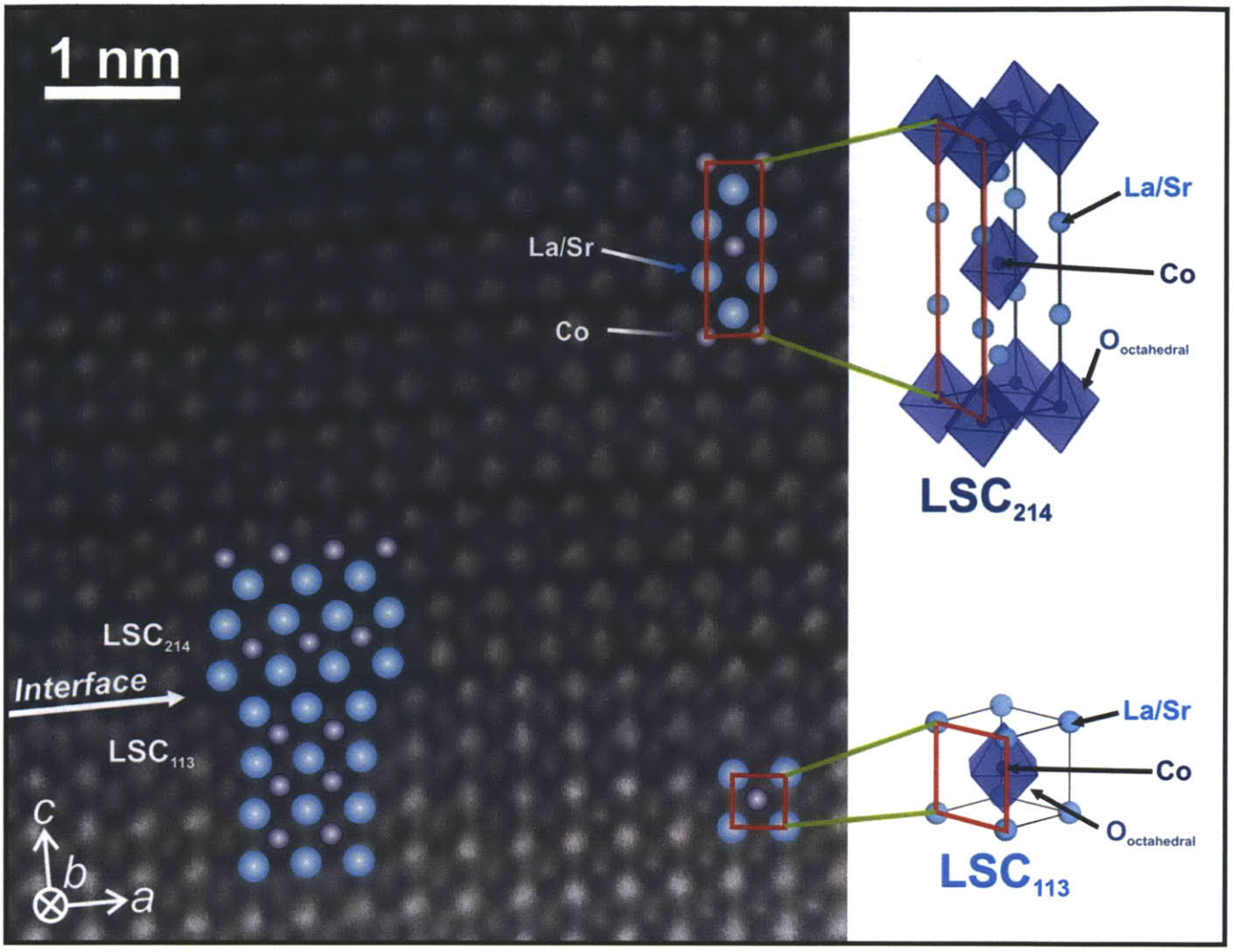

Figure 3-6. HAADF STEM micrograph of the LSC_{113}/LSC_{214} interface for the ~15 nm LSC_{214} covered sample; the schematic shows the unit cell of both materials and the structure at the interface (blue atoms = La/Sr, purple atoms = Co).

Our results indicate that interfacial LSC_{113}/LSC_{214} regions or LSC_{214} thin layers of a few nanometers in thickness on LSC_{113} are responsible for the observed ORR enhancement. Atomic resolution high angle annular dark field (HAADF) STEM imaging revealed that the LSC_{214} layer of ~15 nm grew epitaxially with (001) orientated LSC_{113}, which is in good agreement with XRD results in **Figure 3-2**. The interface is atomically sharp without any amorphous or disordered interface regions, having atomic columns of the La/Sr layers of LSC_{214} and LSC_{113} clearly shown. It is not clearly understood why interfacial LSC_{113}/LSC_{214} boundaries or LSC_{214} thin layers of a few nanometer in thickness on LSC_{113} exhibit enhanced ORR activity. We hypothesize that the enhancement can be attributed to interfacial properties such as strain,[9,15] space charge effects,[8] an

increase in oxygen vacancy concentration,[38] or a change in electronic structure.[39] Since La_2CoO_4 has a high k^*[33] which is comparable to the k^q found for the partially covered LSC_{113}/LSC_{214} samples, the enhanced ORR activity could also be explained by the absence of Sr at the interface. Further studies are needed to elucidate the mechanism of ORR kinetics enhancement of these hetero-structured interfaces.

3.4 Conclusions

In summary, we show ORR activity enhancement up to ~1-3 orders of magnitude on the thin film LSC_{113} surfaces with LSC_{214} surface decoration, and up to ~3-4 orders of magnitude with respect to bulk LSC_{113}. Our results indicate that interfacial LSC_{113}/LSC_{214} regions are responsible for the observed ORR enhancement. The enhancement in ORR kinetics cannot be attributed to changes in oxygen vacancy concentration of the entire film nor a disordered interfacial LSC_{113}/LSC_{214} structure, and future studies are needed to elucidate the origin of enhanced ORR kinetics at interfacial LSC_{113}/LSC_{214} regions. This study illustrates the potential of utilizing hetero-structured oxide surfaces/interfaces to develop highly active surface oxygen exchange materials for applications in the field of solid-state electrochemistry such as solid-electrolyte-based sensors, oxygen conducting membranes, and SOFC cathodes.

3.5 Supporting Information

Experimental Details:

Target Synthesis. $La_{0.8}Sr_{0.2}CoO_{3-\delta}$ (LSC_{113}) was synthesized using solid state reaction from stoichiometric mixtures of La_2O_3, $SrCO_3$, Co_3O_4 (Alfa Aesar, USA) calcined at 1,000 °C in air for 12 hours. The $(La_{0.5}Sr_{0.5})_2CoO_{4+\delta}$ (LSC_{214}) and $Gd_{0.2}Ce_{0.8}O_2$ (GDC) powders were synthesized via the Pechini method. $La(NO_3)_3 \cdot 6H_2O$, $Sr(NO_3)_2$, $Co(NO_3)_2 \cdot 6H_2O$, and separately $Gd(NO_3)_3$, and $Ce(NO_3)_3$ were dissolved into a de-ionized water, ethylene glycol, citric acid (Sigma-Aldrich, USA) mixture to synthesize LSC_{214} and GDC respectively. After esterification at 100 °C, the resin was charred at 400 °C and then calcined at 800 °C in air for 1 hour. The pulsed laser deposition (PLD) targets with a 25 mm diameter were subsequently formed by uniaxial pressing at 50 MPa. The LSC_{214}, LSC_{113}, and GDC targets were all sintered at 1350 °C in air for 20 hours.

Sample Preparation. 9.5 mol% Y_2O_3-stabilized ZrO_2 (YSZ) single crystalline substrates with (001) orientation, dimension 10 x 5 x 0.5 mm, and one-sided polished (surface roughness < 1 nm) (Princeton Scientific, USA) were used as electrolytes. Platinum ink (Pt, #6082, BASF, USA) counter electrodes were painted on the un-polished side of the YSZ and sintered at 800 °C in air for 1 hour. The oxide films were deposited by pulsed laser deposition (PLD) using a KrF excimer laser with λ = 248 nm, 10 Hz pulse rate, and ~50 mJ pulse energy under $p(O_2)$ of 10 mTorr with 500 pulses of GDC (~5 nm) at 450 °C, followed by 15,000 pulses of LSC_{113} (~85 nm, determined by atomic force microscopy (AFM); the film thicknesses of the scanning transmission electron microscopy (STEM) cross sections shown in Figure 4 do not represent typical average values) at 675 °C. Reflection high-energy electron diffraction (RHEED) was utilized to provide in-situ monitoring of GDC/LSC_{113}/LSC_{214} film growth. Immediately after completing the LSC_{113} base film deposition a surface film was subsequently deposited; for the LSC_{113}-reference sample adding an additional 25 pulses LSC_{113}, or LSC_{214} surface coverages consisting of 25 pulses (~0.1 nm, partial coverage), 150 pulses (~0.8 nm, partial coverage), 900 pulses (~5 nm, coverage information (partial or full) is not available), and 2700 pulses (~15 nm, full coverage) pulses. LSC_{214} decoration layer thickness is extrapolated from STEM micrograph shown in **Figure 4c** of the thickest 2700 pulse LSC_{214} coverage on LSC_{113}. After completing the final deposition, the samples are cooled to room temperature over the course of ~1 hour within the PLD chamber at 10 mTorr.

Sample Characterization. Oxide phase purity and orientation of the thin film systems were investigated via high resolution X-ray diffraction (XRD) using a four-circle diffractometer (Panalytical, USA; and Bruker D8, Germany). Surface morphology was examined by optical microscopy (Carl Zeiss, Germany), AFM (Veeco, USA), and scanning electron microscopy (SEM, Carl Zeiss, Germany). Samples for STEM studies were prepared using either traditional mechanical polishing followed by Ar ion milling or focused ion beam (FIB) lift-out. The electron transparent thin film samples were examined using a VG501UX or Nion UltraSTEM100 scanning transmission electron microscope, both operated at 100 kV and equipped with Nion aberration correctors. In high angle annular dark field (HAADF) imaging, an electron probe is scanned across the sample, and the electrons scattered to high angles are collected at every point to form an image. The resulting HAADF micrograph shows brighter contrast in regions where

atomic columns contain heavier atoms and lighter contrast for atomic columns with smaller atomic number (roughly proportional to Z^2).[40]

Micropatterning. The LSC microelectrodes were fabricated by photolithography and the following process: OCG positive photoresist (Arch Chemical Co, USA) was applied on the film surface and patterned using a mask aligner (Karl Süss, Germany, λ =365 nm). The photoresist was developed using Developer 934 1:1 (Arch Chemical Co., USA) developer, and the films were subsequently etched in hydrochloric acid (HCl) to form circular microelectrodes (diameters ~50 μm, ~100 μm, ~150 μm, and ~200 μm, exact diameter determined by optical microscopy). The photoresist was removed with acetone. AFM was then used to measure sample thickness for each film after microelectrode patterning, resulting in LSC_{113}-reference ~85 nm, LSC_{113}/LSC_{214} (~ 0.1 nm) ~83 nm, LSC_{113}/LSC_{214} (~ 0.8 nm) ~86 nm, LSC_{113}/LSC_{214} (~ 5 nm) ~93 nm, LSC_{113}/LSC_{214} (~ 15nm) ~120 nm.

Electrochemical Characterization. Electrochemical impedance spectroscopy (EIS) was collected using a microprobe station setup (Karl Süss, Germany) connected to a frequency response analyzer (Solatron 1260, USA) and a dielectric interface (Solartron 1296, USA). Pt-coated tungsten carbide probes were utilized to contact the LSC electrodes and the porous Pt counter electrode. Sample testing configuration is shown in **Figure 1a**. Temperature was controlled at 550 °C with a heating stage (Linkam TS1500, UK) and measured with a second thermocouple on the sample surface. EIS data were collected between 1 MHz to 1 mHz using a voltage amplitude of 10 mV under Ar / O_2 mixtures in the range from P_{O_2} of 10^{-4} to 1 atm. **Figure 1c-d** details the equivalent circuit and corresponding Nyquist plot for this experimental system. *ZView* software (Scribner Associates, USA) was used to construct the equivalent circuit and perform complex least-square-fitting to extract the fitting parameters to describe the system.

Electrode System	Constrained in-plane lattice parameter a (Å) [LSC_{113}/LSC_{214}]	Constrained normal lattice parameter c (Å) [LSC_{113}/LSC_{214}]	Relaxed film lattice parameter $\hat{a}$ (Å) [LSC_{113}/LSC_{214}]	In-plane strain $\varepsilon_{xx} = \frac{(a-\hat{a})}{\hat{a}}$ [LSC_{113}]	Normal strain $\varepsilon_{zz} = \frac{(c-\hat{c})}{\hat{c}}$ [LSC_{113}]
LSC_{113}-reference	3.853 / n/a	3.831 / n/a	3.840 / n/a	0.33 %	-0.22 %
LSC_{214} ~ 0.1 nm	3.859 / n/a	3.845 / n/a	3.850 / n/a	0.21 %	-0.14 %
LSC_{214} ~ 0.8 nm	3.873 / n/a	3.841 / n/a	3.853 / n/a	0.50 %	-0.33 %
LSC_{214} ~ 5.0 nm	3.869 / n/a	3.830 / n/a	3.846 / n/a	0.60 %	-0.40 %
LSC_{214} ~ 15.0 nm	3.855 / 3.846	3.835 / 12.444	3.843 / 3.811	0.32 %	-0.21 %

Table S3-1. Constrained and relaxed lattice parameters of LSC films extracted from normal and off-normal HRXRD data. The constrained normal and in-plane lattice parameters of the LSC_{113} and LSC_{214} films were calculated from combining the inter-planar distances of the $(002)_{pc}$ and $(011)_{pc}$ peaks and the $(006)_{tetragonal}$ and $(103)_{tetragonal}$ peaks respectively.

For determining the relaxed film lattice parameter $\hat{a}$ (LSC_{113}), we used the equation:

$$\frac{\Delta c}{\hat{c}} = \frac{-2\nu}{1-\nu}\frac{\Delta a}{\hat{a}}$$

Assuming $\hat{a} = \hat{c}$ and $\nu = 0.25$.[41]

	x	$a(x)$ (kJ mol^{-1})	$\Delta h_o^\circ(x)$ (kJ mol^{-1})	$\Delta s_o^\circ(x)$ (J mol^{-1})
LSC pellet (Mizusaki et al.[4])	$x = 0.2$	415	-146	-86.6
	$x = 0.4$	289	-85.5	-69.4
LSC 1.5 µm thin film (Kawada et al.[9])	$x = 0.4$	332	-124	-69.4
LSC_{113}-reference	$x = 0.2$	1100	-113	-87
LSC_{214} ~ 0.1 nm	$x = 0.2$	900	-118	-83
LSC_{214} ~ 0.8 nm	$x = 0.2$	1050	-115	-86
LSC_{214} ~ 5 nm	$x = 0.2$	1130	-118	-83
LSC_{214} ~ 15 nm	$x = 0.2$	1320	-111	-87

Table S3-2. Extracted standard partial molar enthalpy (in equilibrium with 1 atm of O_2) of oxygen $\Delta h_o^\circ(x)$, standard partial molar entropy of oxygen $\Delta s_o^\circ(x)$, and non-ideality factor $a(x)$ for LSC bulk,[42] polycrystalline[34] and LSC_{113} decorated thin films.

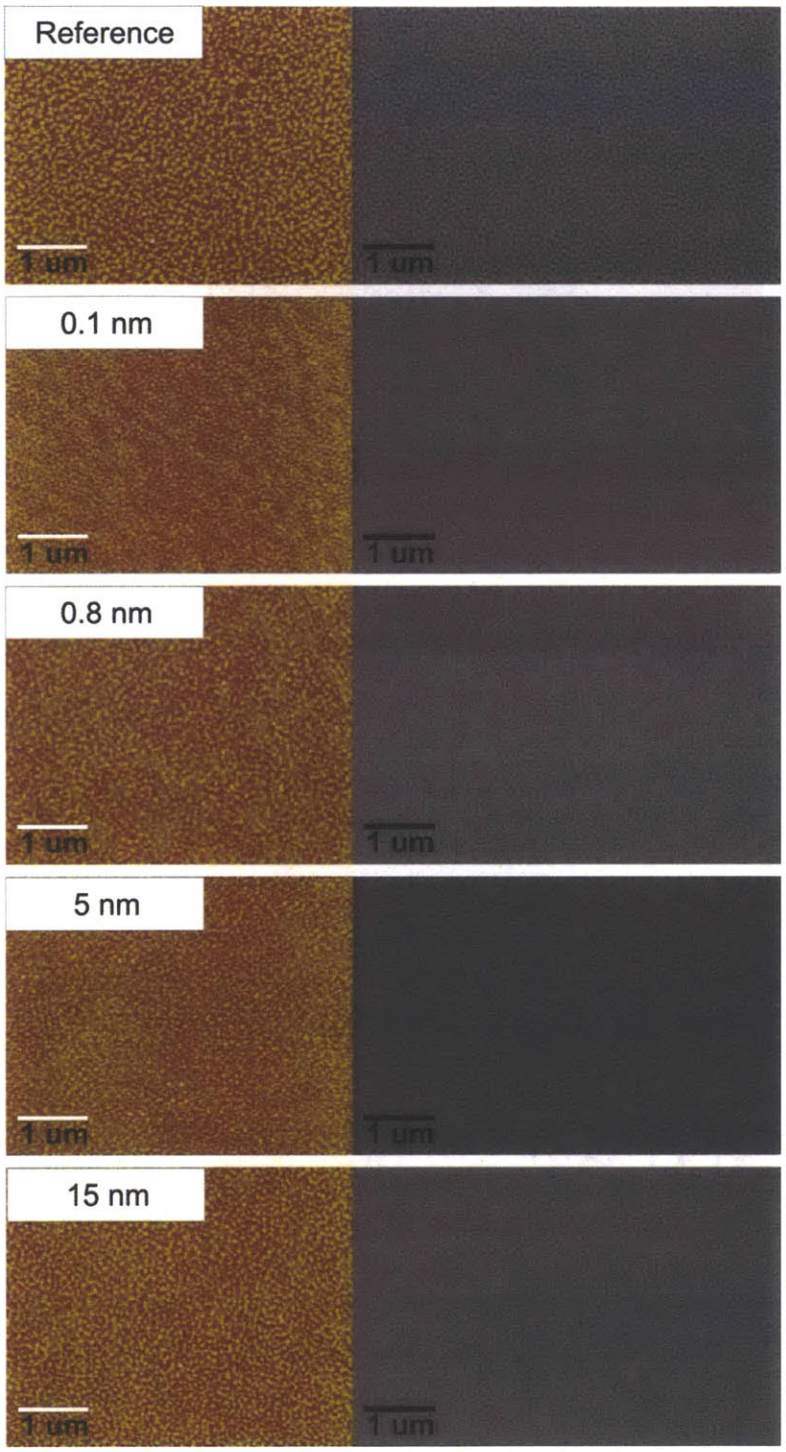

Figure S3-1. Surface AFM (left) and SEM (right) images of the different electrodes; rms roughness: 1.15 nm (reference), 0.75 nm (~0.1 nm coverage), 0.67 nm (~0.8 nm coverage), 0.76 nm (~5 nm coverage), 0.94 nm (~15 nm coverage).

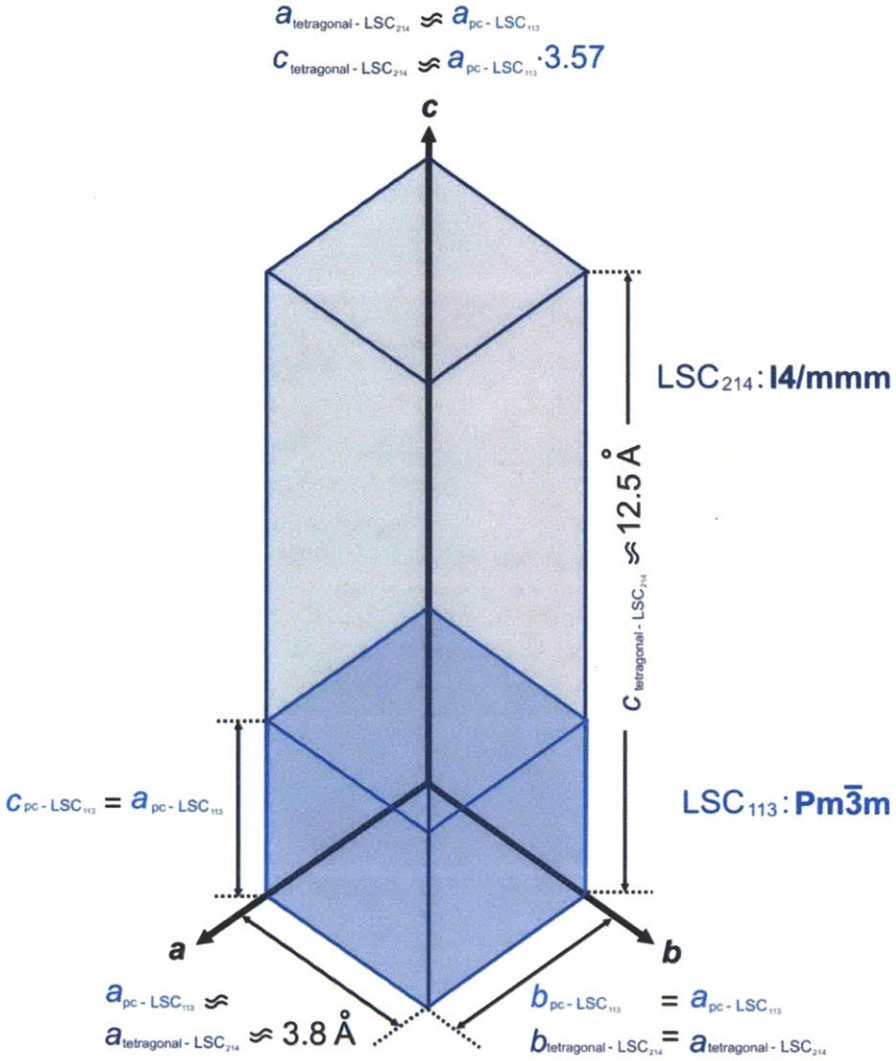

Figure S3-2. Schematic showing relationship between LSC_{113} unit cell in pseudo cubic notation (light blue) and LSC_{214} tetragonal unit cell (dark blue). The space group of LSC_{113} in pseudo cubic notation is Pm-3m ($a_{pc} \approx 3.8$ Å), of LSC_{214} is I4/mmm ($a_{tetragonal} \approx 3.8$ Å, $c_{tetragonal} \approx 12.5$ Å).

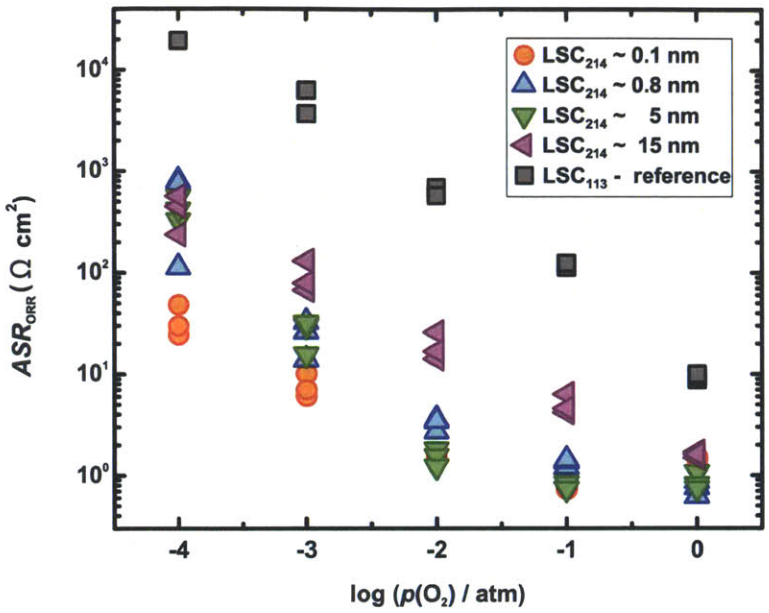

Figure S3-3. Fitting the EIS data to the equivalent circuit shown in **Figure 3-1c**, $R_{electrolyte}$-($R_{electrolyte/electrode\ interface}$/$CPE_{electrolyte/electrode\ interface}$)-($R_{ORR}$/$CPE_{ORR}$), we obtained values for R_{ORR}; and knowing the area of the microelectrode ($A_{electrode} = 0.25\ \pi\ d_{electrode}^2$) we can determine the ORR area specific resistance ($ASR_{ORR} = R_{ORR} \cdot A_{electrode}$). ASR_{ORR} values plotted versus log $p(O_2)$ for the LSC_{113}-reference and the LSC_{113} film with about 0.1 nm, 0.8 nm, 5 nm, and 15 nm LSC_{214} surface coverages at 550 °C are depicted in this Figure. In order to determine the electrical surface exchange coefficient (k^q) from the ASR_{ORR} values, we used this expression:[30]

$$k^q = RT / 4F^2 R_{ORR} A_{electrode} c_o$$

where R is the universal gas constant (8.314 J mol^{-1} K^{-1}), T is the absolute temperature (823 °K), F is the Faraday's constant (96,500 C mol^{-1}), and c_o is the lattice oxygen concentration in LSC. In a first approximation, we estimated c_o for LSC_{113} using:

$$c_o = (3-\delta) / V_m$$

where V_m is the bulk molar volume of LSC_{113} at room temperature (33.66 cm^3 mol^{-1}, increasing temperatures to 550 °C has a negligible effect on the molar volume). δ values for the material at the experimental conditions (p, T) have been used from literature.[42]

The LSC_{214} surface coverage might change the c_o value of the system. For estimating this influence we also calculated k^q values for electrode systems composed only of LSC_{214}. For pure LSC_{214} we could use this expression, with V_m of bulk LSC_{214} at room temperature (54.60 cm^3 mol^{-1})

$$c_o = (4+\delta) / V_m$$

The influence of using the LSC_{214} c_o will increase the value of k^q by approximately 20%. We decides to use c_o values of LSC_{113} for all samples as this is the largest c_o value and will yield the most conservative k^q.

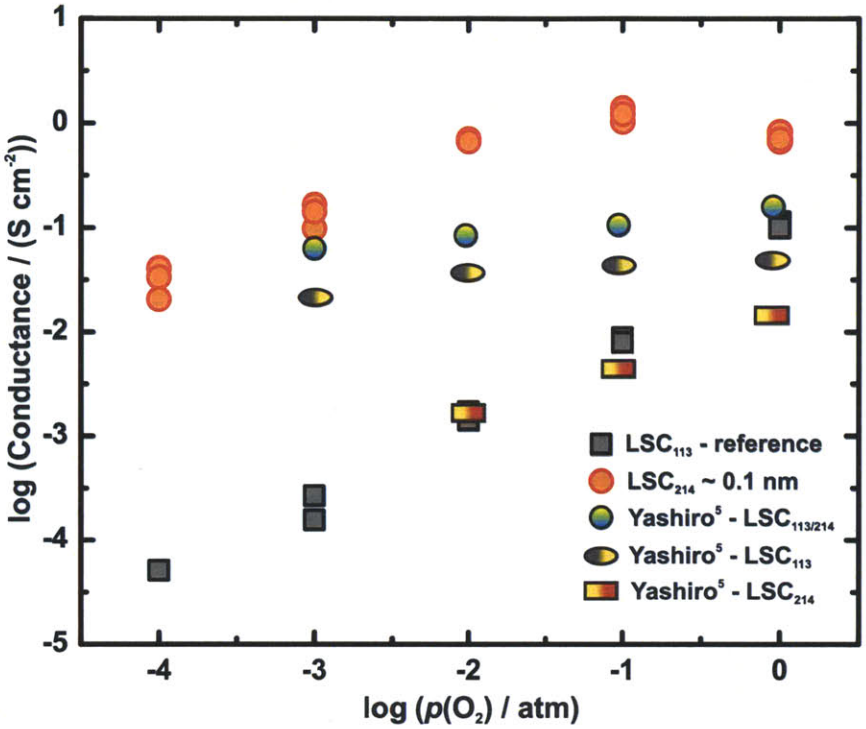

Figure S3-4. Comparison of results of this study to work previously reported by Yashiro et al.[14] investigating polycrystalline materials and porous electrodes ($La_{0.6}Sr_{0.4}CoO_{3-\delta}$, $(La_{0.5}Sr_{0.5})_2CoO_{4+\delta}$; note, it is known that $La_{0.6}Sr_{0.4}CoO_{3-\delta}$ has higher ORR activity then $La_{0.8}Sr_{0.2}CoO_{3-\delta}$). The conductance has been calculated using the expression: $1/ASR_{ORR}$. In addition, we can compare the k values of both studies, as k^q is comparable to the self-surface exchange coefficient, k^*, which can be determined from oxygen isotope exchange evaluated by secondary ion mass spectroscopy (SIMS).[31] Conducting O^{18} exchange at 0.2 bar and 500 °C using $La_{0.6}Sr_{0.4}CoO_{3-\delta}$ / $(La_{0.5}Sr_{0.5})_2CoO_{4+\delta}$ films, Sase et al.[13] reported a k^* of approximately $8 \cdot 10^{-6}$ cm s^{-1} confined to a region close to the interface of $La_{0.6}Sr_{0.4}CoO_{3-\delta}$/$LSC_{214}$/gas phase. In this work we show for example $k^q \sim 2.5 \cdot 10^{-6}$ cm s^{-1} over the entire LSC_{113} / LSC_{214} electrode surface at 550 °C in 10% $p(O_2)$.

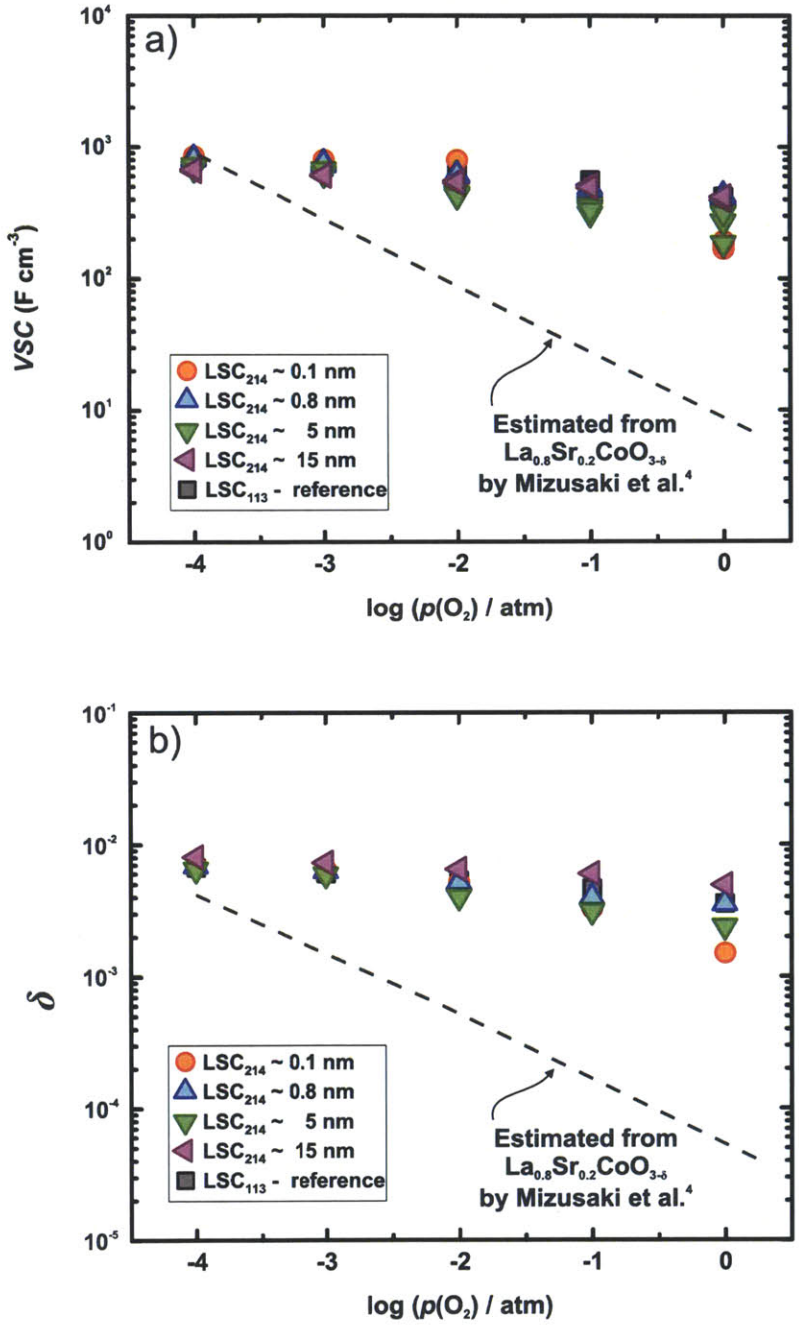

Figure S3-5. Oxygen partial pressure dependency of a) volume specific capacitance (*VSC*) b) oxygen nonstoichiometry δ, results of the LSC_{113}-reference and the LSC_{113} films with about 0.1 nm, 0.8 nm, 5 nm, and 15 nm LSC_{214} surface coverages at 550 °C. The *VSC* of the thin films was obtained from EIS data using the expression[43] $VSC = [1/(A_{\text{electrode}} \cdot thickness_{\text{electrode}}] \, (R_{\text{ORR}}{}^{(1-n)}Q)^{1/n}$, where n and Q are fitting parameters.[43]

Using a method reported by Kawada et al.[34] the *VSC* values of LSC bulk were calculated,

$$VSC = -(4F^2 / V_m)(d\delta / d\mu_o) = (4F^2 / V_m)[a(x) + 3RT / \delta(3-\delta)]^{-1}$$

where $a(x)$ is a factor that describes deviation from ideal solid solution. Oxygen nonstoichiometry (δ) was extracted using the expression:

$$\delta = 3/2 - 1/2\sqrt{9 - 12RT/\left[\left(4F^2/VSC \cdot V_m\right) - a(x)\right]}$$

which is substituted into

$$1/2RT\ln p(O_2) = \left[\Delta h_o^{\circ}(x) - a(x)\delta\right] - T\left[\Delta s_o^{\circ}(x) + R\ln(\delta/(3-\delta))\right]$$

Using this relationship to fit the experimentally determined VSC of the LSC_{113} decorated films at different $p(O_2)$, the δ and thermodynamic parameters include the standard partial molar enthalpy (in equilibrium with 1 atm of O_2) of oxygen $\Delta h_o^{\circ}(x)$, $a(x)$, and standard partial molar entropy of oxygen $\Delta s_o^{\circ}(x)$, at 550 °C are shown in **Table S3-2**. Estimates for bulk $La_{0.8}Sr_{0.2}CoO_{3-\delta}$ VSC and δ are extrapolated from Mizusaki et al.[42] at 550 °C.

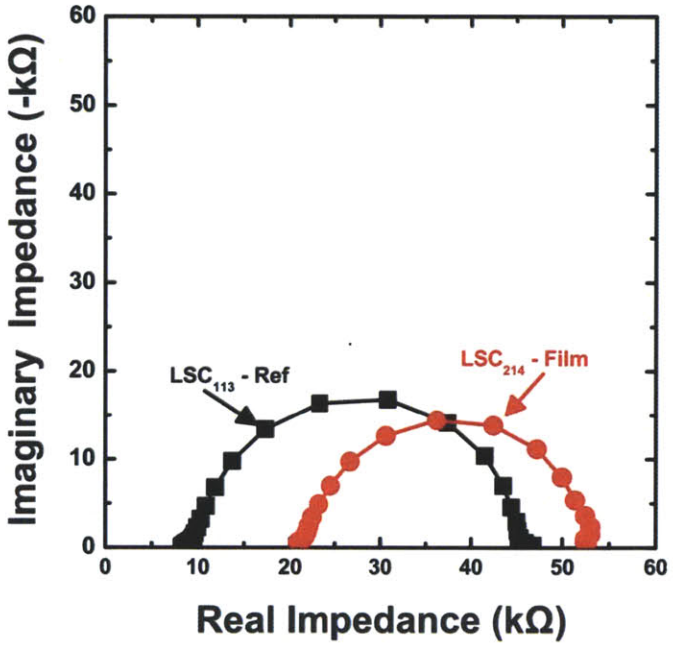

Figure S3-6. Nyquist plot comparing thin film EIS of LSC_{214}/GDC/YSZ(001) deposited by PLD using similar conditions outlined in the Experimental Details (Sample Preparation section above) to LSC_{113}-reference (~85 nm) at 550 °C in 100% $p(O_2)$. LSC_{214} film thickness is ~15 nm, which is comparable to the surface decoration thickness of the fully LSC_{214} covered electrodes. At this testing condition k^q LSC_{113}-reference and LSC_{214}-reference are both ~$2.2 \cdot 10^{-7}$ cm s^{-1}.

3.6 References

1. Adler, S. B. Factors Governing Oxygen Reduction in Solid Oxide Fuel Cell Cathodes. *Chem. Rev.* **2004**, *104*, 4791–4843.

2. Adler, S. B.; Chen, X. Y.; Wilson J. R. Mechanisms and Rate Laws for Oxygen Exchange on Mixed-Conducting Oxide Surfaces. *J. Catal.* **2007**, *245*, 91–109.

3. Lee, Y. L.; Kleis, J.; Rossmeisl, J.; Morgan, D. Ab Initio Energetics of $LaBO_3$(001) (B=Mn, Fe, Co, and Ni) for Solid Oxide Fuel Cell Cathodes. *Physical Review B* **2009,** 80, 224101-1–224101-20.

4. Tarancon, A.; Burriel, M.; Santiso, J.; Skinner, S. J.; Kilner, J. A. Advances in Layered Oxide Cathodes for Intermediate Temperature Solid Oxide Fuel Cells. *J. Mat. Chem.* **2010**, *20*, 3799–3813.

5. Garcia-Barriocanal, J.; Rivera-Calzada, A.; Varela, M.; Sefrioui, Z.; Iborra, E.; Leon, C.; Pennycook, S. J.; Santamaria, J. Colossal Ionic Conductivity at Interfaces of Epitaxial ZrO_2: Y_2O_3/$SrTiO_3$ Heterostructures. *Science* **2008**, *321*, 676–680.

6. Garcia-Barriocanal, J.; Rivera-Calzada, A.; Varela, M.; Sefrioui, Z.; Iborra, E.; Leon, C.; Pennycook, S. J.; Santamaria, J. Response to Comment on "Colossal Ionic Conductivity at Interfaces of Epitaxial ZrO_2:Y_2O_3/$SrTiO_3$ Heterostructures". *Science* **2009**, *324*, 5926.

7. Guo, X. Comment on "Colossal Ionic Conductivity at Interfaces of Epitaxial ZrO_2:Y_2O_3/$SrTiO_3$ Heterostructures". *Science* **2009**, *324*, 5926.

8. Guo, X. X.; Maier, J. Ionically Conducting Two-Dimensional Heterostructures. *Adv. Mat.* **2009**, *21*, 2619–2631.

9. Korte, C.; Schichtel, N.; Hesse, D.; Janek, J. Influence of Interface Structure on Mass Transport in Phase Boundaries between Different Ionic Materials Experimental Studies and Formal Considerations. *Monatshefte fuer Chemie* **2009**, *140*, 1069–1080.

10. Schichtel, N.; Korte, C.; Hesse, D.; Janek, J. Elastic Strain at Interfaces and its Influence on Ionic Conductivity in Nanoscaled Solid Electrolyte Thin Films-theoretical Considerations and Experimental Studies. *PCCP* **2009**, *11*, 3043–3048.

11. Cavallaro, A. et al., J. Electronic Nature of the Enhanced Conductivity in YSZ-STO Multilayers Deposited by PLD. *Solid State Ionics* **2010**, *181*, 592–601.

12. Sase, M.; Hermes, F.; Yashiro, K.; Sato, K.; Mizusaki, J.; Kawada, T.; Sakai, N.; Yokokawa, H. Enhancement of Oxygen Surface Exchange at the Hetero-Interface of $(La,Sr)CoO_3/(La,Sr)_2CoO_4$ with PLD-Layered Films. *J. Electrochem. Soc.* **2008**, 155, B793–B797.

13. Sase, M.; Yashiro, K.; Sato, K.; Mizusaki, J.; Kawada, T.; Sakai, N.; Yamaji, K.; Horita, T.; Yokokawa, H. Enhancement of Oxygen Exchange at the Hetero Interface of $(La,Sr)CoO_3/(La,Sr)_2CoO_4$ in Composite Ceramics. *Solid State Ionics* **2008**, *178*, 1843–1852.

14. Yashiro, K.; Nakamura, T.; Sase, M.; Hermes, F.; Sato, K.; Kawada, T.; Mizusaki, J. Composite Cathode of Perovskite-Related Oxides, $(La,Sr)CoO_{3-delta}/(La,Sr)_2CoO_{4-delta}$, for Solid Oxide Fuel Cells. *Electrochem. Solid State Lett.* **2009**, *12*, B135–B137.

15. la O', G. J.; Sung-Jin, A.; Ethan, C.; Yuki, O.; Michael, D. B.; Hans, M. C.; Yang, S.-H. Catalytic Activity Enhancement for Oxygen Reduction on Epitaxial Perovskite Thin Films for Solid-Oxide Fuel Cells. *Angew. Chem. Intern. Ed.* **2010**, *49*, 5344–5347.

16. De Souza, R. A.; Kilner, J. A. Oxygen transport in $La_{1-x}Sr_xMn_{1-y}Co_yO_{3+/-delta}$ Perovskites - Part I. Oxygen Tracer Diffusion. *Solid State Ionics* **1998**, *106*, 175–187.

17. Brichzin, V.; Fleig, J.; Habermeier, H. U.; Cristiani, G.; Maier, J. The Geometry Dependence of the Polarization Resistance of Sr-doped $LaMnO_3$ Microelectrodes on Yttria-Stabilized Zirconia. *Solid State Ionics* **2002**, *152-153*, 499–507.

18. Brichzin, V.; Fleig, J.; Habermeier, H. U.; Maier, J. Geometry Dependence of Cathode Polarization in Solid Oxide Fuel Cells Investigated by Defined Sr-doped $LaMnO_3$ Microelectrodes. *Electrochem. Solid State Lett.* **2000**, *3*, 403–406.

19. Baumann, F. S.; Fleig, J.; Cristiani, G.; Stuhlhofer, B.; Habermeier, H. U.; Maier, J. Quantitative Comparison of Mixed Conducting SOFC Cathode Materials by Means of Thin Film Model Electrodes. *J. Electrochem. Soc.* **2007**, *154*, B931–B941.

20. Fleig, J.; Baumann, F. S.; Brichzin, V.; Kim, H. R.; Jamnik, J.; Cristiani, G.; Habermeier, H. U.; Maier, J. Thin Film Microelectrodes in SOFC Electrode Research. *Fuel Cells* **2006**, *6*, 284–292.

21. la O', G. J.; Shao-Horn, Y. Oxygen Surface Exchange Kinetics on Sr-Substituted Lanthanum Manganite and Ferrite Thin-Film Microelectrodes. *J. Electrochem. Soc.* **2009**, *156*, B816–B824.

22. la O', G. J.; Savinell, R. F.; Shao-Horn, Y. Activity Enhancement of Dense Strontium-Doped Lanthanum Manganite Thin Films under Cathodic Polarization: A Combined AES and XPS Study. *J. Electrochem. Soc.* **2009**, *156*, B771–B781.

23. la O', G. J.; Shao-Horn, Y. Thickness Dependence of Oxygen Reduction Reaction Kinetics on Strontium-Substituted Lanthanum Manganese Perovskite Thin-Film Microelectrodes. *Electrochem. Solid State Lett.* **2009**, *12*, B82–B85.

24. la O', G. J.; Yildiz, B.; McEuen, S.; Shao-Horn, Y. Probing Oxygen Reduction Reaction Kinetics of Sr-doped $LaMnO_3$ Supported on Y_2O_3-stabilized ZrO_2. *J. Electrochem. Soc.* **2007**, *154*, B427–B438.

25. James, M.; Tedesco, A.; Cassidy, D.; Colella, M.; Smythe, P. J. The Phase Diagram and Crystal Chemistry of Strontium-doped Rare Earth Cobaltates: $Ln_{(2-x)}Sr_{(x)}CoO_{(4+delta)}$ (Ln = La-Dy). *J. Alloys Comp.* **2006**, *419*, 201–207.

26. Sánchez-Andújar, M.; Señarís-Rodríguez, M. A. Synthesis, Structure and Microstructure of the Layered Compounds $Ln_{1-x}Sr_{1+x}CoO_4$ (Ln: La, Nd and Gd). *Solid State Sci.* **2004**, *6*, 21–27.

27. Ishihara, T.; Kudo, T.; Matsuda, H.; Takita, Y. Doped $PrMnO_3$ Perovskite Oxide as a New Cathode of Solid Oxide Fuel-Cells for Low-Temperature Operation. *J. Electrochem. Soc.* **1995**, *142*, 1519–1524.

28. Chen, X. Y.; Yu, J. S.; Adler, S. B. Thermal and Chemical Expansion of Sr-Doped Lanthanum Cobalt Oxide ($La_{1-x}Sr_xCoO_{3-delta}$). *Chem. Mat.* **2005**, *17*, 4537–4546.

29. Fleig, J.; Maier, J. The Polarization of Mixed Conducting SOFC Cathodes: Effects of Surface Reaction Coefficient, Ionic Conductivity and Geometry. *J. Europ. Ceram. Soc.* **2004**, *24*, 1343–1347.

30. Maier, J., Physical Chemistry of Ionic Materials: Ions and Electrons in Solids. John Wiley: Chichester, England ; Hoboken, NJ, 2004; p 537.

31. Maier, J. On the Correlation of Macroscopic and Microscopic Rate Constants in Solid State Chemistry. *Solid State Ionics* **1998**, *112*, 197–228.

32. Wang, L.; Merkle, R.; Maier, J.; Acarturk, T.; Starke, U. Oxygen Tracer Diffusion in Dense $Ba_{0.5}Sr_{0.5}Co_{0.8}Fe_{0.2}O_{3-delta}$ Films. *App. Phys. Lett.* **2009**, 94, 071908-1–071908-3.

33. Munnings, C. N.; Skinner, S. J.; Amow, G.; Whitfield, P. S.; Davidson, I. J., Oxygen Transport in the $La_2Ni_{1-x}Co_xO_{4+delta}$ System. *Solid State Ionics* **2005**, *176*, 1895–1901.

34. Kawada, T.; Suzuki, J.; Sase, M.; Kaimai, A.; Yashiro, K.; Nigara, Y.; Mizusaki, J.; Kawamura, K.; Yugami, H. Determination of Oxygen Vacancy Concentration in a Thin Film of $La_{0.6}Sr_{0.4}CoO_{3-delta}$ by an Electrochemical Method. *J. Electrochem. Soc.* **2002**, *149*, E252–E259.

35. De Souza, R. A.; Kilner, J. A. Oxygen Transport in $La_{1-x}Sr_xMn_{1-y}Co_yO_{3+/-delta}$ Perovskites Part II. Oxygen Surface Exchange. *Solid State Ionics* **1999**, *126*, 153–161.

36. van der Haar, L. M.; den Otter, M. W.; Morskate, M.; Bouwmeester, H. J. M.; Verweij, H. Chemical Diffusion and Oxygen Surface Transfer of $La_{1-x}Sr_xCoO_{3-delta}$ Studied with Electrical Conductivity Relaxation. *J. Electrochem. Soc.* **2002**, *149*, J41–J46.

37. Sathe, V. G.; Pimpale, A. V.; Siruguri, V.; Paranjpe, S. K. Neutron Diffraction Studies of Perovskite-Type Compounds $La_{1-x}Sr_xCoO_3$ (x=0.1, 0.2, 0.3, 0.4, 0.5). *J. Phys. Condens. Mat.* **1996**, *8*, 3889–3896.

38. Fan, B. A.; Liu, X. L. A-deficit LSCF for Intermediate Temperature Solid Oxide Fuel Cells. *Solid State Ionics* **2009**, *180,* 973–977.

39. Dagotto, E. Physics - When Oxides Meet Face to Face. *Science* **2007**, *318,* 1076–1077.

40. Nellist, P. D.; Pennycook, S. J. The Principles and Interpretation of Annular Dark-field Z-Contrast Imaging. *In Advances in Imaging and Electron Physics* **2000**, *113*, 147-203.

41. Christen, H. M.; Specht, E. D.; Silliman, S. S.; Harshavardhan, K. S. Ferroelectric and Antiferroelectric Coupling in Superlattices of Paraelectric Perovskites at Room Temperature. *Physical Review B* **2003,** *68*, 020101-1–020101-4.

42. Mizusaki, J.; Mima, Y.; Yamauchi, S.; Fueki, K.; Tagawa, H. Nonstoichiometry of the Perovskite-Type Oxides $La_{1-X}Sr_xCoO_{3-Omega}$. *Journal of Solid State Chemistry* **1989,** *80*, 102-111.

43. Fleig, J. The Grain Boundary Impedance of Random Microstructures: Numerical Simulations and Implications for the Analysis of Experimental Data. *Solid State Ionics* **2002**, *150*, (1-2), 181-193.

Chapter 4. Oxygen Electrocatalysis on Epitaxial $La_{0.6}Sr_{0.4}CoO_{3-\delta}$ Perovskite Thin Films for Solid Oxide Fuel Cells

4.1 Introduction

The efficiency of solid oxide fuel cells (SOFCs) is limited primarily by the oxygen reduction reaction (ORR) at the cathode, particularly for SOFCs operated at intermediate temperatures. Therefore, there is a need to search for electrode materials with enhanced ORR activity. Mixed electronic and ionic conductors such as ABO_3 perovskites[1-3] and A_2BO_4 Ruddlesden-Popper materials,[4] are promising cathode materials due to their high oxygen ion diffusivity and surface exchange properties. Hetero-structured oxide interfaces have shown surprisingly high oxygen surface exchange properties.[5-11] Recently Sase et al.[9] have reported enhanced ORR kinetics of ~3 orders of magnitude at the interfaces between bulk $La_{0.6}Sr_{0.4}CoO_{3-\delta}$ ($LSC60\text{-}40_{113}$) grains and secondary $(La,Sr)_2CoO_{4+\delta}$ precipitates relative to bulk $LSC60\text{-}40_{113}$, having an estimated surface oxygen coefficient approaching $1\cdot10^{-5}$ $cm\cdot s^{-1}$ at 500 °C. Subsequently these authors show that ~1 order of magnitude enhancement in ORR activity can be obtained for composite cathodes screen-printed with these two oxide materials.[11] More recently, we have reported that surface decoration of $(La_{0.5}Sr_{0.5})_2CoO_{4+\delta}$ (LSC_{214}) particles epitaxially grown on the (001)-oriented $La_{0.8}Sr_{0.2}CoO_{3-\delta}$ thin films, which are epitaxially grown on yttria-stabilized zirconia (YSZ), can lead to marked enhancement in the surface oxygen exchange kinetics up to three orders of magnitude relative to bulk,[5] approaching that of the $LSC60\text{-}40_{113}/LSC_{214}$ interfaces of composite ceramics.[9]

In this study, we investigate the surface oxygen exchange kinetics of (001)-oriented LSC60-40_{113} and LSC_{214}-decorated LSC60-40_{113} thin films epitaxially grown on YSZ. First, as (001)-oriented $La_{0.8}Sr_{0.2}CoO_{3-\delta}$ (LSC80-20_{113}) thin films have shown enhanced ORR kinetics by one order of magnitude relative to bulk,[12] we are interested in understanding if (001)-oriented LSC60-40_{113} thin films would also exhibit enhanced surface oxygen kinetics relative to bulk. Polycrystalline LSC60-40_{113} thin films[13] supported on a sintered GDC substrate show comparable surface oxygen exchange coefficients to that of bulk LSC60-40_{113} pellet.[14] Considering previous studies[15] have shown that X-ray-diffraction-amorphous LSC60-40_{113} films have enhanced ORR activity than crystalline films supported on YSZ(001), single-crystalline, (001)-oriented LSC60-40_{113} films might have different surface oxygen kinetics from polycrystalline LSC60-40_{113} thin films reported previously.[13] Second, although previous work qualitatively confirm the enhancement at the interfaces between polycrystalline LSC60-40_{113} and $(La,Sr)_2CoO_4$ thin films,[8] we aim to quantify the degree of enhancement in the surface oxygen exchange kinetics associated with LSC_{214} decoration on (001)-oriented LSC60-40_{113} films. In this study, we report ORR activities for epitaxial (001)-oriented LSC60-40_{113} films comparable to bulk LSC60-40_{113}. In addition, surface LSC_{214} decoration grown epitaxially on the (001)-oriented LSC60-40_{113} thin films can provide activity enhancement up to 3 orders of magnitude relative to bulk, and have surface oxygen exchange coefficients comparable to those found for LSC_{214}-decorated LSC80-20_{113} reported previously.[5]

4.2 Experimental Methods

LSC60-40_{113} powders were synthesized by a solid-state reaction using a stoichiometric mixture of La_2O_3, $SrCO_3$, and Co_3O_4 (Alfa Aesar, USA) 1,000 °C in air for 12 hours. LSC_{214} and $Gd_{0.2}Ce_{0.8}O_2$ (GDC) was prepared by the Pechini method using $La(NO_3)_3{\cdot}6H_2O$, $Sr(NO_3)_2$, $Co(NO_3)_2{\cdot}6H_2O$, and $Gd(NO_3)_3$ and $Ce(NO_3)_3$, respectively. The precursors were dissolved in de-ionized water with citric acid, and ethylene glycol (Sigma-Aldrich, USA) mixture. After esterification at 100 °C, the resin was charred at 400 °C and then calcined at 1000 °C in air for 12 hours. Pulsed laser deposition (PLD) targets of LSC60-40_{113}, LSC_{214}, GDC with a diameter of 25 mm were fabricated by uniaxial pressing at 50 MPa and sintering at 1,350 °C in air for 20 hours.

Single-crystal 9.5 mol% Y_2O_3-stabilized ZrO_2 (YSZ) substrates with the (001)-orientation and a dimension of 10 × 10 × 0.5 mm (Princeton Scientific, USA, one sided polished) were used

for the substrate for film deposition and the electrolyte for activity measurements. Prior to film deposition, platinum ink (Pt) (#6082, BASF, USA) counter electrodes were painted on the unpolished side of the YSZ and sintered at 800 °C in air for 1 hour. The YSZ substrate was affixed to the PLD substrate holder using a small amount of silver paint (Leitsilber 200, Ted Pella, USA) for thermal contact. PLD was performed using the following parameters: KrF excimer laser (λ = 248 nm), 10 Hz pulse rate, ≈50 mJ pulse energy, distance between target and substrate ~5 cm, and $p(O_2)$ = 10 mTorr. To prevent the reactivity between YSZ and LSC60-40_{113}, 500 pulses of GDC were deposited first at 450 °C (~ 5 nm thick estimated from scanning transmission electron microscopy on similar samples as reported previously,[5] having ~0.01 nm/laser-pulse). This was followed by 5,000, 15,000, or 30,000 pulses of LSC60-40_{113} (~0.005 nm/laser-pulse) at 675 °C to produce films of different thicknesses, which was cooled to room temperature within ~1 h in 10 mTorr $p(O_2)$. LSC_{214}-decorated LSC60-40_{113} films were fabricated by adding 25, 150, 900, and 2700 pulses on the LSC60-40_{113} film of 15,000 pulses, which led to surface LSC_{214} decoration thickness of ~0.1 nm (partial coverage), ~0.8 nm, (partial coverage), ~5 nm (likely full coverage) and ~15 nm (full coverage), respectively, a linear thickness extrapolation was based on previous work of LSC_{214} decoration of LSC80-20_{113} films.[5, 16] A reference film of LSC60-40_{113} decorated with 25 pulses of LSC60-40_{113} was also fabricated for comparison.

The phase purity of oxide powder samples for PLD targets were investigated via high resolution X-ray diffraction (XRD) using a four-circle diffractometer (Panalytical, USA). Thin film XRD was performed using a four-circle diffractometer (Bruker D8, Germany) in normal and off-normal configurations. Film surface morphologies were examined by optical microscopy (Carl Zeiss, Germany) and atomic force microscopy (AFM) (Veeco, USA).

Micrometer-scale, circular LSC60-40_{113} electrodes with and without LSC_{214}-decoration were fabricated by photolithography and the following process: OCG positive photoresist (Arch Chemical Co, USA) was applied on the film surface and patterned using a mask aligner (Karl Süss, Germany, λ =365 nm). The photoresist was developed using Developer 934 1:1 (Arch Chemical Co., USA) developer, and the films were subsequently etched in hydrochloric acid (HCl) to form circular microelectrodes (diameters of 25 μm – 200 μm as determined by optical microscopy, **Figure 4-1a**). The photoresist was removed with acetone. The microelectrode sizes and morphological stability were examined by optical microscopy and AFM before and during

electrochemical testing. AFM was then used to measure the LSC60-40_{113} film thickness after microelectrode patterning, which showed thicknesses of 22, 77 and 157 nm for 5,000, 15,000 and 30,000 pulses, respectively. LSC_{214}-decorated LSC60-40_{113} films were found to have 88, 85, 88, and 97 nm for LSC_{214} coverage of ~0.1, ~0.8, ~5 and ~15 nm, respectively. The thickness of the reference LSC60-40_{113}-covered LSC60-40_{113} was 85 nm.

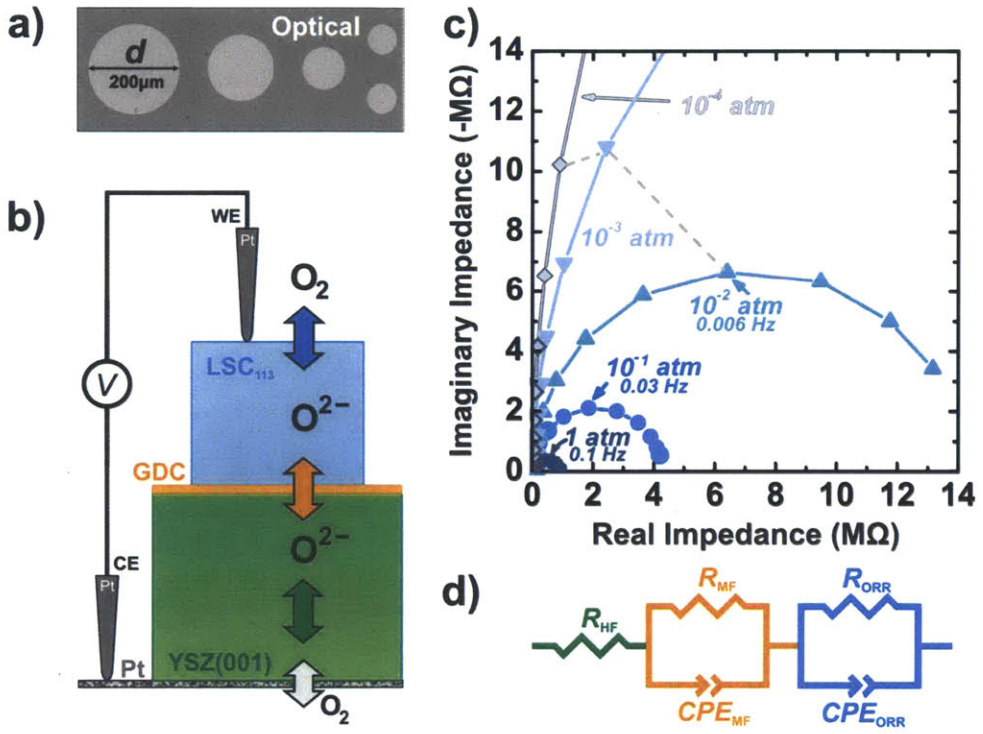

Figure 4-1. (a) Optical images of a LSC60-40_{113}(001)/GDC(001)/YSZ(001)/porous Pt sample and the electrochemical testing configuration, b) schematics of LSC microelectrodes on GDC/YSZ, (c) characteristic Nyquist plot of a 200 μm-microelectrode at 520 °C and varying $p(O_2)$, and (d) equivalent circuit (R_{HF} = YSZ electrolyte resistance, R_{MF} = electrode/electrolyte interface resistance, R_{ORR} = ORR resistance, CPE = constant phase element) used to extract ORR kinetics.

Electrochemical impedance spectroscopy (EIS) measurements of microelectrodes of ~ 200 μm in diameter, which were contacted by Pt-coated tungsten carbide probes, were performed using a microprobe station (Karl Süss, Germany) connected to a frequency response analyzer (Solartron 1260, USA) and dielectric interface (Solartron 1296, USA), as shown in **Figure 4-1b**. The porous Pt counter electrode was placed on a conductive substrate and fixed with Ag paste (Leitsilber 200, Ted Pella, USA). The temperature was controlled at 520 °C (for LSC60-40_{113} thin films) and 550 °C (for LSC60-40_{113} thin films with LSC_{214} surface decoration) with heating

stage (Linkam TS1500, UK) and calibrated using a second thermocouple contacting the thin film surface. Data were collected between 1 MHz and 1 mHz using a voltage amplitude of 10 mV under Ar / O_2 mixtures in the $p(O_2)$ range of $1 \cdot 10^{-4}$ to 1 atm. ZView software (Scribner Associates, USA) was used to analyze the EIS data. Multiple electrodes (at least three) of all films were measured by EIS at each temperature and $p(O_2)$ to ensure that the EIS results were reproducible and representative. The high-frenquency intercept corresponds to the oxygen ion conduction resistance in YSZ and the mid-frequency feature is believed to result from the interface between YSZ and GDC as reported previously.[5]

The film thicknesses of LSC60-40_{113} films are considerably smaller than the critical thickness, t_{crit}, of $\approx$ 20 μm found for bulk LSC60-40_{113} at 518 °C and $p(O_2)$ = 0.23 bar.[14] t_{crit} is defined as D^*/k^*, where D^* is the tracer oxygen diffusivity and k^* the tracer surface exchange coefficient,[17] below which surface oxygen exchange limits the ORR kinetics. Therefore, the ORR kinetics of these films were governed primarily by surface oxygen exchange kinetics. With this understanding, the EIS data (**Figure 4-1c**) were analyzed using a simplified equivalent circuit shown in **Figure 4-1d**, from which the ORR resistance (R_{ORR}) and oxygen surface exchange coefficients were obtained as follows. The extracted low-frequency resistance values ($R_{LF} = R_{ORR}$) were used to calculate the surface exchange coefficients k^q by:[5, 12, 18]

$$k^q = \frac{RT}{4F^2 R_{ORR} A_{electrode} c_0} \quad (1)$$

where R is the universal gas constant (8.314 J $mol^{-1} \cdot K^{-1}$), T is the absolute temperature (783 K), F is the Faraday's constant (96,500 $C \cdot mol^{-1}$), $A_{electrode}$ is the area of the microelectrode, and c_0 is the lattice oxygen concentration in LSC.

4.3 Results and Discussion

Normal X-ray diffraction (XRD) data (**Figure 4-2a**) clearly show the presence of the $(00l)_{pc}$ of LSC60-40_{113} and the $(00l)_{cubic}$ (l is even) peaks of GDC, and YSZ, which indicates $(001)_{pc}$LSC60-40_{113} // $(001)_{cubic}$GDC // $(001)_{cubic}$YSZ. The subscript "pc" denotes the pseudocubic notation, where the rhombohedral structure of LSC60-40_{113} bulk is approximated with an average for all film thicknesses of $a_{pc} \approx 3.847$ Å (**Table 4-1**).[5, 12] With LSC_{214} coverage equal to or greater

than ~5 nm in thickness, the $(00l)_{tetragonal}$ peaks (l is even) of LSC_{214} become visible (**Figure 4-2b**), which indicates $(001)_{tetragonal}LSC_{214}$ // $(001)_{pc}LSC60\text{-}40_{113}$ // $(001)_{cubic}GDC$ // $(001)_{cubic}YSZ$. These peaks give rise to $c_{tetragonal}$ = 12.5 Å for LSC_{214}, which is comparable to previously reported values.[19, 20] Off-normal phi-scan analysis shows that $LSC60\text{-}40_{113}\{101\}_{pc}$, $GDC\{202\}_{cubic}$ and $YSZ\{202\}_{cubic}$ have strong peaks with 4-fold cubic symmetry (**Figure S4-1a**),[21] which reveals the in-plane crystallographic relationships between GDC and YSZ (a cube-on-cube alignment), and $LSC60\text{-}40_{113}$ and GDC (a in-plane 45° rotation), having $[100]_{pc}LSC60\text{-}40_{113}//[110]_{cubic}GDC//[110]_{cubic}YSZ$ (**Figure S4-1b**).[21] These results are in agreement with our previously published findings for $LSC80\text{-}20_{113}$ thin films.[5, 12] The in-plane crystallographic relationship between $LSC60\text{-}40_{113}$ and LSC_{214} was not independently measured but it is likely to have $[100]_{pc}LSC60\text{-}40_{113}$ // $[100]_{tetragonal}LSC_{214}$ as shown previously for LSC_{214} decoration on (001)-oriented $LSC80\text{-}20_{113}$.[5]

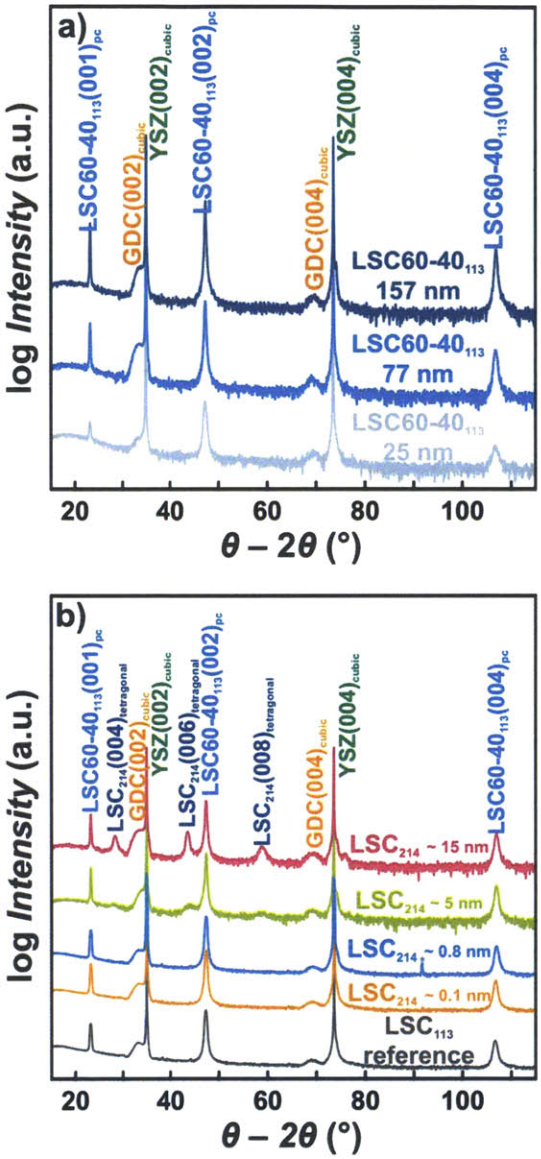

Figure 4-2. Normal XRD data of a) LSC60-40_{113} films of 25, 77 and 157 nm on $GDC(001)_{cubic}$/YSZ $(001)_{cubic}$ substrate, b) LSC60-40_{113} reference and LSC_{214}-decorated ~85 nm thick LSC60-40_{113} films. The (*) denotes a singular unknown artifact peak for the ~0.8 nm LSC_{214} surface decorated film.

LSC60-40_{113} films were found dilated in-plane and compressed in the direction normal to the film surface at room temperature with good crystallinity (**Table 4-1** and **Figure S4-2**[21]). It is interesting to note that the in-plane and normal strains decrease with increasing film thickness from 25 to 157 nm. The origin of these strains might be a consequence of different thermal expansion coefficients between YSZ (~11×10^{-6} $°C^{-1}$)[22] and LSC60-40_{113} films (~15.8×10^{-6} $°C^{-1}$ for bulk[23]). Experiments are ongoing to examine how these strains change upon heating to high

temperatures. Of significance to note is that the LSC60-40_{113} films have slightly smaller relaxed lattice parameters than bulk (3.855 Å[24]) at room temperature. The relaxed lattice parameter, $\hat{a}_{pc}$, can be estimated by assuming a Poisson ratio of 0.25[25] for LSC60-40_{113}, which gives rise to $\hat{a}_{pc}$ = 3.847 Å, 3.849 Å and 3.845 Å for the films of 25, 77 and 157 nm, respectively. Having different relaxed unit cell volume from bulk materials is commonly noted for PLD films, which may result from different oxygen nonstoichiometry[12, 23, 25] and/or microstructure.[12, 26] Unlike (001)-oriented epitaxial LSC80-20_{113} films that have larger relaxed lattice parameter than bulk,[5, 12] (001)-oriented epitaxial LSC60-40_{113} films were found to have smaller relaxed lattice parameters than bulk, which is indicative of lower oxygen vacancies in the films.

Table 4-1. Constrained and relaxed lattice parameters of LSC60-40_{113} films extracted from normal and off-normal XRD data from 100 mm^2 samples. Constrained normal and in-plane lattice parameters of LSC60-40_{113} films were calculated from combining the inter-planar distance of the $(002)_{pc}$ and $(101)_{pc}$ peaks. For reference lattice parameter and strain values for LSC80-20_{113} films is provided in **Table S4-1**.[12,21]

Materials	Constrained in-plane a (Å)	Constrained normal c (Å)	Relaxed film lattice parameter[a] $\hat{a}$ (Å)	In-plane strain $\varepsilon_{xx} = \frac{(a-\hat{a})}{\hat{a}}$	Normal strain $\varepsilon_{zz} = \frac{(c-\hat{a})}{\hat{a}}$
LSC60-$40_{113\text{-}25nm}$ (pc)	3.870	3.831	3.847	0.60 %	-0.40 %
LSC60-$40_{113\text{-}77nm}$ (pc)	3.870	3.836	3.849	0.53 %	-0.35 %
LSC60-$40_{113\text{-}157nm}$ (pc)	3.860	3.834	3.845	0.41 %	-0.27 %

[a] $\hat{a}$ was calculated from $\frac{\Delta c}{\hat{c}} = \frac{-2\nu}{1-\nu}\frac{\Delta a}{\hat{a}}$, assuming $\hat{a} = \hat{c}$ and ν = 0.25 for LSC60-40_{113}.

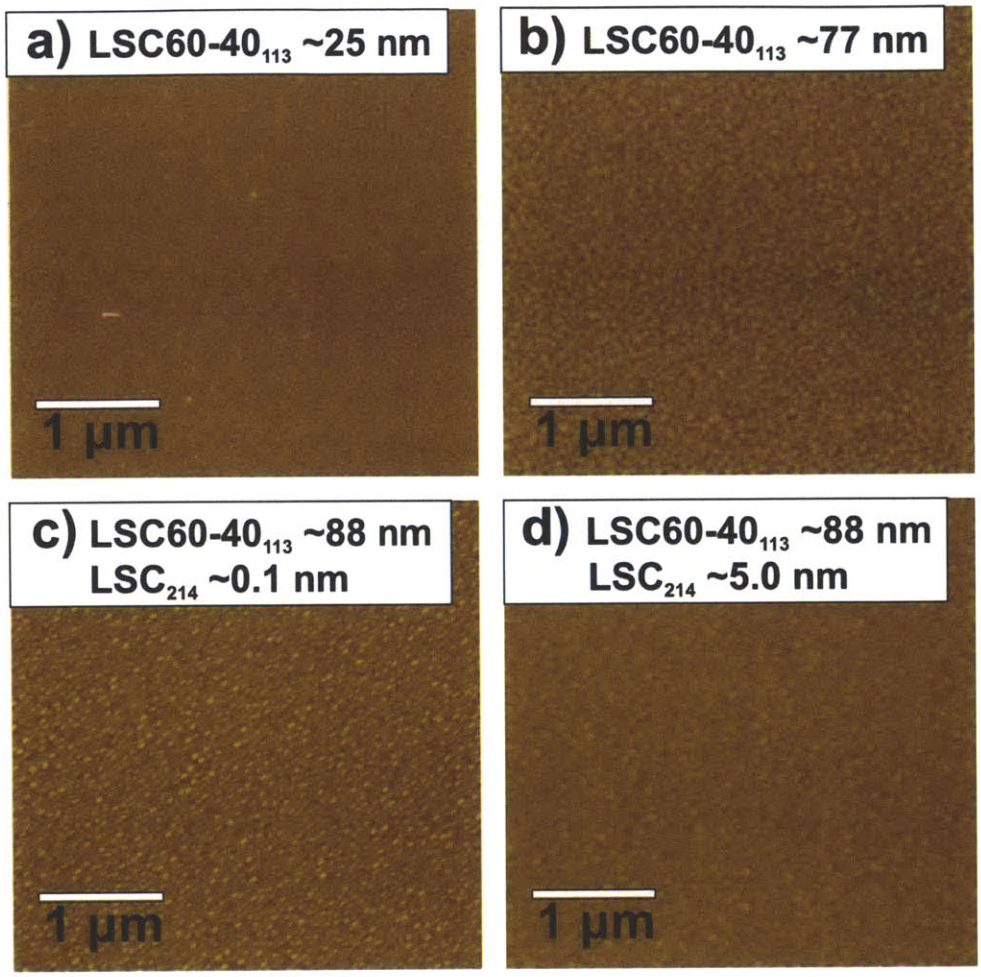

Figure 4-3. AFM measurements of **a)** LSC60-40_{113} ~ 25 nm with RMS of 0.8 nm **b)** LSC60-40_{113} ~ 77 nm with RMS of 0.8 nm, **c)** LSC60-40_{113} ~ 88 nm with LSC_{214} ~0.1 nm with RMS of 1.1 nm, and **d)** LSC60-40_{113} ~ 88 nm with LSC_{214} ~5 nm with RMS of 0.6 nm. AFM images are shown with maximum height of 20 nm.

AFM imaging revealed that the surface roughness of as-deposited LSC60-40_{113} films have low root-mean-squared (RMS) roughness less than ~1 nm (**Figures 4-3** and **S4-3**[21]). AFM images of LSC60-40_{113} of 25 nm, 77 nm, LSC_{214}-decorated 0.1 nm and 5.0 nm are shown in **Figure 4-3**, and AFM images of remaining films are shown in **Figure S4-3**.[21] With LSC_{214} coverage on LSC60-40_{113} films, there was no significant change in the surface roughness. The surface roughness of these LSC60-40_{113} and LSC_{214}-decorated LSC60-40_{113} films are comparable to those of LSC80-20_{113} and LSC_{214}-decorated LSC80-20_{113} films, respectively.[5]

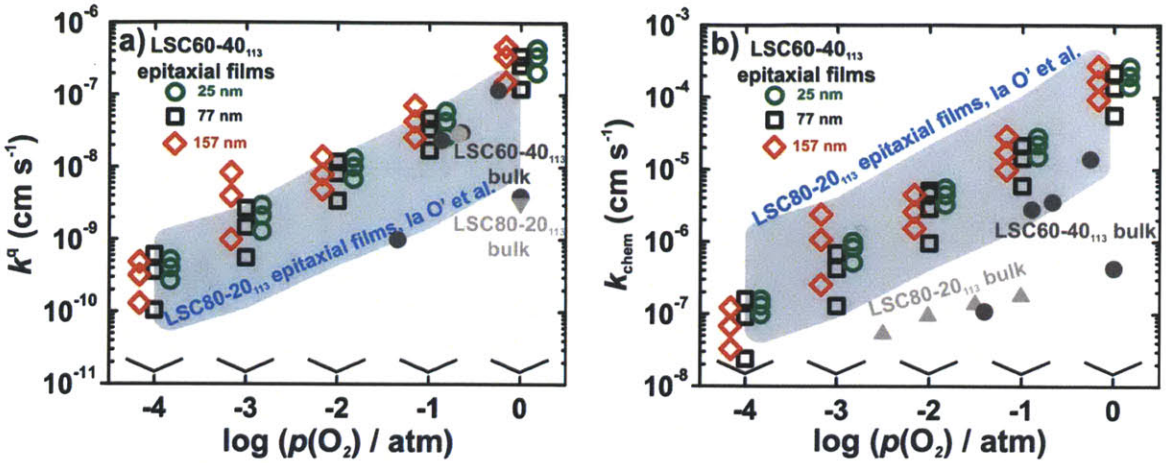

Figure 4-4. a) k^q and b) k_{chem} from LSC60-40$_{113}$ microelectrodes of 25, 77 and 157 nm calculated from EIS spectra collected at 520 °C. Extrapolated bulk k^* (approximately equivalent to k^q)[26] values obtained from previous data of (●) Sase et al.,[9] (●) Berenov et al,[14] (▼) De Souza et al.,[32] (▲) van der Haar et al.[31] are plotted for comparison. Blue shaded regions are the range of k^q and k_{chem} obtained from LSC80-20$_{113}$ film (film thicknesses of 20 nm to 130 nm).[12]

EIS data of all LSC60-40$_{113}$ thin films were found to be very similar in shape, and typical features in the Nyquist plots are shown in the schematic in **Figures 4-1c** and **S4-4**.[21] The predominant semicircle (assigned to the impedance of surface oxygen exchange kinetics) was found to increase with decreasing $p(O_2)$. The electrical surface exchange coefficient, k^q, was extracted from the real impedance while chemical surface exchange coefficient, k_{chem}, which describes the rate of surface oxygen exchange with chemical driving force, was estimated from the semicircle peak frequency (Supplementary Information[21]). The electrical surface exchange (k^q) and chemical surface exchange (k_{chem}) coefficients of LSC60-40$_{113}$ films of different thicknesses at 520 °C are plotted as a function of oxygen partial pressure, $p(O_2)$ in **Figures 4-4a** and **4-4b**, respectively. All LSC60-40$_{113}$ films exhibited comparable k^q and k_{chem}, which appeared to be thickness independent. It is interesting to note that the strains in LSC60-40$_{113}$ thin films measured at room temperature do not appear to correlate with surface oxygen exchange coefficients (**Figure S4-5**).[21] Assuming k^q can be approximated as k^*,[27] these k^q and k_{chem} values of the LSC60-40$_{113}$ thin films are comparable to those extrapolated for bulk LSC60-40$_{113}$,[9, 14] as shown in **Figure 4-4**. It should be mentioned that the (001)-oriented epitaxial LSC60-40$_{113}$ films in this study have comparable surface oxygen coefficients (~3×10^{-8} cm·s^{-1} at 0.1 atm) than those from polycrystalline LSC60-40$_{113}$ films extrapolated to 520 °C at $p(O_2)$ of 0.1 atm or lower.

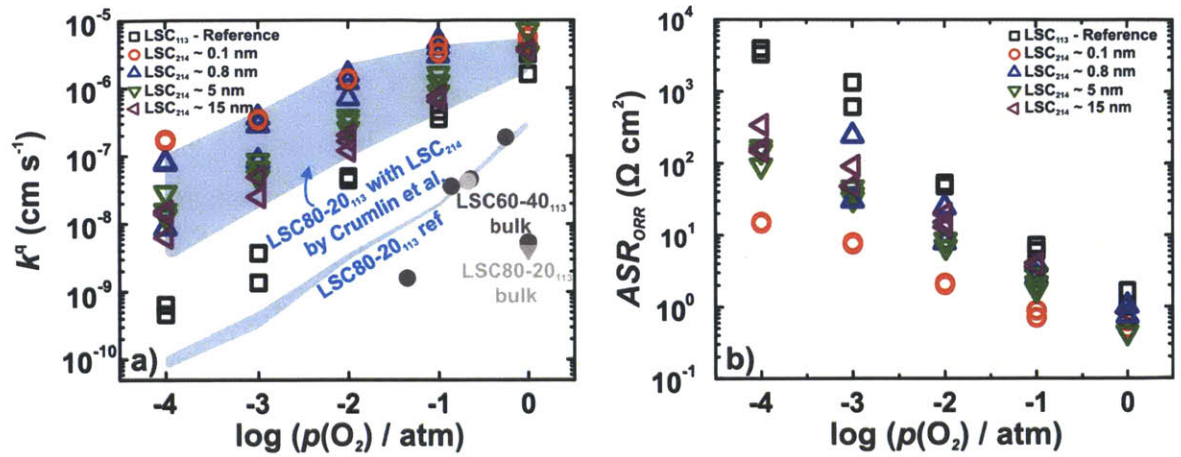

Figure 4-5. a) Oxygen partial pressure dependency of the surface exchange coefficients, k^q, and b) area specific resistances of the LSC60-40_{113} films with LSC_{214} surface coverage of ~0.1, ~0.8, ~5 and ~15 nm and the LSC60-40_{113}-reference at 550 °C. Extrapolated bulk k^* (approximately equivalent to k^q)[26] values obtained from previous studies of (●) Sase et al.,[9] (●) Berenov et al,[14] (▼) De Souza et al.[32] are plotted for comparison. Blue shaded region are the range of k^q values obtained from LSC_{214}-decorated LSC80-20_{113} films (LSC_{214} decoration thicknesses of ~0.1 nm to ~15 nm).[5]

LSC_{214} surface decoration on LSC60-40_{113} films led to markedly smaller real impedance and much greater surface oxygen exchange kinetics relative to LSC60-40_{113} and the LSC60-40_{113}-covered reference film (**Figure S4-6**).[21] At $p(O_2)$ of $1{\cdot}10^{-4}$ and $1{\cdot}10^{-2}$ atm, LSC_{214}-decoration increased k^q up to ~2 orders of magnitude relative to the reference LSC60-40_{113} film, having low coverage of 0.1 and 0.8 nm exhibiting the highest k^q values, as shown in **Figure 4-5a**. At $p(O_2)$ greater than 10^{-2} atm, the enhancement with surface coverage was ~1 order of magnitude. At these high $p(O_2)$ conditions, the very high k^q values (~$1{\cdot}10^{-6}$ cm·s^{-1} or higher) can decrease the critical thickness assuming a constant diffusion coefficient, and thus lead to ORR impedance to be influenced by bulk oxygen ion diffusion in addition to surface oxygen exchange. The much decreased $p(O_2)$ dependency of k^q for LSC_{214}-decorated LSC60-40_{113} films with low coverage at these high $p(O_2)$ further supports that ORR kinetics are limited also by bulk oxygen ion diffusion in the films of ~90 nm as typically oxygen ion diffusion is inversely proportional to $p(O_2)$.[14] Therefore, EIS measurements in the low $p(O_2)$ range from $1{\cdot}10^{-4}$ to $1{\cdot}10^{-2}$ atm better reflect the enhancement in the surface exchange kinetics associated with LSC_{214}-decoration. The k^q values of LSC_{214}-decorated LSC60-40_{113} films (0.1 nm) obtained from this study is ~2-3 orders of magnitude higher than that of bulk LSC60-40_{113}.[9, 14] Interestingly, the

LSC_{214}-decorated $LSC60\text{-}40_{113}$ films have comparable surface exchange coefficients to that estimated for the interfaces between bulk $La_{0.6}Sr_{0.4}CoO_{3-\delta}$ ($LSC60\text{-}40_{113}$) grains and secondary $(La,Sr)_2CoO_4$ precipitates relative at 500 °C and 0.2 atm.[9] Such high surface oxygen kinetics is comparable to those of the most active cathode materials such as thin-film $Ba_{0.5}Sr_{0.5}Co_{0.8}Fe_{0.2}CoO_{3-\delta}$ [k^* = ~$1\cdot10^{-6}$ cm·s^{-1} at 500 °C and 0.5 bar of $p(O_2)$[28]] and bulk La_2CoO_4 [k^* = ~$3\cdot10^{-6}$ cm·s^{-1} at 500 °C and 0.2 bar of $p(O_2)$[29]]. Moreover, the ORR area specific resistance ($R_{ORR}\cdot Area_{electrode}$) of these LSC_{214}-decorated $LSC60\text{-}40_{113}$ films (**Figure 4-5b**) at 550 °C and are smaller than 1 Ωcm^2 at 0.1 atm and greater, which are among the lowest reported to date.[30]

The $p(O_2)$ dependency of k ($k \propto P_{O_2}^m$) can be indicative of the rate-limiting step of ORR.[31] The $p(O_2)$ dependency of k^q for the $LSC60\text{-}40_{113}$ films of different thicknesses was found comparable, having m_{25nm} = 0.72, m_{77nm} = 0.69, and m_{157nm} = 0.76. Similar values were found for k_{chem}: m_{25nm} = 0.80, $m_{77\,nm}$ = 0.78, and m_{157nm} = 0.85. The obtained dependencies for k^q are in good agreement with those reported for bulk $La_{0.3}Sr_{0.7}CoO_{3-\delta}$ and $La_{0.5}Sr_{0.5}CoO_{3-\delta}$.[32] Interestingly, the $p(O_2)$ dependencies of k^q for the LSC_{214}-decorated $LSC60\text{-}40_{113}$ films in the range from $1\cdot10^{-4}$ to $1\cdot10^{-2}$ atm, having $m_{0.1nm}$ = 0.42, $m_{0.8nm}$ = 0.60, $m_{5.0nm}$ = 0.61, and $m_{15.0nm}$ = 0.53, are lower than the $LSC60\text{-}40_{113}$ films and reference sample (m_{ref} = 0.90). It should also be mentioned that these $p(O_2)$ dependencies are lower than that of LSC_{214}-decorated $LSC80\text{-}20_{113}$ (m ~ 0.90) reported previously.[5] Following the work of Adler et al,[2] such $p(O_2)$ dependencies suggest that the ORR rate-limiting step for $LSC60\text{-}40_{113}$ is dissociative adsorption (m between 0.43 and 0.92).

The k^q and k_{chem} values of (001)-oriented epitaxial $LSC60\text{-}40_{113}$ films in this study are comparable to those of (001)-oriented epitaxial $LSC80\text{-}20_{113}$ thin films reported previously[5, 12] (the range of max. and min. k^q and k_{chem} values shaded in blue in **Figure 4-4**), where $LSC60\text{-}40_{113}$ have activities toward the upper end of the activity spread of $LSC80\text{-}20_{113}$ films. This is in contrast to the fact that bulk $LSC60\text{-}40_{113}$[9, 14] has surface exchange coefficients significantly higher than $LSC80\text{-}20_{113}$.[33, 34] The enhancement associated with LSC_{214} decoration for $LSC60\text{-}40_{113}$ is similar to that reported for $LSC80\text{-}20_{113}$ coated with LSC_{214},[5, 12] where LSC_{214}-decorated $LSC60\text{-}40_{113}$ and $LSC80\text{-}20_{113}$ surface have very comparable surface oxygen exchange kinetics (having similar k^q and k_{chem} values in **Figure 4-5a**).

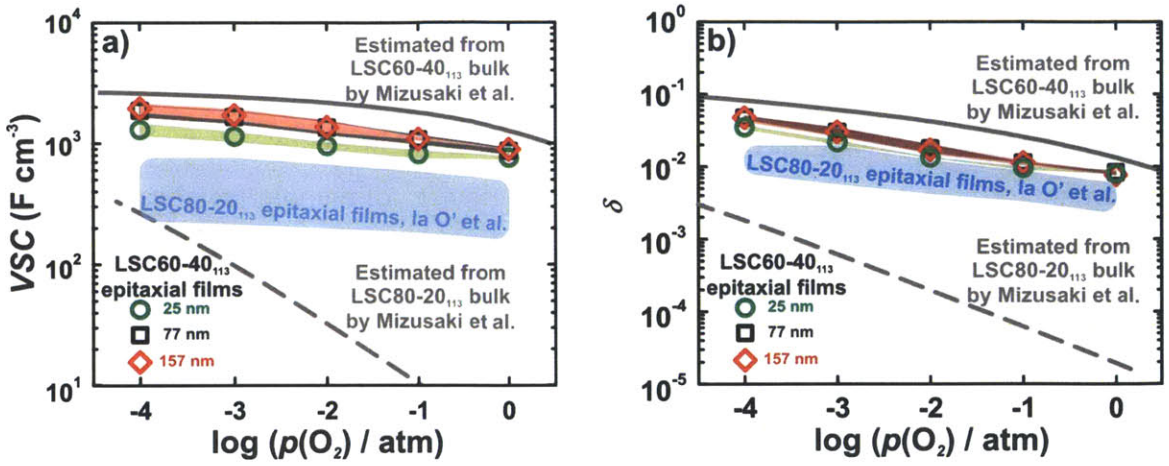

Figure 4-6. Oxygen partial pressure dependency of a) volume specific capacitance (*VSC*), b) oxygen nonstoichiometry δ of LSC60-40$_{113}$ of 25, 77, and 157 nm at 520 °C. Blue shaded regions are the range of *VSC* and δ from LSC80-20$_{113}$.[12] Values of bulk LSC60-40$_{113}$[34, 36] and LSC80-20$_{113}$[36] were calculated by using a method reported by Kawada et al.[34]

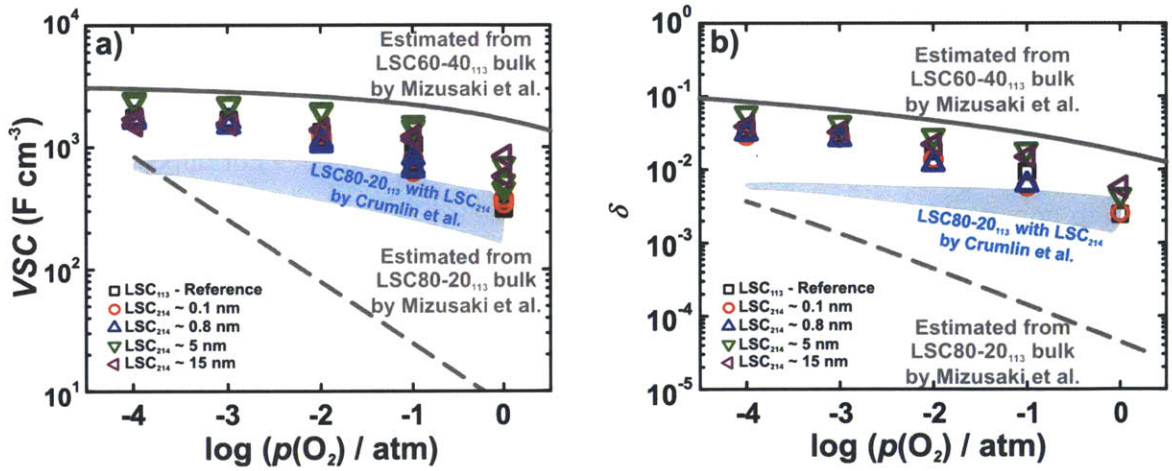

Figure 4-7. Oxygen partial pressure dependency of a) volume specific capacitance (VSC), *b*) average oxygen nonstoichiometry δ of LSC60-40$_{113}$-reference and the ~82 nm LSC60-40$_{113}$ films with ~0.1 nm, ~0.8 nm, ~5 nm, and ~15 nm LSC$_{214}$ surface coverage at 550 °C. Blue shaded regions are the range of *VSC* and δ from LSC80-20$_{113}$ with LSC$_{214}$ decoration.[5] Values of bulk LSC60-40$_{113}$[34, 36] and LSC80-20$_{113}$[36] were calculated by using a method reported by Kawada et al.[34]

We further show that LSC$_{214}$ decoration does not greatly influence the oxygen nonstoichiometry (δ) in the LSC60-40$_{113}$ films, which strongly depends on the La/Sr ratio in the perovskite structure. The oxygen nonstoichiometry (δ) in the LSC60-40$_{113}$ films at 520 °C was estimated using volume-specific capacitance (*VSC*). *VSC*s, indicative of changes in the oxygen

nonstoichiometry induced by changes in the electrical potential, were extracted from EIS data (Supporting Information).[21] LSC60-40_{113} films of different thicknesses at 520 °C had comparable *VSC*s (**Figure 4-6a**), which were smaller those of bulk LSC60-40_{113} extrapolated from thermodynamic parameters.[35] We can exclude the contribution of the interfacial capacitance[36] to the VSCs of LSC60-40_{113} films as plotting the area specific capacitance (*ASC*) obtained from EIS data as a function of film thickness in **Figure S4-7** yields zero intercept in *ASC*. Correspondingly, oxygen nonstiochiometry, δ, of the LSC60-40_{113} films, which was calculated from the thermodynamic parameters (**Table S4-2**)[21] of oxygen vacancy formation in the films based on the $p(O_2)$ dependency of *VSC*, was slightly smaller than that estimated for LSC60-40_{113} bulk,[37] and was similar to that of polycrystalline LSC60-40_{113} films reported by Kawada *et* al.[35] The lower oxygen nonstoichiometry of LSC60-40_{113} films at 520 °C is consistent with smaller relaxed unit cells of LSC60-40_{113} films than bulk LSC60-40_{113} at room temperature (Table 1). The (001)-oriented epitaxial LSC60-40_{113} films of this study had higher oxygen nonstiochiometry than similarly prepared LSC80-20_{113} films but the strong influence of the La/Sr ratio albeit its influence on the oxygen nonstiochiometry was found much smaller for thin films than bulk powder samples. As expected, LSC_{214} surface decoration does not appear to influence the oxygen nonstiochiometry of LSC60-40_{113} films, where LSC_{214}-decorated LSC60-40_{113} films had similar oxygen nonstoichiometry and *VSC*s (**Figure 4-7a**) to those without decoration.

The thermodynamic enhancement factor (scaling factor between k_{chem} and k^q, and can be related to the density of states near the Fermi Level)[38-40] was determined from k_{chem}/k^q (**Figure S4-8**).[21] The thermodynamic enhancement factors of these LSC60-40_{113} films are much higher than that for bulk LSC60-40_{113} reported previously,[37] indicating that it is more difficult to incorporate oxygen ions into the perovskite structure of the films. Similar observations have been made for polycrystalline LSC60-40_{113} films[35] and nanocrystalline LSC50-50_{113} films.[41] Interestingly, the thermodynamic enhancement factor appears to increase with the magnitude of in-plane and normal strains of LSC60-40_{113} films measured at room temperature (**Figure S4-9**).[21] Increased thermodynamic enhancement factor can be related to decreased density of states near the Fermi Level of LSC films,[38-40] which requires further studies. This is in contrast to the lack of measurable influence of strains in the LSC60-40_{113} films at room temperature on the surface exchange kinetics (**Figures 4-4** and **S4-5**[21]). Moreover, the decoration of LSC_{214} on the surface of LSC60-40_{113} films[8, 35] (similar to LSC80-20_{113} films[5]), which greatly enhances the surface

exchange kinetics, does not appear to considerably change the thermodynamic non-ideality factor (**Table S4-2**),[21] which is in agreement with the hypothesis that LSC_{214} decoration does not significantly alter the thermodynamics of the entire film.

$LSC60\text{-}40_{113}$ films showed comparable surface oxygen exchange kinetics and oxygen nonstoichiometry to $LSC60\text{-}40_{113}$ bulk, as shown in **Figures 4-6b** and **4-7b**. This is in contrast to previous findings of $LSC80\text{-}20_{113}$ films,[5, 12] which showed much enhanced surface oxygen exchange kinetics (k^q) coupled with higher oxygen nonstoichiometry than $LSC80\text{-}20_{113}$ bulk (blue shaded regions). Interestingly, $LSC60\text{-}40_{113}$ and $LSC80\text{-}20_{113}$ films can have very comparable surface oxygen exchange coefficients (**Figures 4-4a** and **4-4b**) but they have considerably dissimilar oxygen stoichiometry.[35,37] These observations suggest that oxygen nonstoichiometry in the films might not control the surface oxygen exchange kinetics, unlike the e_g filling of surface transition metal ions that govern the ORR and OER activities on perovskites in basic solutions over several orders of magnitude.[42, 43] This hypothesis does not preclude the possibility that a certain amount of oxygen nonstoichiometry is necessary for high surface oxygen exchange kinetics, and further increase in δ might not lead to activity enhancement. It should be cautioned, however, that oxygen nonstoichiometry shown in **Figures 4-6b** and **4-7b** represents the bulk film values, which can be considerably different from that on the surface.

4.4 Conclusions

We show that the surface oxygen exchange kinetics and oxygen nonstoichiometry of (001)-oriented $LSC60\text{-}40_{113}$ films grown epitaxially on YSZ are comparable to those of $LSC60\text{-}40_{113}$ bulk.[13, 14] This is in contrast to (001)-oriented $LSC80\text{-}20_{113}$ films with enhanced activities and oxygen nonstoichiometry relative to $LSC80\text{-}20_{113}$ bulk[32, 33] reported previously.[12] In addition, (001)-oriented epitaxial $LSC60\text{-}40_{113}$ films have similar surface oxygen exchange coefficient to polycrystalline $LSC60\text{-}40_{113}$ films[13] reported previously. LSC_{214} surface decoration on the (001)-oriented $LSC60\text{-}40_{113}$ films leads to ORR activity enhancement up to ~3 orders of magnitude with respect to bulk $LSC60\text{-}40_{113}$. The enhancement associated with LSC_{214} decoration for $LSC60\text{-}40_{113}$ is similar to that reported for $LSC80\text{-}20_{113}$-covered LSC_{214},[5, 12] where LSC_{214}-decorated $LSC60\text{-}40_{113}$ and $LSC80\text{-}20_{113}$ surfaces have very comparable surface oxygen exchange kinetics. Moreover, these LSC_{214}-decorated $LSC60\text{-}40_{113}$ films (**Figure 4-5b**) have the area specific resistance approaching ~0.45 Ωcm^2 at 1 atm and 550 °C, which are among the

lowest reported to date.[30] While the enhancement in ORR kinetics cannot be attributed to changes in the oxygen vacancy concentration of the entire films and film strains measured at room temperature, it is proposed that interfacial LSC_{113}/LSC_{214} regions are responsible for the observed ORR enhancement. Future studies are needed to elucidate the origin of enhanced ORR kinetics at interfacial LSC_{113}/LSC_{214} regions. This study illustrates the potential of utilizing hetero-structured oxide surfaces/interfaces to develop highly active surface oxygen exchange materials for applications in the field of solid-state electrochemistry such as micro SOFC cathodes, solid-electrolyte-based sensors, and oxygen conducting membranes.

4.5 Supporting Information

Experimental Details

Film Characterization

Thin film X-ray diffraction was performed using a four-circle diffractometer (Bruker D8, Karlsruhe, Germany). Measurements were performed in normal and off-normal configurations. As-deposited LSC60-40_{113} $(002)_{pc}$ and $(004)_{pc}$ films were found dilated in-plane and compressed in the direction normal to the film surface at room temperature, which is clearly shown in the high-resolution X-ray diffraction scans in **Figure S4-2.** The constrained in-plane lattice parameter of LSC60-40_{113} determined from the off-normal $(011)_{pc}$ peak position and the constrained lattice parameter of LSC normal to the film surface determined from the $(002)_{pc}$ peak positions are listed in **Table 4-1**. The LSC60-40_{113} films are clearly under tensile in-plane strain, and the corresponding relaxed pc lattice parameter, $\hat{a}_{pc}$, can be estimated by assuming a Poisson ratio, v, of 0.25 for LSC60-40_{113},[25] yielding $\hat{a}_{pc}$ = 3.847 Å, 3.849 Å and 3.845 Å for the films of 25, 77, and 157 nm thickness, respectively. Subscript "pc" denotes the pseudocubic notation, in which the rhombohedral structure of LSC60-40_{113}[44] is approximated. The in-plane and normal strains are summarized in **Table 4-1.**

Electrochemical Impedance Spectroscopy

EIS experiments were completed under varying Ar to O_2 mixtures between $p(O_2)$ of $1 \cdot 10^{-4}$ *atm* and 1 *atm*. *ZView* software (Scribner Associates, USA) was used to construct the equivalent circuit and perform complex least squares fitting. The EIS data were fitted using a

standard resistor (R_{HF}) for *HF* and resistors (R_i) in parallel with a constant phase elements (CPE_i) for *MF* and *LF* (R_{HF}-(R_{MF}/CPE_{MF})-(R_{LF}/CPE_{LF})). The *CPE* impedance can be written as $Z = 1/Q(j\omega)^n$, where is the angular frequency, Q is the non-ideal "capacitance", and n is the non-ideality factor of *CPE*. The fitted values of n for semi-circle CPE_{LF} were found to range from ~ 0.96 to 1.0 over the entire $p(O_2)$ range examined.

In this study, the ORR kinetics of epitaxial bare and LSC_{214} surface decorated LSC60-40_{113} thin films was examined using EIS measurements conducted on patterned epitaxial LSC microelectrodes fabricated by photolithography and acid etching. EIS data from the LSC microelectrodes were collected using a microprobe station setup, where platinum (Pt) coated tungsten micro-needles were used to contact the LSC working electrode and a porous Pt counter electrode on the bottom side of the YSZ substrate. EIS data collected from the epitaxial LSC60-40_{113} films of 25, 77 and 157 nm at 520 °C (**Figures 4-1c** and **S4-4**) and LSC_{214} decorated LSC60-40_{113} show similar features, and three distinctive features were noted, which are labeled as high-frequency (*HF*), middle-frequency (*MF*) and low-frequency (*LF*). The *HF* feature was found unchanged with $p(O_2)$, and its magnitude and activation energy (~1.15 eV) were comparable to those of oxygen ion conduction in YSZ reported previously.[45] The *MF* feature, which was found to have a $p(O_2)$ independent was attributed to interfacial transport of oxygen ions between the LSC film and the GDC layer as previously observed on $La_{0.5}Sr_{0.5}CoO_{3-\delta}$ /8YSZ.[46]

The *LF* feature changed significantly with $p(O_2)$, with its real impedance decreasing with increasing $p(O_2)$ from $1 \cdot 10^{-4}$ atm to 1 atm. This confirms that the ORR kinetics on the LSC thin film electrodes is limited by surface oxygen exchange.[47] Electrical and chemical surface oxygen exchange coefficients were calculated from the *LF* real and imaginary impedance as a function of $p(O_2)$, respectively. The electrical surface exchange coefficient (k^q), which is comparable to k^*,[27] was determined using the expression,[18,49]

$$k^q = RT/4F^2 R_{LF} A_{electrode} c_o \quad (1)$$

where R is the universal gas constant (8.314 J mol^{-1} K^{-1}), T is the absolute temperature, F is the Faraday's constant (96,500 C mol^{-1}), R_{LF} is the LF real resistance, $A_{electrode}$ is the area of the microelectrode and c_o is the lattice oxygen concentration in LSC where

$$c_o = (3-\delta)/V_m, \quad (2)$$

V_m is the molar volume of LSC at room temperature, where increasing temperatures to 520 °C or 550 °C has a negligible effect on the molar volume). It should be noted that bulk LSC molar volume of 32.82 cm^3 mol^{-1} was used in the calculation of k^q and oxygen nonstoichiometry as the influence of larger molar volumes of the thin films on k^q and is less than 3%. In addition, the chemical surface exchange coefficient (k_{chem}) was determined using the expression of[46,49]

$$k_{chem} = l/\tau \quad (3)$$

where l is the film thickness, and τ is the reciprocal of the angular peak frequency of the LF semicircle.

VSC, indicative of changes in the oxygen nonstoichiometry induced by changes in the electrical potential, can be obtained from EIS data via the expression

$$VSC = -\left(4F^2/V_m\right)\left(d\delta/d\mu_O\right) = \left(4F^2/V_m\right)\left[a(x) + 3RT/\delta(3-\delta)\right]^{-1}, \quad (4)$$

where *a(x)* is a factor that describes deviation from ideal solid solution, specifically how the enthalpy of oxygen in LSC changes with δ. The *a(x)* value of LSC powder was obtained from of the work of Mizusaki *et al.*[37] while δ values were extrapolated to 520 °C and 550 °C using the thermodynamic parameters reported in the same study.

Recently, the oxygen tracer surface exchange coefficient, k^* of $La_{0.6}Sr_{0.4}CoO_{3-\delta}$, measured in the temperature range of 406–680 °C and the oxygen partial pressure range 0.044–1.019 bar, has been reported.[14] The chemical surface exchange coefficient (k_{chem}) was determined using the expression of

$$k^* = k_{chem}/\gamma$$[50]

where γ was obtained from thermogravimetric measurements at 700 °C and assumed to be constant within the temperature range 525–700 °C.

Strain Effect

Figure S4-5 shows strain as a function of film thickness for LSC60-40_{113} and LSC80-20_{113}. LSC80-20_{113} films did not reveal a straightforward dependency of k and strain values. Decreasing the film thickness of LSC60-40_{113} from 157 nm to 25 nm, the amount of strain in the films became slightly larger as shown in **Figure S4-5** and **Table 4-1**. Again, there is no clear correlation between strain and k values for LSC60-40_{113} films.

The observed results suggest that there is no direct correlation between strain and surface exchange coefficient, or the conducted experiments do not allow a statement for one of the following reasons: (i) change in strain of the films is too small or sensitivity of used techniques (XRD, EIS) is not sufficient, (ii) the surface, which affects k^q predominately, has a different strain state than the bulk film (values determined by XRD reflect an average strain value for the bulk film; in reality the strain may differ in film regions close to the interface LSC/GDC and regions closer to the LSC surface; any surface reconstruction will also affect the surface strain), (iii) information on how these strains change at the EIS testing temperature may be necessary.

Table S4-1. Constrained and relaxed lattice parameters of LSC80-20_{113} films extracted from normal and off-normal XRD data from 100 mm^2 samples. Constrained normal and in-plane lattice parameters of LSC80-20_{113} films were calculated from combining the inter-planar distance of the $(002)_{pc}$ and $(101)_{pc}$ peaks.[12]

Materials	Constrained in-plane a (Å)	Constrained normal c (Å)	Relaxed film lattice parameter[a] $\hat{a}$ (Å)	In-plane strain $\varepsilon_{xx} = \frac{(a-\hat{a})}{\hat{a}}$	Normal strain $\varepsilon_{zz} = \frac{(c-\hat{a})}{\hat{a}}$
LSC80-$20_{113\text{-}20nm}$ (pc)[12]	3.890	3.829	3.853	0.95 %	-0.63 %
LSC80-$20_{113\text{-}45nm}$ (pc)[12]	3.915	3.825	3.861	1.40 %	-0.93 %
LSC80-$20_{113\text{-}130nm}$ (pc)[12]	3.862	3.843	3.851	0.30 %	-0.20 %

[a] $\hat{a}$ was calculated from $\frac{\Delta c}{\hat{c}} = \frac{-2\nu}{1-\nu}\frac{\Delta a}{\hat{a}}$, assuming $\hat{a} = \hat{c}$ and $\nu = 0.25$ for LSC80-20_{113}.

Table S4-2. Calculated thermodynamic non-ideality factor, *a(x)*, for LSC bulk and polycrystalline and epitaxial thin-film. Detailed procedure to obtain parameters is explained in the experimental section and Kawada *et al.*[35]

$La_{(1-x)}Sr_xCoO_3$	*surface decoration*	***a(x)*** (kJ mol^{-1})
$LSC60\text{-}40_{113}$ 1.5 μm thin film (Kawada *et al.*)[35]	*NA*	332
$LSC60\text{-}40_{113}$ pellet (Mizusaki *et al.*)[37]	*NA*	289
$LSC60\text{-}40_{11325nm}$ (001) epi-film (in this work)	*NA*	533 ~ 665
$LSC60\text{-}40_{11377nm}$ (001) epi-film (in this work)	*NA*	364 ~ 450
$LSC60\text{-}40_{113157nm}$ (001) epi-film (in this work)	*NA*	349 ~ 421
$LSC60\text{-}40_{113}$ (001) epi-film (in this work)	$LSC60\text{-}40_{113}$ ~ *0.1 nm*	398
$LSC60\text{-}40_{113}$ (001) epi-film (in this work)	LSC_{214} ~ *0.1 nm*	405
$LSC60\text{-}40_{113}$ (001) epi-film (in this work)	LSC_{214} ~ *0.8 nm*	388
$LSC80\text{-}20_{113}$ pellet (Mizusaki *et al.*)[37]	*NA*	418
	NA	289
$LSC80\text{-}20_{113\text{-}20nm}$ (001) epi-film (previously reported)[12]	*NA*	2,700 ~ 3,400
$LSC80\text{-}20_{113\text{-}45nm}$ (001) epi-film (previously reported)[12]	*NA*	1,000 ~ 1,500
$LSC80\text{-}20_{113130nm}$ (001) epi-film (previously reported)[12]	*NA*	1,400 ~ 1,700
$LSC80\text{-}20_{113}$ (001) epi-film (previously reported)[5]	$LSC80\text{-}20_{113}$ ~ *0.1 nm*	1100
$LSC80\text{-}20_{113}$ (001) epi-film (previously reported)[5]	LSC_{214} ~ *0.1 nm*	900
$LSC80\text{-}20_{113}$ (001) epi-film (previously reported)[5]	LSC_{214} ~ *0.8 nm*	1050
$LSC80\text{-}20_{113}$ (001) epi-film (previously reported)[5]	LSC_{214} ~ *5 nm*	1130
$LSC80\text{-}20_{113}$ (001) epi-film (previously reported)[5]	LSC_{214} ~ *15 nm*	1320

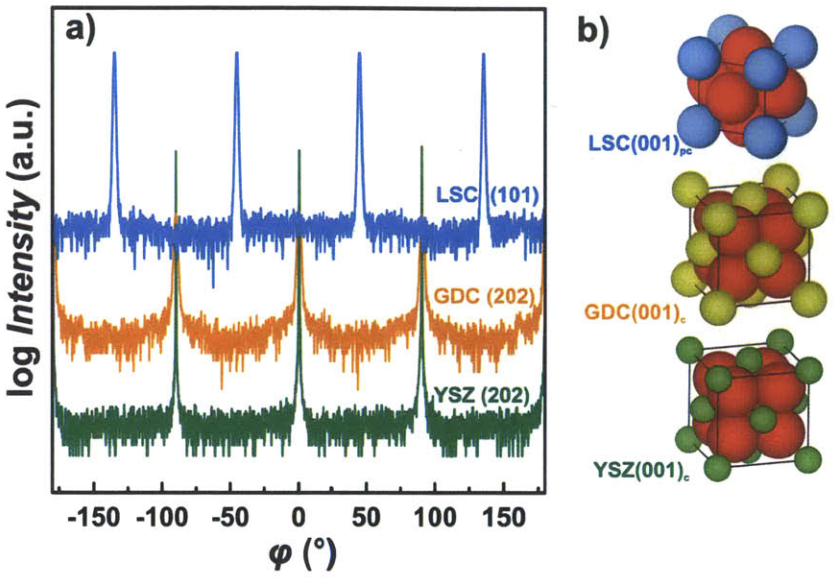

Figure S4-1. a) Off-normal X-ray diffraction patterns for the 77 nm LSC60-40_{113} film, GDC $(001)_{cubic}$ and YSZ $(001)_{cubic}$. The LSC60-40_{113} $\{110\}_{pc}$ reflections have a 45° offset with the GDC and YSZ $\{220\}_{cubic}$ in the ϕ-angle, **b)** schematic depicting the atomic structure alignment of LSC60-40_{113}/GDC/YSZ.

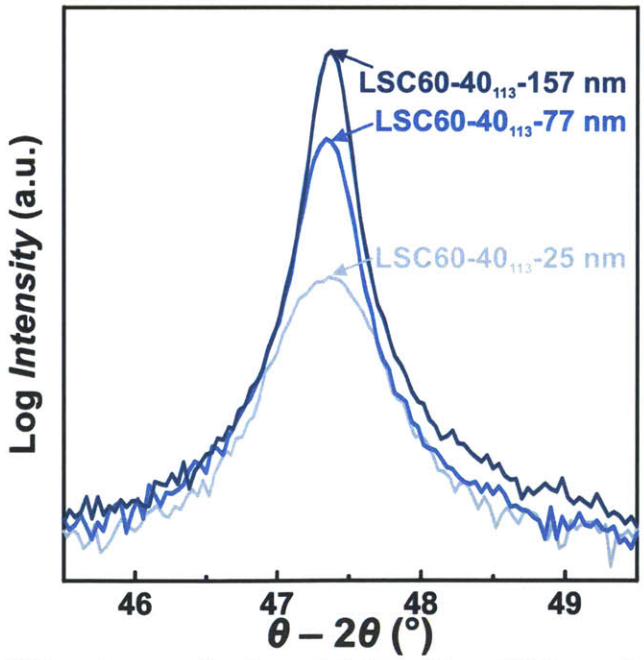

Figure S4-2. X-ray diffraction results from LSC60-40_{113} $(002)_{pc}$ reflection of 25, 77, and 157 nm. As film is getting thicker, the peak shift of LSC60-40_{113} $(002)_{pc}$ to the lower angle, indicating relaxation of the tensile strain, is clearly observed.

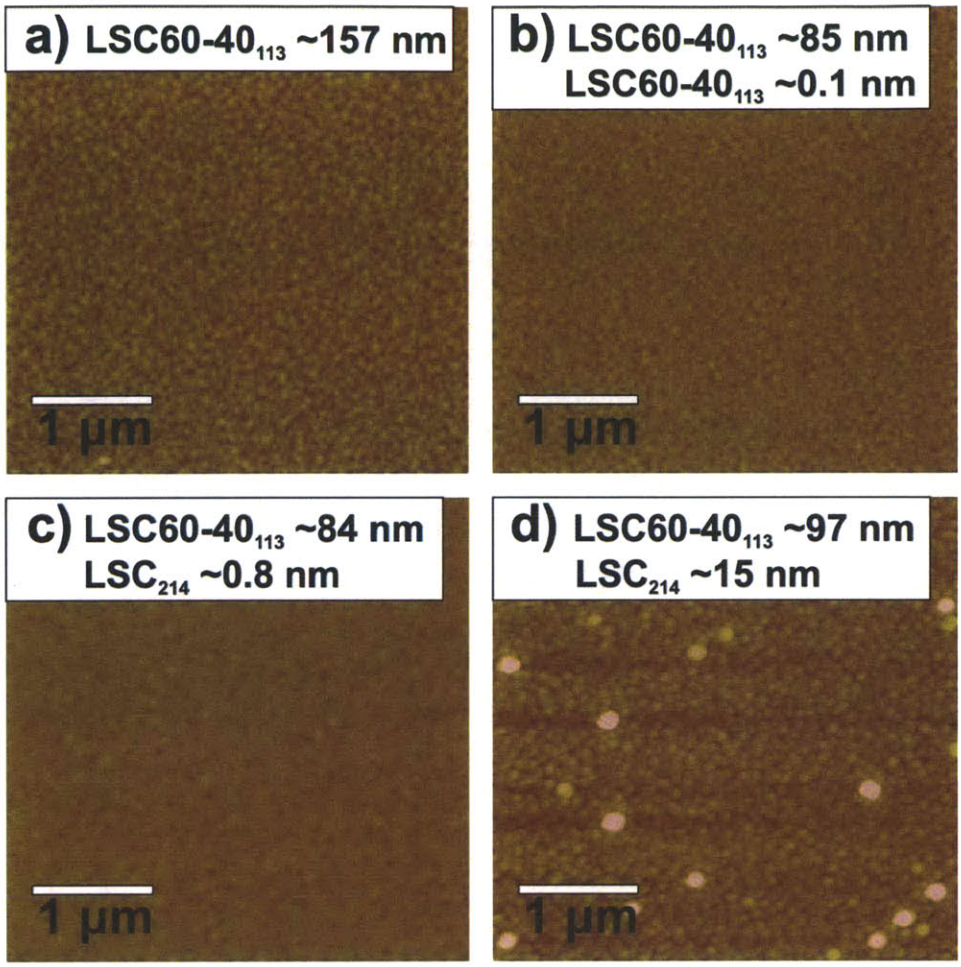

Figure S4-3. AFM images of **a)** LSC60-40_{113} ~ 157 nm, **b)** LSC60-40_{113} with 25 pulses LSC60-40_{113} surface decoration ~ 85 nm dense films, **c)** LSC60-40_{113} with ~0.8nm LSC_{214} surface decoration ~ 84 nm, and **d)** LSC60-40_{113} with ~15 nm LSC_{214} surface decoration ~ 97 nm (bright spots we believe are small precipitate phases that formed during PLD, these features are not seen on any other films and do not appear to influence EIS measurements). AFM images are shown with maximum height of 20 nm.

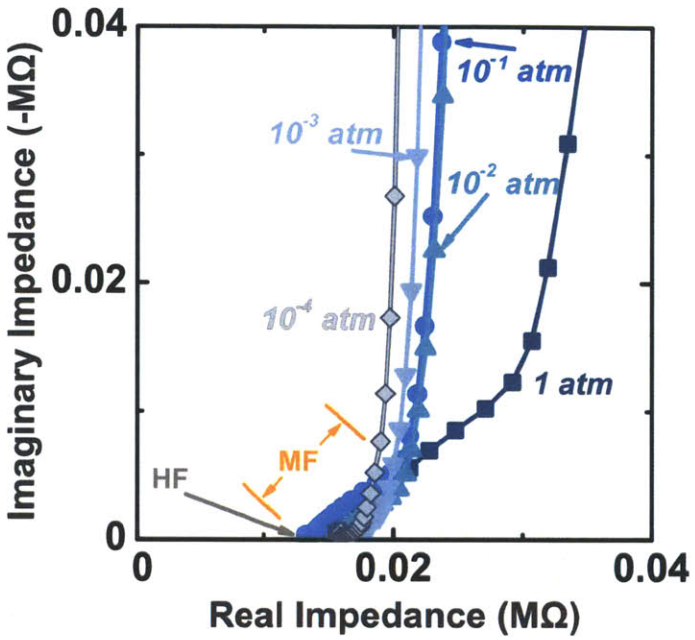

Figure S4-4. LSC60-40_{113} R_{HF} (YSZ electrolyte resistance) and R_{MF} (electrode/electrolyte interface resistance) region in Nyquist plot at 520 °C in 1 to $1 \cdot 10^{-4}$ atm $p(O_2)$.

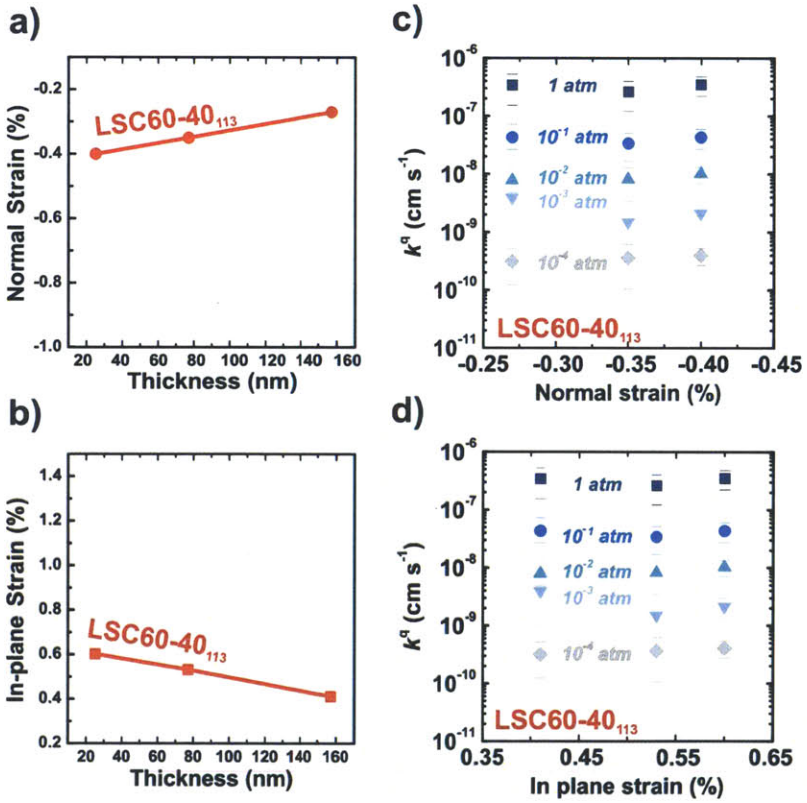

Figure S4-5. (a) Normal strain and **(b)** In-plane versus film thickness of LSC60-40_{113} (red color). **(c)** Normal strain, **(d)** In-plane strain dependency of k^q from LSC60-40_{113} at various oxygen partial pressures.

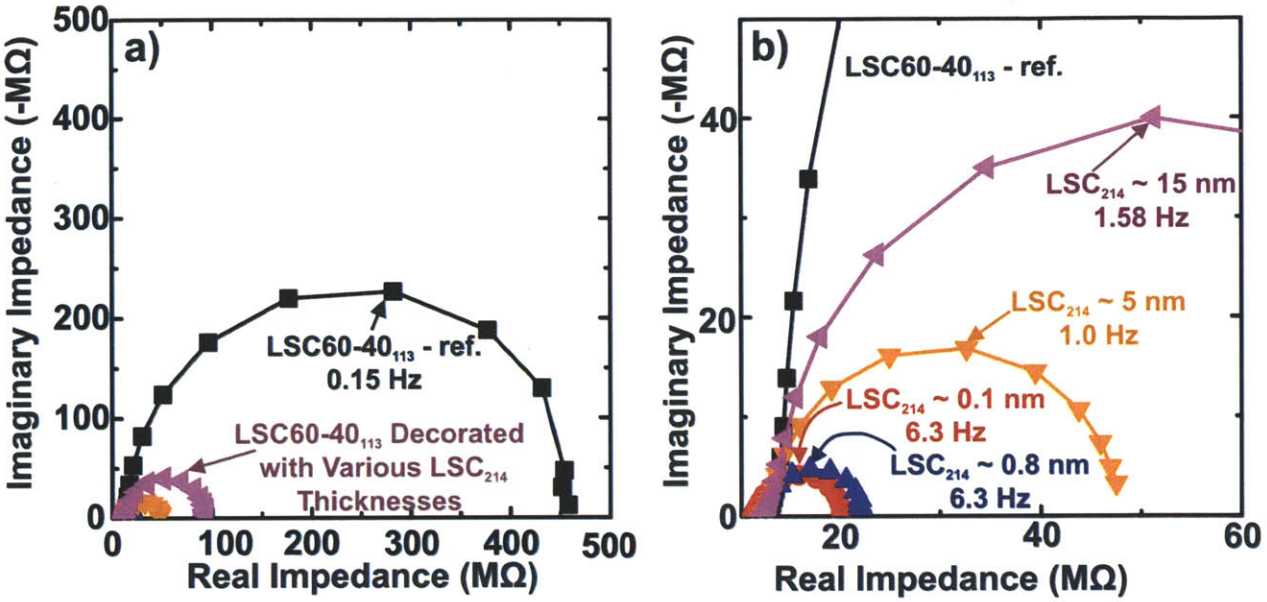

Figure S4-6. (a) Nyquist plots for LSC60-40_{113} films decorated with LSC_{214}, **(b)** is a magnification at 550 °C and $1 \cdot 10^{-2}$ atm $p(O_2)$.

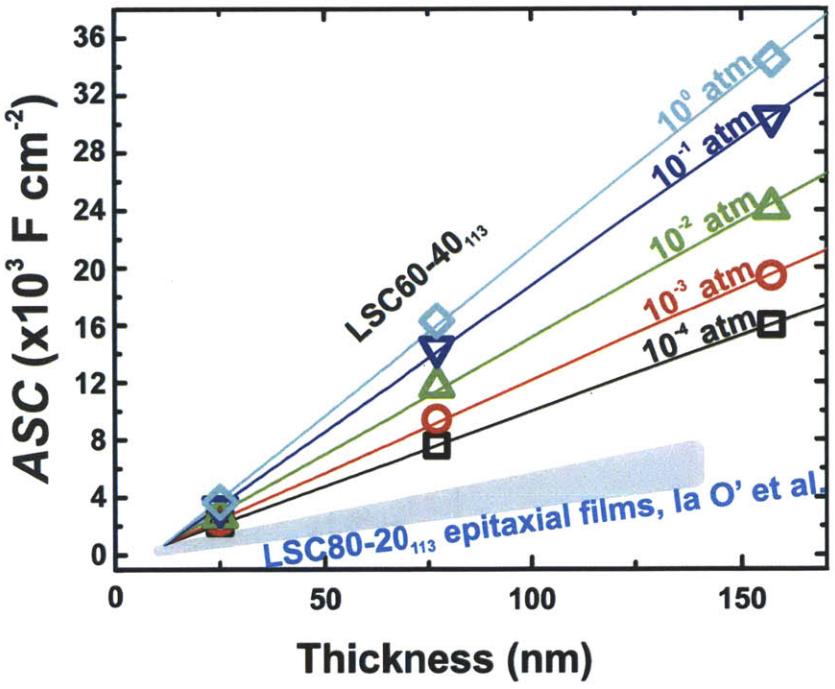

Figure S4-7. Area specific capacitance of LSC LSC60-40_{113} and LSC80-20_{113} (blue shaded region) measured at 520 °C under varying $p(O_2)$ from $1 \cdot 10^{-4}$ to 1 atm as a function of film thickness. The intercept gives the sum of interfacial capacitances.

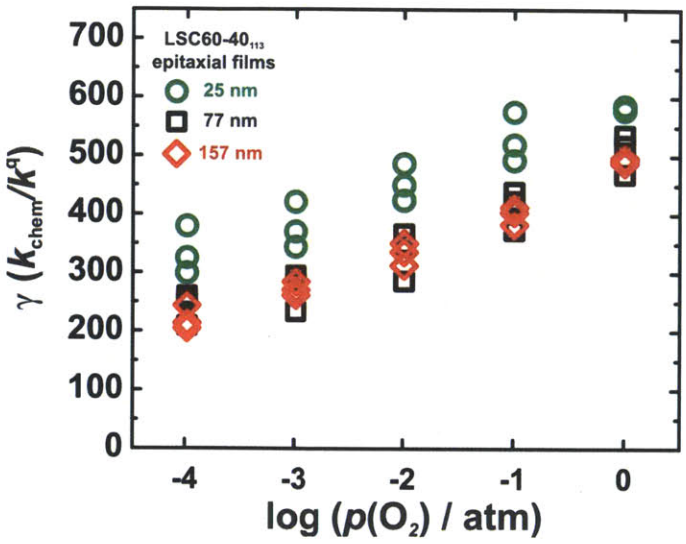

Figure S4-8. Gama, γ, of LSC LSC60-40_{113} of 25, 77, and 157 nm measured at 520 °C under varying $p(O_2)$ from $1 \cdot 10^{-4}$ to 1 atm.

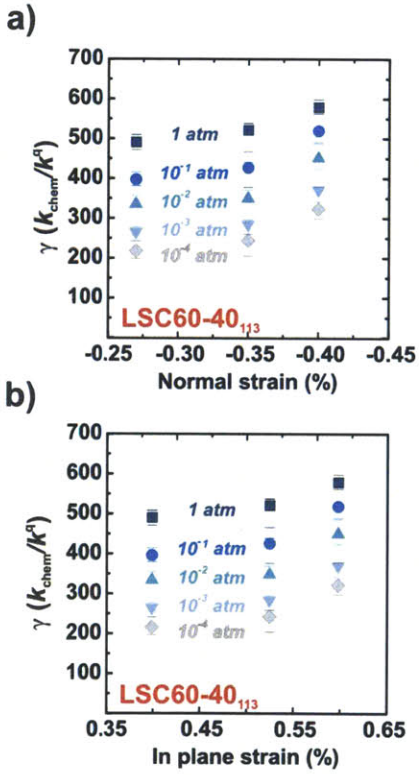

Figure S4-9. (a) Normal strain, **(b)** In-plane strain dependency on γ from LSC60-40_{113} films of different thicknesses (strains measured at room temperature) at various oxygen partial pressures.

4.6 References

1. S. B. Adler, *Chem. Rev.*, **104**, 4791 (2004).
2. S. B. Adler, X. Y. Chen and J. R. Wilson, *J. Catal.*, **245**, 91 (2007).
3. Y. L. Lee, J. Kleis, J. Rossmeisl and D. Morgan, *Phys. Rev. B*, **80** (2009).
4. A. Tarancon, M. Burriel, J. Santiso, S. J. Skinner and J. A. Kilner, *J. Mater. Chem.*, **20**, 3799 (2010).
5. E. J. Crumlin, E. Mutoro, S. J. Ahn, G. J. la O, D. N. Leonard, A. Borisevich, M. D. Biegalski, H. M. Christen and Y. Shao-Horn, *J. Phys. Chem. Lett.*, **1**, 3149 (2010).
6. A. Cavallaro, M. Burriel, J. Roqueta, A. Apostolidis, A. Bernardi, A. Tarancon, R. Srinivasan, S. N. Cook, H. L. Fraser, J. A. Kilner, D. W. McComb and J. Santiso, *Solid State Ionics*, **181**, 592 (2010).
7. W. Donner, C. Chen, M. Liu, A. J. Jacobson, Y.-L. Lee, M. Gadre and D. Morgan, *Chem. Mater.*, **23**, 984 (2011).
8. M. Sase, F. Hermes, K. Yashiro, K. Sato, J. Mizusaki, T. Kawada, N. Sakai and H. Yokokawa, *J. Electrochem. Soc.*, **155**, B793 (2008).
9. M. Sase, K. Yashiro, K. Sato, J. Mizusaki, T. Kawada, N. Sakai, K. Yamaji, T. Horita and H. Yokokawa, *Solid State Ionics*, **178**, 1843 (2008).
10. N. Schichtel, C. Korte, D. Hesse and J. Janek, *Phy. Chem. Chem. Phys.*, **11**, 3043 (2009).
11. K. Yashiro, T. Nakamura, M. Sase, F. Hermes, K. Sato, T. Kawada and J. Mizusaki, *Electrochem. Solid State Lett.*, **12**, B135 (2009).
12. G. J. la O, S. J. Ahn, E. Crumlin, Y. Orikasa, M. D. Biegalski, H. M. Christen and Y. Shao-Horn, *Angew. Chem. Int. Edit.*, **49**, 5344 (2010).
13. T. Kawada, K. Masuda, J. Suzuki, A. Kaimai, K. Kawamura, Y. Nigara, J. Mizusaki, H. Yugami, H. Arashi, N. Sakai and H. Yokokawa, *Solid State Ionics*, **121**, 271 (1999).
14. A. V. Berenov, A. Atkinson, J. A. Kilner, E. Bucher and W. Sitte, *Solid State Ionics*, **181**, 819 (2010).
15. J. Januschewsky, M. Ahrens, A. Opitz, F. Kubel and J. Fleig, *Adv. Funct. Mater.*, **19**, 3151 (2009).
16. E. Mutoro, E. J. Crumlin, H. Pöpke, B. Luerssen, M. Amati, M. K. Abyaneh, M. D. Biegalski, H. M. Christen, L. Gregoratti, J. Janek and Y. Shao-Horn, *J. Phys. Chem. Lett.*, **3**, 40 (2012).

17. H. J. M. Bouwmeester, H. Kruidhof and A. J. Burggraaf, *Solid State Ionics*, **72**, 185 (1994).
18. J. Maier, *Physical Chemistry of Ionic Materials: Ions and Electrons in Solids* p. 537, John Wiley, Chichester, England ; Hoboken, NJ (2004).
19. M. James, A. Tedesco, D. Cassidy, M. Colella and P. J. Smythe, *J. Alloy Compd.*, **419**, 201 (2006).
20. M. Sánchez-Andújar and M. A. Señarís-Rodríguez, *Solid State Sci.*, **6**, 21 (2004).
21. See supplementary material at http://dx.doi.org/xyz/xyzjes for additional information.
22. T. Ishihara, T. Kudo, H. Matsuda and Y. Takita, *J. Electrochem. Soc.*, **142**, 1519 (1995).
23. X. Y. Chen, J. S. Yu and S. B. Adler, *Chem. Mater.*, **17**, 4537 (2005).
24. R. Sonntag, S. Neov, V. Kozhukharov, D. Neov and J. E. ten Elshof, *Physica B*, **241**, 393 (1997).
25. H. M. Christen, E. D. Specht, S. S. Silliman and K. S. Harshavardhan, *Phys. Rev. B*, **68**, 4 (2003).
26. G. Kim, S. Wang, A. J. Jacobson, Z. Yuan, W. Donner, C. L. Chen, L. Reimus, P. Brodersen and C. A. Mims, *Appl. Phys. Lett.*, **88**, 3 (2006).
27. J. Maier, *Solid State Ionics*, **112**, 197 (1998).
28. L. Wang, R. Merkle, J. Maier, T. Acarturk and U. Starke, *Appl. Phys. Lett.*, **94**, 3 (2009).
29. C. N. Munnings, S. J. Skinner, G. Amow, P. S. Whitfield and I. J. Davidson, *Solid State Ionics*, **176**, 1895 (2005).
30. Z. P. Shao and S. M. Haile, *Nature*, **431**, 170 (2004).
31. R. A. De Souza, *Physical Chemistry Chemical Physics*, **8**, 890 (2006).
32. L. M. van der Haar, M. W. den Otter, M. Morskate, H. J. M. Bouwmeester and H. Verweij, *J. Electrochem. Soc.*, **149**, J41 (2002).
33. R. A. De Souza and J. A. Kilner, *Solid State Ionics*, **126**, 153 (1999).
34. Y. X. Lu, C. Kreller and S. B. Adler, *J. Electrochem. Soc.*, **156**, B513 (2009).
35. T. Kawada, J. Suzuki, M. Sase, A. Kaimai, K. Yashiro, Y. Nigara, J. Mizusaki, K. Kawamura and H. Yugami, *J. Electrochem. Soc.*, **149**, E252 (2002).
36. W. C. Chueh and S. M. Haile, *Phys. Chem. Chem. Phys.*, **11**, 8144 (2009).
37. J. Mizusaki, Y. Mima, S. Yamauchi, K. Fueki and H. Tagawa, *J. Solid State Chem.*, **80**, 102 (1989).

38. M. H. R. Lankhorst, H. J. M. Bouwmeester and H. Verweij, *Phys. Rev. Lett.*, **77**, 2989 (1996).

39. M. H. R. Lankhorst, H. J. M. Bouwmeester and H. Verweij, *J. Solid State Chem.*, **133**, 555 (1997).

40. M. H. R. Lankhorst, H. J. M. Bouwmeester and H. Verweij, *Solid State Ionics*, **96**, 21 (1997).

41. S. Y. Wang, J. Yoon, G. Kim, D. X. Huang, H. Y. Wang and A. J. Jacobson, *Chem. Mater.*, **22**, 776 (2010).

42. J. Suntivich, H. A. Gasteiger, N. Yabuuchi, H. Nakanishi, J. B. Goodenough and Y. Shao-Horn, *Nature Chem.*, **3**, 647 (2011).

43. J. Suntivich, K. J. May, H. A. Gasteiger, J. B. Goodenough and Y. Shao-Horn, *Science Express*, 10.1126/science.1212858 (2011).

44. R. H. E. van Doorn, A. J. Burggraaf, *Solid State Ionics*, **128**, 65 (2000).

45. P. S. Manning, J. D. Sirman, R. A. DeSouza, J. A. Kilner, *Solid State Ionics*, **100**, 1 (1997).

46. Y. L. Yang, C. L. Chen, S. Y. Chen, C. W. Chu, A. J. Jacobson, *J. Electrochem. Soc.*, **147**, 4001 (2000).

47. S. B. Adler, J. A. Lane, B. C. H. Steele, *J. Electrochem. Soc.* 1996, **143**, 3554 (1996).

48. J. Fleig, J. Maier, *J. Eur. Ceram. Soc.*, 24, 1343 (2004).

49. G. Kim, S. Wang, A. J. Jacobson, L. Reimus, P. Brodersen, C. A. Mims, *J. Mater. Chem.*, 17, 2500 (2007).

50. J. A. Lane, S. J. Benson, D. Waller, J. A. Kilner, *Solid State Ionics*, 121, 201 (1999).

Chapter 5. Surface Strontium Enrichment on Highly Active Perovskites for Oxygen Electrocatalysis in Solid Oxide Fuel Cells

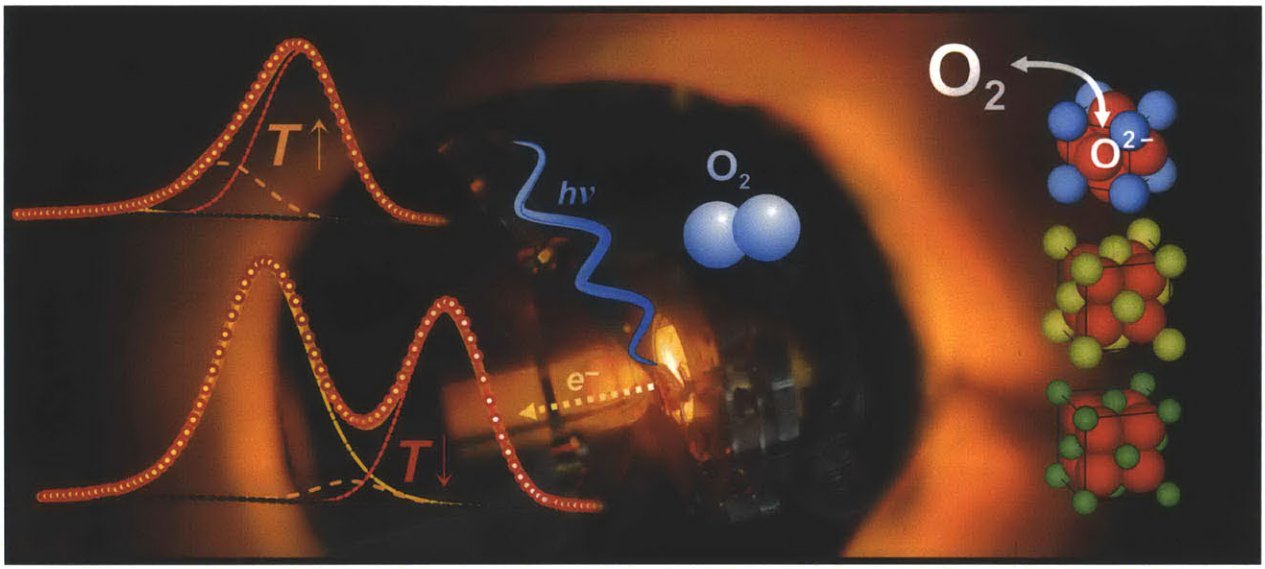

Look into the synchrotron-based ambient pressure X-ray photoelectron spectroscopy (APXPS) chamber where a highly active oxygen reduction catalyst, $La_{0.8}Sr_{0.2}CoO_{3-\delta}$ (LSC), is investigated *in situ* as function of the temperature.

5.1 Introduction

Transition-metal perovskite oxides are used commonly to promote the kinetics of oxygen electrocatalysis in electrolytic and fuel cells,[1-7] which can potentially enable the development of cost-effective energy storage and conversion technologies to allow the use of renewable energy on demand. Lack of fundamental understanding in the oxygen electrocatalysis mechanism on the

molecular level limits the development of highly active oxide catalysts to enhance device efficiency. Recent studies[8, 9] have shown that understanding the surface chemistry and electronic structure of single-crystal catalyst surfaces can lead to the discovery of remarkably active surfaces for oxygen electrocatalysis, such as the $Pt_3Ni(111)$ surface with Pt segregation on the topmost layer exhibiting an oxygen reduction activity one order of magnitude higher than Pt(111). Tuning perovskite surfaces is also shown to greatly influence the activity for oxygen electrocatalysis ($O_2 + 4e^- \leftrightarrow 2O^{2-}$) at high temperatures.[10-12] In particular, up to three orders of magnitude in activity enhancement can be achieved by decorating the (001) surface of $La_{0.8}Sr_{0.2}CoO_{3-\delta}$ (LSC, a mixed electronic and ionic conductor)[1,13] with epitaxially grown small particles of $(La_{0.5}Sr_{0.5})_2CoO_{4\pm\delta}$.[6, 11] However, little is known about the oxide surface chemistry that governs oxygen electrocatalysis near ambient oxygen partial pressures at elevated temperatures. *Ex situ* surface analysis tools[14, 15] fail to capture surface compositions governing the electrocatalytic activity as the catalyst surface composition may change as a function of temperature and oxygen partial pressure. Conventional *in situ* compositional surface characterization techniques[16, 17] such as X-ray photoelectron spectroscopy (XPS) operate at low pressures, which may provide information considerably different from those under ambient oxygen pressure at elevated temperatures relevant to practical device operation.[18]

Recent progress in the development of *in situ* characterization techniques[3, 17-21] can provide novel fundamental understanding of oxygen reduction and evolution reactions near ambient pressures. In particular, *in situ* synchrotron-based ambient pressure, X-ray photoelectron spectroscopy (APXPS),[21] has revealed electrochemically active oxidation/reduction regions of a ceria electrode in a single chamber solid oxide electrochemical cell.[18] In this article, we employ APXPS (**Figure 5-1a**) to examine how the surface chemistry of a single-crystal LSC(001) film grown on yttria-stabilized zirconia (YSZ) single crystal substrate and an LSC pellet change as a function of temperature. Of particular interest is to understand why epitaxial LSC(001) thin films can show markedly enhanced activities for oxygen electrocatalysis ($O_2 + 4e^- \leftrightarrow 2\ O^{2-}$) relative to LSC powder.[12] Differences in the surface chemistry changes of the LSC(001) film and LSC pellet are compared and used to develop hypotheses, which can explain the enhanced activity of the film.

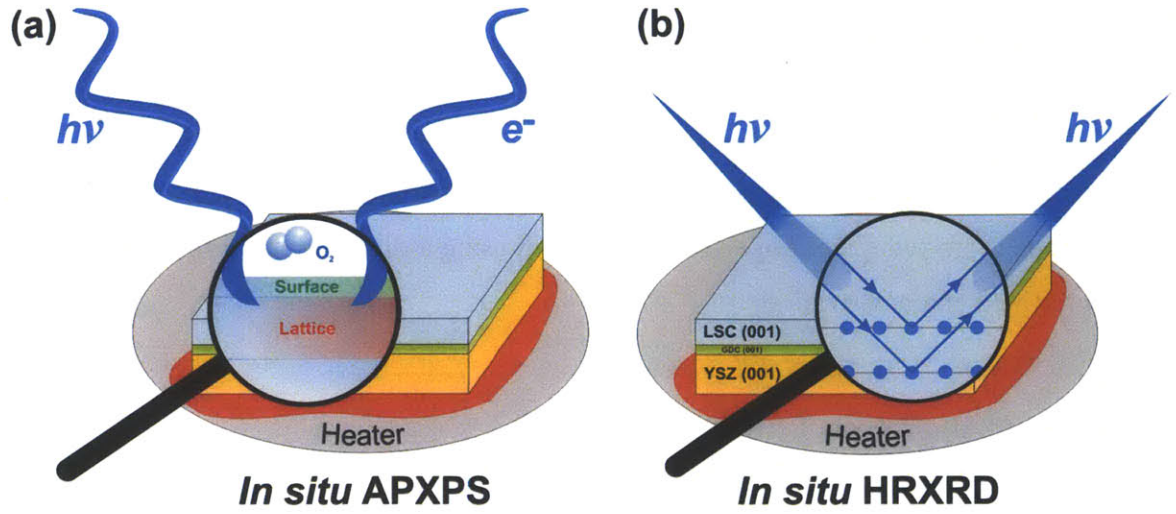

Figure 5-1. *In situ* APXPS and *in situ* XRD experimental configurations. The epitaxial LSC(001) film was supported by a single crystalline YSZ(001) substrate with a (001)-oriented gadolinium-doped ceria (GDC) buffer layer. **(a)** *In situ* APXPS probes the elemental compositions of the outermost "surface" (marked green in the zoom out) and the perovskite "lattice" in the near surface region (marked in red in the zoom out) as a function of temperature at near ambient pressure up to $p(O_2)$ of $1 \cdot 10^{-3}$ atm. **(b)** *In situ* XRD detects the crystal structure and strains of the LSC film materials as a function of temperature at a $p(O_2)$ of 1 atm.

5.2 Experimental Methods

Material Synthesis

Using pulsed laser deposition (PLD) and conditions reported previously,[10-12] an $La_{0.8}Sr_{0.2}CoO_{3-\delta}$ (LSC) thin film of ~85 nm in thickness was grown epitaxially on a 10 x 5 x 0.5 mm single crystalline yttria-stabilized zirconia (Princeton Scientific) with the (001) orientation having an epitaxial buffer layer of gadolinium-doped ceria (GDC) of ~5 nm in thickness. The other surface of YSZ was coated with a porous Pt counter electrode (Pt ink, #6082, BASF), which was sintered at 800 °C in air for 1 hour before PLD deposition (using an identical parameters as reported previously:[10-12] a KrF excimer laser with a wave length, λ, of 248 nm, a pulse frequency, f, of 10 Hz, and a pulse energy, E, of ~50 mJ (measured close to the substrate surface) under an oxygen partial pressure, $p(O_2)$, of 50 mTorr with 500 pulses of GDC at a substrate temperature of ~450 °C, followed by 15,000 pulses of LSC at ~550 °C. The synthesis details of the investigated polycrystalline LSC pellet, and the LSC and GDC PLD targets can be found in **Supporting Information §5.5**. The LSC(001) surface was found to have roughness less than

~0.5 nm from atomic force microscopy in **Figure S5-2**. The single-crystalline nature of the LSC film was determined by normal and off-normal XRD measurements (**Supporting Information §5.5**) and confirmed by high-resolution scanning transmission electron microscopy (HRSTEM) of cross-sectioned, similarly prepared samples.[11] The LSC(001)/GDC(001)/YSZ(001)/Pt sample was then divided into two pieces of ~ 5 x 5 x 0.5 mm using a diamond knife for *in situ* HRXRD and *in situ* APXPS characterization.

In situ High-resolution X-ray Diffraction (HRXRD)

In situ HRXRD was conducted on a four-circle diffractometer (Panalytical) in a $p(O_2)$ = 1 atm and a controlled temperature stage (DHS 900, Anton Paar). Silver paste was used to adhere the thin film sample to the heating plate. The heating rate was ~10 °C/min and the temperature was hold for 20 minutes at each temperature (25 °C, 150 °C, 250 °C, 350 °C, 450 °C, and 550 °C) before XRD data were collected. Sample realignment was conducted after at each temperature to maximize the XRD intensities. A full range *theta-2theta* normal scan (θ-2θ = 10° - 120 °, 0.04 °/step, 2 s/step) was collected first. Subsequently, *theta-2theta* normal scans of $LSC(002)_{pc}$ (0.01 °/step, 3 s/step) and $YSZ(004)_{cubic}$ (0.005 °/step, 1 s/step) were collected. Lastly, off-normal scans of $LSC(101)_{pc}$ (0.02 °/step, 5 s/step) and $YSZ(202)_{cubic}$ (0.004 °/step, 1 s/step) peaks were obtained. As the thermocouple for this experiment was placed inside the heating stage, a small difference between set and actual temperatures on the sample surface cannot be ruled out.

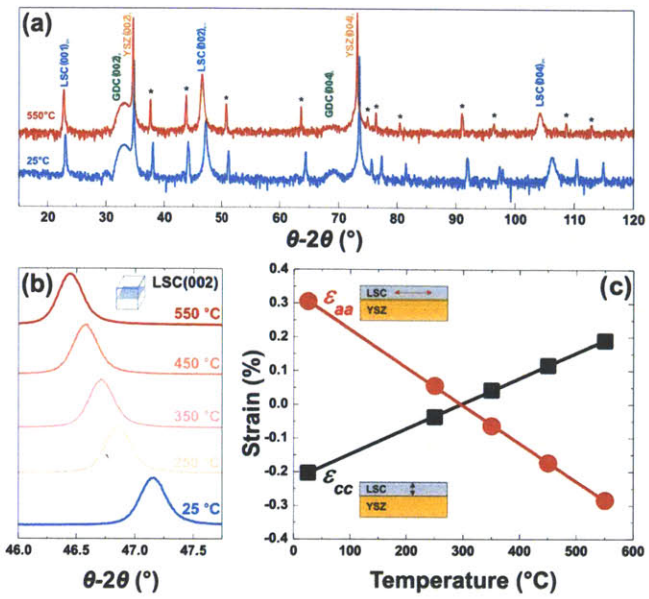

Figure 5-2. Structural stability and strains of the LSC(001) thin film. **(a)** A full-range normal scan in the θ-2θ Bragg-Brentano geometry at 25 °C and 550 °C, showing no phase change upon heating in $p(O_2)$ of 1 atm. The stared (*) peaks originated from the heater, and the peaks of the LSC film, GDC buffer layer and YSZ substrate are indexed to the pc ($a_{pc} \approx 3.8$ Å), cubic ($a_c \approx 5.4$ Å) and cubic ($a_c \approx 5.1$ Å) structure, respectively. **(b)** A normal scan of the $LSC(002)_{pc}$ peak showing shifts towards lower angles in the 2-*theta* position with increasing temperature. **(c)** The in-plane strains, ε_{aa} (red) and the out-of-plane strains, ε_{cc} (black) of the LSC film as a function of temperature.

In situ Ambient Pressure X-ray Photoelectron Spectroscopy (APXPS) Characterization

Near ambient pressure and high temperature XPS data of the LSC(001) film and the LSC pellet were collected at the Beamlines 9.3.2[22] and 11.0.2[21] at Lawrence Berkeley National Laboratory's (LBNL) Advanced Light Source (ALS). The pellet and thin film samples were separately investigated and placed directly onto a ceramic heater, which was held in place by spring loaded Au-Pd coated tungsten tips.[23] A thermocouple was mounted directly onto the sample surface for surface temperature measurements. A piece of Au foil was placed on top for a part of the sample for BE calibration. All BEs were referenced to the Au 4f at 84.0 eV. The spectra were collected in the following sequence (collection time about 2 h per sequence): low resolution survey (BE = 10 eV - 595 eV), high resolution O 1s and Au 4f at a photon energy of 700 eV, and C 1s, La 4d, Sr 3d, Co 3p and Au 4f, at a photon energy of 390 eV. These spectra were collected at the following conditions: $p(O_2) = 6.6 \cdot 10^{-9}$ atm at T = 25 °C, $p(O_2) = 1 \cdot 10^{-3}$ atm at T = 25 °C, $p(O_2)$ =

$1 \cdot 10^{-3}$ atm at T = 220 °C, $p(O_2) = 1 \cdot 10^{-3}$ atm at T = 370 °C, $p(O_2) = 1 \cdot 10^{-3}$ atm at T = 520 °C. The heating rate was about 10 °C/min and the temperature was held constant for 20 min before beginning to collect data at each temperature. The following cross sections were used[24] to calculate cross-section-normalized intensities: 2.619 Mbarn for Sr 3d a 390 eV and 0.2819 Mbarn for O 1s at 700 eV.

5.3 Results and Discussions

Structural stability of epitaxial LSC(001) thin film with increasing temperature

In situ high-resolution X-ray diffraction (HRXRD) (**Figure 5-1b**) was first conducted to show that epitaxial LSC(001) thin films were structurally stable upon heating to 550 °C in an oxygen partial pressure of 1 atm. LSC thin films of ~85 nm were grown using pulsed laser deposition (PLD) on a $(001)_{cubic}$-oriented YSZ single crystal (0.5 mm thick) with a ~5 nm epitaxial $(001)_{cubic}$ layer of gadolinium-doped ceria (GDC) as a buffer layer. Normal and off-normal HRXRD analysis indicated $LSC(001)_{pc}//GDC(001)_{cubic}/\ /YSZ(001)_{cubic}$ and $[110]_{pc}LSC//[110]_{cubic}GDC//[110]_{cubic}YSZ$ (**Supporting Information §5.5** and **Figure S5-1**) similar to previous work,[12] where the subscript "pc" denotes the pseudocubic notation. The low surface roughness and epitaxial nature of the LSC(001) film was further confirmed by atomic force microscopy (**Figure S5-2**), and a high-resolution transmission electron microscopy cross-section of a similarly prepared LSC film.[11] Upon heating to 550 °C, only peak shifts towards low diffraction angles were noted for the spectra of $LSC(001)_{pc}//GDC(001)_{cubic}//YSZ(001)_{cubic}$, as shown in **Figures 5-2a, b** and **Figure S5-3**. Moreover, the high crystallinity of the LSC film was maintained to 550 °C, as indicated by a nearly constant full width at half maximum of $(200)_{pc}$ and $(101)_{pc}$ peaks of ~0.25 °.

The LSC(001) film was found to have a larger relaxed unit cell volume than LSC powder from room temperature to 550 °C (**Table S5-1** and **Figure S5-4**).[25, 26] This difference may suggest that the LSC film has a larger oxygen vacancy nonstoichiometry (δ) than LSC powder, which is supported by previous EIS analyses.[12] In addition, in-plane (ε_{aa}) and out-of-plane (ε_{cc}) strains of the epitaxial LSC thin film were found to be temperature dependent (**Figure 5-2c** and

Supporting Information §5.5), which could be attributed to the difference in the thermal expansion coefficients between the LSC film ($14.9 \cdot 10^{-6}$ K^{-1}) and the YSZ[27] substrate ($8.8 \cdot 10^{-6}$ K^{-1}).[28] In-plane strains changed from tensile to compressive, while the out-of-plane strains varied from compressive to tensile upon heating. It should be mentioned that the strains of the LSC film relevant to O_2 electrocatalysis measurements[12, 29] at ~520 °C were ~–0.23 % in-plane compressive and ~0.16 % out-of-plane tensile, which differed considerably from those measured at room temperature (in-plane ~0.30 % and out-of-plane ~ –0.20 %).

Ambient pressure XPS spectra of LSC film with different photon energies

Ambient pressure XPS spectra of the LSC(001) film taken with different incident photon energies at ~370 °C in an oxygen pressure of $1 \cdot 10^{-3}$ atm allowed us to separate perovskite "lattice" and "surface" components for Sr 3d (**Figure 5-3a**) and O 1s (**Figure 5-3b**). The Sr 3d peak was found to exhibit three unique features, which could be fitted by two sets of Sr $3d_{5/2}$ and $3d_{3/2}$ doublets with an energy separation of ~1.8 eV and a branching ratio of 1.5.[30, 31] With increasing photon energy, the intensities of the low-energy set of Sr 3d ($3d_{5/2}$ at ~132.3 eV and $3d_{3/2}$ at ~133.7 eV) were found to increase in comparison to those of the high-energy set (**Figure 5-3a**). As the inelastic mean free path (*IMFP*) of photoelectrons in an XPS measurement becomes larger[32] with increasing kinetic energy (e.g. *IMFP* of ~7.5 Å at 300 eV to ~19.1 Å at 1140 eV, **Supporting Information §5.5**), the contribution from the perovskite lattice to the Sr 3d and O 1s excitation should increase[16] and the contribution from surface species should decrease with increasing incident photon energy. Therefore, the low-energy component can be assigned to the near-surface region of the perovskite lattice, which is referred to as the "lattice" component, and the high-energy (~133.0 eV - 134.0 eV) peak set can be associated with the perovskite surface termination and surface secondary phases, which is referred to as the "surface" component in this study (**Figure S5-5**). Such assignments are also consistent with previous work.[31] Details of XPS fitting parameters, peak positions, and assigned components can be found in **Table S5-2**. As carbonaceous species were removed from the LSC surface upon heating to 220 °C (**Figure S5-6**) in agreement with previous work,[33] the "surface" component may include Sr^{2+} in the perovskite termination layer, $Sr(OH)_2$-like (~133.2 eV),[30] and/or SrO-like (~133.0 eV)[31] secondary phases, which may also include La and Co cations. Similar "lattice" and

"surface" components to those of Sr 3d were found in the O 1s spectra (**Figure 5-3b**). The low-energy component (~528.9 eV) can be assigned to the "lattice" oxygen component. The intermediate- (~530.1 eV) and high-energy (~531.8 eV) components can be related to the perovskite lattice termination layer (529.8 - 531.0 eV)[31,34,35] and surface secondary phases such as metal (hydr)oxides (530.6 - 531.6 eV),[30, 34, 36] respectively.

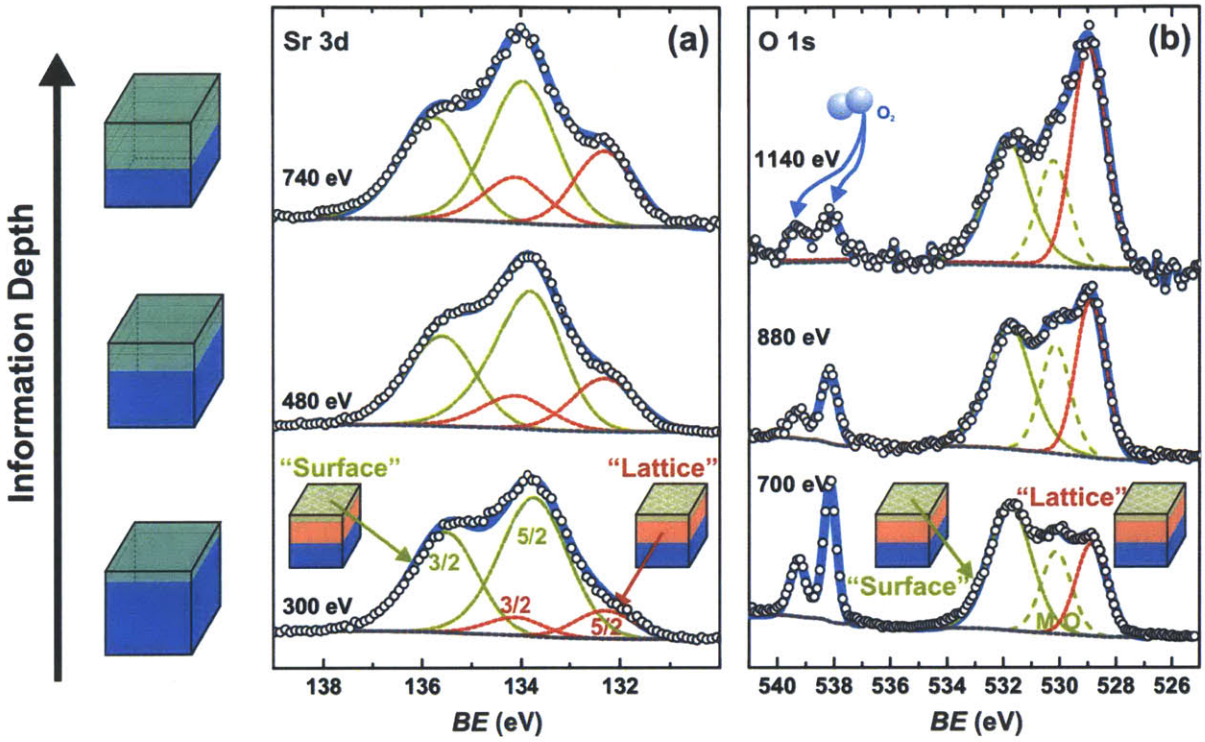

Figure 5-3. *In situ* APXPS spectra of the LSC film as a function of incident X-ray energy. This collection of **(a)** O 1s and **(b)** Sr 3d at three different photon energies provides information from the surface to varying depth into the LSC film at 370 °C in $p(O_2)$ of $1 \cdot 10^{-3}$ atm. The "lattice" component for the perovskite structure in the near surface regions is shown in red while the "surface" component for surface secondary phases on the film is shown in green. White circles are for the measured data, blue lines indicate the sum of fits, and grey dotted lines correspond to the background. Note that the two oxygen peaks at the highest binding energy (*BE* ~ 538 eV and 539.5 eV) correspond to molecular O_2 in the gas phase.[37]

Ambient pressure XPS spectra of LSC film and pellet with increasing temperature

In situ APXPS data of the LSC(001) film showed that the "lattice" components of Sr 3d (**Figure 5-4a**) and O 1s (**Figure 5-4b**) became more pronounced than the "surface" component with increasing temperature from 220 °C to 520 °C in an oxygen pressure of $1 \cdot 10^{-3}$ atm. It is

interesting to note that the high-energy "surface" oxygen component was reduced significantly with increasing temperature and disappeared at 520 °C, while the intermediate-energy "surface" oxygen component was increased slightly relative to the "lattice" component upon heating. The changes in the Sr 3d and O 1s spectra observed for the LSC(001) film surface with increasing temperature are striking when considering no significant change was noted for those of a polycrystalline LSC pellet (**Figures 5-4c,d**), which could be fitted with comparable "lattice" and "surface" components to those used for the LSC(001) film. It should be mentioned that surface carbonate phases could be excluded from the LSC film and pellet due to absence of a C 1s peak at temperatures greater than 220 °C (**Figure S5-6**). The implication of this observation for practical solid oxide fuel cell (SOFC) operation is that surface carbonates such as $La_2(CO_3)_3$, $SrCO_3$, and $CoCO_3$ are absent from the surface of porous cathodes based on LSC powder and films.

Unlike Sr 3d and O 1s, no significant change was found in the spectra of La 4d and Co 3p for the film (**Figures S5-7a,b**) nor the bulk pellet (**Figures S5-7c,d**) with increasing temperature. Due to the complexity of La 4d (which consists of La $4d_{5/2}$ at ~101.9 eV[38,39] and La $4d_{3/2}$ at 104.7 eV[38,39] with an energy separation of ~2.8 eV), their complex satellite structure,[38-40] and an overlap with the Co 3s peak (~103 eV),[34] we could not distinguish "surface" and "lattice" components. It was also challenging to separate "lattice" and "surface" components for Co 3p due to a very large peak width. The inability to separate "lattice" and "surface" components for La 4d and Co 3p limits us from identifying the exact compositions of these components on the LSC surface.

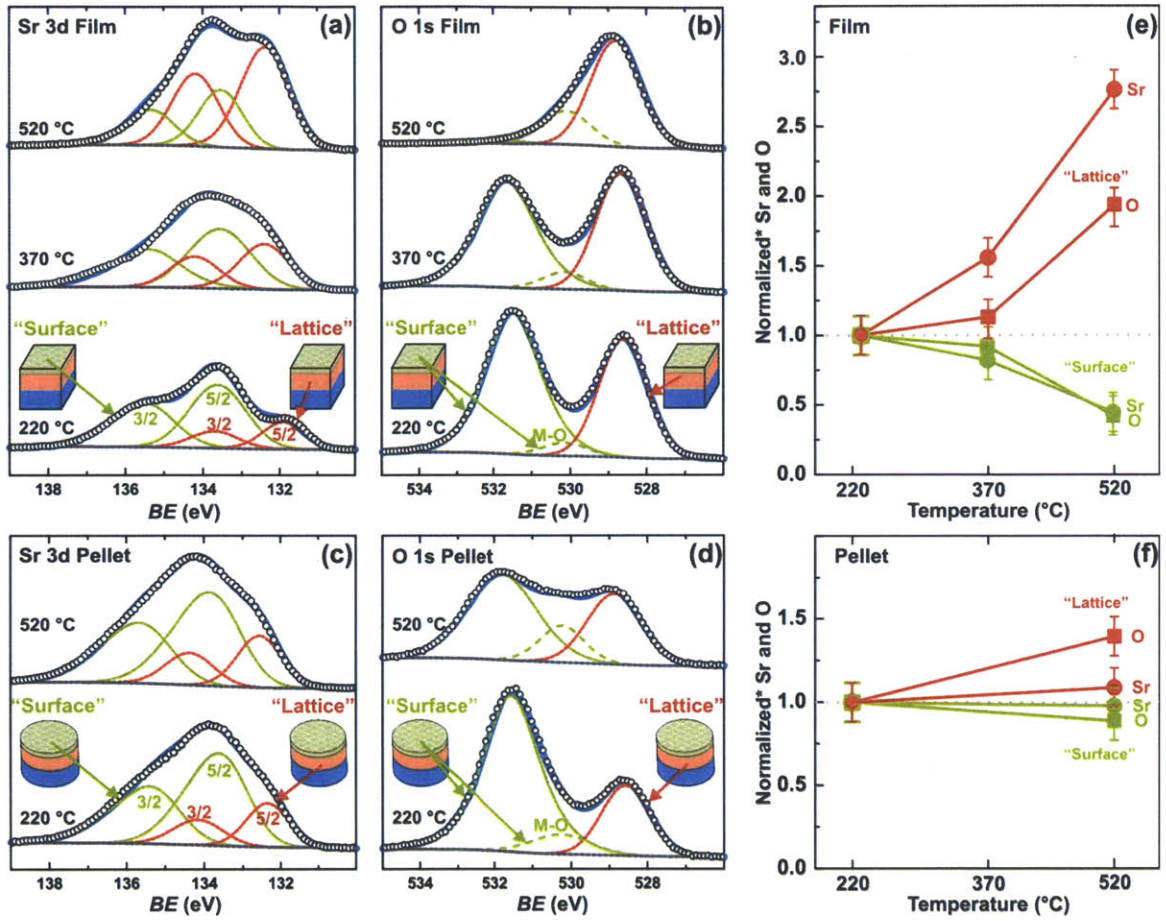

Figure 5-4. *In situ* APXPS data of the LSC film and pellet with increasing temperature. **(a)** Film Sr 3d (E_{photon} = 390 eV), **(b)** Film O 1s (E_{photon} = 700 eV), **(c)** pellet Sr 3d and **(d)** pellet O 1s at 220 °C, 370 °C (film only), and 520 °C in $p(O_2)$ of $1 \cdot 10^{-3}$ atm. The "lattice" component of the perovskite structure in the near-surface region is shown in red while the "surface" component for surface secondary phases (including both surface components) is shown in green. White circles are for the measured data, blue lines indicate the sum of fits, and grey dotted lines correspond to the background. The changes in the relative contributions of "lattice" and "surface" to the total Sr 3d or the total O 1s cross-section-normalized intensity (lattice: red, surface: green) of **(e)** the film and **(f)** the pellet with increasing temperature. *Normalized to the value, *i.e.* to $p(O_2) = 1 \cdot 10^{-3}$ atm and T = 220 °C. The error bars were estimated based on a standard deviation of the raw intensity of 10% (**Supporting Information §5.5**).

Surface chemistry changes of the LSC film and pellet with increasing temperature

Pronounced increases in the intensity of the "lattice" components of Sr 3d and O 1s relative to those of the "surface" components for the LSC(001) thin film with increasing temperature (**Figures 5-4a,b**) can be explained by the following two changes in the film surface chemistry. First, reduction of surface secondary phases on the film surface can allow the collection of higher XPS signals of the "lattice" components of the pervoskite structure. Second, Sr can become enriched in the perovskite structure (or the "lattice" component) in the near-surface region. XPS evidence that demonstrates the occurrence of both surface chemistry changes is discussed in detail below.

Reduction of surface secondary phases on the LSC(001) film with increasing temperature. The contribution of the "surface" Sr component to the combined "lattice" and "surface" Sr intensities, which was normalized by the Sr photoionized cross-section, was reduced by 50 % from 220 °C to 520 °C while the "lattice" Sr contribution was increased by 280 % (**Figure 5-4e**). In addition, the contribution of the "surface" O component was reduced by 50 % in the same temperature range while the "lattice" O contribution was increased by 200 % (**Figure 5-4e**). These observations indicate that the amount of surface secondary phases on the film surface was reduced upon heating to 520 °C at oxygen partial pressure of $1 \cdot 10^{-3}$ atm. On the other hand, decreasing the oxygen pressure from $1 \cdot 10^{-3}$ to $1 \cdot 10^{-7}$ atm at 520 °C was found to bring out more secondary Sr-based phases on the film surface as indicated by the increase in the Sr "surface" intensities and the reduction in the Sr "lattice" intensities (**Figures S5-8a-d** and **S5-9a**). This observation suggests that making PLD films in oxygen partial pressure lower than ambient at elevated temperatures can produce surfaces with higher amount of secondary Sr-containing phases. This hypothesis is supported by the facts that (i) with increasing temperature at oxygen partial pressure $1 \cdot 10^{-3}$ atm, no significant changes were noted for the relative "surface" and "lattice" intensities of Sr and O for the LSC pellet, which was sintered in air at 800 °C (**Figure 5-4f**); and (ii) decreasing oxygen partial pressure led to a small increase in the amount of surface secondary phases for the LSC pellet (**Figures S5-8e-h** and **S5-9b**). Considering these observations, it is proposed here that surface Sr-containing secondary phases are not stable with respect to the LSC perovskite epitaxial film at $1 \cdot 10^{-3}$ atm. They can become incorporated

("dissolved") into the perovskite structure of the film with increasing temperature to 520 °C at an oxygen partial pressure of $1 \cdot 10^{-3}$ atm, and can precipitate and grow on the film surface at 520 °C with decreasing oxygen partial pressure.

The amount of surface secondary phases was smaller for the film than for the pellet at 520 °C in an oxygen partial pressure of $1 \cdot 10^{-3}$ atm, as shown in **Figures 5-4e,f**. This is further supported by the fact that the intensity ratio of Sr "lattice" to "surface" component for the LSC(001) film (~5.6) was much larger than that for the LSC pellet (~1.1). As the pellet has many different perovskite surface terminations, which can have different relative stabilities with respect to surface secondary phases as reported previously for $SrRuO_3$ surfaces,[41] the overall LSC pellet surface might yield a higher amount of secondary phases than the LSC(001) surface. Further APXPS studies are needed to provide insights into how different surface terminations can influence the perovskite stability relative to surface secondary phases. The reduced amount of secondary phases on the film can play a critical role in enhanced electrocatalysis as discussed below.

"Lattice" Sr enrichment in the near-surface region of the LSC(001) film with increasing temperature. Sr enrichment in the "lattice" component with increasing temperature was revealed by normalizing the "lattice" Sr concentration to combined "lattice" concentrations of Sr 3d and O 1s. The "lattice" Sr and O concentrations were estimated by dividing the "lattice" Sr and O intensities by the Sr and O photo-ionization cross-sections, respectively. The "lattice" concentration of Sr 3d was increased by ~180 % from 220 °C to 520 °C (**Figure 5-5**), indicative of Sr enrichment in the perovskite structure in the near-surface region. On the other hand, the "lattice" concentration of O 1s was reduced by ~7 % over the same temperature range (**Figure 5-5**). Considering experimental uncertainty based on a standard deviation of 10 % for raw XPS intensities, the standard deviation for the "lattice" concentration in Fig. 5 can be estimated to be ~24.5 % (**Supporting Information §5.5**), which indicates that the enrichment of "lattice" O vacancies in the near-surface region cannot be detected by XPS with certainty. Sr enrichment in the perovskite structure towards the LSC film surface is further substantiated by the facts that (i) no substantial changes were noted for the concentrations of Sr 3d, O 1s, La 4d and Co 3p based on combined intensities of the "lattice" and "surface" components for the LSC thin film and (ii)

no systematic changes were noted for the "surface" concentrations of Sr 3d and O1s (**Figure S5-10a**). Such Sr enrichment in the LSC lattice towards the film surface is fundamentally different from the appearance of secondary Sr-rich phases on the surface,[31, 42-44] which is often described as "surface Sr segregation". While previous studies[43, 45] have shown surface Sr segregation on single-crystalline lanthanum strontium manganite thin films by XPS and total reflection X-ray fluorescence, this is the first report of Sr enrichment in the perovskite lattice towards the surface revealed *in situ* at high temperatures and near-ambient pressures.

The LSC pellet did not show Sr enrichment in the "lattice" component of Sr 3d with increasing temperature (**Figures 5-5** and **S5-10b**). First, as different surfaces of the LSC pellet may be enriching or depleting in Sr and O, the overall LSC pellet surface may yield in no surface Sr and O enrichment with increasing temperature. Second, epitaxial LSC thin films with higher concentration of oxygen vacancies[12] might enable larger Sr enrichment than LSC powder. Third, as in-plane and out-of-plane strains found in the LSC(001) film increase with increasing temperature from ~220 °C (**Figure 5-2**), which differs from the nominally strain-free LSC pellet bulk, the influence of increasing strains in the film on the Sr and oxygen vacancy enrichment in the LSC(001) film in the same temperature range cannot be excluded, especially considering recent findings[29, 46] suggesting that strains can alter the oxygen vacancy energetics and vacancy concentrations in LSC and $La_{0.5}Sr_{0.5}CoO_{3-\delta}$. Further APXPS studies are needed to provide insights into how different surface terminations and strains can influence "lattice" Sr enrichment in the near-surface region.

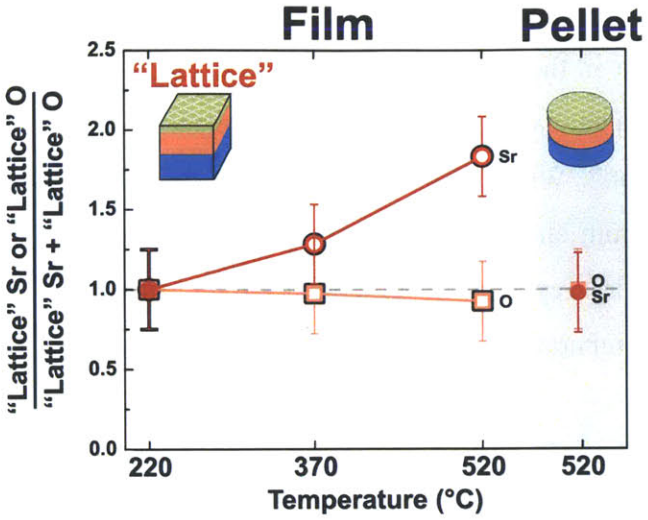

Figure 5-5. "Lattice" Sr enrichment of the LSC(001) film in the near-surface region with increasing temperature. The cross-section-normalized "lattice" intensity of Sr 3d or O 1s was divided by the combined Sr and O "lattice" cross-section-normalized intensities as a function of temperature at $p(O_2)$ of $1 \cdot 10^{-3}$ atm for the film and pellet, which was referenced at the value obtained at 220 °C. The error bars were estimated based on a standard deviation of the raw intensity of 10 % (**Supporting Information §5.5**).

We propose that the observed Sr enrichment in the perovskite lattice towards the LSC(001) film surface with increasing temperature (**Figure 5-5**) can be attributed to the coupling of Sr-oxygen-vacancy interaction and surface enrichment tendencies of Sr and oxygen vacancies in the LSC perovskite structure. Intuitively, this hypothesis involves the following. If we assume that the film perovskite surface has a lower energy of vacancy formation than the film bulk (an effect predicted previously by ab initio studies),[47] raising temperature will create more vacancies at the perovskite surface than the bulk. Due to the opposite formal charges (Kröger-Vink-notation) of the oxygen vacancy (2+) and the Sr (1–, substituted for La^{3+} on the A-site of the perovskite), the presence of increased vacancy content will drive Sr in the perovskite structure toward the surface. This effect would lead to both reduction in O content and Sr enrichment at the perovskite surface with reduced oxygen chemical potential associated with increasing temperature. This hypothesis is supported by the fact that the observed Sr perovskite surface enrichment for the LSC(001) film with increasing temperature (**Figure 5-5**) was reproduced by applying a modified canonical Lankhorst model[48] to the LSC defect thermodynamics (**Figure S5-11**). In this analysis, we used the thermodynamic parameters of similarly prepared LSC(001) films reported previously.[11] The influence of the surface was described by a surface oxygen

vacancy segregation energy (the reduction in the oxygen vacancy formation energy from the film to the surface), Sr segregation energy, and density-of-states-based interaction term, where the surface oxygen vacancy segregation energy was 1.28 eV (close to the ~2 eV predicted from previous ab initio calculations of $LaCoO_3$).[47] The details of this analysis are given in the **Supporting Information §5.5**.

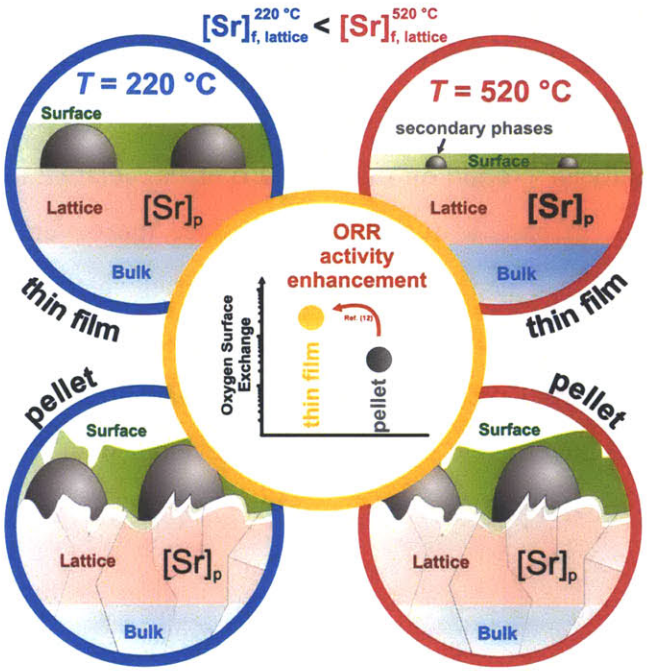

Figure 5-6 Schematic summarizing the experimental findings and relating them to the enhanced catalytic activity of the LSC(001) film surface relative to LSC powder at 520 °C. With increasing temperature, the pellet does not change significantly in the amount of surface phases nor the Sr concentration of the pervoskite lattice in the near-surface region. In contrast, both reduction in secondary phases and enrichment in the lattice Sr concentration are observed for the LSC(001) film with increasing temperature at oxygen partial pressure approaching to SOFC operation conditions, which might be responsible for its enhanced ORR activity relative to LSC porous electrode.[12]

5.4 Conclusions

This work reveals that the LSC(001) film surface is quite different from the average surface of the LSC pellet in aspects critical to oxygen electrocatalysis at elevated temperatures and near ambient oxygen pressures. Upon heating to 520 °C at moderate oxygen partial pressure ($1 \cdot 10^{-3}$ atm) the film surface develops 1) a lower coverage of surface secondary phases than the pellet surface and 2) Sr enrichment in the perovskite structure in the near-surface region while the

pellet surface has no detectable "lattice" Sr enrichment, as shown in **Figure 5-6**. These changes between film and pellet surfaces can explain the enhanced activity of the LSC(001) film for oxygen electrocatalysis relative to LSC powder[10-12] at temperatures and oxygen partial pressures approaching to SOFC operating conditions. The presence of secondary surface phases can promote the oxygen surface exchange rate[10, 11] at low coverage but reduce the activity at high coverage[10] (**Figure S5-12**). In addition, Sr enrichment in the perovskite structure in the near-surface region can increase the activity as it is well known that increasing Sr in bulk $La_{1-x}Sr_xCoO_{3-\delta}$ perovskite materials leads to higher ORR activity.[4] It is proposed that the enhanced activity for O_2 electrocatalysis[12] found on the LSC(001) films relative to porous LSC electrodes can be attributed, at least in part, to the ability to reduce the coverage of surface secondary phases and produce Sr-enriched perovskite surface sites at elevated temperatures (**Figure 5-6**). This work highlights that understanding and tuning the surface chemistry of perovskites at temperatures and oxygen partial pressure conditions relevant to device operation is critical to identify parameters that govern the activity, and develop highly active catalysts for O_2 electrocatalysis at elevated temperatures.

5.5 Supporting Information

Synthesis of the pulsed laser deposition (PLD) target.[10-12] $La_{0.8}Sr_{0.2}CoO_{3-\delta}$ (LSC) powder for the PLD target was synthesized using solid state reaction from stoichiometric mixtures of La_2O_3, $SrCO_3$, Co_3O_4 (Alfa Aeser, USA) and calcined at 1,000 °C in air for 12 hours. The $Gd_{0.2}Ce_{0.8}O_{2-\delta}$ (GDC) powder was synthesized via Pechini method using $Gd(NO_3)_3$ and $Ce(NO_3)_3$, which were dissolved in a mixture of ethylene glycol and citric acid (Sigma-Aldrich, USA) in de-ionized water. After esterification at ~100 °C, the resin was charred at 400 °C and then calcined at 800 °C in air for 1 hour. Phase purity was confirmed using X-ray powder diffraction (XRD) (Panalytical). Subsequently PLD targets of 25 mm in diameter were formed by uniaxial pressing at ~50 MPa and sintered at 1350 °C in air for 20 hours.

Synthesis of the pellet sample for in situ APXPS. The $La_{0.8}Sr_{0.2}CoO_{3-\delta}$ (LSC) pellet for *in situ* APXPS was synthesised via the Pechini method using $La(NO_3)_3{\cdot}6H_2O$, $Sr(NO_3)_2$, $Co(NO_3)_2{\cdot}6H_2O$ (Alfa Aesar) which were dissolved into a mixture of de-ionized water, ethylene glycol, and citric acid (Sigma-Aldrich, USA), followed by esterification at 100 °C, charring the

resin at 400 °C and a final calcinations step at 800 °C in air for 1 hour. Phase purity was confirmed using powder XRD (Rigaku). Then, a pellet (25 mm diameter) was prepared by uniaxial pressing at ~50 MPa and sintered at 800 °C in air for 20 hours. Prior to introducing the pellet sample into the APXPS chamber, the pellet was cleaved and the freshly prepared surface was investigated.

Epitaxial thin film synthesis. (001)-oriented single crystals of 9.5% mol Y_2O_3-stabilized ZrO_2 (YSZ), one-side polished (surface roughness < 1 nm) and with the dimensions of 10 mm x 5 mm x 0.5 mm (Princeton Scientific, USA) were used as electrolyte and substrates for the pulsed laser deposition (PLD). The gadolinium-doped ceria (GDC) electrolytic protection layer (for avoiding reaction of YSZ with LSC at high temperature) and the LSC thin films were deposited by PLD using a KrF excimer laser with a wave length, λ, of 248 nm, a pulse frequency, f, of 10 Hz, and a pulse energy, E, of ~ 50 mJ (measured close to the substrate surface) under and oxygen partial pressure, $p(O_2)$, of 50 mTorr with 500 pulses of GDC (~5 nm, estimated using scanning transmission electron microscopy) at a substrate temperature of ~450 °C, followed by 15,000 pulses of LSC (~85 nm, estimated using atomic force microscopy (AFM, Vecco, USA)) at ~550 °C. Reflection high-energy electron diffraction was utilized to provide *in situ* monitoring of the epitaxial growth of the oxide films.

Sample Roughness. AFM was used to visualise the surface morphology of the film after PLD preparation (**Figure S5-2**) and to determine the RMS surface roughness of < 0.5 nm.

Experimental details of in situ HRXRD. In situ high resolution XRD was conducted on a four-circle diffractometer (Panalytical) equipped with a controlled temperature stage (DHS 900, Anton Paar) in an oxygen partial pressure, $p(O_2)$, of 1 atm (flux ~2 sccm). Silver paste was used to adhere the thin film sample with the YSZ single crystal to the heating plate. Starting at 25 °C, a heating rate of ~10 °C/min was chosen and after increasing the temperature (temperature steps: 25 °C, 150 °C, 250 °C, 350 °C, 450 °C, and 550 °C) the temperature was always held constant for 20 minutes to reach thermal equilibrium before XRD data were collected. Sample realignment was conducted after each temperature step to optimize the intensity of the YSZ(004) and YSZ(202) peaks for all normal and off-normal scans, respectively. This procedure included

the correction of slight de-adjustments due to the thermal expansion of the sample (height offset and angles). After alignment of the YSZ(004), a full range (θ-2θ = 10° - 120°) *theta-2theta* normal scan (0.04 °/step, 2 s/step) was collected first. Subsequently, *theta-2theta* normal scans of LSC(002) (0.01 °/step, 3 s/step) and YSZ(004) (0.005 °/step, 1 s/step) were collected. Lastly upon alignment of the YSZ(202) peak, the off-normal scans of LSC(101) (0.02 °/step, 5 s/step) and YSZ(202) (0.004 °/step, 1 s/step) peaks were obtained. The collection time for the entire sequence was ~4 hours at each temperature. As the thermocouple for this experiment was placed inside the heating stage, a small difference between measured and actual temperatures on the sample surface cannot be ruled out.

Relaxed lattice parameter determination by in situ HRXRD. The Relaxed lattice parameter $\hat{a}$ is derived from the following equation (where $\hat{a}$ is the pseudocubic lattice parameter for the film in an unstrained state),[12,49] $\frac{(c-\hat{c})}{\hat{c}} = \frac{-2\nu}{1-\nu}\frac{(a-\hat{a})}{\hat{a}}$, assuming $\hat{a} = \hat{c}$ and $\nu = 0.25$.[49] The in-plane strain is given by: $\varepsilon_{aa} = \frac{(a-\hat{a})}{\hat{a}}$ and the out-of-plane strain by: $\varepsilon_{cc} = \frac{(c-\hat{c})}{\hat{c}}$, assuming $\hat{a} = \hat{c}$.

Temperature induced peak shift in in situ HRXRD: Based on Bragg's Law, a shift towards smaller 2θ-values with increasing temperature is expected for materials having a positive thermal expansion coefficients, such as LSC, GDC, and YSZ (with increasing temperature the spacing between the planes increases ($d_{T=25^\circ C} < d_{T=520^\circ C}$) and thus $\theta_{T=25^\circ C} > \theta_{T=520^\circ C}$).

Unit cell volume calculation using in situ HRXRD data. The temperature dependence of the LSC and YSZ unit cell volume are shown in **Figure S5-4**. Based on the Y-doping concentration of the used ZrO_2 single crystals (YSZ) their crystal structure is cubic (lattice parameter $a = b = c$), and thus the lattice parameter, a, can directly be determined from the YSZ (202) reflection. Once a is known, the unit cell volume of YSZ can be calculated as a^3. LSC is pseudo cubic, where the c-axis lattice parameter can be determined from the LSC (002) reflection, and assuming a- and b-axis lattice parameters are equivalent, they can be determined from the geometrical relationship between the c axis and the LSC (101) reflection. Once c and $a = b$ are determined, the unit cell volume can be obtained by $c \cdot a^2$.

The volumetric thermal expansion coefficients (TEC) of the LSC(001) thin film ($14.9 \cdot 10^{-6}$ K^{-1}) and of the YSZ substrate ($8.8 \cdot 10^{-6}$ K^{-1}) found in this study were in agreement with those reported in literature ($16.5 \cdot 10^{-6}$ K^{-1} for bulk LSC[26] and 8.5 - $10.8 \cdot 10^{-6}$ K^{-1} for YSZ[27]). Using systematic shifts of LSC $(00l)_{pc}$ and YSZ $(00l')_{cubic}$ (l = 1, 2, 4 and l' = 2, 4) with increasing temperature (**Figure 5-2b**), the out-of-plane lattice parameter of LSC and the cubic YSZ substrate were found, respectively. Considering that off-normal XRD data of LSC$(101)_{pc}$ (**Figure S5-3**) allowed the determination of in-plane lattice parameters (assuming $a = b$), the LSC unit cell volume and the volumetric thermal expansion were obtained (**Figure S5-4**). It is worth mentioning that the in-plane ($8.6 \cdot 10^{-6}$ K^{-1}) and out-of-plane ($27.1 \cdot 10^{-6}$ K^{-1}) TECs of the LSC thin film are considerably different from those of polycrystalline LSC bulk reported in literature,[26] which may be attributed to the presence of strains in the LSC films induced by its mechanical constrain to the YSZ substrate in comparison to nominally strain-free LSC powder.[26]

Experimental details of in situ APXPS. Ambient pressure and high temperature XPS data of the LSC(001) film and the LSC pellet were collected at the Beamlines 9.3.2 and 11.0.2 at Lawrence Berkeley National Laboratory's (LBNL) Advanced Light Source (ALS). The pellet and thin film samples were separately investigated and placed directly onto a ceramic heater, which was held in place by spring loaded Au-Pd coated tungsten tips.[23] The pellet was cleaved before mounting on the sample holder to investigate a freshly prepared surface. No other pre-cleaning (e.g. sputtering the surface) was carried out. A thermocouple was placed directly onto the sample surface for accurate surface temperature measurements. A piece of Au foil was placed on top of part of the sample for binding energy calibration. All binding energies are referenced to the Au 4f at 84.0 eV. The spectra were collected in the following sequence (collection time about 2 h per sequence): low resolution survey (BE = –10 - 595 eV), high resolution O 1s and Au 4f at a photon energy of 700 eV, and C 1s, La 4d, Sr 3d, Co 3p and Au 4f, at a photon energy of 390 eV. These spectra were collected at the following conditions: $p(O_2) = 6.6 \cdot 10^{-9}$ atm at T = 25 °C, $p(O_2) = 1 \cdot 10^{-3}$ atm at T = 25 °C, $p(O_2) = 1 \cdot 10^{-3}$ atm at T = 220 °C, $p(O_2) = 1 \cdot 10^{-3}$ atm at T = 370 °C, $p(O_2) = 1 \cdot 10^{-3}$ atm at T = 520 °C, $p(O_2) = 1 \cdot 10^{-5}$ atm at T = 520 °C, $p(O_2) = 1 \cdot 10^{-7}$ atm at T = 520 °C. The heating rate was about 10 °C/min and the temperature was held constant for 20 min before beginning to collect data at each temperature. Due to a problem with the beamline

intensity while studying the LSC pellet at $p(O_2) = 1 \cdot 10^{-3}$ atm at $T = 370$ °C the data was not included.

In situ APXPS: calibration of the binding energy (BE) of the spectra. The *BE* for the spectra collected at room temperature was calibrated to the C 1s photoemission peak of adventitious hydrocarbons at 285.0 eV. A piece of gold foil was placed on part of the sample surface to assist *BE* calibration (Au 4f 7/2 = 84.0 eV) when carbon was removed from the surface at elevated temperatures.

In situ APXPS: Determination of the Inelastic-Mean-Free-Path (IMFP). The IMFP was calculated using the NIST Standard Reference Database 71 "NIST Electron Inelastic-Mean-Free-Path Database" version 1.2. The software program provides the ability to predict the IMFP for inorganic compounds supplying the stoichiometric composition of La (0.8), Sr (0.2), Co (1), O (3), the number of valence electrons per molecule (assumed to be 24), the density (6.931 g/cm^3) and a band gap energy (for which we are assuming 0 eV as LSC is metallic like at high temperatures; additionally when assuming a band gap of an insulator 5 eV, the IMFP increases by ~0.03 nm). For incident photon beam energies ranging from 300 eV to 1140 eV the IMFP was estimated to be ~0.75 nm to 1.91 nm, respectively.

Curve fitting of in situ APXPS spectra. Analysis of the photoemission lines was done after subtracting a Shirley-type background using a combined Gaussian-Lorentzian line shape, and except for Sr 3d and Co 3p symmetric line shape were used for fitting. Additional constraints for fitting the Sr 3d spectra include the Sr $3d_{5/2}$ and $3d_{3/2}$ doublet with an energy separation of 1.8 eV and a branching ratio of 1.5. The integrated areas (Casa XPS) for each component were then utilized for the analysis. The *BE*, full-width-half-maximum (FWHM), and integrated area for each component is provided in Table S1. Details about Co 3s peak intensity fitting: The intensity of the Co 3s peak which is overlapping with the La 4d region, is only a fraction of the overall intensity in this region and has been considered by taking the atomic subshell photoionization cross-sections[24] for Co 3s and La 4d into account ($Intensity_{Co\ 3s} \sim 0.1 \times Intensity_{La\ 4d}$).

In situ APXPS normalization procedure. Governed by the ideal gas law ($pV = nRT$ with p = pressure, V = volume, n = molar number of molecules, R = ideal gas constant, T = temperature), the amount of gas molecules within the chamber is coupled to both temperature and gas pressure. Therefore as the temperature is elevated, the number of gas molecules needs to be decreased in order to maintain a constant pressure within the APXPS chamber. The reduction in the number of gas molecules will inherently increase the intensity of the X-ray beam and the ejected photoelectrons from the sample surface. In order to remove this artificial intensity increase, a normalization procedure shown in **Figure S5-10** is utilized. The integrated intensity of the entire elemental region (or the components, respectively) is extracted from the fitting (value shown in **Table S5-2** and **S5-3**). To demonstrate the normalization procedure, the raw intensity values for the LSC thin film are plotted versus temperature on the left side of **Figure S5-10**. The integrated intensity areas for each element are divided by the sum of the integrated areas of all elements at the given condition. After obtaining this ratio at each condition, the final normalization step divides the ratio by its respective normalized value at T = 220 °C and $p(O_2) = 1x10^{-3}$ atm or T = 520 °C and $p(O_2) = 1 \cdot 10^{-3}$ atm for the temperature and pressure dependant data, respectively. This procedure yields the normalized intensity values shown on the right side of **Figure S5-10** (which is the same data shown in **Figure 5-5**).

In situ APXPS error analysis: The error bars (ΔI_N) of the normalized area intensities, I_N, shown in **Figures 5-4, 5-5, S5-9, S5-10,** and **S5-11** were estimated by assuming a standard deviation, *SD*, of 10% for the intensities of as-collected XPS data and fitted components. No error was considered for the XPS photoionization cross-sections, σ. This estimation results in an error of about 14 % for the changes of the individual component of Sr or O relative to that component at 220 °C (**Figures 5-4** and **S5-9**), and an error of about 25 % for the changes in the Sr concentration relative to the combined Sr and O in the perovskite structure (**Figures 5-5, S5-10, S5-11**), as shown below.

$$\Delta I_N = \sqrt{\left(SD_{\text{Sr or O}}\right)^2 + \left(SD_{\text{Sr or O@220° C}}\right)^2} \approx \pm 14.1\%$$

$$\Delta I_N = \sqrt{\left(SD_{\text{Sr or O}}\right)^2 + \left(SD_{\text{Sr}}\right)^2 + \left(SD_{\text{O}}\right)^2 + \left(SD_{\text{Sr or O@220° C}}\right)^2 + \left(SD_{\text{Sr@220° C}}\right)^2 + \left(SD_{\text{O@220° C}}\right)^2} \approx \pm 24.5\%$$

Thermodynamic Model For Surface Segregation/Enrichment in (La,Sr)$CoO_{3-\delta}$ (LSC). This model is an extension of the bulk defect model first developed by Lankhorst to describe LSC.[48] Here, we describe the basic bulk (or equivalently, an epitaxial film model) as well as its extension to model surface segregation/enrichment. Finally, we briefly discuss how we obtain the model parameters.

Bulk LSC defect model. The chemical potential of oxygen in the LSC bulk is defined as[4, 48, 50]

$$\mu_O(bulk) - \mu_O^\circ(bulk) = \left[h_O(bulk) - T\cdot s_O(bulk)\right] - \left[h_O^\circ(bulk) - T\cdot s_O^\circ(bulk)\right]$$

$$= \left[h_O(bulk) - h_O^\circ(bulk)\right] - T\left[s_O(bulk) - s_O^\circ(bulk)\right] \quad .....(1)$$

where T is temperature, h_O and s_O are the partial molar enthalpy and entropy of O, respectively, and h_O° and s_O° are reference state values for these quantities. Following Lankhorst,[48] the partial molar enthalpy, $h_O(bulk) - h_O^\circ(bulk)$, and the partial molar entropy of oxygen, $s_O(bulk) - s_O^\circ(bulk)$, in the LSC bulk can be defined as the following

$$h_O(bulk) - h_O^\circ(bulk) = \Delta h_O^\circ(bulk) - 2\cdot\left(\frac{2\delta^{bulk} - x_{Sr}^{bulk}}{g_{bulk}(\varepsilon)}\right) \quad .....(1.a)$$

$$s_O(bulk) - s_O^\circ(bulk) = k_b\cdot\ln\left(\frac{\delta_{bulk}}{3-\delta_{bulk}}\right) + \Delta s_O^{vib}(bulk) \quad .....(1.b)$$

Where k_b is the Boltzmann constant, δ^{bulk} is the bulk oxygen vacancy content in the perovskite lattice (per 3 oxygen sites), x_{Sr}^{bulk} is the bulk Sr concentration, and $g_{bulk}(\varepsilon)$ is the density of states at the Fermi level of the bulk.

At equilibrium between the oxygen gas phase and the LSC solid phase, the chemical potential of the oxygen gas phase is equal to the oxygen chemical potential of the LSC bulk, which yields

$$\frac{1}{2}\left(\mu_{O_2}(gas) - \mu_{O_2}^\circ(gas)\right) = \mu_O(bulk) - \mu_O^\circ(bulk)$$

$$\Rightarrow \frac{k_bT}{2}\cdot\ln(P_{O_2}) - \frac{T}{2}\cdot\Delta s_{O_2}^{vib}(gas)$$

$$= \Delta h_O^\circ(bulk) - 2\cdot\left(\frac{2\delta^{bulk} - x_{Sr}^{bulk}}{g_{bulk}(\varepsilon)}\right) - T\left(k_b\cdot\ln\left(\frac{\delta_{bulk}}{3-\delta_{bulk}}\right) + \Delta s_O^{vib}(solid)\right) \quad .....(2)$$

By moving the last term on the left hand side to the right hand side and combining both the solid and gas phase vibrational entropy terms into a new term $\Delta s_O^{\circ}(\Delta s_O^{\circ} = \Delta s_O^{vib}(solid) - \frac{\Delta s_O^{vib}(gas)}{2})$, we obtain

$$\frac{k_b T}{2}\cdot \ln(P_{O_2}) = \Delta h_O^{\circ}(bulk) - 2\cdot(\frac{2\delta^{bulk} - x_{Sr}^{bulk}}{g_{bulk}(\varepsilon)}) - T\left(k_b \cdot \ln(\frac{\delta_{bulk}}{3-\delta_{bulk}}) + \Delta s_O^{\circ}\right) \quad .....(3)$$

Oxygen vacancy surface segregation. To model the oxygen surface segregation we write an equivalent to Eqn. (3) for the LSC surface as follows:

$$\frac{1}{2}(\mu_{O_2}(gas) - \mu_{O_2}^{\circ}(gas)) = \mu_O(surf) - \mu_O^{\circ}(surf) = \left[h_O(surf) - h_O^{\circ}(surf)\right] - T\left[s_O(surf) - s_O^{\circ}(surf)\right]$$

$$\Rightarrow \frac{k_b T}{2}\cdot \ln(P_{O_2}) \; - \frac{T}{2}\cdot \Delta s_{O\ 2}^{vib}(gas) = \Delta h_O^{\circ}(surf) - 2\cdot(\frac{2\delta^{surf} - x_{Sr}^{surf}}{g_{surf}(\varepsilon)}) - T\left(k_b \cdot \ln(\frac{\delta_{surf}}{3-\delta_{surf}}) + \Delta s_O^{vib}(solid)\right)$$

$$\Rightarrow \Delta h_O^{\circ}(surf) - 2\cdot(\frac{2\delta^{surf} - x_{Sr}^{surf}}{g_{surf}(\varepsilon)}) - T\left(k_b \cdot \ln(\frac{\delta_{surf}}{3-\delta_{surf}}) + \Delta s_O^{\circ}\right) = \frac{k_b T}{2}\cdot \ln(P_{O_2}) \quad .....(4)$$

Where δ^{surf} is the surface oxygen vacancy content in the perovskite lattice, x_{Sr}^{surf} is the surface Sr concentration, $g_{surf}(\varepsilon)$ is the density of states at the Fermi level of the surface. The driving force for the O vacancy surface segregation can be obtained by subtracting Eqn.(3) from Eqn.(4), and the following equation describes the O vacancy surface segregation:

$$k_b T\cdot \ln(\frac{3-\delta_{bulk}}{\delta_{bulk}}\cdot\frac{\delta_{surf}}{3-\delta_{surf}}) = -\Delta E_{O\_vac}^{seg} - 2\cdot(\frac{2\delta_{surf} - x_{Sr}^{surf}}{g_{surf}(\varepsilon)} - \frac{2\delta_{bulk} - x_{Sr}^{bulk}}{g_{bulk}(\varepsilon)}) \quad ..... (5)$$

Where $\Delta E_{O\_vac}^{seg} = \Delta h_O^{\circ}(surf) - \Delta h_O^{\circ}(bulk)$. Note that it is the value of $\Delta E_{O\_vac}^{seg} = \Delta h_O^{\circ}(surf) - \Delta h_O^{\circ}(bulk)$ that will drive the surface segregation. Also, for clarity, note that the *a(x)* term in Lankhorst[9] is equal to $4/g_{bulk}(\varepsilon)$.

Sr surface segregation/enrichment. The chemical potential of Sr in the LSC bulk can be written as

$$\mu_{\mathrm{Sr}}(bulk) - \mu^{\circ}_{\mathrm{Sr}}(bulk) = \Delta\mu^{\circ}_{\mathrm{Sr}}(bulk) = \Delta h^{\circ}_{\mathrm{Sr}}(bulk) + h^{\mathrm{nonideal}}_{\mathrm{Sr}}(bulk) + k_b T \cdot \ln(\frac{x^{bulk}_{Sr}}{1 - x^{bulk}_{Sr}}) \quad .....(6)$$

where $h^{\mathrm{nonideal}}_{\mathrm{Sr}}(bulk) = \frac{(x^{bulk}_{Sr} - 2\delta_{bulk})}{g_{bulk}(\varepsilon)}$. Similarly, for the chemical potential of Sr at the LSC surface can be written as

$$\mu^{\mathrm{surf}}_{\mathrm{Sr}} = \Delta h^{\circ}_{\mathrm{Sr}}(surf) + h^{\mathrm{nonideal}}_{\mathrm{Sr}}(surf) + k_b T \cdot \ln(\frac{x^{surf}_{Sr}}{1 - x^{surf}_{Sr}}) \quad .....(7)$$

where $h^{nonideal}_{Sr}(surf) = \frac{(x^{surf}_{Sr} - 2\delta_{surf})}{g_{surf}(\varepsilon)}$. Note here we assume the difference of the vibrational contribution in the Sr chemical potential between the LSC bulk and surfaces very small so that the vibrational contribution can be neglected in the Sr segregation reaction. The driving force for the Sr surface segregation can be obtained by subtracting Eqn.(6) from Eqn.(7), and the following equation describes the Sr surface segregation

$$k_b T \cdot \ln(\frac{x^{bulk}_{Sr}}{1 - x^{bulk}_{Sr}} \cdot \frac{1 - x^{surf}_{Sr}}{x^{surf}_{Sr}}) = \Delta E^{seg}_{Sr} - (\frac{2\delta_{surf} - x^{surf}_{Sr}}{g_{surf}(\varepsilon)} - \frac{2\delta_{bulk} - x^{bulk}_{Sr}}{g_{bulk}(\varepsilon)}) \quad ..... (8)$$

where $\Delta E^{seg}_{Sr} = \Delta h^{\circ}_{Sr}(surf) - \Delta h^{\circ}_{Sr}(bulk)$.

Obtaining model parameters. Combining Eqn.(5) and Eqn.(8), one can solve for the surface oxygen vacancy, δ_{surf}, and surface Sr concentration, x^{surf}_{Sr} as a function of parameters of $\Delta E^{seg}_{O\_vac}$, ΔE^{seg}_{Sr}, $g_{bulk}(\varepsilon)$, $g_{surf}(\varepsilon)$, x^{bulk}_{Sr} and δ_{bulk} for a given T and $p(O_2)$. The model parameters of the LSC bulk[4,48,50] and epitaxial films[2] have been reported in the literature and are used in our model, and we assumed $g_{surf}(\varepsilon) = g_{bulk}(\varepsilon)$. This leaves two undetermined variables, $\Delta E^{seg}_{O\_vac}$ and ΔE^{seg}_{Sr} which are used to fit with the experimental data for the epitaxial LSC thin film (**Figure S5-11**). Our fit to the data yielded the fitted values: $\Delta E^{seg}_{O\_vac} = -1.28$ eV, and $\Delta E^{seg}_{Sr} = 0.35$ eV.

Table S5-1. Constrained and relaxed lattice parameters of the LSC film extracted from normal and off-normal HRXRD data as temperature was increased from 25 °C to 550 °C.

Temperature	Constrained in-plane lattice parameter (Å)	Constrained out-of-plane lattice parameter (Å)	Relaxed film lattice parameter $\hat{a}$ (Å)	In-plane strain $\varepsilon_{aa} = \frac{(a-\hat{a})}{\hat{a}}$	Out-of-plane strain $\varepsilon_{cc} = \frac{(c-\hat{c})}{\hat{c}}$
25 °C	3.871	3.852	3.860	0.30 %	-0.20 %
250 °C	3.878	3.875	3.876	0.06 %	-0.04 %
350 °C	3.882	3.886	3.884	-0.06 %	0.04 %
450 °C	3.886	3.897	3.892	-0.17 %	0.12 %
550 °C	3.889	3.907	3.900	-0.29 %	0.19 %

Table S5-2. Detailed photon energy depth resolved XPS peak positions and information on the fitting parameters.

Photon Energy	Name	LSC Film		
		BE (eV)	*FWHM* (eV)	Area
300 eV	Sr 3d 5/2 - Surface	133.7	1.6	19373.7
	Sr 3d 3/2 - Surface	135.5	1.5	12915.8
	Sr 3d 5/2 - Lattice	132.3	1.4	3274.3
	Sr 3d 3/2 - Lattice	134.1	1.4	2180.6
480 eV	Sr 3d 5/2 - Surface	133.8	1.5	32394.5
	Sr 3d 3/2 - Surface	135.6	1.6	21596.3
	Sr 3d 5/2 - Lattice	132.3	1.5	12000.0
	Sr 3d 3/2 - Lattice	134.1	1.6	7991.9
740 eV	Sr 3d 5/2 - Surface	134.0	1.6	12315.2
	Sr 3d 3/2 - Surface	135.8	1.5	8210.2
	Sr 3d 5/2 - Lattice	132.3	1.4	5500.0
	Sr 3d 3/2 - Lattice	134.1	1.5	3662.9
700 eV	O 1s - Surface	531.8	1.8	25124.4
	O 1s - Surface (M-O)	530.2	1.3	11491.0
	O 1s - Lattice	528.9	1.3	13168.3
880 eV	O 1s - Surface	531.8	1.8	13400.8
	O 1s - Surface (M-O)	530.2	1.3	7763.4
	O 1s - Lattice	528.9	1.2	11069.6
1140 eV	O 1s - Surface	531.9	1.8	2951.0
	O 1s - Surface (M-O)	530.2	1.4	1786.6
	O 1s - Lattice	529.0	1.4	3839.2

Table S5-3. Detailed XPS peak positions and information on the fitting parameters.

	Name	LSC Pellet			LSC Film		
		BE (eV)	*FWHM* (eV)	Area	*BE* (eV)	*FWHM* (eV)	Area
$T = 220$ °C, $p(O_2) = 1 \cdot 10^{-3}$ atm	O 1s - Surface	531.6	1.8	415.7	531.5	1.7	1699.1
	O 1s - Surface (M-O)	530.3	1.8	50.3	530.2	1.4	120.3
	O 1s - Lattice	528.6	1.5	145.5	528.6	1.5	1165.2
	C 1s - Carbonates, O-C=O	289.4	2.0	15.9	289.1	2.0	39.0
	C 1s - C-O	287.2	2.0	13.9	286.8	2.0	24.5
	C 1s - Adventitious	285.0	1.8	12.9	284.9	1.7	8.5
	La 4d	-	-	205.3	-	-	2999.4
	Co 3s	102.9	2.5	25.0	102.9	2.2	140.0
	Sr 3d 5/2 - Surface	133.6	1.7	539.9	133.6	1.7	1763.5
	Sr 3d 3/2 - Surface	135.4	1.8	360.0	135.4	1.7	1175.7
	Sr 3d 5/2 - Lattice	132.3	1.3	211.0	131.9	1.3	569.9
	Sr 3d 3/2 - Lattice	134.1	1.5	140.5	133.7	1.4	379.5
	Co 3p	-	-	90.5	-	-	553.1
	Na 2s	-	-	11.5	-	-	12.3
$T = 370$ °C, $p(O_2) = 1 \cdot 10^{-3}$ atm	O 1s - Surface	NA	NA	NA	531.7	1.8	1758.3
	O 1s - Surface (M-O)	NA	NA	NA	530.2	1.4	205.3
	O 1s - Lattice	NA	NA	NA	528.7	1.5	1542.6
	C 1s - Carbonates, O-C=O	NA	NA	NA	288.6	2.0	18.6
	C 1s - C-O	NA	NA	NA	286.8	2.0	27.7
	C 1s - Adventitious	NA	NA	NA	284.9	1.8	17.6
	La 4d	NA	NA	NA	-	-	3474.1
	Co 3s	NA	NA	NA	102.9	2.5	175.0
	Sr 3d 5/2 - Surface	NA	NA	NA	133.6	1.9	1621.2
	Sr 3d 3/2 - Surface	NA	NA	NA	135.4	1.9	1080.8
	Sr 3d 5/2 - Lattice	NA	NA	NA	132.4	1.5	994.8
	Sr 3d 3/2 - Lattice	NA	NA	NA	134.2	1.5	662.6
	Co 3p	NA	NA	NA	-	-	631.7
	Na 2s	NA	NA	NA	-	-	78.0
$T = 520$ °C, $p(O_2) = 1 \cdot 10^{-3}$ atm	O 1s - Surface	531.8	2.2	539.3	531.7	1.0	58.7
	O 1s - Surface (M-O)	530.2	1.4	143.1	530.1	1.5	706.0
	O 1s - Lattice	528.9	1.7	335.8	528.8	1.5	2305.9
	C 1s - Carbonates, O-C=O	289.5	2.0	33.0	288.8	1.0	2.8
	C 1s - C-O	287.2	2.0	22.3	286.7	2.0	27.8
	C 1s - Adventitious	285.3	2.0	10.7	284.9	2.0	35.5
	La 4d	-	-	336.4	-	-	3453.1
	Co 3s	102.9	2.5	27.0	102.9	2.5	147.0
	Sr 3d 5/2 - Surface	133.8	1.8	1080.4	133.5	1.3	1085.5
	Sr 3d 3/2 - Surface	135.6	1.9	720.3	135.3	1.4	723.7
	Sr 3d 5/2 - Lattice	132.6	1.3	470.1	132.4	1.5	2230.8
	Sr 3d 3/2 - Lattice	134.4	1.4	313.1	134.2	1.4	1485.7
	Co 3p	-	-	112.7	-	-	569.7
	Na 2s	-	-	1.7	-	-	18.1
$T = 520$ °C, $p(O_2) = 1 \cdot 10^{-5}$ atm	O 1s - Surface	531.8	2.2	875.2	531.4	1.9	481.1
	O 1s - Surface (M-O)	530.3	1.4	285.9	530.2	1.4	1311.7
	O 1s - Lattice	528.8	1.7	646.2	528.8	1.6	5045.0
	C 1s - Carbonates, O-C=O	289.4	2.0	60.6	288.9	2.0	146.2

	C 1s - C-O	287.2	2.0	50.7	286.8	2.0	166.8
	C 1s - Adventitious	285.3	1.8	20.1	284.8	2.0	97.2
	La 4d	-	-	483.6	-	-	7037.2
	Co 3s	102.9	2.5	47.0	102.9	2.5	290.0
	Sr 3d 5/2 - Surface	133.6	1.8	1936.2	133.6	1.7	4719.3
	Sr 3d 3/2 - Surface	135.4	1.9	1290.8	135.3	1.8	3146.2
	Sr 3d 5/2 - Lattice	132.6	1.2	617.5	132.6	1.5	3009.2
	Sr 3d 3/2 - Lattice	134.4	1.1	411.3	134.4	1.4	2004.2
	Co 3p	-	-	185.3	-	-	1141.0
	Na 2s	-	-	2.9	-	-	25.0
T = 520 °C, $p(O_2)$ = 1·10^{-7} atm	O 1s - Surface	531.9	2.2	733.6	531.4	1.8	346.9
	O 1s - Surface (M-O)	530.4	1.4	303.4	530.2	1.3	1199.0
	O 1s - Lattice	528.9	1.7	721.6	528.8	1.6	5310.1
	C 1s - Carbonates, O-C=O	289.5	2.0	65.9	288.9	2.0	171.3
	C 1s - C-O	287.2	2.0	53.6	286.8	2.0	190.4
	C 1s - Adventitious	285.3	1.7	19.9	284.9	2.0	100.5
	La 4d	-	-	520.9	-	-	6923.9
	Co 3s	102.9	2.5	50.0	102.9	2.5	300.0
	Sr 3d 5/2 - Surface	133.7	1.8	1915.3	133.4	1.7	5252.1
	Sr 3d 3/2 - Surface	135.4	1.9	1276.9	135.1	1.8	3501.4
	Sr 3d 5/2 - Lattice	134.5	1.1	377.2	132.5	1.5	3144.1
	Sr 3d 3/2 - Lattice	132.7	1.3	566.3	134.3	1.4	2093.9
	Co 3p	-	-	198.3	-	-	1183.2
	Na 2s	-	-	3.0	-	-	30.6

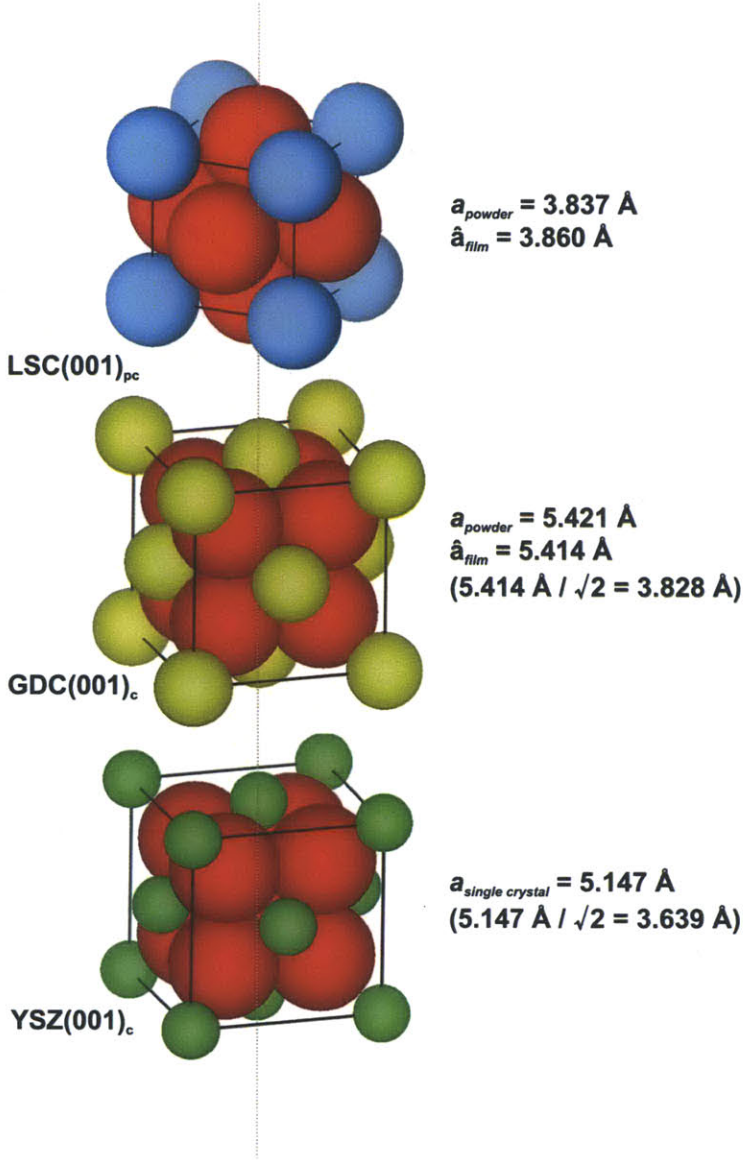

Figure S5-1. Schematic of the in-plane crystallographic relationship between the LSC(001)$_{pc}$, GDC(001)$_{cubic}$, and YSZ(001)$_{cubic}$: a cube-on-cube alignment of YSZ and GDC and a 45° rotation of GDC and LSC along the (001) axis. This rotational relationship has been determined by off-normal *phi*-scans (HRXRD).[1]

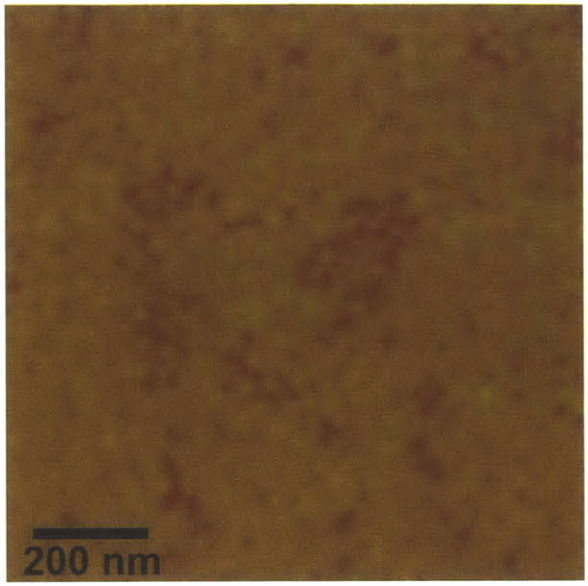

Figure S5-2. Atomic force microscopy (AFM) image of the as-prepared LSC(001) thin film surface revealing a surface roughness <0.5 nm. The maximum height of this image (dark colour to white) is 20 nm.

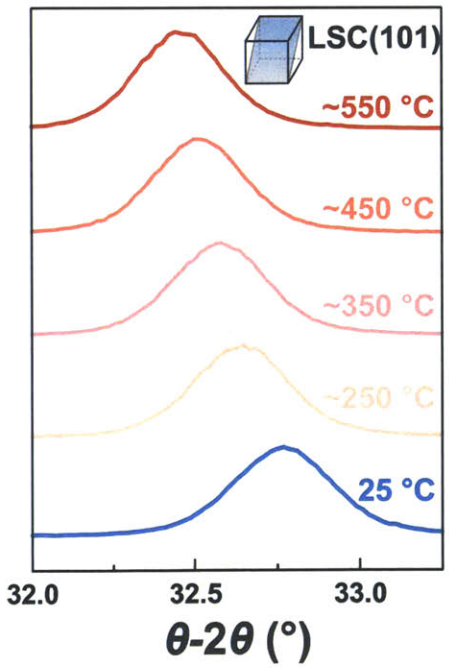

Figure S5-3. *In situ* HRXRD data of the off-normal $LSC(101)_{pc}$ as a function of temperature in a $p(O_2)$ of 1 atm. Here, we observe the peak shifts towards lower angle in the *theta-2theta* with increasing temperature from 25 °C to 550 °C.

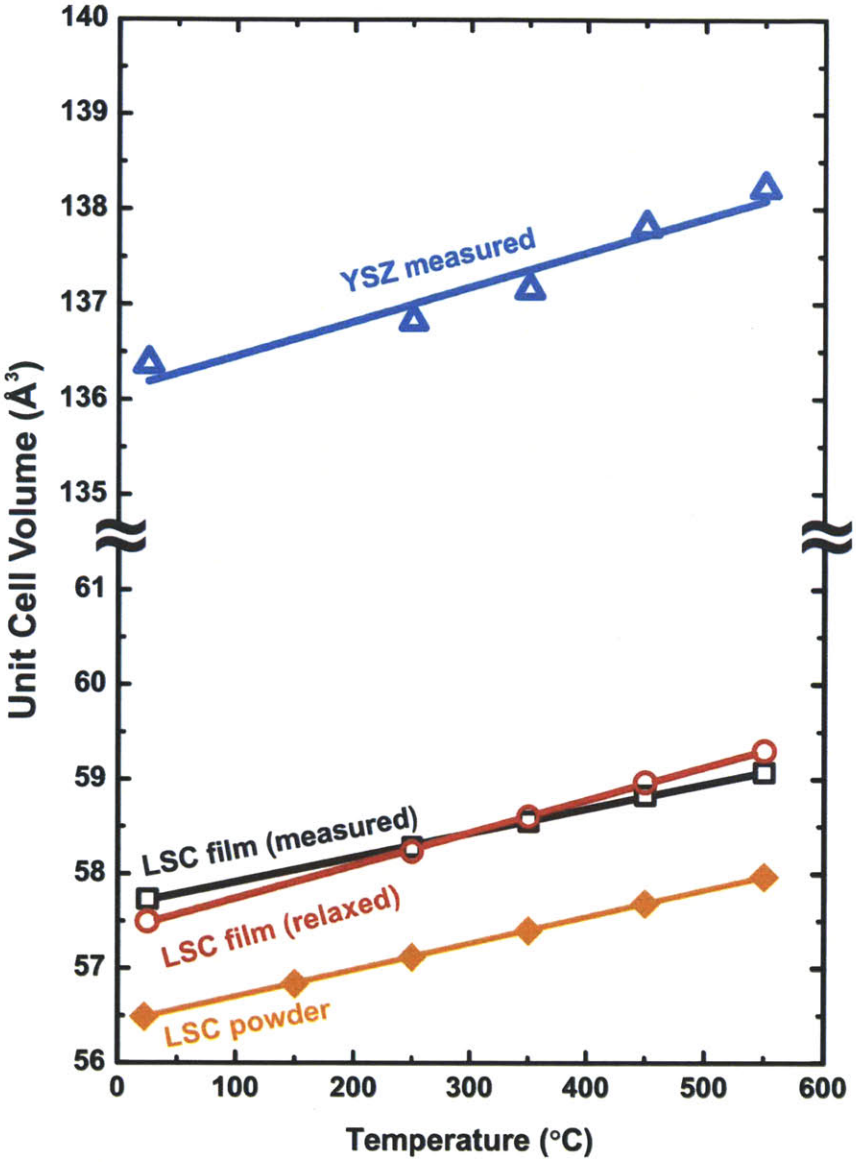

Figure S5-4. *In situ* HRXRD data of the unit cell volume of the epitaxial $(001)_{pc}$-LSC thin film and the single crystalline $(001)_{cubic}$-YSZ substrate as a function of temperature in a $p(O_2)$ of 1 atm. The "LSC measured" curve represents the *a* and *c*-lattice parameters directly measured from the HRXRD, while the "LSC relaxed" curve uses Poisson's ratio to extrapolate an unstrained (relaxed) unit cell volume. As a reference, an extrapolated unit cell volume for LSC powder as a function of temperature is provided utilizing a room temperature pseudo cubic lattice parameter of a_{pc} = 3.837 Å[25] and thermal expansion coefficient of $16.5 \cdot 10^{-6}$ K^{-1}.[26]

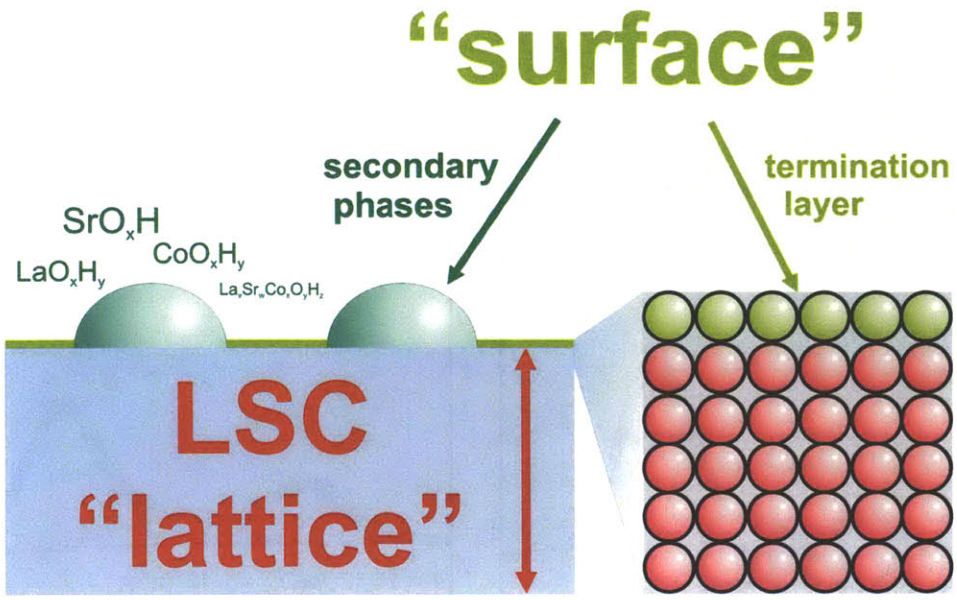

Figure S5-5. Schematic detailing the "surface" and "lattice" of LSC. The term "surface" (marked in green) includes secondary phases on the surface, such as oxides and hydroxides of the cations La, Sr, and Co or other non-perovskite $La_vSr_wCo_xO_yH_z$ phases, and the termination layer of LSC. The term "lattice" is used for regular bonded atoms in the perovskite structure (marked in red). The probed "lattice" is a surface near region of about 2 nm in depth. This distinction between "surface" and "lattice" is based on the ability of XPS to separate between these two components based on different binding energies (*BE*).

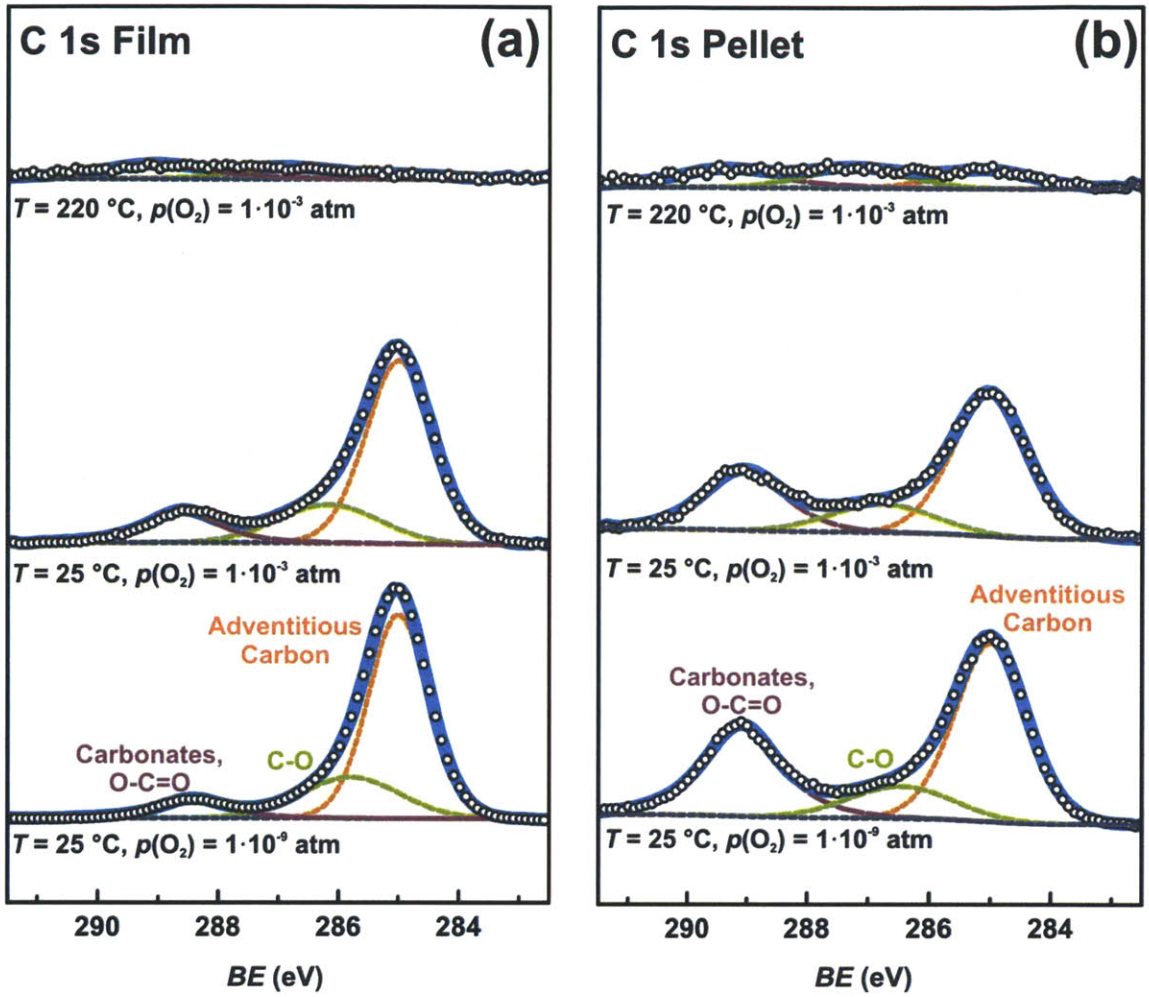

Figure S5-6. *In situ* APXPS data of the C 1s region (E_{photon}= 390 eV) as a function of oxygen partial pressure and temperature. Increasing the oxygen partial pressure from UHV (~$1{\cdot}10^{-9}$ atm) to $1{\cdot}10^{-3}$ atm, the amount of carbon on the surface of **(a)** the LSC thin film and **(b)** the LSC pellet are slightly reduced. By elevating the temperature from 25 °C to 220 °C at this pressure ($1{\cdot}10^{-3}$ atm) both surfaces are nearly carbon free. The component at lowest binding energy (*BE*) correlates to adventitious carbon (orange, 285.0 eV), the highest *BE* component is assigned to carbonates (purple), the component at about 286 eV is assigned to C-O species (green), (white circles: measured data, blue line: sum of fits, grey dotted line: background).

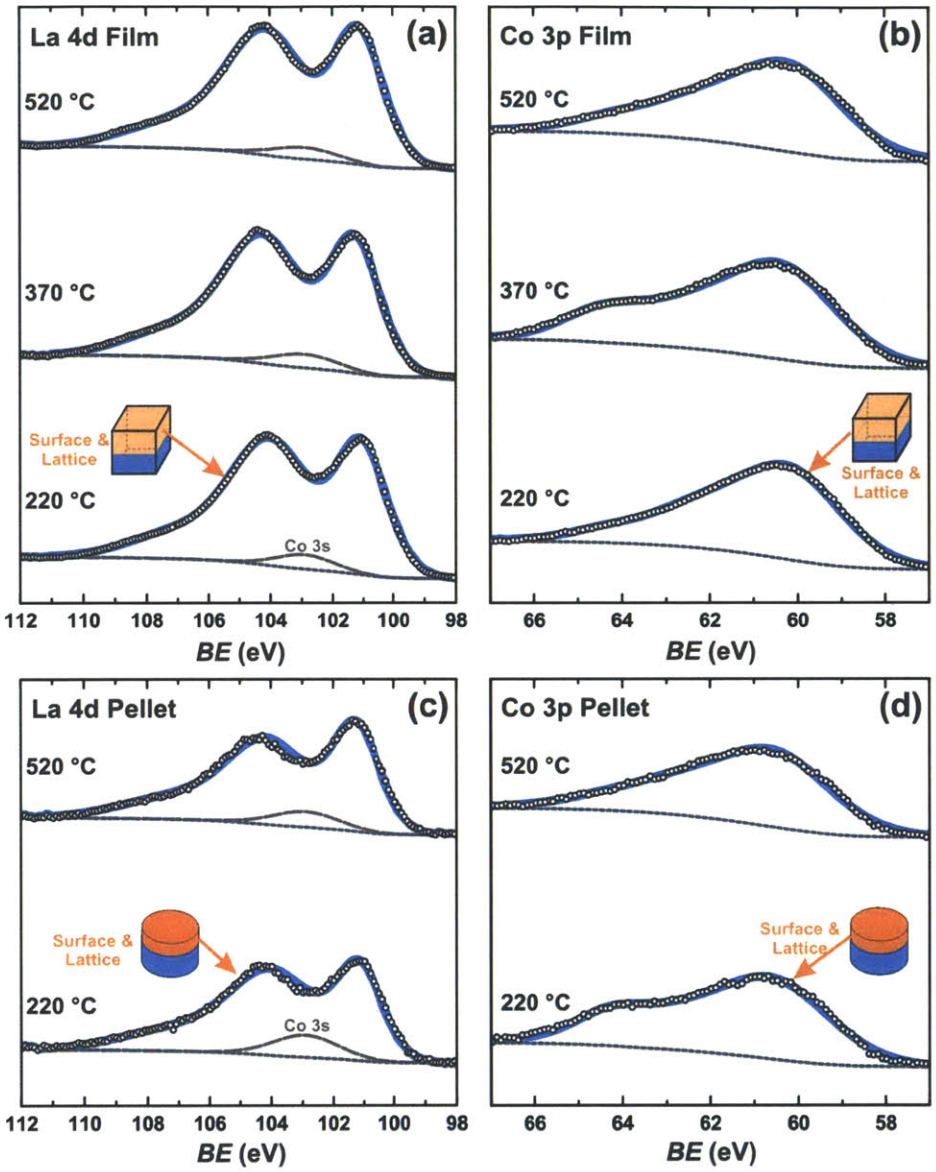

Figure S5-7. *In situ* APXPS data of the LSC film and pellet as a function of temperature. **(a)** Film La 4d (E_{photon}= 390 eV) and **(b)** Co 3p (E_{photon} = 390 eV), **(c)** pellet La 4d and **(d)** Co 3p at 220 °C, 370 °C (film only), and 520 °C in $p(O_2) = 1{\cdot}10^{-3}$ atm (white circles: measured data, grey dotted line: background). It is interesting to note that a small feature at ~64.5 eV appeared for the thin film and pellet at 370 °C and 220 °C, respectively, which disappeared upon further heating to 520 °C. Understanding the physical origin of this feature requires further studies, which could be related to a change in the oxidation state of cobalt and/or the (dis)appearance of a sodium impurity (Na 2s at ~ 64.2 eV).[50]

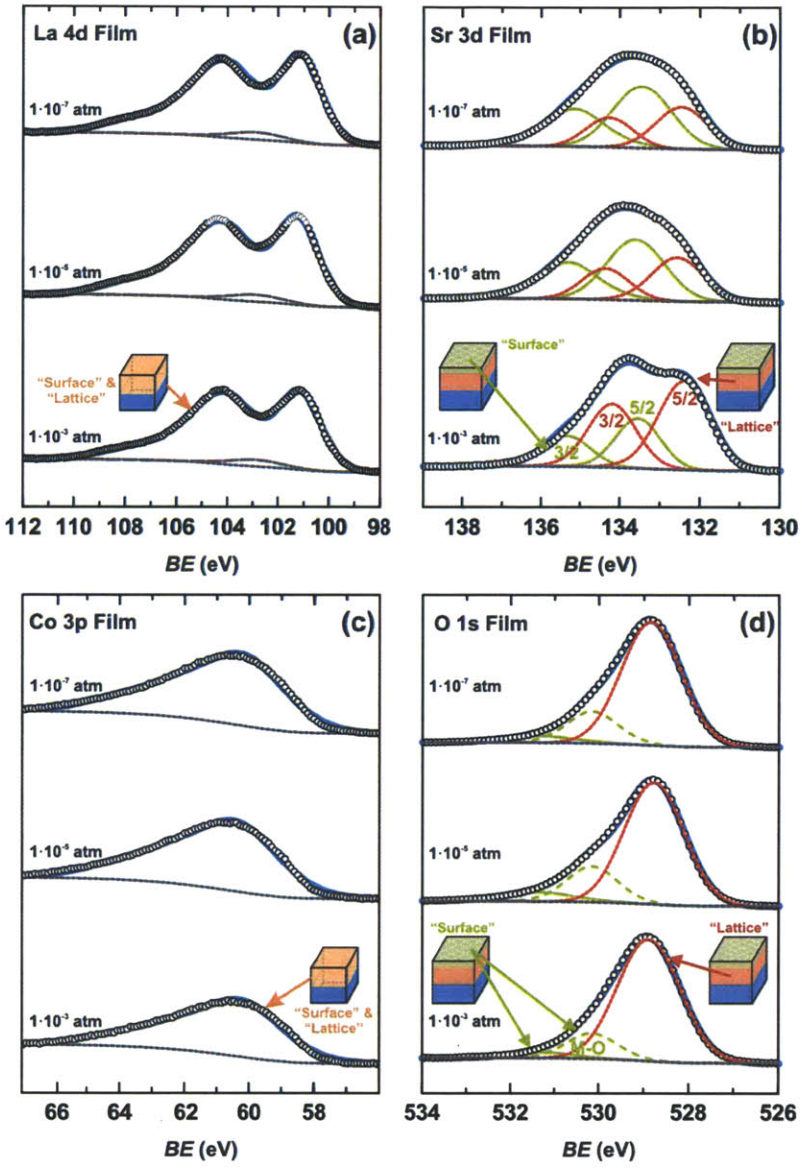

Figure S5-8a-d. *In situ* APXPS data of the LSC thin film oxygen partial pressure dependency at T = 520 °C: **(a)** La 4d (E_{photon} = 390 eV), **(b)** Sr 3d (E_{photon} = 390 eV), **(c)** Co 3p (E_{photon} = 390 eV), and **(d)** O 1s (E_{photon} = 700 eV). For the Sr 3d and O 1s the "lattice" component of the perovskite is shown in red, while the "surface" component (secondary phases on the surface and LSC's termination layer) is shown in green. (White circles: measured data, blue line for O1s: sum of fits, grey dotted line: background).

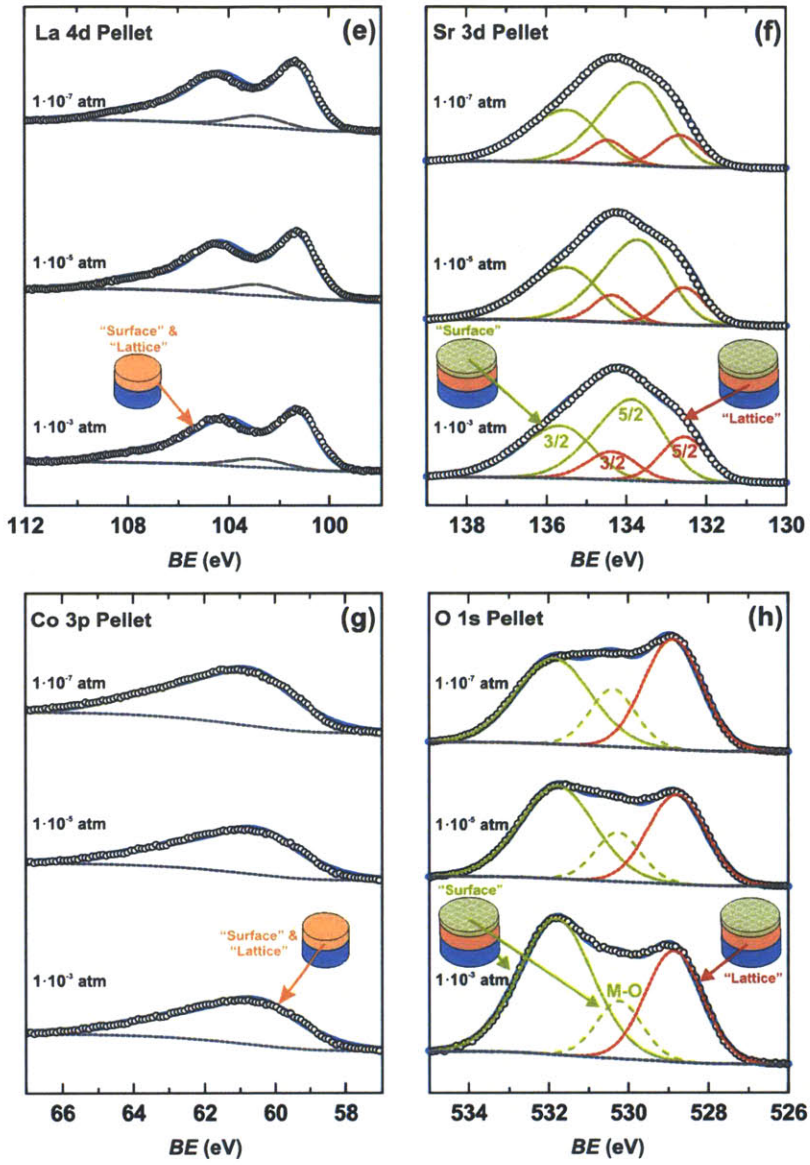

Figures S5-8e-h. *In situ* APXPS data of the LSC pellet oxygen partial pressure dependency at T = 520 °C: **(e)** La 4d (E_{photon} = 390 eV), **(f)** Sr 3d (E_{photon} = 390 eV), **(g)** Co 3p (E_{photon} = 390 eV), and **(h)** O 1s (E_{photon} = 700 eV). For the Sr 3d and O 1s, the "lattice" component of the perovskite is shown in red, while the "surface" component (secondary phases on the surface and LSC's termination layer) is shown in green. (White circles: measured data, blue line for Sr 3d: sum of fits, grey dotted line: background).

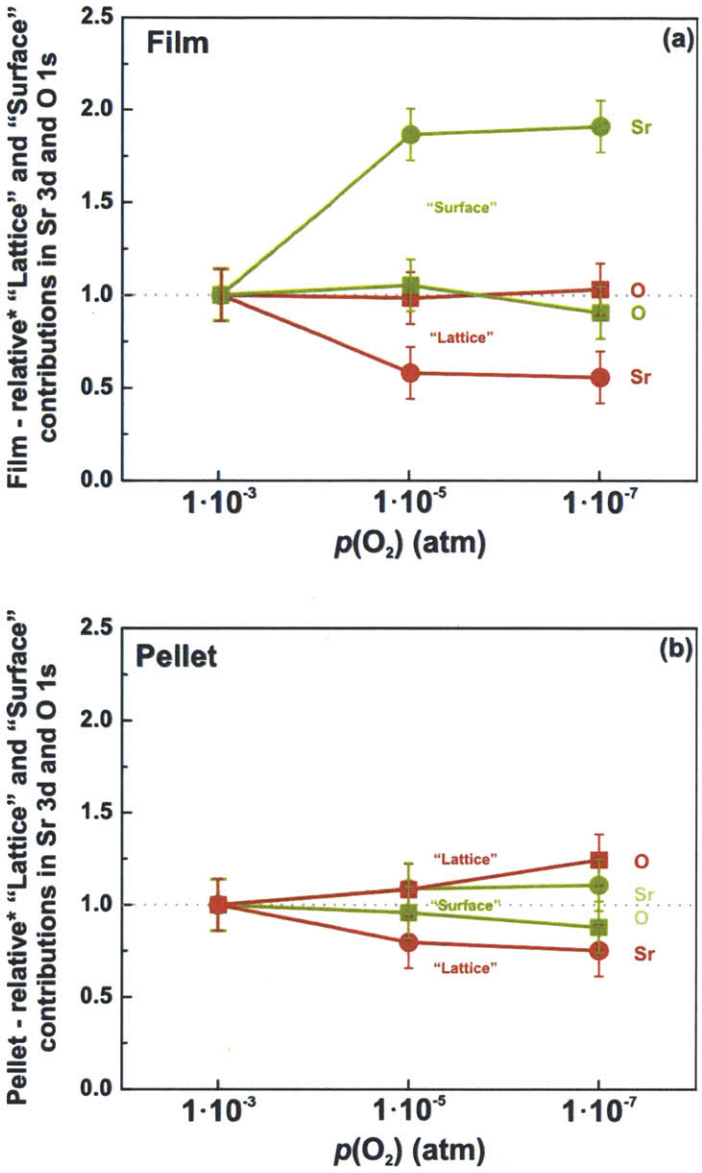

Figures S5-9. *In situ* APXPS data of the LSC film and pellet as a function of oxygen partial pressure. Normalized* change in the Sr and O intensity (lattice: red, surface: green) with decreasing $p(O_2)$ for **(a)** the film and **(b)** the pellet. The error bars have been estimated by assuming a standard deviation of the raw intensity of 10 %. (* Normalization procedure: first, the raw intensities of the Sr and O "lattice" (or "surface" component, respectively) are divided by the photo-ionization cross sections of Sr or O, respectively. Second, the obtained values are normalized by the initial value, *i.e.* divided by the obtained value at $p(O_2) = 1 \cdot 10^{-3}$ atm and T = 520 °C).

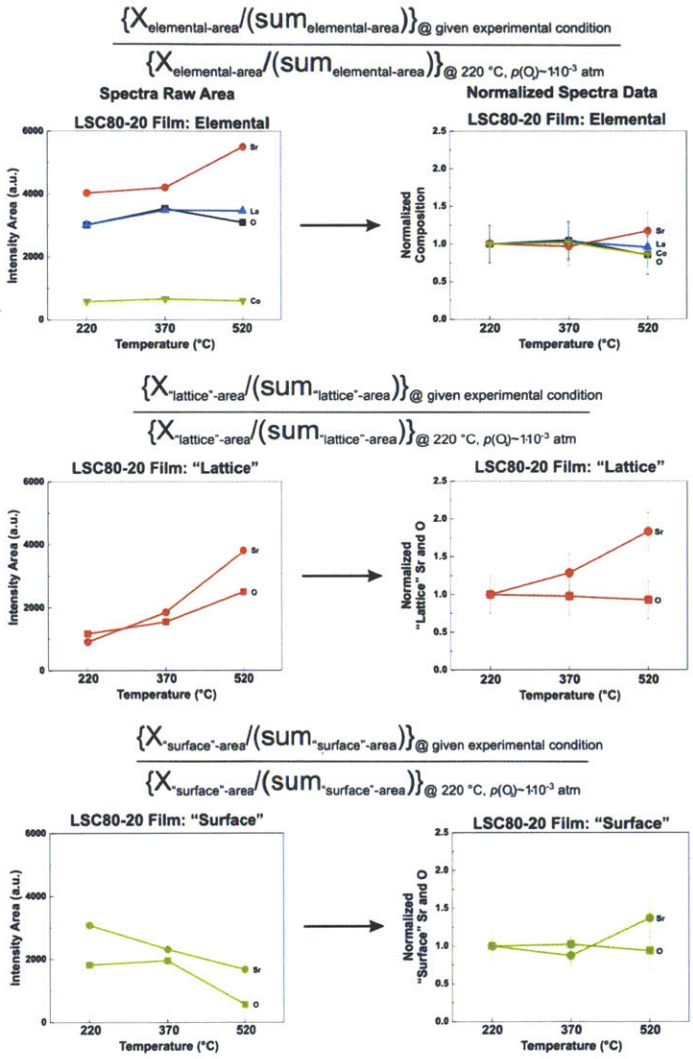

Figures S5-10a. Procedure to convert the raw data (shown on the left hand side) into the normalized data (shown on the right hand side) for the LSC thin film. As shown in the equations, first the raw intensities, I, are divided by the photo-ionization cross sections, σ, of the respective elements. Second, these cross-section-normalized intensity, I_σ, values are divided by the sum of all depicted values in each graph at each temperature. Third, the obtained values, $I_{N,\sigma}$, are normalized to the first condition, i.e. to the value at $T = 220$ °C and $p(O_2) = 1\cdot10^{-3}$ atm. This procedure is utilized for the total elemental regions (La 4d–Co 3s, Sr 3d, Co 3p, O 1s, depicted in the first line), for the Sr and O "lattice" component (second line), and for the Sr and O "surface" component (third line).

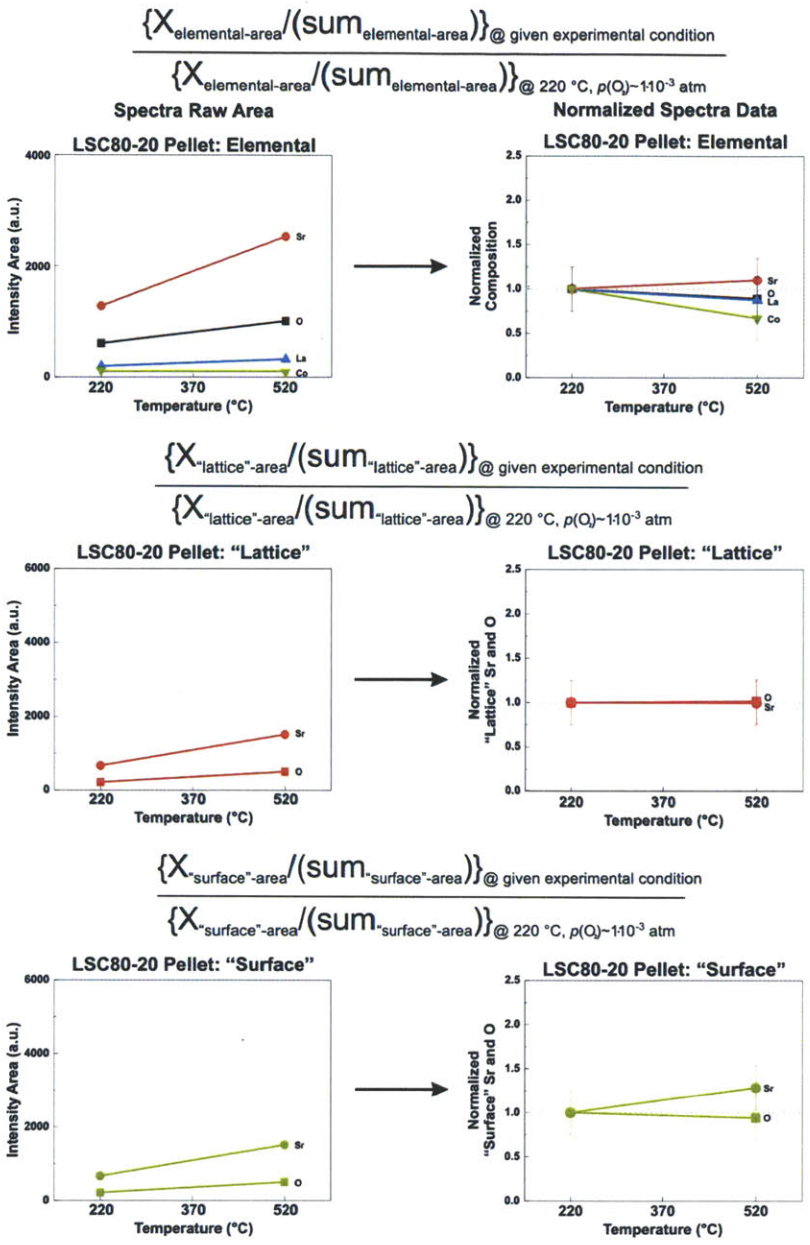

Figures S5-10b. Procedure to convert the raw data (shown on the left hand side) into the normalized data (shown on the right hand side) for the LSC pellet, which is identical to the procedure used for the film (**Figures S5-10a**). As shown in the equations, first the raw intensities, I, are divided by the photo-ionization cross sections of the respective elements. Second, these cross-section-normalized intensity values, I_{σ}, are divided by the sum of all depicted values in each graph. Third, the obtained values are normalized, $I_{N,\sigma}$, to the first condition, i.e. to the value at $T = 220$ °C and $p(O_2) = 1 \cdot 10^{-3}$ atm. This procedure is utilized for the total elemental regions (La 4d–Co 3s, Sr 3d, Co 3p, O 1s, depicted in the first line), for the Sr and O "lattice" component (second line), and for the Sr and O "surface" component (third line).

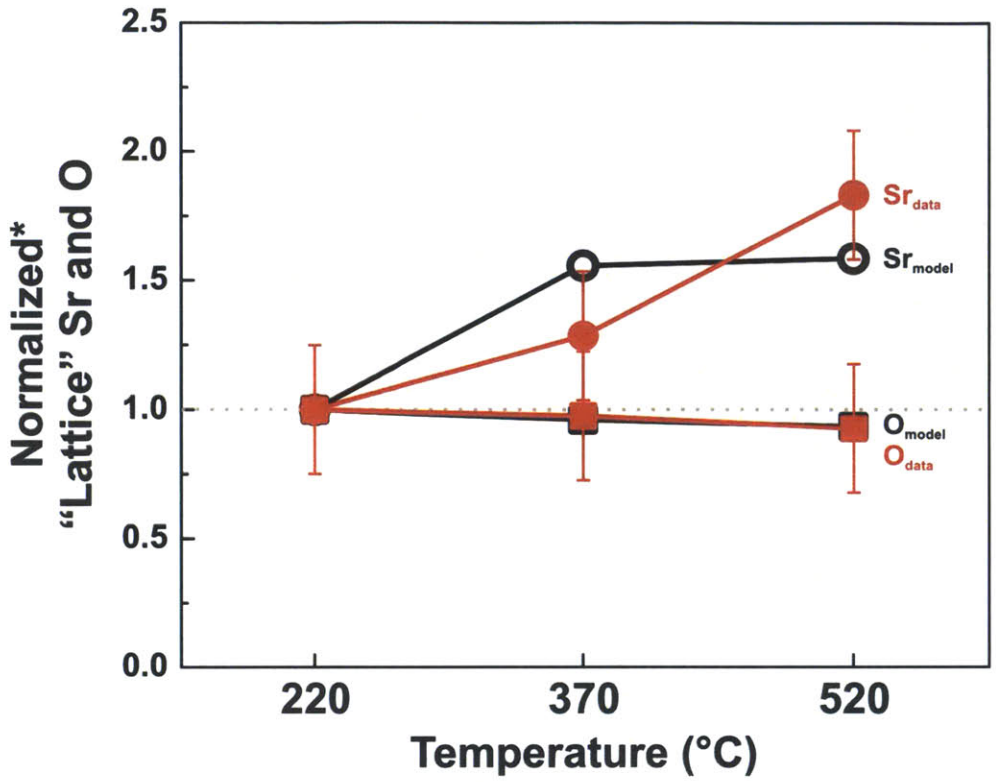

Figure S5-11. Normalized "lattice" Sr and O (red) with increasing temperature at $p(O_2) = 1 \cdot 10^{-3}$ atm for the epitaxial thin film (as shown in **Figure 5-5**) with corresponding predicted values by the modified canonical Lankhorst model[48] (black). (* Data normalization procedure: first, the raw intensities of the Sr and O "lattice" are divided by the photo-ionization cross sections of Sr or O, respectively. Second, these cross-section-normalized intensity values for Sr or O "lattice" are divided by the sum of these values (Sr + O "lattice") at each $p(O_2)$ condition. Third, the obtained values are normalized by the initial value, i.e. divided by the obtained value at $p(O_2) = 1 \cdot 10^{-3}$ atm and $T = 220$ °C. Model normalization procedure: the obtained values are normalized by the initial value, *i.e.* divided by the obtained value at $p(O_2) = 1 \cdot 10^{-3}$ atm and $T = 220$ °C).

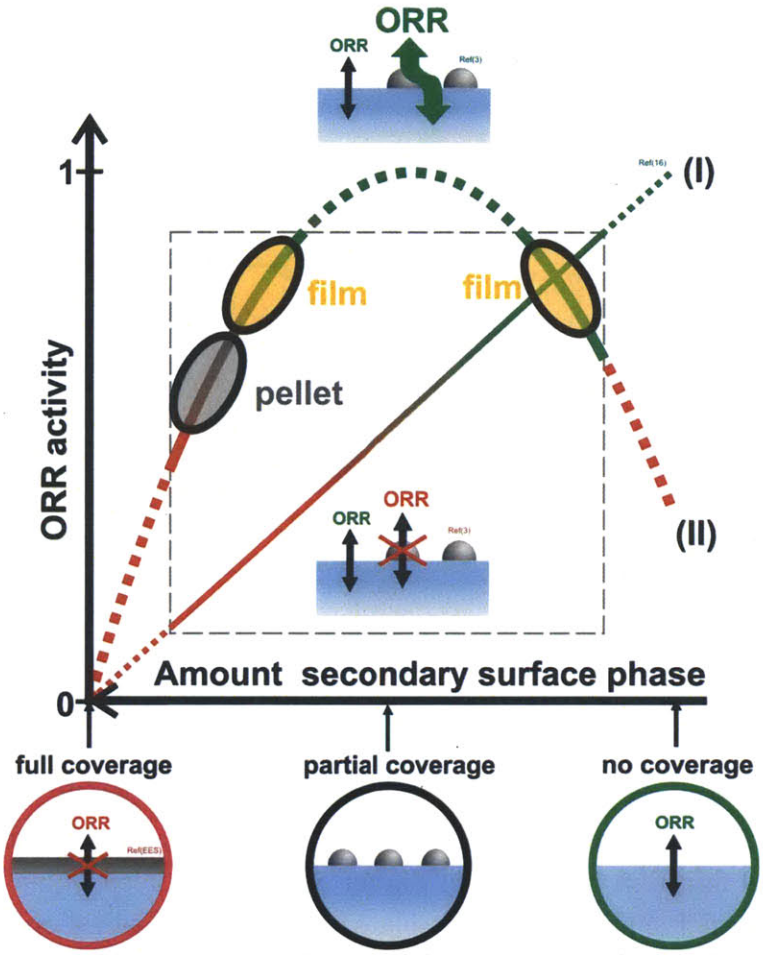

Figure S5-12: Schematic showing the influence of the amount of Sr-rich secondary phases on the LSC surface on the ORR activity. For a full coverage with an insulating Sr-rich surface phase no ORR activity is expected.[10] A hypothetically secondary free LSC surface has a certain, higher ORR activity. For partial coverages two cases are possible and have been reported in literature: (I) a different ORR mechanism occurs for partial coverage leading to a higher ORR activity than for a film without coverage,[10] (II) the part of the surface covered with secondary phases is blocked for oxygen exchange, while the particle-free surface contributes to the oxygen exchange leading to an ORR activity between full and no coverage.[44] Depending on the present phase or the specific mixture of phases ($SrO/Sr(OH)_2/SrCO_3/Sr_xX_yO$) and potential solid state reactions forming new phases (e.g. $La,Sr)_2CoO_4$[10,11] both cases can occur in this system.[10,11,44] A possible location of the pellet (grey) and the film (yellow) investigated in this study is marked: based on previous ORR measurements we can exclude a full coverage, and XPS exhibited that both samples have a certain amount of coverage. Compared to the pellet, the film showed lower coverage and higher ORR activity. As reported previously,[10] a certain Sr-rich surface decoration is more ORR active than the unmodified LSC film surface, therefore the film is not located at the maximum of the ORR-coverage curve.

5.6 References

1. S. B. Adler, *Chem Rev*, 2004, **104**, 4791-4843.
2. J. Suntivich, H. A. Gasteiger, N. Yabuuchi, H. Nakanishi, J. B. Goodenough and Y. Shan-Horn, *Nature Chem.*, 2011, **3**, 546-550.
3. A. Kumar, F. Ciucci, A. N. Morozovska, S. V. Kalinin and S. Jesse, *Nature Chem.*, 2011, **3**, 707-713.
4. T. Kawada, J. Suzuki, M. Sase, A. Kaimai, K. Yashiro, Y. Nigara, J. Mizusaki, K. Kawamura and H. Yugami, *J Electrochem Soc*, 2002, **149**, E252-E259.
5. H. A. Gasteiger and N. M. Markovic, *Science*, 2009, **324**, 48-49.
6. M. Sase, K. Yashiro, K. Sato, J. Mizusaki, T. Kawada, N. Sakai, K. Yamaji, T. Horita and H. Yokokawa, *Solid State Ionics*, 2008, **178**, 1843-1852.
7. A. Yamada, Y. Suzuki, K. Saka, M. Uehara, D. Mori, R. Kanno, T. Kiguchi, F. Mauvy and J. C. Grenier, *Adv. Mat.*, 2008, **20**, 4124-4128.
8. J. K. Norskov, T. Bligaard, J. Rossmeisl and C. H. Christensen, *Nature Chem.*, 2009, **1**, 37-46.
9. V. R. Stamenkovic, B. Fowler, B. S. Mun, G. Wang, P. N. Ross, C. A. Lucas and N. M. Markovic, *Science*, 2007, **315**, 493-497.
10. E. Mutoro, E. J. Crumlin, M. D. Biegalski, H. M. Christen and Y. Shao-Horn, *Energy Environ. Sci.*, 2011, **4**, 3689-3696
11. E. J. Crumlin, E. Mutoro, S.-J. Ahn, G. J. la O', D. N. Leonard, A. Borisevich, M. D. Biegalski, H. M. Christen and Y. Shao-Horn, *J. Phys. Chem. Lett.*, 2010, **1**, 3149-3155.
12. G. J. la O', S. J. Ahn, E. Crumlin, Y. Orikasa, M. D. Biegalski, H. M. Christen and Y. Shao-Horn, *Angew Chem Int Edit*, 2010, **49**, 5344-5347.
13. J. B. Goodenough, *Rep. Progr. Phys.*, 2004, **67**, 1915-1993.
14. G. J. la O, R. F. Savinell and Y. Shao-Horn, *J Electrochem Soc*, 2009, **156**, B771-B781.
15. Y. Orikasa, T. Ina, T. Nakao, A. Mineshige, K. Amezawa, M. Oishi, H. Arai, Z. Ogumi and Y. Uchimoto, *J. Phys. Chem. C*, 2011, **115**, 16433-16438.
16. M. Imamura, N. Matsubayashi and H. Shimada, *J. Phys. Chem. B*, 2000, **104**, 7348-7353.
17. B. Luerssen, E. Mutoro, H. Fischer, S. Gunther, R. Imbihl and J. Janek, *Angew. Chem. Int. Edit.*, 2006, **45**, 1473-1476.

18. C. Zhang, M. E. Grass, A. H. McDaniel, S. C. DeCaluwe, F. El Gabaly, Z. Liu, K. F. McCarty, R. L. Farrow, M. A. Linne, Z. Hussain, G. S. Jackson, H. Bluhm and B. W. Eichhorn, *Nature Mat.*, 2010, **9**, 944-949.
19. M. B. Pomfret, J. Marda, G. S. Jackson, B. W. Eichhorn, A. M. Dean and R. A. Walker, *J. Phys. Chem. C*, 2008, **112**, 5232-5240.
20. N. Balke, S. Jesse, A. N. Morozovska, E. Eliseev, D. W. Chung, Y. Kim, L. Adamczyk, R. E. Garcia, N. Dudney and S. V. Kalinin, *Nature Nanotech.*, 2010, **5**, 749-754.
21. D. F. Ogletree, H. Bluhm, E. D. Hebenstreit and M. Salmeron, *Nucl.Instrum. Meth. A*, 2009, **601**, 151-160.
22. M. E. Grass, P. G. Karlsson, F. Aksoy, M. Lundqvist, B. Wannberg, B. S. Mun, Z. Hussain and Z. Liu, *Review of Scientific Instruments*, 2010, **81**.
23. J. A. Whaley, A. H. McDaniel, F. El Gabaly, R. L. Farrow, M. E. Grass, Z. Hussain, Z. Liu, M. A. Linne, H. Bluhm and K. F. McCarty, *Rev. Sci. Instrum.*, 2010, **81**, 086104-086107.
24. J. J. Yeh and I. Lindau, *Atom Data Nucl Data* 1985, **32**, 1.
25. R. H. E. van Doorn and A. J. Burggraaf, *Solid State Ionics*, 2000, **128**, 65-78.
26. X. Chen, J. Yu and S. B. Adler, *Chem. Mat.*, 2005, **17**, 4537–4546.
27. F. Tietz, *Ionics*, 1999, **5**, 129-138.
28. S. Terblanche, *J. Appl. Crystal.*, 1989, **22**, 2.
29. Z. Cai, Y. Kuru, J. Woo Han, Y. Chen and B. Yildiz, *J. Am. Chem. Soc.*, 2011, **133**, 17696–17704.
30. R. P. Vasquez, *J. Electron Spectros.*, 1991, **56**, 217-240.
31. P. A. W. van der Heide, *Surf Interface Anal*, 2002, **33**, 414-425.
32. C. J. Powell and A. Jablonski, *Nucl.Instrum. Meth. A*, 2009, **601**, 54-65.
33. J.-H. Joo, R. Merkle, J. Maier, M. Kubicek, J. Januschewsky, J. Fleig, A. Oestereich, Z. Hlavathy, M. Hävecker, A. Knop-Gericke and R. Schlögl, *diffusion-fundamentals.org*, 2010, **12**, 67-67.
34. N. S. McIntyre and M. G. Cook, *Anal. Chem.*, 1975, **47**, 2208-2213.
35. Y. Uwamino, T. Ishizuka and H. Yamatera, *J. Electron Spectros.*, 1984, **34**, 67-78.
36. A. Galenda, M. M. Natile, V. Krishnan, H. Bertagnolli and A. Glisenti, *Chem. Mat.*, 2007, **19**, 2796-2808.

37. H. Bluhm, M. Havecker, A. Knop-Gericke, E. Kleimenov, R. Schlogl, D. Teschner, V. I. Bukhtiyarov, D. F. Ogletree and M. Salmeron, *J. Phys. Chem. B*, 2004, **108**, 14340-14347.

38. W. Y. Howng and R. J. Thorn, *J. Phys. Chem. Solids*, 1980, **41**, 75-81.

39. W. Howng and R. Thorn, *Chem. Phys. Lett.*, 1978, **56**, 463-465.

40. Y. A. Teterin, A. Y. Teterin, A. M. Lebedev and K. E. Ivanov, *J. Electron Spectros.*, 2004, **137**, 607-612.

41. J. Shin, S. V. Kalinin, H. N. Lee, H. M. Christen, R. G. Moore, E. W. Plummer and A. P. Baddorf, *Surf. Sci.*, 2005, **581**, 118–132.

42. Q. H. Wu, M. L. Liu and W. Jaegermann, *Mat. Lett.*, 2005, **59**, 1480-1483.

43. R. Bertacco, J. P. Contour, A. Barthelemy and J. Olivier, *Surf. Sci.*, 2002, **511**, 366-372.

44. M. Kubicek, A. Limbeck, T. Fromling, H. Hutter and J. Fleig, *J Electrochem Soc*, 2011, **158**, B727-B734.

45. T. T. Fister, D. D. Fong, J. A. Eastman, P. M. Baldo, M. J. Highland, P. H. Fuoss, K. R. Balasubramaniam, J. C. Meador and P. A. Salvador, *Appl. Phys. Lett.*, 2008, **93**, 151904-1519043

46. W. Donner, C. L. Chen, M. Liu, A. J. Jacobson, Y. L. Lee, M. Gadre and D. Morgan, *Chem. Mat.*, 2011, **23**, 984-988.

47. Y. L. Lee, J. Kleis, J. Rossmeisl and D. Morgan, *Phys. Rev. B*, 2009, **80**, 224101.

48. M. H. R. Lankhorst, H. J. M. Bouwmeester and H. Verweij, *Phys. Rev. Lett.*, 1996, **77**, 2989-2992.

49. H. M. Christen, E. D. Specht, S.S. Silliman, and K. S. Harshavardhan, *Phys. Rev. B*, 2003, **68**, 4.

50. A. Barrie, F. J. Street, *J. Electron. Spectros*, 1975, **7**, 1-31.

Chapter 6. *In situ* Ambient Pressure XPS and High Resolution XRD of Epitaxial LSC Peroskites Near Operating Conditions Under Applied Potentials

Reproduced in part with permission from Ethan J. Crumlin, Eva Mutoro, Zhi Liu, Michael D. Biegalski, Wesley T. Hong, Hans M. Christen, Hendrik Bluhm, and Yang Shao-Horn, In situ Ambient Pressure XPS and High Resolution XRD of Epitaxial LSC Perovskites Near Operating Conditions Under Applied Potentials, (In Preparation).

6.1 Introduction

Mixed electronic and ionic conductors such as perovskites ($ABO_{3-\delta}$)[1-3] and Ruddlesden-Popper (A_2BO_4)[4] materials are promising cathode materials for solid oxide fuel/electrolyzer cells (SOFC/SOEC), oxygen separation membranes, and sensors due to their electronic/ionic conductivities and catalytic activities.[1-4] Recently, heterostructured oxide interfaces have demonstrated enhanced transport and oxygen surface exchange ($O_2 + 4e^- \leftrightarrow 2O^{2-}$) properties.[5-13] In particular, the oxygen reduction reaction (ORR) on $La_{0.8}Sr_{0.2}CoO_{3-\delta}$ (LSC_{113}) surfaces decorated with Sr(hydr)oxide[8] or $(La_{0.5}Sr_{0.5})_2CoO_{4\pm\delta}$($LSC_{214}$)[6] particles has shown increased oxygen surface exchange coefficients up to one and three orders of magnitude, respectively. Improving our understanding of the mechanism(s) governing ORR on these highly active oxides will greatly contribute to future catalyst design and development. Employing *in situ* surface and bulk analysis tools such as X-ray photoelectron spectroscopy (XPS) and X-ray diffraction (XRD) can greatly contribute to this understanding. XRD does not require high-vacuum conditions and extensive *in situ* investigations have been conducted to probe the material's phase composition, transitions, and expansions as a function of temperature and pressures.[14-16] In a 4% H_2 reducing

environment, LSC_{113} has been shown to induce oxygen vacancy ordering at 325 °C and decomposition to La_2O_3, SrO and Co metal at 550 °C, all of which revert back to LSC_{113} upon exposure to oxygen at high temperatures.[15] In addition, previous work revel epitaxial LSC_{113} under 1 atm oxygen to have an enlarged unit cell volume whose strain transitions from tensile to compression along the *a*-axis (in the same plane as the substrate) and compression to tension along the *c*-axis (normal to the substrate) as temperature is increased from 25 °C to 550 °C.[16] Synchrotron-based XPS provides high intensities to support *in situ* measurements via scanning photoelectron microscopy (SPEM) or temperature-programmed XPS investigating reaction mechanisms or surface elemental changes when exposed to very low pressures of gasses ($<10^{-9}$ atm), and varying temperature or applied bias.[9,17-20] The Advanced Light Source (ALS) possesses a synchrotron high-intensity X-ray source coupled with a differentially pumped electrostatic lens system that is capable of conducting *in situ* ambient pressure ($< 10^{-2}$ atm) X-ray photoelectron spectroscopy (APXPS) at elevated temperatures[16,21-23] and applied electrochemical potentials.[24,25] Previous results have shown that the high catalytic activity of epitaxial LSC_{113} thin films relative to bulk pellet of LSC_{113} may be induced by the thin film's enrichment of Sr within the near-surface lattice region upon increasing to 520 °C.[16] In this work, we will discuss three main studies: (i) the reversibility of Sr enrichment within the near-surface lattice region of epitaxial LSC_{113} thin films that are thermally cycled between 220 °C – 520 °C using *in situ* APXPS; (ii) structural and phase changes of epitaxial LSC_{113} thin film upon electrochemical polarization using *in situ* high-resolution X-ray diffraction (HRXRD); (iii) comparison of the atomic compositional changes that occur for electrochemically polarized LSC_{113}, LSC_{214}, and LSC_{214}-decorated LSC_{113} ($LSC_{113/214}$) thin films using *in situ* APXPS. These investigations will help develop an understanding for the governing properties responsible for the significantly higher oxygen catalytic activities observed in epitaxial $LSC_{113/214}$ thin films relative to LSC_{113}.

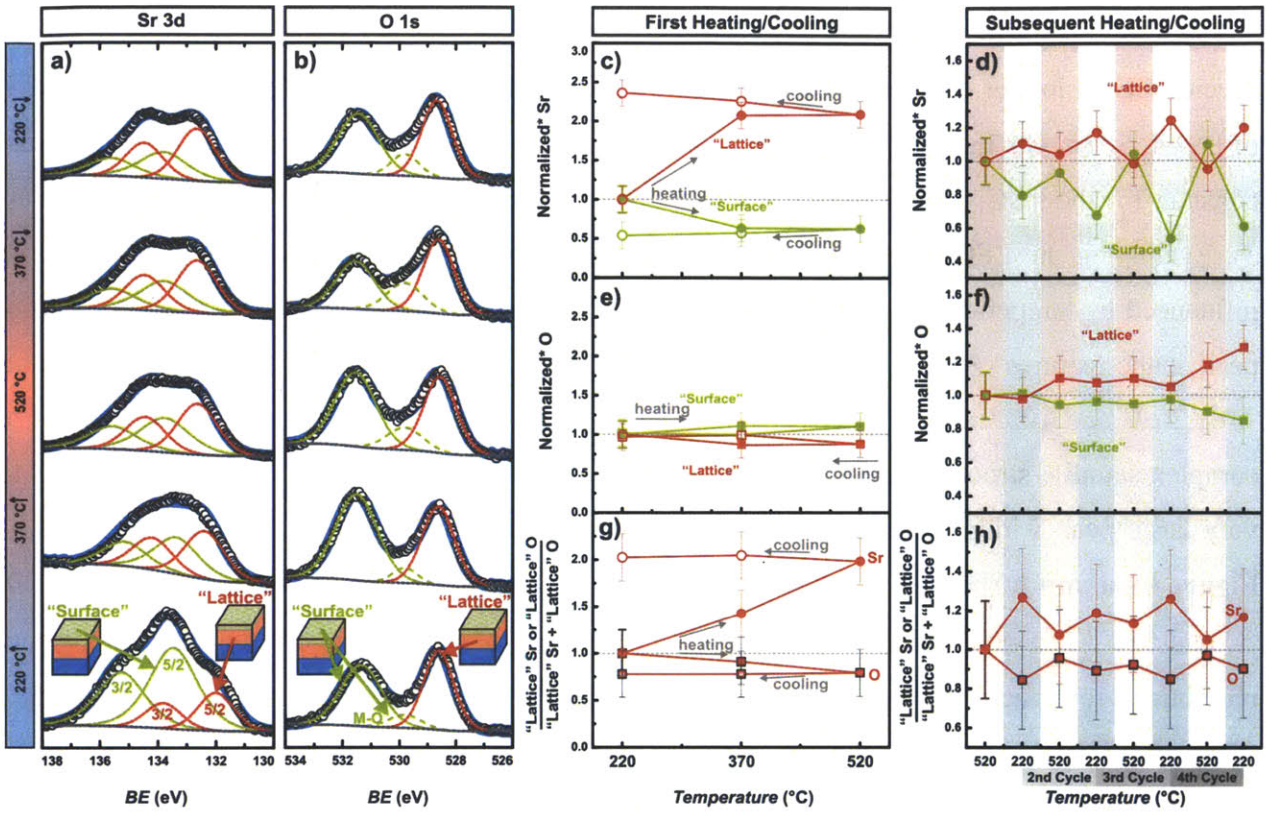

Figure 6-1. *In situ* APXPS data of the LSC film as a function of temperature. (a) Sr 3d (E_{photon} = 390 eV), (b) O 1s (E_{photon} = 690 eV) spectra at 220 °C, 370 °C, 520 °, then decreased to 370 °C and 220 °C at a $p(O_2)$ of $1 \cdot 10^{-3}$ atm. The "lattice" component of the perovskite structure in the near-surface region is shown in red while the "surface" component for the secondary phases (including both surface components) is shown in green. White circles are for the measured data, blue lines indicate the sum of fits, and grey dotted lines correspond to the background. Changes in the relative contributions of "lattice" and "surface" to the total during: (c) first Sr 3d cycle and (d) subsequent Sr 3d cycle (e) first O 1s, (f) subsequent O1s cross-section-normalized intensity (lattice: red, surface green), (g) first "Lattice" Sr enrichment, and (h) subsequent "Lattice" Sr enrichment of the LSC(001) film in the near-surface region (determined by the cross-section-normalized "lattice" intensity of Sr 3d or O 1s was divided by the combined Sr and O "lattice" cross-section-normalized intensities) as a function of temperature and referenced to the initial 220 °C values, and 520 °C values for subsequent temperature cycling.

6.2 Results and Discusion

Using *in situ* HRXRD, no new phases were observed as an epitaxial LSC_{113} thin film was heated from 25 °C to 550 °C in a $p(O_2)$ of 1 atm. This result confirms the film's stability at elevated temperatures (**Figure S6-1**), and corroborates results previously reported.[16] *In situ* APXPS was utilized to understand how the film's surface elemental composition changes during

a single and multiple temperature cycling between 220 °C (the temperature in which carbon species are no longer detected on the sample surface[16]) and 520 °C in $p(O_2)$ of $1 \cdot 10^{-3}$atm. XPS of La 4d, Sr 3d, Co 3p, and O 1s (**Figure S6-2**) reveal the La, Sr, Co, O concentrations remained constant for the LSC_{113} films during the first and subsequent temperature cycling's (**Figure S6-3**). Evaluating the LSC_{113} spectra in detail, La 4d and Co 3p peak shapes did not appear to be influenced by temperature cycling, while Sr 3d and O 1s showed the most amount of variance in peak shape features (**Figure 6-1a, 6-1b, S6-2**). Because the La 4d (La $4d_{5/2}$ and $4d_{3/2}$ doublet at ~101.2 eV and 103.9 eV, respectively, with an energy separation of ~2.8 eV)[26,27] consists of a complex satellite structure and overlaps with the Co 3s peak (~102.8 eV),[28] and the Co 3p has a very large peak width, we could not separate these spectra into detailed component features.[16] **Figure 6-1a and b** show Sr 3d and O 1s spectra during a single temperature cycle between 220 °C and 520 °C in $p(O_2)$ of $1 \cdot 10^{-3}$atm, which have been fitted with components representing the previously reported "lattice" (near-surface region of the perovskite lattice) and "surface" (associated with surface secondary phases and perovskite surface termination) species[16]. Additional details are provided in the **Supporting Information**. The Sr 3d spectrum was found to exhibit a large central peak with shoulder features on either side at 220 °C. By increasing temperature to 520 °C, the spectrum shape transformed to a single broad plateau and separated into two defined peak features when cooled to 220 °C (**Figure 6-1a**). During subsequent temperature cycles, the Sr 3d spectrum systematically changed between the broad plateau at 520 °C and the two defined peaks at 220 °C (**Figure S6-2b**). All temperature cycled Sr 3d spectra could be fitted by two sets of Sr $3d_{5/2}$ and $3d_{3/2}$ doublets with an energy separation of ~1.8 eV and a branching ratio of 1.5.[29,30] The binding energy (*BE*) for the low-energy set of Sr $3d_{5/2}$ at ~ 132.4 eV and Sr $3d_{3/2}$ at ~ 134.2 eV is the Sr "lattice" component, while the high-energy set of Sr $3d_{5/2}$ at ~133.5eV and Sr $3d_{3/2}$ at ~135.3 eV is referred to as the Sr "surface" component (where Sr-based secondary phases include SrO-like at ~133.0 eV[29] and $Sr(OH)_2$-like at ~133.2 eV[30]). The O 1s spectrum showed no clear trend in spectral shape change of the two main features, which exist throughout both single and multiple temperature cycling, which can be fit with three symmetric components (**Figure 6-1b, S6-2b**). The low-energy component *BE* of ~528.6 eV can be assigned to the O "lattice" within the perovskite phase. The intermediate- and high-energy components (at *BE*~529.8 eV and 532.5 eV, respectively) correlate to the perovskite lattice termination layer (529.8 – 531.0 eV)[28,29,31] and surface secondary phases such as metal

(hydr)oxides (530.6 – 531.6 eV),[28,30,32] respectively, both of which will be referred to as O "surface" components.

As temperature increased from 220 °C to 520 °C, there was a significant reduction in the relative contribution of the Sr "surface" component, giving rise to a relative increase in the Sr "lattice" contribution (**Figure 6-1c**), which follows the same trend as previously reported.[16] Interestingly upon cooling, the relative "lattice" contribution continued to increase slightly. This finding may suggest that higher temperatures may irreversibly induce and/or stabilize slightly larger quantities of Sr "surface" phases. The O 1s spectra revealed minimal changes occurred in the relative contributions between oxygen "surface" and "lattice" species as the sample was thermally cycled (**Figure 6-1e**). This O 1s observation contrasts with our previously reported observations, in which a large decrease in oxygen "surface" components resulted from an increase in temperature.[16] This may be a result of the variations in the surface composition between samples, as well as instrumental variations that are imposed by using different endstations and sample holders at ALS (allowing for variations in temperature/thermocouple placement). In **Figure 6-1g**, as temperature was increased from 220 °C to 520 °C, the Sr and O "lattice" were increased by ~100% and decreased ~20%, respectively. This is indicative of "lattice" Sr and "lattice" oxygen vacancy enrichment (a coupling attributed to the Sr-oxygen vacancy interaction)[16] in the near-surface perovskite region, reaffirming a trend previously reported.[16] Interestingly, as the sample was cooled to 220 °C, "lattice" Sr slightly increased (**Figure 6-1g**). This observation suggests that upon heating a significant amount of Sr enriches the near-surface "lattice" region, and upon cooling Sr further enriches the near-surface "lattice" region.

To determine if the Sr "lattice" enrichment is reversible upon cooling from 520 °C to 220 °C, a pristine LSC_{113} thin film (another piece from the same sample that was thermally cycled once) was thermally cycled multiple times between 520 °C and 220 °C. Interestingly, we continued to see a systematic variation in the relative Sr "surface" to "lattice" contributions and Sr "lattice" enrichment as the temperature was thermally cycled between 520 °C and 220 °C (**Figure 6-1d, h**); congruently O showed minimal variation in the relative "surface" to "lattice" contributions (**Figure 6-1f**). Due to the Sr-oxygen vacancy coupling, the observed reduction in the "lattice" oxygen follows the increase in "lattice" Sr which simultaneously increases the "lattice" oxygen vacancies in the near-surface region (**Figure 6-1h**).[16] Despite the initial, large, irreversible Sr

"lattice" enrichment upon heating to 520 °C, there was a certain amount of Sr that underwent a reversible change as the sample's temperature was further cycled between 520 °C and 220 °C. Based on this behavior, we hypothesize that "surface" Sr phases can be stabilized at 520 °C, while at lower temperatures (220 °C) these "surface" phases are reincorporated into the LSC_{113} perovskite lattice.

In situ HRXRD was used to understand how the LSC_{113} phase is influenced by cathodic potentials from 0 V to -0.8 V in increments of -0.2 V (**Figure 6-2a**). Normal and off-normal HRXRD analysis indicated $LSC_{113}(001)_{pc}//GDC(001)_{cubic}//YSC(001)_{cubic}$ and $(110)_{pc}LSC_{113}//(110)_{cubic}GDC//(110)_{cubic}YSZ$ (**Supplementary Information §6.4)** similar to previous work,[16,33] where the subscript "pc" denotes the pseudocubic notation. As the applied cathodic potential is increased we observe the $LSC_{113}(002)_{pc}$ and $(101)_{pc}$ peaks shifting to lower diffraction angles (**Fig 6-2b and S6-4**), while the YSZ(002) is unaffected, **Figure 6-2c**. The high crystallinity of the LSC_{113} film was maintained at 550 °C across all applied potentials, as indicated by a nearly constant full width at half maximum of $LSC_{113}(002)$ and $LSC_{113}(101)$ peaks of ~0.25°. After all cathodic potentials were applied, a full range *theta-2theta* scan was collected without an applied bias revealing no evidence for LSC_{113} decomposition into secondary phases (**Figure S6-1**), and the respective high-resolution scans of the $LSC_{113}(002)$ and (101) peaks return to approximately their initial starting values before polarization (**Figure 6-2b, S6-4**). Using the $LSC_{113}(002)$ and (101) reflections, the unit cell volume can be determined (**Figure 6-2d**). As the potential is increased from 0 V to -0.4 V the unit cell volume slowly increases by ~0.2%, then begins to sharply increase its volume by over 4.5% when applying -0.8 V bias.

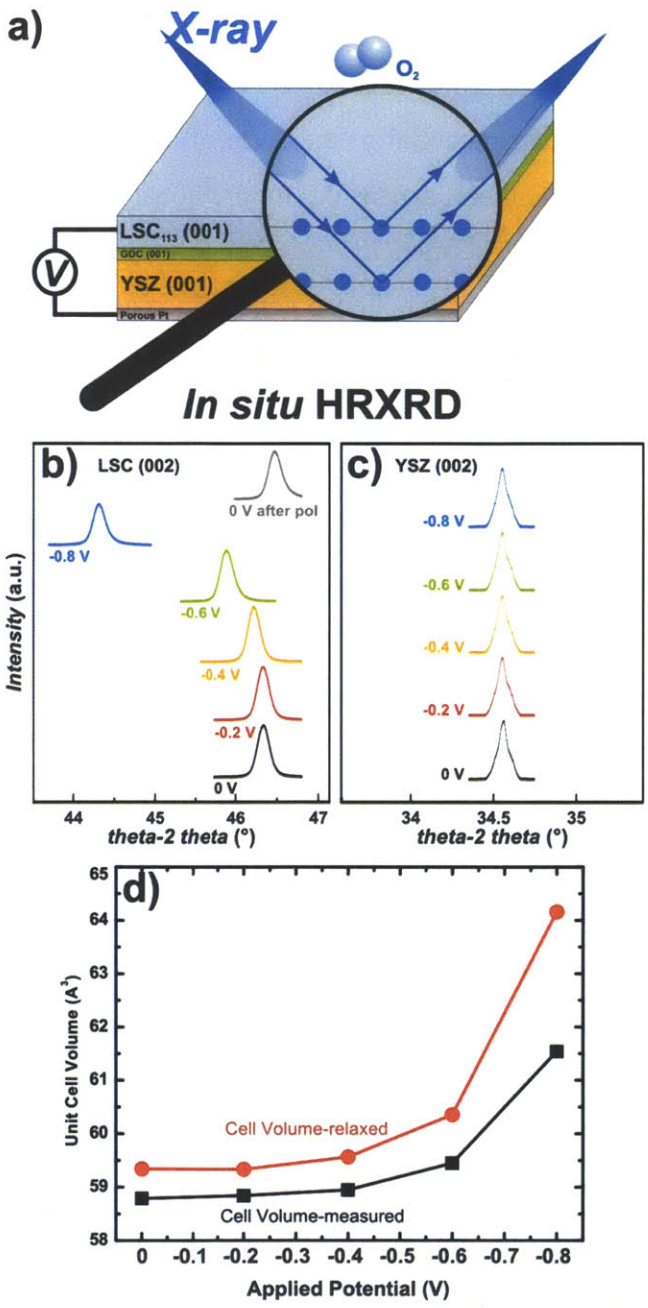

Figure 6-2. *In situ* HRXRD (a) experimental configuration observes the crystal structure and strain of the epitaxial LSC(001) film supported by a single crystalline YSZ(001) substrate with a (001)-oriented gadolinium-doped ceria (GDC) buffer layer as a function of applied cathodic potential at ~550 °C and $p(O_2)$ of 1 atm. (b) LSC(002) peaks shift toward lower angles in the *theta* – 2 *theta* position with increasing applied potential, while (c) $YSZ(002)_c$ peaks remain fixed. (d) The relaxed (red) and measured (black) unit cell volume of the LSC film as a function of applied potential.

When an electrochemical potential is applied to the LSC_{113} thin film, thermodynamic electrochemical equilibrium needs to be maintained. Using the Nernst equation, we can express the maximum induced chemical potential in the form of an effective $p(O_2)$. This allows us to relate the observed electrochemical expansion to previously reported chemical expansions[34] (where a chemical expansion is defined by the change in unit cell volume as a function of oxygen non-stoichiometry, δ). As the applied potential increases, the effective $p(O_2)$ increases. Consequently, LSC_{113} will adjust its non-stoichiometry (for cathodic potentials, δ will increase) to accommodate the new electrochemical equilibrium.[35,36] During the low applied potentials (0 V to -0.4 V) the initial increase in volume can be related to a chemical expansion similar to those previously reported for bulk LSC_{113} as a function of δ.[34] However, this interpretation does not explain the significant divergence that occurs with larger applied potentials (-0.4 V to -0.8 V). Therefore another mechanism needs to be invoked to explain LSC_{113}'s significant expansion. We hypothesize that as the applied potential is increased beyond -0.4 V, LSC_{113} begins to transform from a perovskite phase to an oxygen vacancy-ordered perovskite (and potentially a brownmillerite phase) at -0.8 V. This phase transition has previously been reported for various LSC_{113} perovskite compositions at higher temperatures and reducing gas environments.[14,15,34] To the authors' knowledge, this is the first experimental indication for LSC_{113}'s reversible phase transformation induced by electrochemical polarization. This observation brings forth the concern for physical damage to an SOFC if bulk LSC_{113} electrodes were capable of similar phase transformation under operating conditions and potentials.[37] Due to limited sample and instrument availability, we were unable to conduct similar experiments for the LSC_{214} and $LSC_{113/214}$ samples. However, we hypothesize that the $LSC_{113/214}$ sample will show behavior similar to the results presented in this work as the base films are identical, and that the LSC_{214} will remain within its Ruddelson-Popper phase until it decomposes to simple oxide phases[38,39] and is no longer ionically and/or electronically conductive, which did not occur in our preceding experiments.[8,9]

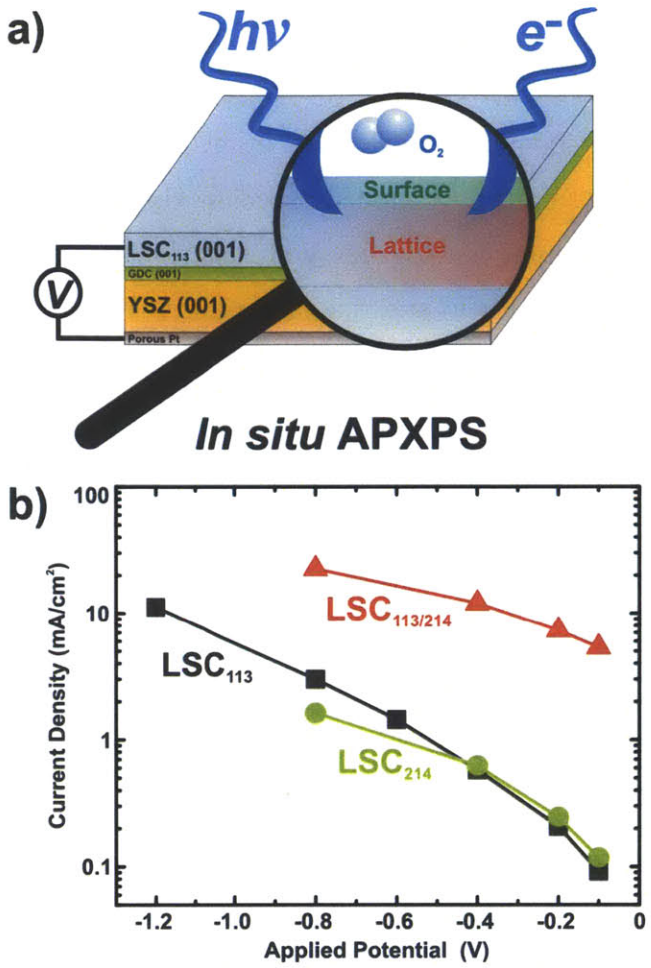

Figure 6-3. *In situ* APXPS (a) experimental configuration probes the elemental compositions as a function of applied potential and (b) plot of the current density versus applied potential for LSC_{113}, LSC_{214}, and $LSC_{113/214}$.

Prior to cathodic polarization, the behavior of La 4d, Sr 3d, Co 3p, and O 1s within a pristine LSC_{113}, LSC_{214}, and $LSC_{113/214}$ samples[6,9,16,33] were observed as a function of temperature (**Figures S6-5 to S6-7**). The LSC_{214} thin film showed stable La, Sr, Co, O concentrations with increased temperature (**Figure S6-5b, S6-6b**), similar to the LSC_{113} thin film (**Figure S6-5a, S6-6a** show comparable trends to the previously discussed LSC_{113} films shown in **Figure 6-1 and Figure S6-2**). Interestingly, the $LSC_{113/214}$ thin film showed a significant increase in total Sr concentration upon reaching 520 °C (**Figure S6-5c, S6-6c**). The La 4d and Co 3p spectral shapes for LSC_{113} (similar to the aforementioned results), LSC_{214}, and $LSC_{113/214}$ did not appear to be influenced by increasing temperature from 220 °C to 520 °C in $p(O_2)$ of $1 \cdot 10^{-3}$ atm, while Sr 3d and O 1s showed the most striking changes (**Figure S6-5**). The Sr 3d and O 1s spectra of these

different LSC films were fit to the same "surface" and "lattice" components with similar *BE*'s previously discussed (**Table S6-2**). At 220 °C, LSC_{214} Sr 3d spectra had a large central peak that was surrounded by a larger shoulder to the left and a smaller shoulder on the right, corresponding to a large fraction of Sr "surface" to "lattice" species. Upon heating to 520 °C, the features became less pronounced, forming a main peak with a small shoulder to the right, indicative of a more uniform quantity of Sr "surface" and "lattice" species. The LSC_{214} O 1s spectrum had two main peaks, with the largest contribution coming from the highest *BE* O "surface" peak (~531.9 eV) at 220 °C. Upon increasing the temperature to 520 °C, O 1s "surface" and "lattice" components became more comparable in area (**Figure S6-5b**). The $LSC_{113/214}$ Sr 3d spectrum at 220 °C (which had similar features to the LSC_{113} Sr 3d spectrum, however with more definition) consisted of a main central peak surrounded by a tail feature to the left and a more defined peak to the right, corresponding to a larger contribution of Sr "lattice" species. Upon heating to 520 °C, all the features merged into one main peak, representative of a more equal distribution of "surface" and "lattice" species. The O 1s spectrum consisted of two main features comprised of similar amounts of high-*BE* "surface" and "lattice" species at 220 °C, and upon heating to 520 °C the highest *BE* "surface" component was reduced relative to the "lattice" component (**Figure S6-5c**). Comparing the LSC_{113}, LSC_{214}, and $LSC_{113/214}$ films' relative "surface" to "lattice" contributions (**Figure S6-7**), we see that $LSC_{113/214}$ Sr "lattice" contribution significantly decreased upon increasing temperature from 220 °C to 370 °C, and recovered to ~80% of its original contribution at 520 °C, with the oxygen "lattice" contribution following similar changes, however with smaller variation (**Figure S6-7c**). This is the exact opposite trend of bare LSC_{113} (**Figure S6-7a**). Conversely, the relative contribution of LSC_{214} Sr and O "lattice" species significantly increased over 80% and 100% respectively upon heating to 520 °C (**Figure S6-7b**). When considering the enrichment of both Sr and O within the "lattice" and "surface," LSC_{214} showed no significant change with temperature, while $LSC_{113/214}$ showed an enrichment of both "surface" and "lattice" Sr (**Figures S6-7b-c**). This enrichment of Sr at both the "lattice" and "surface" may play a key role in the enhanced surface exchange coefficients previously reported.[6]

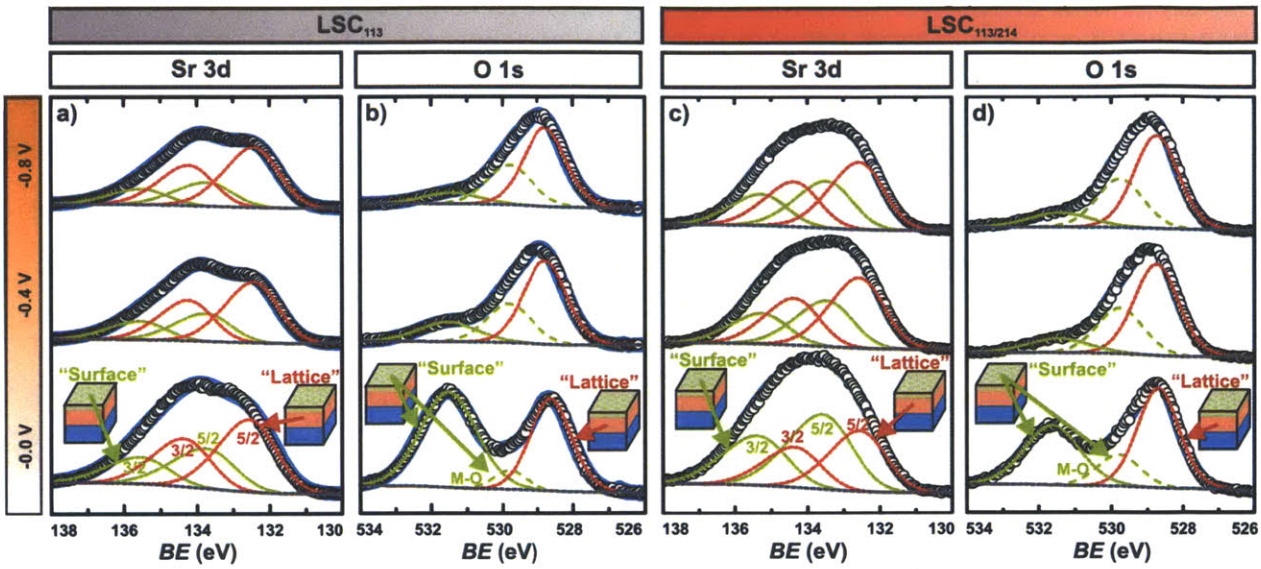

Figure 6-4. *In situ* APXPS of LSC_{113} (a) Sr 3d (E_{photon} = 390 eV), (b) O 1s (E_{photon} = 690 eV) and $LSC_{113/214}$ (c) Sr 3d (E_{photon} = 390 eV), (d) O 1s (E_{photon} = 690 eV) spectra as a function of applied potential 0 V, -0.4 V, and -0.8 V at 520 °C and a $p(O_2)$ of $1 \cdot 10^{-3}$ atm. The "lattice" component of the perovskite structure in the near-surface region is shown in red while the "surface" component for the secondary phases (including both surface components) is shown in green. White circles are for the measured data, blue lines indicate the sum of fits, and grey dotted lines correspond to the background.

After reaching 520 °C, the LSC_{113}, LSC_{214}, and $LSC_{113/214}$ thin films were investigated using *in situ* APXPS (**Figure 6-3a**) to understand the surface compositional changes as a function of applied potential, which exhibited a characteristic Butler-Volmer-like behavior in the current – voltage profile shown in **Figure 6-3b**. $LSC_{113/214}$ has a higher oxygen reduction reaction (ORR) activity than both LSC_{113} and LSC_{214}, which both reflect similar activity trends to identically-prepared films previously reported.[6]

Considering the La 4d, Sr 3d, Co 3p, and O 1s spectra for LSC_{113}, LSC_{214}, and $LSC_{113/214}$ (**Figure 6-4, S6-8**) we observe stable overall elemental concentrations throughout all applied potentials at 520 °C in a $p(O_2)$ of $1 \cdot 10^{-3}$ atm for all three LSC films (**Figure S6-9**), and La 4d and Co 3p spectral shapes do not appear to be influenced by the applied potentials (**Figure S6-8**). As previously discussed, Sr 3d and O 1s spectra (**Figure 6-4, S6-8**) for the three different LSC films were the most influenced by the applied potentials, and were fitted to the same "surface" and "lattice" components and similar *BE*'s previously discussed and provided in **Table S6-2**. The Sr 3d spectra for LSC_{113}, LSC_{214}, and $LSC_{113/214}$ showed similar peak shapes and slight changes as

the applied bias was increased, however no new features appeared. The O 1s spectra underwent the most visible changes with applied potential. As the applied cathode potential was increased, we observed that the highest oxygen "surface" *BE* species (at *BE* ~ 532 eV) vanished for both LSC_{113} and $LSC_{113/214}$ thin films, while the same "surface" oxygen component for the LSC_{214} film appeared to be minimally influenced by the applied potentials.

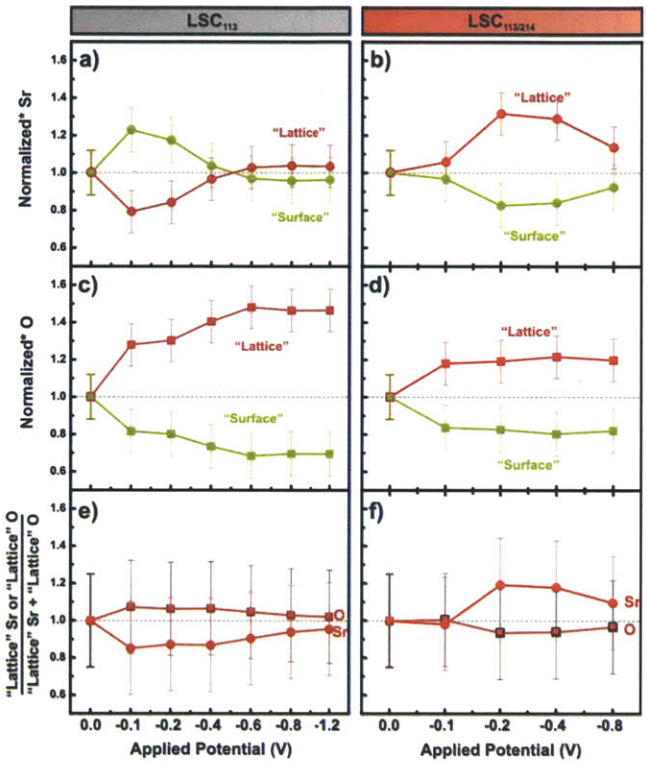

Figure 6-5. The changes in the relative contributions of "lattice" and "surface" to the total (a) LSC_{113}Sr 3d, (b) $LSC_{113/214}$Sr 3d, (c) LSC_{113} O 1s and (d) $LSC_{113/214}$ O 1s cross-section-normalized intensity (lattice: red, surface green). (e) LSC_{113} "Lattice" Sr enrichment, (f) $LSC_{113/214}$ "Lattice" Sr enrichment, in the near-surface region (determined by the cross-section-normalized "lattice" intensity of Sr 3d or O 1s was divided by the combined Sr and O "lattice" cross-section-normalized intensities) as a function of applied potential and referenced to the initial 0 V applied potential values, at 520 °C and $p(O_2)$ of $1 \cdot 10^{-3}$ atm.

Taking into account the relationship between relative Sr and O "surface" and "lattice" contributions, LSC_{214} showed very little influence with applied potentials (**Figure S6-10a, b**), while LSC_{113} and $LSC_{113/214}$ showed significant changes (**Figure 6-5**). Initially, the LSC_{113} Sr "surface" contribution increased relative to the "lattice" component, however as the applied potential increased from -0.4 V to -1.2 V the trends reversed with Sr "lattice" becoming the

larger contribution of total Sr composition (**Figure 6-5a**). The O 1s spectrum showed a significant reduction in the "surface" oxygen species with the increase in applied potential (**Figure 6-5c**). This reduction is similar to what has been observed in previously reported results as temperature was increased;[16] this may suggest that there was an electrochemical short on the previous sample which helped facilitate the reduction in surface phases once the temperature reached 520 °C. Interestingly, **Figure 6-5e** shows that under applied cathodic potentials, Sr "lattice" species withdrew back into the bulk of the electrode, and slowly increased as potentials increased from -0.4 V to -1.2 V. A possible explanation for this observation is that the near-surface "lattice" region is saturated with Sr and oxygen vacancies, preventing further accumulation. Therefore, as the cathodic potential is applied, vacancies can only be increased within the bulk of the LSC electrode. The increase of LSC_{113}'s unit cell volume, which can be directly correlated to the oxygen nonstoichiometry[16,34] (**Figure 6-1**), provides direct evidence for the increase in oxygen vacancies within the bulk of the film as a function of applied cathodic potentials. As additional vacancies are formed within the bulk LSC electrode, the driving force governing the near-surface "lattice" Sr enrichment is reduced, thereby facilitating Sr's incorporation back into the bulk of the electrode away from the surface. As the applied potential was increased beyond -0.4, the Sr "lattice" contribution and enrichment reversed directions, which may be explained by the onset of oxygen vacancy ordering.

$LSC_{113/214}$ increased its relative Sr and O "lattice" contribution as the applied bias was increased (**Figure 6-5b,d**). This is the opposite behavior observed for Sr in LSC_{113}, while LSC_{214} showed minimal influence (**Figure S6-10**). Consequently, this appears to create an increased enrichment in "lattice" Sr with applied potentials, which again deviates from bare LSC_{113} (**Figure 6-5e,f**). Therefore, if we hypothesize that the base film of the $LSC_{113/214}$ follows the same structural behavior as bare LSC_{113}, the phase change from perovskite to oxygen vacancy-ordered and brownmillerite phases does not appear to induce the same surface elemental composition behavior when LSC_{113} is decorated with LSC_{214}. The observed increase in "lattice" Sr may explain the enhanced current densities of $LSC_{113/214}$.

6.3 Conclusions

In summary, we have shown that the surface composition of epitaxial LSC_{113} thin films have a small amount of reversible Sr surface enrichment and dilution under temperature cycling,

preceded by a significant irreversible Sr enrichment in the near-surface perovskite region upon the initial temperature increase from 220 °C to 520 °C at a $p(O_2)$ of $1 \cdot 10^{-3}$ atm. In addition, we observe for the first time that LSC_{113} undergoes a reversible phase transition from a perovskite structure to vacancy-ordered/brownmillerite phase upon cathodic electrochemical polarization at 550 °C at a $p(O_2)$ of 1 atm. Furthermore, using *in situ* APXPS to directly compare the surface composition of LSC_{113}, LSC_{214}, and $LSC_{113/214}$ films as a function of temperature and applied potential, we observe Sr concentration increases on the surface and within the near-surface perovskite region of the $LSC_{113/214}$ film, while bare LSC_{113} shows the opposite effect under applied potentials and LSC_{214} is essentially uninfluenced. We believe the heterostructued interface between LSC_{214}-decorated LSC_{113} plays a significant role in enriching Sr near the surface[40], resulting in the enhanced current exchange density and previously reported surface exchange coefficients.[16] This work highlights the importance of *in situ* characterization and, more importantly, furthers our understanding of the role surface modification of perovskites has on surface composition, providing insight into the parameters governing activity which will be used for the development of highly active catalysts.

6.4 Supporting Information

6.4.1 Experimental Methods

Synthesis of the pulsed laser deposition (PLD) target.[6,8,16,33] $La_{0.8}Sr_{0.2}CoO_{3-\delta}$ (LSC) powder for the PLD target was synthesized using a solid-state reaction from stoichiometric mixtures of La_2O_3, $SrCO_3$, Co_3O_4 (Alfa Aeser, USA) and calcined at 1,000 °C in air for 12 hours. The $(La_{0.5}Sr_{0.5})_2CoO_{4\pm\delta}$ (LSC_{214}) and $Gd_{0.2}Ce_{0.8}O_{2-\delta}$ (GDC) powder was synthesized via Pechini method using $La(NO_3)_3 \cdot 6H_2O$, $Sr(NO_3)_2$, $Co(NO_3)_2 \cdot 6H_2O$, and separately $Gd(NO_3)_3$ and $Ce(NO_3)_3$, which were dissolved in a mixture of ethylene glycol and citric acid (Sigma-Aldrich, USA) in de-ionized water. After esterification at ~100 °C, the resin was charred at 400 °C and then calcined at 800 °C in air for 1 hour. Phase purity was confirmed using X-ray powder diffraction (XRD) (Panalytical). Subsequently PLD targets of 25 mm in diameter were formed by uniaxial pressing at ~50 MPa. The LSC_{214}, LSC_{113}, and GDC targets were all sintered at 1350 °C in air for 20 hours.

Epitaxial thin film synthesis. (001)-oriented single crystals of 9.5% mol Y_2O_3-stabilized ZrO_2 (YSZ), one-side polished (surface roughness < 1 nm) and with the dimensions of 10 mm x 5 mm x 0.5 mm and 10 mm x 10 mm x 0.5 mm (Princeton Scientific, USA), were used as electrolyte and substrates for the pulsed laser deposition (PLD). Platinum ink (Pt, #6082, BASF, USA) counter electrodes were painted on the unpolished side of the YSZ and sintered in air at 800 °C for 1 hour. For the *in situ* high resolution XRD (HRXRD) with polarization, a reference electrode was included on the sample: a small corner of the polished side was roughened with a diamond file and Pt ink was applied and sintered in air at 800 °C for 1 hour, then masked to avoid contact with the LSC_{113} during deposition. The gadolinium-doped ceria (GDC) electrolytic protection layer (for avoiding reaction of YSZ with LSC at high temperature) and the LSC_{113} thin films were deposited by PLD using a KrF excimer laser with a wavelength of 248 nm, a pulse frequency of 10 Hz, and a pulse energy of ~ 50 mJ (measured close to the substrate surface) under an oxygen partial pressure, $p(O_2)$, of 50 mTorr with 500 pulses of GDC (~5 nm, estimated using scanning transmission electron microscopy) at a substrate temperature of ~450 °C, followed by 15,000 pulses of LSC_{113} (~85 nm, estimated using atomic force microscopy (AFM, Vecco, USA)) at ~550 °C. Immediately after completing the LSC_{113} deposition on one of the samples, a thin surface-decoration film of 150 pulses LSC_{214} was deposited (~0.8 nm, estimated from STEM micrograph previous reported[6]). The pure LSC_{214} film consisted of 10,000 laser pulses (~50 nm). After completing the depositions of each sample, the samples were cooled to room temperature over the course of ~ 1 hour within the PLD chamber at 50 mTorr. Reflection high-energy electron diffraction was utilized to provide *in situ* monitoring of the epitaxial growth of the oxide films.

Experimental details of in situ HRXRD. In situ HRXRD was conducted on a four-circle diffractometer (Panalytical) equipped with a controlled temperature stage (DHS 900, Anton Paar) in an oxygen partial pressure, $p(O_2)$, of 1 atm (flux ~2 sccm). Silver paste was used to adhere the 10 mm x 10 mm x 0.5 mm LSC_{113}/GDC/YSZ/Pt sample to the heating plate. Starting at 25 °C, a heating rate of ~10 °C/min was chosen, increasing the temperature to 550 °C where electrochemical potentials would be applied (applied potential steps: 0 V, −0.2 V, −0.4 V, −0.6 V, and −0.8 V). For each temperature and applied potential, the system was always held constant for 20 minutes to reach thermal and electrochemical equilibrium before XRD data was collected.

The current flowed from the LSC_{113} film (working electrode) to the sintered Pt electrode (counter) on the opposite side of the YSZ substrate, and the voltage was measured between the LSC_{113} (working electrode) and the small sintered Pt electrode (reference) on the same side of the LSC_{113} film. Electrical contacts were lightly silver pasted to all electrodes and connected to a power supply. Sample realignment was conducted after each temperature and applied potential step to optimize the intensity of the YSZ(004) and YSZ(202) peaks for all normal and off-normal scans, respectively. This procedure included the correction of slight de-adjustments due to the thermal or electrochemical expansion of the sample (height offset and angles). After alignment of the YSZ(004), a full range (θ–2θ = 10° - 120°) *theta*–*2theta* normal scan (0.04 °/step, 2 s/step) was collected first. Subsequently, *theta*–*2theta* normal scans of LSC(002) (0.01 °/step, 3 s/step) and YSZ(004) (0.005 °/step, 1 s/step) were collected. Lastly upon alignment of the YSZ(202) peak, the off-normal scans of LSC(101) (0.02 °/step, 5 s/step) and YSZ(202) (0.004 °/step, 1 s/step) peaks were obtained. Extracted peak positions are provided in **Table S6-1**. The collection time for the entire sequence was ~4 hours at each temperature and applied potential. As the thermocouple for this experiment was placed inside the heating stage, a small difference between measured and actual temperatures on the sample surface cannot be ruled out.

Unit cell volume calculation using in situ HRXRD data. The temperature dependence of the LSC unit cell volume is shown in **Figure 6-2**. LSC_{113} is pseudocubic, where the *c*-axis lattice parameter can be determined from the LSC (002) reflection. Assuming *a*- and *b*-axis lattice parameters are equivalent, they can be determined from the geometrical relationship between the *c* axis and the LSC (101) reflection. Once *c* and $a = b$ are determined, the unit cell volume can be obtained by $c \cdot a^2$.

Relaxed lattice parameter determination by in situ HRXRD. The Relaxed lattice parameter $\hat{a}$ is derived from the following equation (where $\hat{a}$ is the pseudocubic lattice parameter for the film in an unstrained state),[16,33] $\frac{(c-\hat{c})}{\hat{c}} = \frac{-2\nu}{1-\nu}\frac{(a-\hat{a})}{\hat{a}}$, assuming $\hat{a} = \hat{c}$ and $\nu = 0.25$.[16]

Experimental details of in situ APXPS. Ambient pressure and high temperature XPS data of the LSC_{113}, LSC_{214} and $LSC_{113/214}$ films were collected at the beamline 11.0.2 at Lawrence Berkeley

National Laboratory's (LBNL) Advanced Light Source (ALS). The thin film samples were separately investigated and placed directly onto a ceramic heater, which was held in place by spring-loaded Au-Pd coated tungsten tips.[8] No other pre-cleaning (e.g. sputtering the surface) was carried out. A thermocouple was placed directly onto the sample surface for accurate surface temperature measurements. A piece of Au foil was placed on top of part of the sample for attempted use as binding energy reference. Due to charging effects, all binding energies are instead referenced to the La 4d peak at 101.2 eV.[8] The spectra were collected in the following sequence (collection time about 2 h per sequence): low resolution survey (BE = –10 - 595 eV), high resolution O 1s and Au 4f at a photon energy of 690 eV, and C 1s, La 4d, Sr 3d, Co 3p and Au 4f, at a photon energy of 390 eV. These spectra were collected at $p(O_2) = 1 \cdot 10^{-3}$ atm with the following conditions:

LSC_{113} sample 1 (V = 0 V): T = 220 °C, T = 370 °C, T = 520 °C, T = 370 °C, and T = 220 °C.

LSC_{113} sample 2 (V = 0 V): T_1 = 520 °C, T_2 = 220 °C, T_3 = 520 °C, T_4 = 220 °C, T_5 = 520 °C, T_6 = 220 °C, T_7 = 520 °C, and T_8 = 220 °C (T_x, where x represents the sequential ordering of the temperature step).

LSC_{113} sample 3: V = 0 V at T = 220 °C, V = 0 V at T = 370 °C, V = 0 V at T = 520 °C, V = -0.1 V at T = 520 °C, V = -0.2 V at T = 520 °C, V = -0.4 V at T = 520 °C, V = -0.6 V at T = 520 °C, V = -0.8 V at T = 520 °C, and V = -1.2 V at T = 520 °C.

LSC_{214} sample: V = 0 V at T = 220 °C, V = 0 V at T = 370 °C, V = 0 V at T = 520 °C, V = -0.1 V at T = 520 °C, V = -0.2 V at T = 520 °C, V = -0.4 V at T = 520 °C, and V = -0.8 V at T = 520 °C.

$LSC_{113/214}$ sample: V = 0 V at T = 220 °C, V = 0 V at T = 370 °C, V = 0 V at T = 520 °C, V = -0.1 V at T = 520 °C, V = -0.2 V at T = 520 °C, V = -0.4 V at T = 520 °C, and V = -0.8 V at T = 520 °C.

The heating rate was about 10 °C/min and the temperature and applied potential was held constant for 20 min before beginning to collect data at each experimental condition.

In situ APXPS: calibration of the binding energy (BE) of the spectra. The BE for the spectra collected at room temperature were calibrated to the C 1s photoemission peak of adventitious hydrocarbons at 285.0 eV. A piece of gold foil was placed on part of the sample surface to assist

BE calibration (Au $4f_{7/2}$ = 84.0 eV) when carbon was removed from the surface at elevated temperatures. However the Au $4f_{7/2}$ did not work with applied potential due to differential charging. Therefore, we utilized the following procedure: the spectra without applied potential for each temperature were aligned to Au $4f_{7/2}$ (*BE* = 84.0 eV) and the binding energy position of the La 4d peak (the feature which showed the least change at various conditions) was determined (La 4d: *BE* ~101.2 eV). All subsequent spectra at the same temperature and oxygen partial pressure (with applied potential biases) were aligned to this La 4d peak. As the obtained binding energy values are in good agreement with reported literature values, this alignment procedure seems reasonable for these particular samples and similar to previously reported work.[16]

Curve fitting of in situ APXPS spectra. Analysis of the photoemission lines was done after subtracting a Shirley-type background using a symmetric combined Gaussian-Lorentzian line shape for fitting. Additional constraints for fitting the Sr 3d spectra include the Sr $3d_{5/2}$ and $3d_{3/2}$ doublet with an energy separation of 1.8 eV and a branching ratio of 1.5. The integrated areas (Casa XPS) for each component were then utilized for the analysis. The *BE*, full-width-half-maximum (FWHM), and integrated area for each component is provided in **Table S6-2**. Details about Co 3s peak intensity fitting: The intensity of the Co 3s peak, which overlaps with the La 4d region, is only a fraction of the overall intensity in this region and has been considered by taking the atomic subshell photoionization cross-sections[8] for Co 3s and La 4d into account ($Intensity_{Co\ 3s} \sim 0.1 \times Intensity_{La\ 4d}$).

In situ APXPS normalization procedure. The integrated intensity of the entire elemental region (or the components) is extracted from the fitting (value shown in **Table S6-2 and S6-3**). To demonstrate the normalization procedure, the raw intensity values divided by the photoionization cross-sections for the LSC thin films are plotted versus the change in condition on the top of **Figure S6-3, S6-5, and S6-9**. The photoionization cross-section normalized areas for each element are divided by the sum of the integrated photoionization cross-section normalized areas of all elements at the given condition, shown in the middle of **Figure S6-3, S6-5, and S6-9**. After obtaining this ratio at each condition, the final normalization step divides the previously obtained concentrations by its respective normalized value at T = 220 °C and $p(O_2) = 1x10^{-3}$ atm or T = 520 °C and $p(O_2) = 1 \cdot 10^{-3}$ atm (with 0 V applied bias). This procedure yields the

normalized intensity values shown on the bottom of **Figure S6-3, S6-5, and S6-9**. This processes is also used to generate the Sr and O component analyzed data presented in **Figure 6-1, 6-5, S6-6, and S6-10**.

In situ APXPS error analysis. The error bars (ΔI_N) of the normalized area intensities, I_N, shown in **Figure 6-1, 6-5, S6-3, S6-5, S6-6, S6-9 and S6-10** were estimated by assuming a standard deviation, *SD*, of 10% for the intensities of as-collected XPS data and fitted components. No error was considered for the XPS photoionization cross-sections, σ. This estimation results in an error of about 14 % for the changes of the individual component of Sr or O relative to the initial component (**Figure 6-1c to 6-1f, 6-5a to 6-5d, S6-6(top) and S6-10a-b**), and an error of about 25 % for the changes in the Sr concentration relative to the combined Sr and O in the lattice (**Figure 6-1g to 6-1h, 6-5e to 6-5f, S6-6(bottom), S6-10c**).

Table S6-1: Measured lattice parameters of the LSC film extracted from normal and off-normal HRXRD data as polarization is increased from 0 V to −0.8 V at 550 °C in a $p(O_2)$ of 1 atm.

Applied potential (V)	Constrained in-plane lattice parameter a (Å)	Constrained out-of-plane lattice parameter c (Å)	Relaxed film lattice parameter $\hat{a}$ (Å)	Measured unit cell volume V_m (Å^3)	Relaxed unit cell volume V_r (Å^3)	$\frac{\Delta V_m}{V_m}\times 100$ (%)	$\frac{\Delta V_r}{V_r}\times 100$ (%)
0	3.9157	3.8759	3.8998	58.825	59.309	0.00	0.00
−0.2	3.9159	3.8763	3.9001	58.840	59.323	0.03	0.02
−0.4	3.9249	3.8754	3.9051	58.948	59.553	0.21	0.41
−0.6	3.9514	3.8788	3.9224	59.448	60.345	1.06	1.75
−0.8	4.0845	3.8816	4.0033	61.541	64.160	4.62	8.18

Table S6-2a: LSC_{113} single temperature cycle detailed XPS peak positions and information on the fitting parameters.

Condition	Name	*BE* (eV)	*FWHM* (eV)	Area
LSC_{113}, *T* = 220 °C, increase	O 1s - Surface	531.3	1.7	814.2
	O 1s - Surface (M-O)	529.8	1.3	140.0
	O 1s - Lattice	528.6	1.3	788.6
	Sr 3d 3/2 - Surface	135.3	1.9	2057.7
	Sr 3d 5/2 - Surface	133.5	1.9	3086.5
	Sr 3d 3/2 - Lattice	133.8	1.5	696.0
	Sr 3d 5/2 - Lattice	132.0	1.5	1045.0
	La 4d	-	-	7362.6
	Co 3p	-	-	1579.3
LSC_{113}, *T* = 370 °C, increase	O 1s - Surface	531.5	1.7	1076.4
	O 1s - Surface (M-O)	529.8	1.0	113.4
	O 1s - Lattice	528.6	1.4	769.8
	Sr 3d 3/2 - Surface	135.2	1.8	957.4
	Sr 3d 5/2 - Surface	133.4	1.8	1436.1
	Sr 3d 3/2 - Lattice	134.2	1.6	1063.3
	Sr 3d 5/2 - Lattice	132.4	1.6	1596.5
	La 4d	-	-	6505.9
	Co 3p	-	-	1353.0
LSC_{113}, *T* = 520 °C	O 1s - Surface	531.6	1.7	918.6
	O 1s - Surface (M-O)	529.8	1.5	248.7
	O 1s - Lattice	528.6	1.4	765.1
	Sr 3d 3/2 - Surface	135.6	2.0	1496.8
	Sr 3d 5/2 - Surface	133.8	2.0	2245.2
	Sr 3d 3/2 - Lattice	134.4	1.6	1688.7
	Sr 3d 5/2 - Lattice	132.6	1.6	2535.7
	La 4d	-	-	6910.6
	Co 3p	-	-	1384.1
LSC_{113}, *T* = 370 °C, decrease	O 1s - Surface	531.5	1.6	518.8
	O 1s - Surface (M-O)	529.8	1.5	286.0
	O 1s - Lattice	528.6	1.3	658.6
	Sr 3d 3/2 - Surface	135.6	2.0	1140.9
	Sr 3d 5/2 - Surface	133.8	2.0	1711.3
	Sr 3d 3/2 - Lattice	134.5	1.6	1524.4
	Sr 3d 5/2 - Lattice	132.7	1.6	2288.9
	La 4d	-	-	5461.0
	Co 3p	-	-	1179.7
LSC_{113}, *T* = 220 °C, decrease	O 1s - Surface	531.4	1.7	679.9
	O 1s - Surface (M-O)	529.8	1.1	168.3
	O 1s - Lattice	528.7	1.3	668.5
	Sr 3d 3/2 - Surface	135.6	1.9	1026.1
	Sr 3d 5/2 - Surface	133.8	1.9	1539.1
	Sr 3d 3/2 - Lattice	134.5	1.5	1525.3
	Sr 3d 5/2 - Lattice	132.7	1.5	2290.2
	La 4d	-	-	5616.1
	Co 3p	-	-	1222.5

Table S6-2b: LSC_{113} multiple temperature cycled detailed XPS peak positions and information on the fitting parameters.

Condition	Name	*BE* (eV)	*FWHM* (eV)	Area
LSC_{113}, *T* = 520 °C	O 1s - Surface	531.6	1.9	1767.7
	O 1s - Surface (M-O)	529.8	1.0	141.0
	O 1s - Lattice	528.6	1.4	1018.8
	Sr 3d 3/2 - Surface	135.5	1.8	1272.5
	Sr 3d 5/2 - Surface	133.7	1.8	1908.7
	Sr 3d 3/2 - Lattice	134.5	1.6	2471.2
	Sr 3d 5/2 - Lattice	132.7	1.6	3710.5
	La 4d	-	-	8780.2
	Co 3p	-	-	2092.6
LSC_{113}, *T* = 220 °C, 1st – 2nd cycle	O 1s - Surface	531.5	1.7	1253.7
	O 1s - Surface (M-O)	529.8	1.0	122.1
	O 1s - Lattice	528.7	1.2	707.5
	Sr 3d 3/2 - Surface	135.5	1.8	951.9
	Sr 3d 5/2 - Surface	133.7	1.8	1427.9
	Sr 3d 3/2 - Lattice	134.5	1.5	2577.0
	Sr 3d 5/2 - Lattice	132.7	1.5	3869.4
	La 4d	-	-	6218.2
	Co 3p	-	-	1239.8
LSC_{113}, *T* = 520 °C, 2nd cycle	O 1s - Surface	531.6	1.8	1722.1
	O 1s - Surface (M-O)	529.8	1.1	176.6
	O 1s - Lattice	528.7	1.4	1179.8
	Sr 3d 3/2 - Surface	135.5	1.8	1482.8
	Sr 3d 5/2 - Surface	133.7	1.8	2224.3
	Sr 3d 3/2 - Lattice	134.5	1.6	3218.4
	Sr 3d 5/2 - Lattice	132.7	1.6	4832.4
	La 4d	-	-	9256.8
	Co 3p	-	-	1976.9
LSC_{113}, *T* = 220 °C, 2nd – 3rd cycle	O 1s - Surface	531.5	1.7	1329.5
	O 1s - Surface (M-O)	529.8	1.0	132.3
	O 1s - Lattice	528.7	1.3	869.9
	Sr 3d 3/2 - Surface	135.5	1.8	833.7
	Sr 3d 5/2 - Surface	133.7	1.8	1250.5
	Sr 3d 3/2 - Lattice	134.5	1.5	2809.4
	Sr 3d 5/2 - Lattice	132.7	1.5	4218.3
	La 4d	-	-	6210.8
	Co 3p	-	-	1402.4
LSC_{113}, *T* = 520 °C, 3rd cycle	O 1s - Surface	531.7	1.7	1416.8
	O 1s - Surface (M-O)	529.8	1.3	278.4
	O 1s - Lattice	528.7	1.3	1047.4
	Sr 3d 3/2 - Surface	135.4	1.8	1701.5
	Sr 3d 5/2 - Surface	133.6	1.8	2552.2
	Sr 3d 3/2 - Lattice	134.5	1.6	3122.1
	Sr 3d 5/2 - Lattice	132.7	1.6	4687.8
	La 4d	-	-	9789.0
	Co 3p	-	-	2087.4
LSC_{113}, *T* = 220 °C, 3rd – 4th cycle	O 1s - Surface	531.5	1.6	1235.3
	O 1s - Surface (M-O)	529.8	1.0	140.9
	O 1s - Lattice	528.7	1.3	790.5
	Sr 3d 3/2 - Surface	135.6	1.8	629.8
	Sr 3d 5/2 - Surface	133.8	1.8	944.7
	Sr 3d 3/2 - Lattice	134.5	1.5	2847.0
	Sr 3d 5/2 - Lattice	132.7	1.5	4274.8
	La 4d	-	-	5958.0
	Co 3p	-	-	1284.8
LSC_{113}, *T* = 520 °C, 4th cycle	O 1s - Surface	531.7	1.8	1531.9
	O 1s - Surface (M-O)	529.8	1.0	220.3
	O 1s - Lattice	528.7	1.4	1221.5
	Sr 3d 3/2 - Surface	135.4	1.9	1910.4
	Sr 3d 5/2 - Surface	133.6	1.9	2865.7
	Sr 3d 3/2 - Lattice	134.5	1.6	3212.4
	Sr 3d 5/2 - Lattice	132.7	1.6	4823.4
	La 4d	-	-	9336.0
	Co 3p	-	-	2029.0
LSC_{113}, *T* = 220 °C, 4th cycle	O 1s - Surface	531.5	1.6	965.1
	O 1s - Surface (M-O)	529.8	1.2	242.2
	O 1s - Lattice	528.7	1.2	976.0
	Sr 3d 3/2 - Surface	135.5	1.8	799.1
	Sr 3d 5/2 - Surface	133.7	1.8	1198.6
	Sr 3d 3/2 - Lattice	134.5	1.5	3060.4
	Sr 3d 5/2 - Lattice	132.7	1.5	4595.2
	La 4d	-	-	6414.6
	Co 3p	-	-	1249.5

Table S6-2c: LSC_{113} increase in temperature and under applied potential detailed XPS peak positions and information on the fitting parameters.

Condition	Name	*BE* (eV)	*FWHM* (eV)	Area
LSC_{113}, *T* = 220 °C, *V* = 0 V	O 1s - Surface	531.3	1.7	665.1
	O 1s - Surface (M-O)	529.8	1.5	212.7
	O 1s - Lattice	528.6	1.2	952.5
	Sr 3d 3/2 - Surface	135.3	1.9	1441.6
	Sr 3d 5/2 - Surface	133.5	1.9	2162.5
	Sr 3d 3/2 - Lattice	134.0	1.6	1147.4
	Sr 3d 5/2 - Lattice	132.2	1.6	1722.8
	La 4d	-	-	7629.6
	Co 3p	-	-	1518.1
LSC_{113}, *T* = 370 °C, *V* = 0 V	O 1s - Surface	531.6	1.8	766.5
	O 1s - Surface (M-O)	529.8	1.2	164.7
	O 1s - Lattice	528.7	1.3	860.5
	Sr 3d 3/2 - Surface	135.2	1.7	1310.4
	Sr 3d 5/2 - Surface	133.4	1.7	1965.5
	Sr 3d 3/2 - Lattice	134.2	1.6	1795.1
	Sr 3d 5/2 - Lattice	132.4	1.6	2695.4
	La 4d	-	-	9511.9
	Co 3p	-	-	1906.9
LSC_{113}, *T* = 520 °C, *V* = 0 V	O 1s - Surface	531.5	1.8	1845.6
	O 1s - Surface (M-O)	529.8	1.1	213.3
	O 1s - Lattice	528.6	1.4	1354.0
	Sr 3d 3/2 - Surface	135.6	1.9	2586.1
	Sr 3d 5/2 - Surface	133.8	1.9	3879.1
	Sr 3d 3/2 - Lattice	134.5	1.6	2847.5
	Sr 3d 5/2 - Lattice	132.7	1.6	4275.5
	La 4d	-	-	9944.1
	Co 3p	-	-	1764.2
LSC_{113}, *T* = 520 °C, *V* = −0.1 V	O 1s - Surface	531.5	1.8	721.6
	O 1s - Surface (M-O)	529.8	1.5	641.9
	O 1s - Lattice	528.7	1.4	1404.0
	Sr 3d 3/2 - Surface	135.4	1.9	3310.8
	Sr 3d 5/2 - Surface	133.6	1.9	4966.2
	Sr 3d 3/2 - Lattice	134.2	1.5	2344.6
	Sr 3d 5/2 - Lattice	132.4	1.5	3520.5
	La 4d	-	-	8017.1
	Co 3p	-	-	1515.7
LSC_{113}, *T* = 520 °C, *V* = −0.2 V	O 1s - Surface	531.4	2.0	632.6
	O 1s - Surface (M-O)	529.8	1.3	572.3
	O 1s - Lattice	528.8	1.4	1415.0
	Sr 3d 3/2 - Surface	135.4	2.0	3095.7
	Sr 3d 5/2 - Surface	133.6	2.0	4643.5
	Sr 3d 3/2 - Lattice	134.2	1.5	2440.8
	Sr 3d 5/2 - Lattice	132.4	1.5	3664.9
	La 4d	-	-	8994.7
	Co 3p	-	-	1661.8
LSC_{113}, *T* = 520 °C, *V* = −0.4 V	O 1s - Surface	531.5	1.9	475.3
	O 1s - Surface (M-O)	529.8	1.5	738.3
	O 1s - Lattice	528.8	1.4	1523.5
	Sr 3d 3/2 - Surface	135.4	1.9	2551.0
	Sr 3d 5/2 - Surface	133.6	1.9	3826.5
	Sr 3d 3/2 - Lattice	134.2	1.5	2610.7
	Sr 3d 5/2 - Lattice	132.4	1.5	3919.9
	La 4d	-	-	8393.7
	Co 3p	-	-	1495.3
LSC_{113}, *T* = 520 °C, *V* = −0.6 V	O 1s - Surface	531.5	1.6	269.8
	O 1s - Surface (M-O)	529.8	1.5	777.7
	O 1s - Lattice	528.8	1.4	1488.0
	Sr 3d 3/2 - Surface	135.4	1.8	2321.6
	Sr 3d 5/2 - Surface	133.6	1.8	3482.4
	Sr 3d 3/2 - Lattice	134.2	1.5	2705.1
	Sr 3d 5/2 - Lattice	132.4	1.5	4061.8
	La 4d	-	-	8216.2
	Co 3p	-	-	1416.0
LSC_{113}, *T* = 520 °C, *V* = −0.8 V	O 1s - Surface	531.4	1.9	276.1
	O 1s - Surface (M-O)	529.8	1.5	797.2
	O 1s - Lattice	528.8	1.4	1482.8
	Sr 3d 3/2 - Surface	135.4	1.8	2391.3
	Sr 3d 5/2 - Surface	133.6	1.8	3587.0
	Sr 3d 3/2 - Lattice	134.2	1.5	2848.6
	Sr 3d 5/2 - Lattice	132.4	1.5	4277.1
	La 4d	-	-	8495.4
	Co 3p	-	-	1468.3
LSC_{113}, *T* = 520 °C, *V* = −1.2 V	O 1s - Surface	531.4	1.8	232.6
	O 1s - Surface (M-O)	529.8	1.5	909.3
	O 1s - Lattice	528.8	1.4	1579.0

	Sr 3d 3/2 - Surface	135.4	1.8	2632.1
	Sr 3d 5/2 - Surface	133.6	1.8	3948.1
	Sr 3d 3/2 - Lattice	134.2	1.5	3107.6
	Sr 3d 5/2 - Lattice	132.4	1.5	4666.0
	La 4d	-	-	9512.0
	Co 3p	-	-	1605.2

Table S6-2d: LSC_{214} increase in temperature and under applied potential detailed XPS peak positions and information on the fitting parameters.

Condition	Name	*BE* (eV)	*FWHM* (eV)	Area
LSC_{214}, *T* = 220 °C, *V* = 0 V	O 1s - Surface	531.3	1.6	1070.3
	O 1s - Surface (M-O)	530.0	1.5	115.7
	O 1s - Lattice	528.6	1.2	262.6
	Sr 3d 3/2 - Surface	135.3	1.6	3378.5
	Sr 3d 5/2 - Surface	133.5	1.6	5067.7
	Sr 3d 3/2 - Lattice	133.8	1.6	801.1
	Sr 3d 5/2 - Lattice	132.0	1.6	1202.8
	La 4d	-	-	3460.0
	Co 3p	-	-	612.8
LSC_{214}, *T* = 370 °C, *V* = 0 V	O 1s - Surface	531.9	1.7	1021.4
	O 1s - Surface (M-O)	529.8	1.5	125.3
	O 1s - Lattice	528.7	1.4	661.8
	Sr 3d 3/2 - Surface	135.7	2.0	3746.9
	Sr 3d 5/2 - Surface	133.9	2.0	5620.4
	Sr 3d 3/2 - Lattice	134.2	1.6	1728.0
	Sr 3d 5/2 - Lattice	132.4	1.6	2594.6
	La 4d	-	-	4412.2
	Co 3p	-	-	834.8
LSC_{214}, *T* = 520 °C, *V* = 0 V	O 1s - Surface	532.0	1.8	1251.4
	O 1s - Surface (M-O)	529.8	1.5	202.7
	O 1s - Lattice	528.8	1.4	885.2
	Sr 3d 3/2 - Surface	135.8	2.0	5138.0
	Sr 3d 5/2 - Surface	134.0	2.0	7707.0
	Sr 3d 3/2 - Lattice	134.3	1.6	2838.1
	Sr 3d 5/2 - Lattice	132.5	1.6	4261.4
	La 4d	-	-	6296.0
	Co 3p	-	-	1199.6
LSC_{214}, *T* = 520 °C, *V* = −0.1 V	O 1s - Surface	532.0	1.8	887.1
	O 1s - Surface (M-O)	529.8	1.5	268.0
	O 1s - Lattice	528.7	1.4	796.6
	Sr 3d 3/2 - Surface	135.6	2.0	4772.8
	Sr 3d 5/2 - Surface	133.8	2.0	7159.2
	Sr 3d 3/2 - Lattice	134.4	1.6	2753.0
	Sr 3d 5/2 - Lattice	132.6	1.6	4133.6
	La 4d	-	-	5610.3
	Co 3p	-	-	1131.0
LSC_{214}, *T* = 520 °C, *V* = −0.2 V	O 1s - Surface	532.0	1.9	735.8
	O 1s - Surface (M-O)	529.8	1.5	327.5
	O 1s - Lattice	528.7	1.4	962.2
	Sr 3d 3/2 - Surface	135.5	2.0	5151.9
	Sr 3d 5/2 - Surface	133.7	2.0	7727.8
	Sr 3d 3/2 - Lattice	134.4	1.6	3130.3
	Sr 3d 5/2 - Lattice	132.6	1.6	4700.1
	La 4d	-	-	5664.1
	Co 3p	-	-	1140.9
LSC_{214}, *T* = 520 °C, *V* = −0.4 V	O 1s - Surface	531.9	1.9	829.2
	O 1s - Surface (M-O)	529.8	1.5	309.8
	O 1s - Lattice	528.7	1.4	942.5
	Sr 3d 3/2 - Surface	135.8	2.0	5672.7
	Sr 3d 5/2 - Surface	134.0	2.0	8509.1
	Sr 3d 3/2 - Lattice	134.4	1.6	3181.6
	Sr 3d 5/2 - Lattice	132.6	1.6	4777.2
	La 4d	-	-	6470.9
	Co 3p	-	-	1126.4
LSC_{214}, *T* = 520 °C, *V* = −0.8 V	O 1s - Surface	532.0	1.8	1460.8
	O 1s - Surface (M-O)	529.8	1.5	396.2
	O 1s - Lattice	528.8	1.4	1064.4
	Sr 3d 3/2 - Surface	135.8	2.0	5487.8
	Sr 3d 5/2 - Surface	134.0	2.0	8231.7
	Sr 3d 3/2 - Lattice	134.4	1.6	2804.5
	Sr 3d 5/2 - Lattice	132.6	1.6	4210.9
	La 4d	-	-	5883.9
	Co 3p	-	-	1125.8

Table S6-2e: $LSC_{113/214}$ increase in temperature and under applied potential detailed XPS peak positions and information on the fitting parameters.

Condition	Name	*BE* (eV)	*FWHM* (eV)	Area
$LSC_{113/214}$, T = 220 °C, V = 0 V	O 1s - Surface	531.2	1.6	774.8
	O 1s - Surface (M-O)	529.8	1.5	214.4
	O 1s - Lattice	528.4	1.2	789.7
	Sr 3d 3/2 - Surface	135.2	2.0	1023.7
	Sr 3d 5/2 - Surface	133.4	2.0	1535.6
	Sr 3d 3/2 - Lattice	133.7	1.3	817.1
	Sr 3d 5/2 - Lattice	131.9	1.3	1226.9
	La 4d	-	-	6130.9
	Co 3p	-	-	977.2
$LSC_{113/214}$, T = 370 °C, V = 0 V	O 1s - Surface	531.4	1.7	1607.8
	O 1s - Surface (M-O)	529.8	1.0	182.3
	O 1s - Lattice	528.6	1.3	1313.0
	Sr 3d 3/2 - Surface	135.5	2.0	2648.4
	Sr 3d 5/2 - Surface	133.7	2.0	3972.6
	Sr 3d 3/2 - Lattice	133.7	1.3	873.0
	Sr 3d 5/2 - Lattice	131.9	1.3	1310.8
	La 4d	-	-	10025.7
	Co 3p	-	-	1742.9
$LSC_{113/214}$, T = 520 °C, V = 0 V	O 1s - Surface	531.6	1.8	939.4
	O 1s - Surface (M-O)	529.8	1.4	380.6
	O 1s - Lattice	528.7	1.4	1202.4
	Sr 3d 3/2 - Surface	135.5	2.0	3031.5
	Sr 3d 5/2 - Surface	133.7	2.0	4547.3
	Sr 3d 3/2 - Lattice	134.4	1.6	1665.0
	Sr 3d 5/2 - Lattice	132.6	1.6	2500.0
	La 4d	-	-	7061.7
	Co 3p	-	-	986.6
$LSC_{113/214}$, T = 520 °C, V = −0.1 V	O 1s - Surface	531.6	1.9	661.8
	O 1s - Surface (M-O)	529.8	1.5	801.2
	O 1s - Lattice	528.8	1.4	1877.4
	Sr 3d 3/2 - Surface	135.2	1.9	4243.5
	Sr 3d 5/2 - Surface	133.4	1.9	6365.3
	Sr 3d 3/2 - Lattice	134.3	1.5	2539.5
	Sr 3d 5/2 - Lattice	132.5	1.5	3813.1
	La 4d	-	-	11699.3
	Co 3p	-	-	1989.6
$LSC_{113/214}$, T = 520 °C, V = −0.2 V	O 1s - Surface	531.6	2.0	519.4
	O 1s - Surface (M-O)	529.8	1.5	870.3
	O 1s - Lattice	528.8	1.4	1824.0
	Sr 3d 3/2 - Surface	135.3	1.8	3681.9
	Sr 3d 5/2 - Surface	133.5	1.8	5522.8
	Sr 3d 3/2 - Lattice	134.4	1.5	3220.7
	Sr 3d 5/2 - Lattice	132.6	1.5	4836.0
	La 4d	-	-	11650.0
	Co 3p	-	-	1902.6
$LSC_{113/214}$, T = 520 °C, V = −0.4 V	O 1s - Surface	531.5	2.0	373.8
	O 1s - Surface (M-O)	529.8	1.5	928.3
	O 1s - Lattice	528.8	1.5	1793.6
	Sr 3d 3/2 - Surface	135.3	1.8	3702.6
	Sr 3d 5/2 - Surface	133.5	1.8	5554.0
	Sr 3d 3/2 - Lattice	134.4	1.5	3116.9
	Sr 3d 5/2 - Lattice	132.6	1.5	4680.0
	La 4d	-	-	11503.4
	Co 3p	-	-	1746.6
$LSC_{113/214}$, T = 520 °C, V = −0.8 V	O 1s - Surface	531.4	2.0	371.9
	O 1s - Surface (M-O)	529.8	1.5	948.4
	O 1s - Lattice	528.8	1.5	1755.1
	Sr 3d 3/2 - Surface	135.2	1.8	4093.1
	Sr 3d 5/2 - Surface	133.4	1.8	6139.6
	Sr 3d 3/2 - Lattice	134.3	1.5	2759.2
	Sr 3d 5/2 - Lattice	132.5	1.5	4143.0
	La 4d	-	-	12035.1
	Co 3p	-	-	1776.5

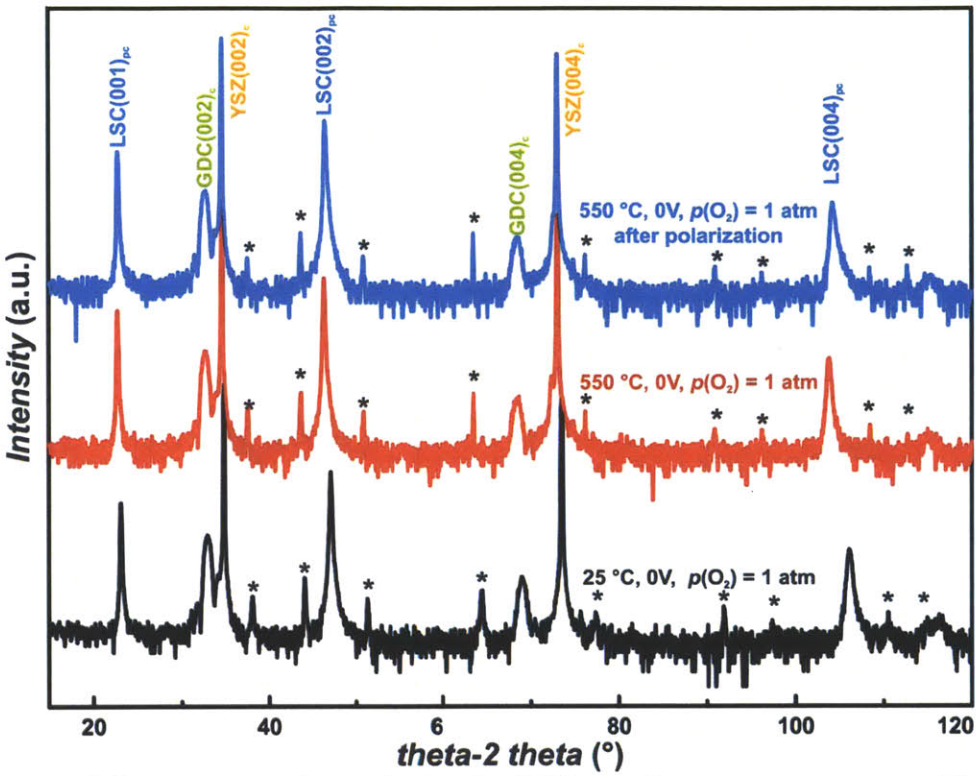

Figure S6-1. A full-range normal scan in the $\theta - 2\theta$ Bragg-Brentano geometry at 25 °C (black), 550 °C before (red) and after (blue) polarization showing no phase changes upon heating at $p(O_2)$ of 1 atm. The starred (*) peaks originated from the heater, and the peaks of the LSC_{113} film, GDC buffer layer and YSZ substrate are indexed to the pc ($a_{pc} \sim 3.8$ Å), cubic ($a_c \sim 5.4$ Å) and cubic ($a_c \sim 5.1$ Å) structure, respectively.

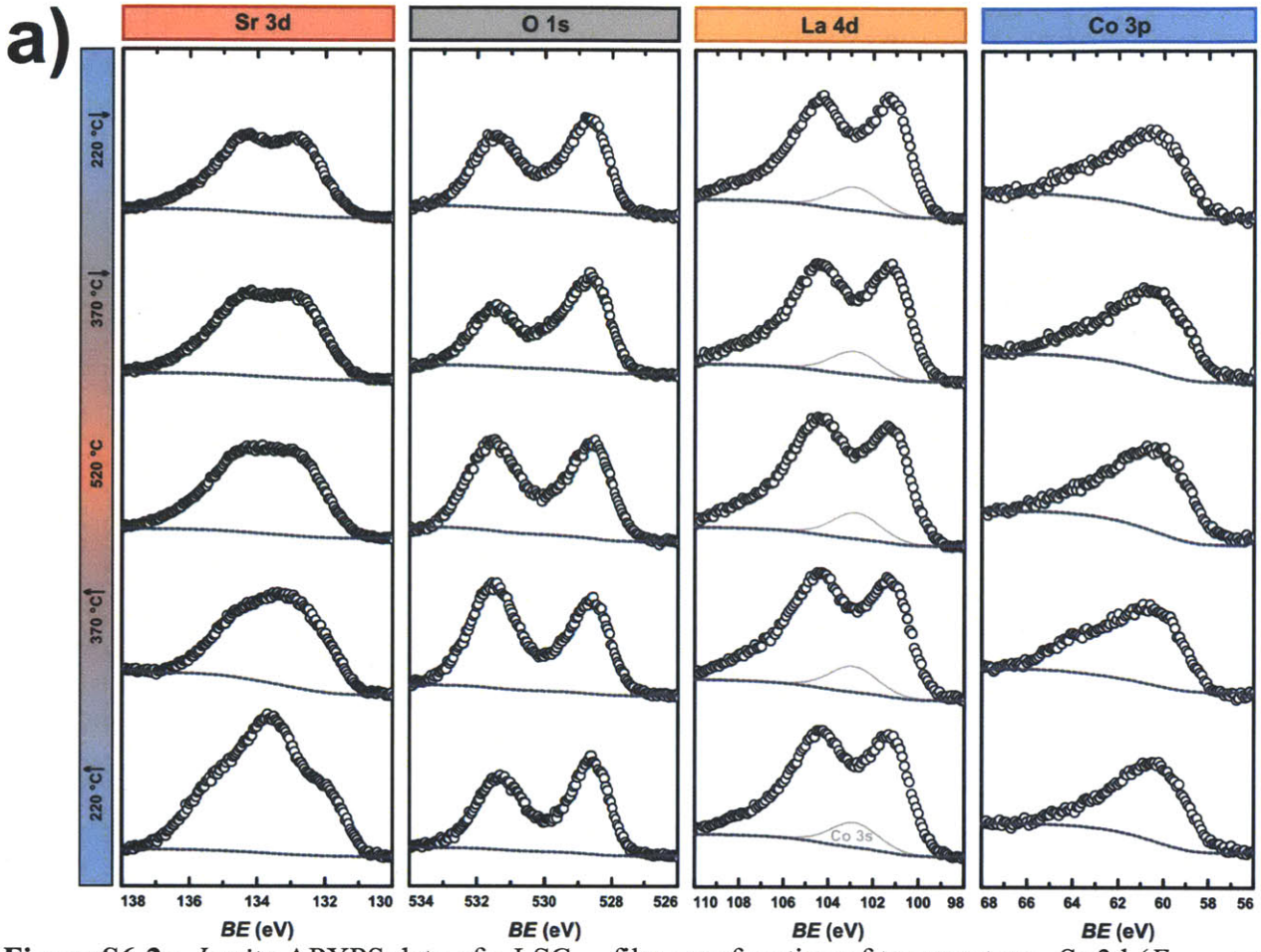

Figure S6-2a. *In situ* APXPS data of a LSC_{113} film as a function of temperature. Sr 3d (E_{photon} = 390 eV), O 1s (E_{photon} = 690 eV), La 4d (E_{photon} = 390 eV) and Co 3p (E_{photon} = 390 eV) spectra at 220 °C, 370 °C, 520 °C then decreased to 370 °C and 220 °C at a $p(O_2)$ of $1 \cdot 10^{-3}$ atm. White circles are for the measured data, blue lines indicate the sum of fits, and grey dotted lines correspond to the background.

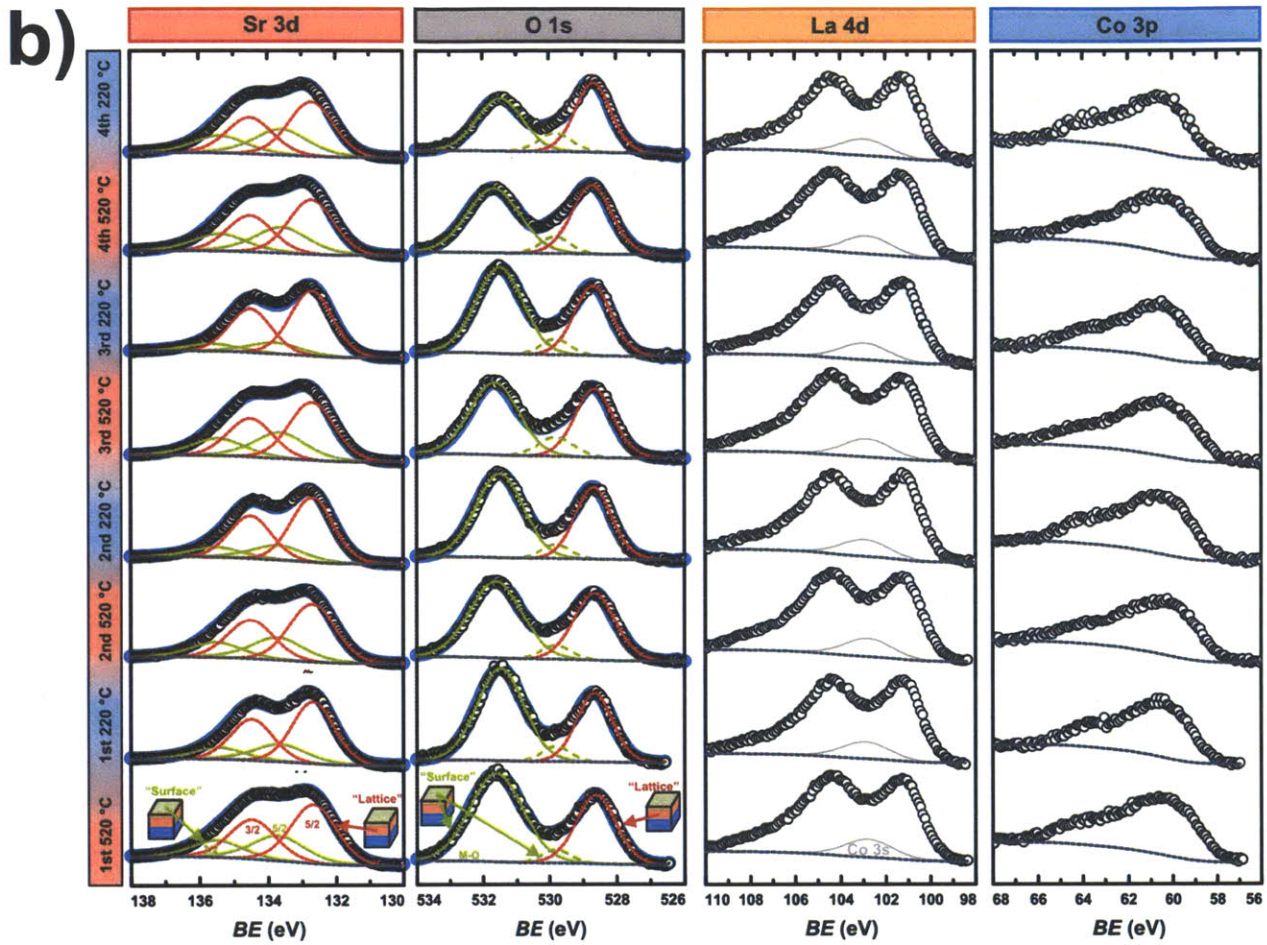

Figure S6-2b. *In situ* APXPS data of another piece of LSC_{113} film as a function of temperature. Sr 3d (E_{photon} = 390 eV), O 1s (E_{photon} = 690 eV), La 4d (E_{photon} = 390 eV) and Co 3p (E_{photon} = 390 eV) spectra at 520 °C decreased to 220 °C and subsequent temperature cycles at a $p(O_2)$ of $1 \cdot 10^{-3}$ atm. The "lattice" component of the perovskite structure in the near-surface region is shown in red while the "surface" component for the secondary phases (including both surface components) is shown in green. White circles are for the measured data, blue lines indicate the sum of fits, and grey dotted lines correspond to the background.

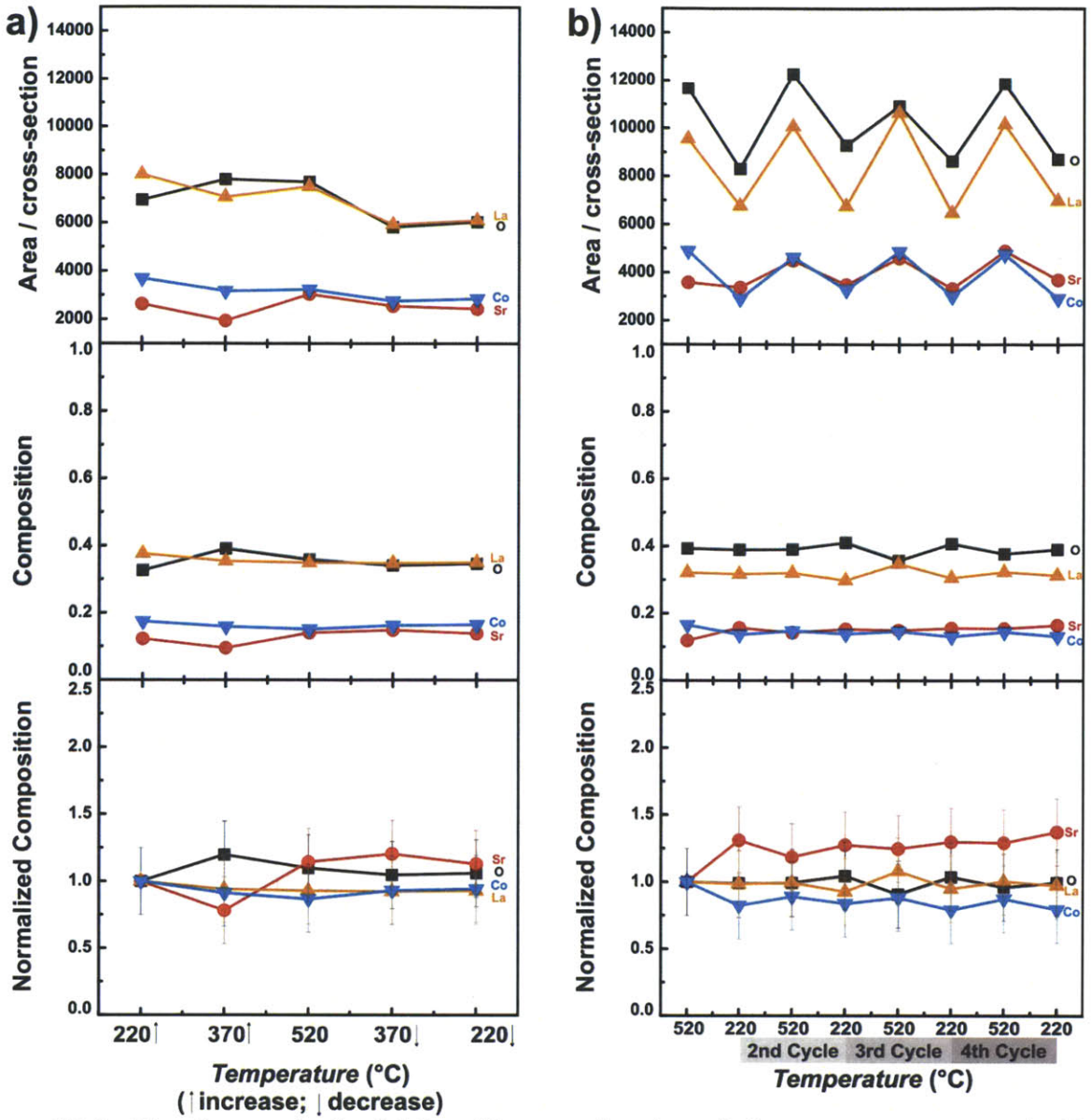

Figure S6-3. The changes in the LSC_{113} film as a function of **a)** one temperature cycle (from spectra shown in **Figure S2a**), and **b)** another LSC_{113} film as a function of subsequent temperature cycling (from spectra shown in **Figure S2b**). (top) Is the raw area intensities for La 4d, Sr 3d, Co 3p, and O 1s divided by their respective photo-ionization cross sections; (middle) the cross-section normalized intensity values are divided by the sum of all elemental values at each temperature, creating an effective concentration; (bottom) the concentration values for each element are normalized to the first condition, at 220 °C and $p(O_2)$ $1 \cdot 10^{-3}$ atm.

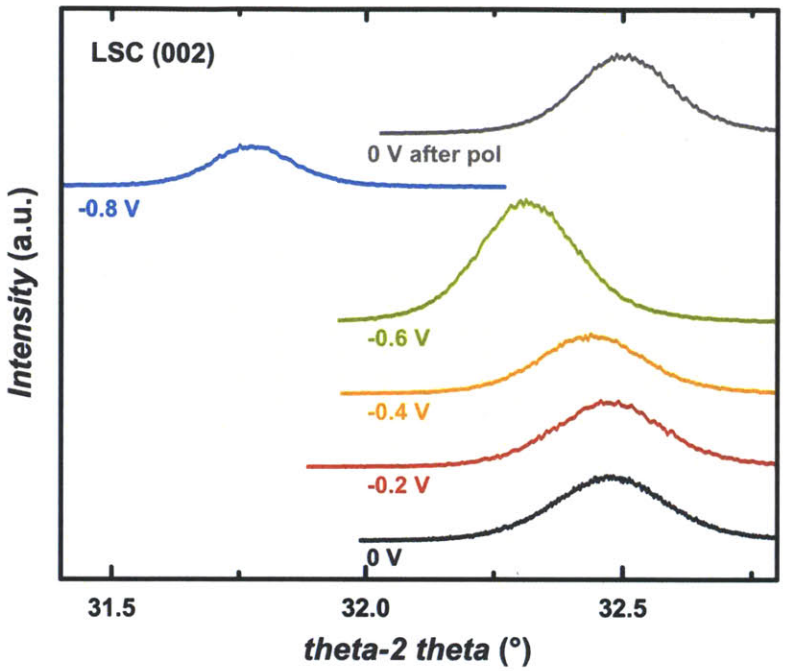

Figure S6-4. *In situ* HRXRD data of the off-normal LSC(101)pc as a function of applied potential at 550 °C in a $p(O_2)$ of 1 atm. Here, we observe the peak shifts towards lower angle in the *theta – 2theta* with increasing applied potentials up to −0.8 V and recovers to near similar position once the potential is removed.

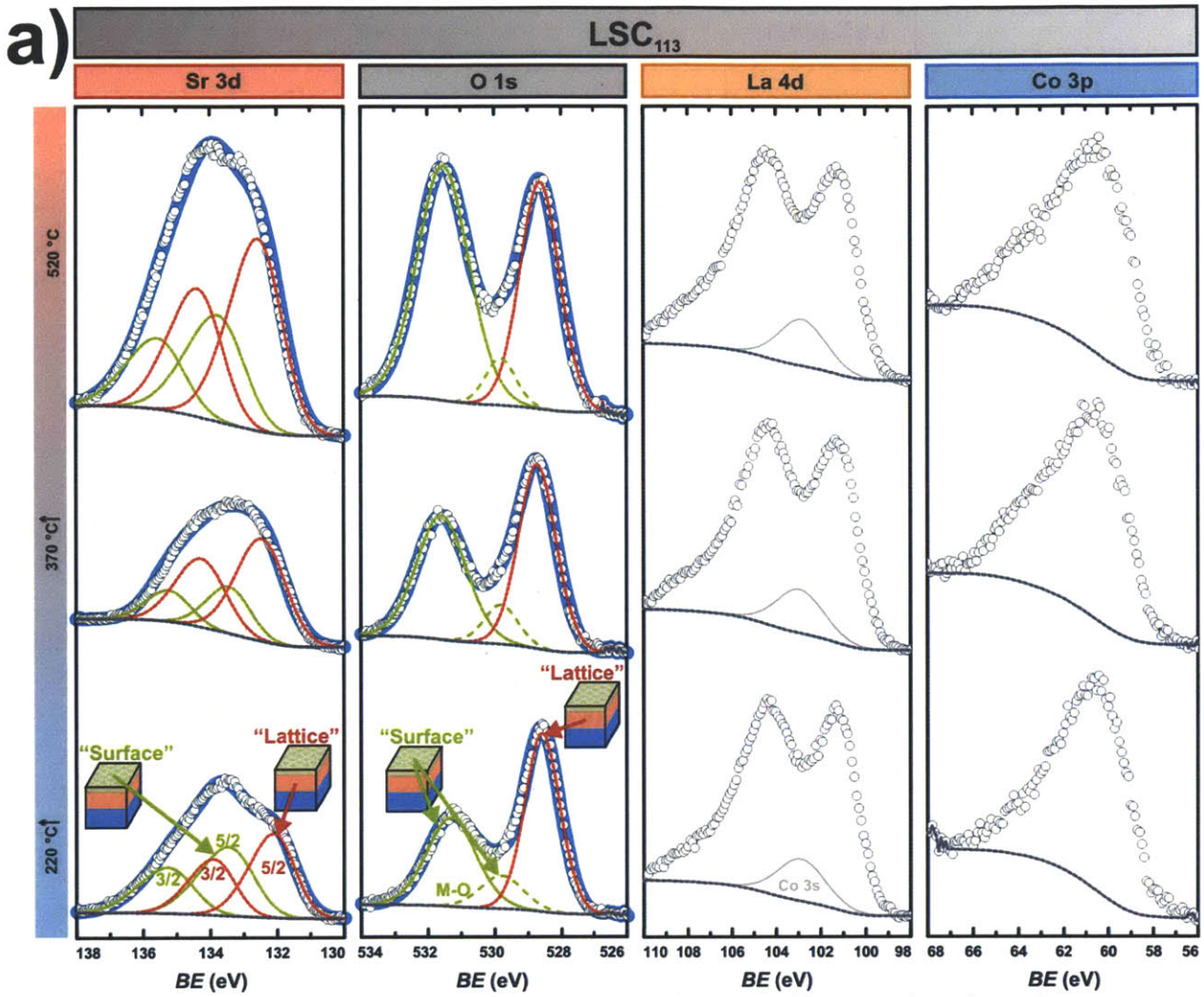

Figure S6-5a. *In situ* APXPS data of another piece of LSC_{113} film as a function of temperature before electrochemical polarization (**Figure S6-8a**). Sr 3d (E_{photon} = 390 eV), O 1s (E_{photon} = 690 eV), La 4d (E_{photon} = 390 eV) and Co 3p (E_{photon} = 390 eV) spectra at 220 °C, 370 °C, and 520 °C at a $p(O_2)$ of $1 \cdot 10^{-3}$ atm. The "lattice" component of the perovskite structure in the near-surface region is shown in red while the "surface" component for the secondary phases (including both surface components) is shown in green. White circles are for the measured data, blue lines indicate the sum of fits, and grey dotted lines correspond to the background.

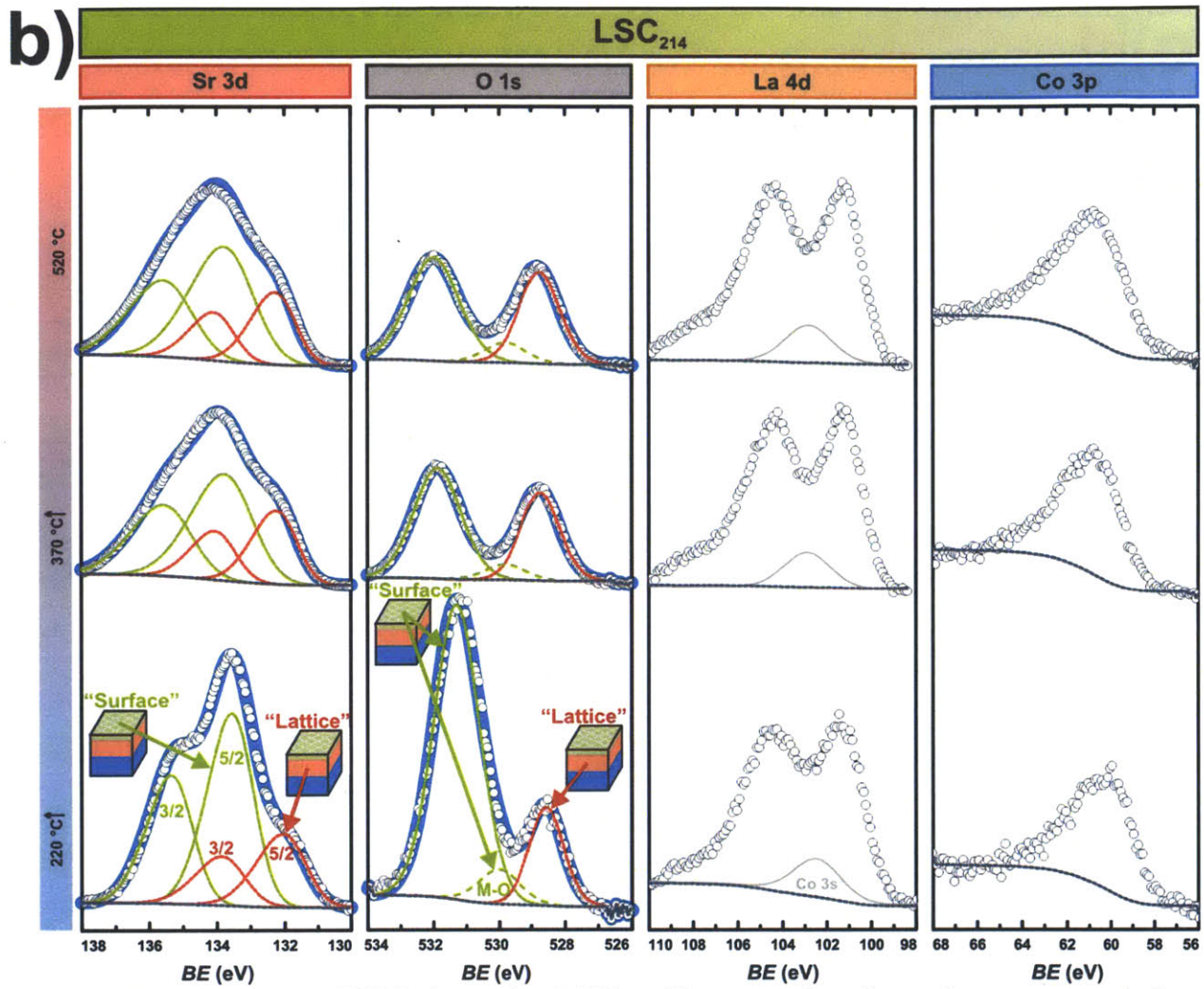

Figure S6-5b. *In situ* APXPS data of a LSC_{214} film as a function of temperature before electrochemical polarization (**Figure S6-8b**). Sr 3d (E_{photon} = 390 eV), O 1s (E_{photon} = 690 eV), La 4d (E_{photon} = 390 eV) and Co 3p (E_{photon} = 390 eV) spectra at 220 °C, 370 °C, and 520 °C at a $p(O_2)$ of $1 \cdot 10^{-3}$ atm. The "lattice" component of the perovskite structure in the near-surface region is shown in red while the "surface" component for the secondary phases (including both surface components) is shown in green. White circles are for the measured data, blue lines indicate the sum of fits, and grey dotted lines correspond to the background.

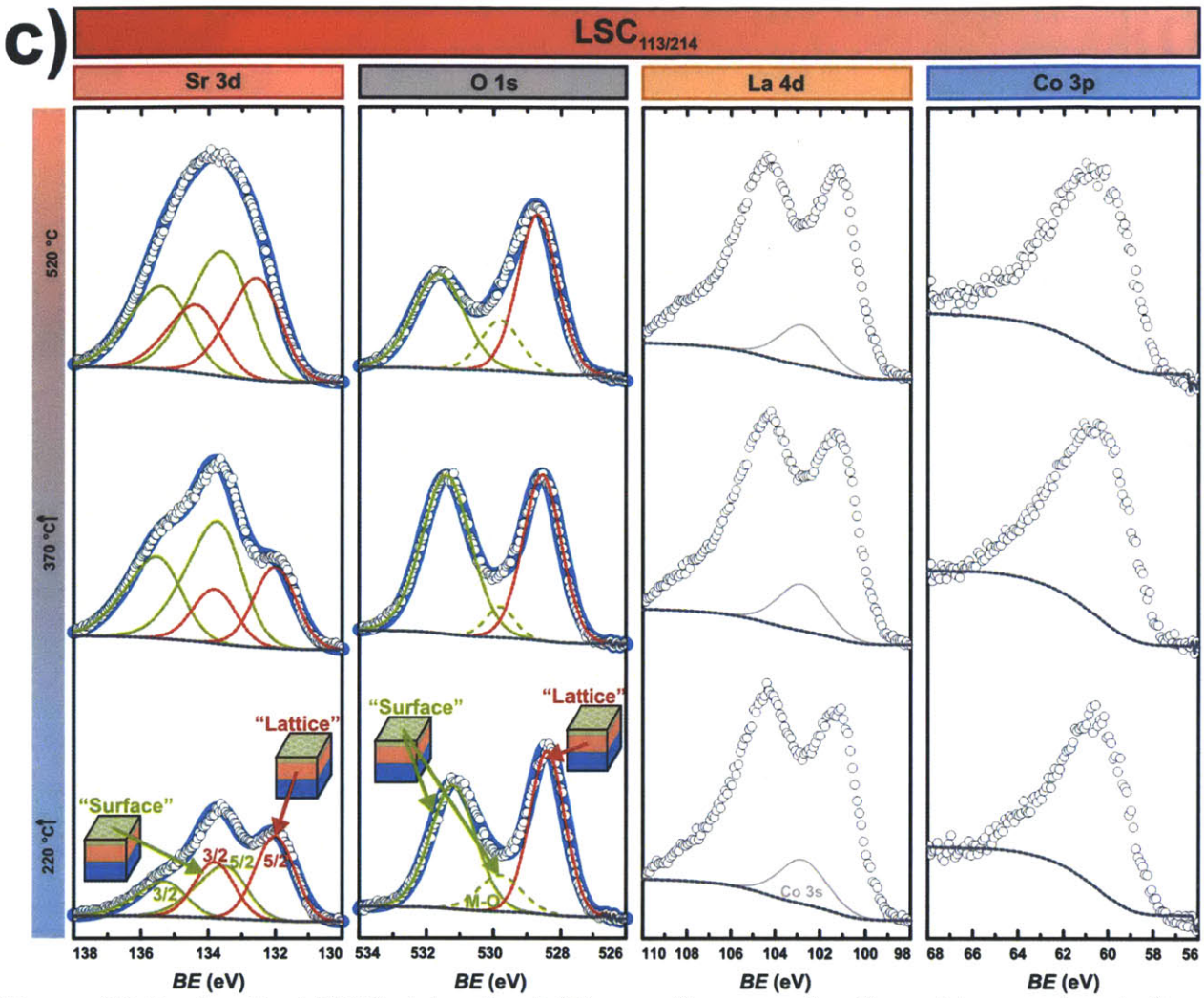

Figure S6-5c. *In situ* APXPS data of a $LSC_{113/214}$ film as a function of temperature before electrochemical polarization (**Figure S6-8c**). Sr 3d (E_{photon} = 390 eV), O 1s (E_{photon} = 690 eV), La 4d (E_{photon} = 390 eV) and Co 3p (E_{photon} = 390 eV) spectra at 220 °C, 370 °C, and 520 °C at a $p(O_2)$ of $1 \cdot 10^{-3}$ atm. The "lattice" component of the perovskite structure in the near-surface region is shown in red while the "surface" component for the secondary phases (including both surface components) is shown in green. White circles are for the measured data, blue lines indicate the sum of fits, and grey dotted lines correspond to the background.

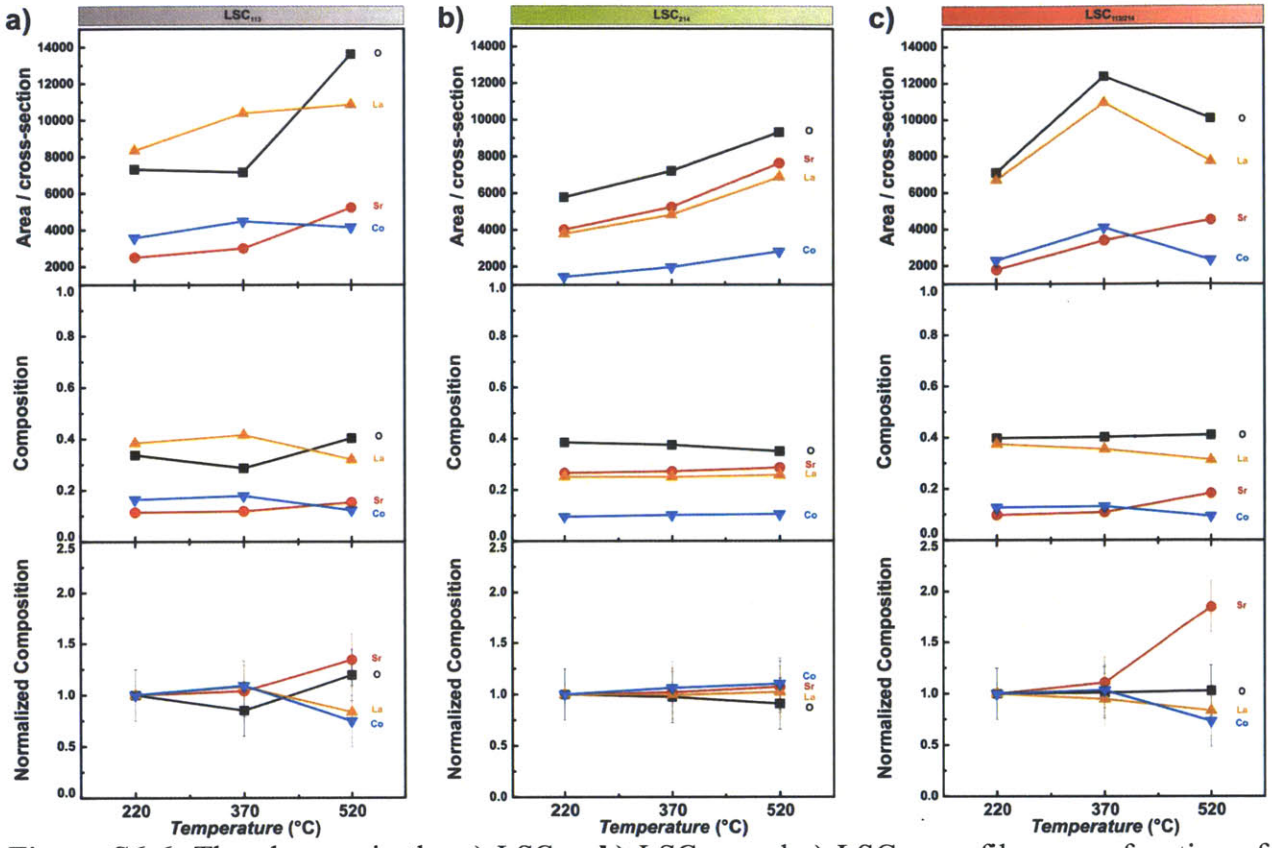

Figure S6-6. The changes in the **a)** LSC_{113} **b)** LSC_{214} and **c)** $LSC_{113/214}$ films as a function of temperature before electrochemical polarization (from spectra shown in **Figure S6-5**), (**top**) is the raw area intensities for La 4d, Sr 3d, Co 3p, and O 1s divided by their respective photo-ionization cross sections; (**middle**) the cross-section normalized intensity values are divided by the sum of all elemental values at each temperature, creating an effective concentration; (**bottom**) the concentration values for each element are normalized to the first condition, at 220 °C and $p(O_2)$ $1 \cdot 10^{-3}$ atm.

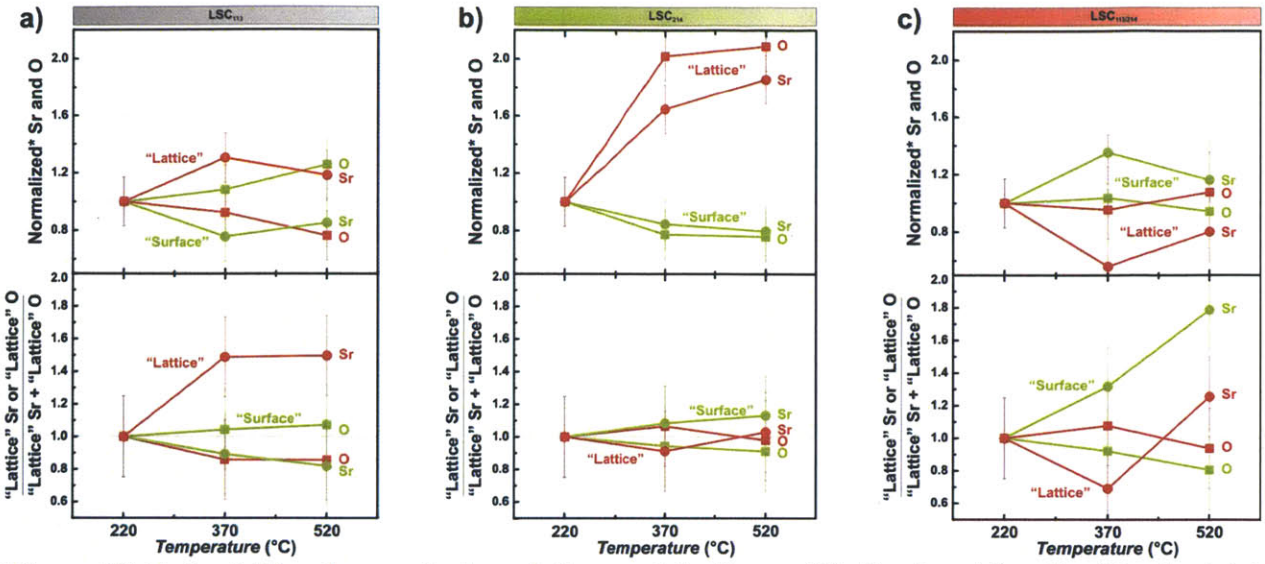

Figure S6-7. (top) The changes in the relative contributions of "lattice" and "surface" to the total Sr 3d and O 1s, cross-section-normalized intensity (lattice: red, surface green), (**bottom**) "Lattice" (and "Surface") Sr and O enrichment, of the changes in the **a)** LSC_{113} **b)** LSC_{214} and **c)** $LSC_{113/214}$ films as a function of temperature before electrochemical polarization (from spectra shown in **Figure S6-5**), film in the near-surface region (determined by the cross-section-normalized "lattice" (or "surface") intensity of Sr 3d or O 1s was divided by the combined Sr and O "lattice" (or "surface") cross-section-normalized intensities) as a function of temperature and referenced to the initial 220 °C values.

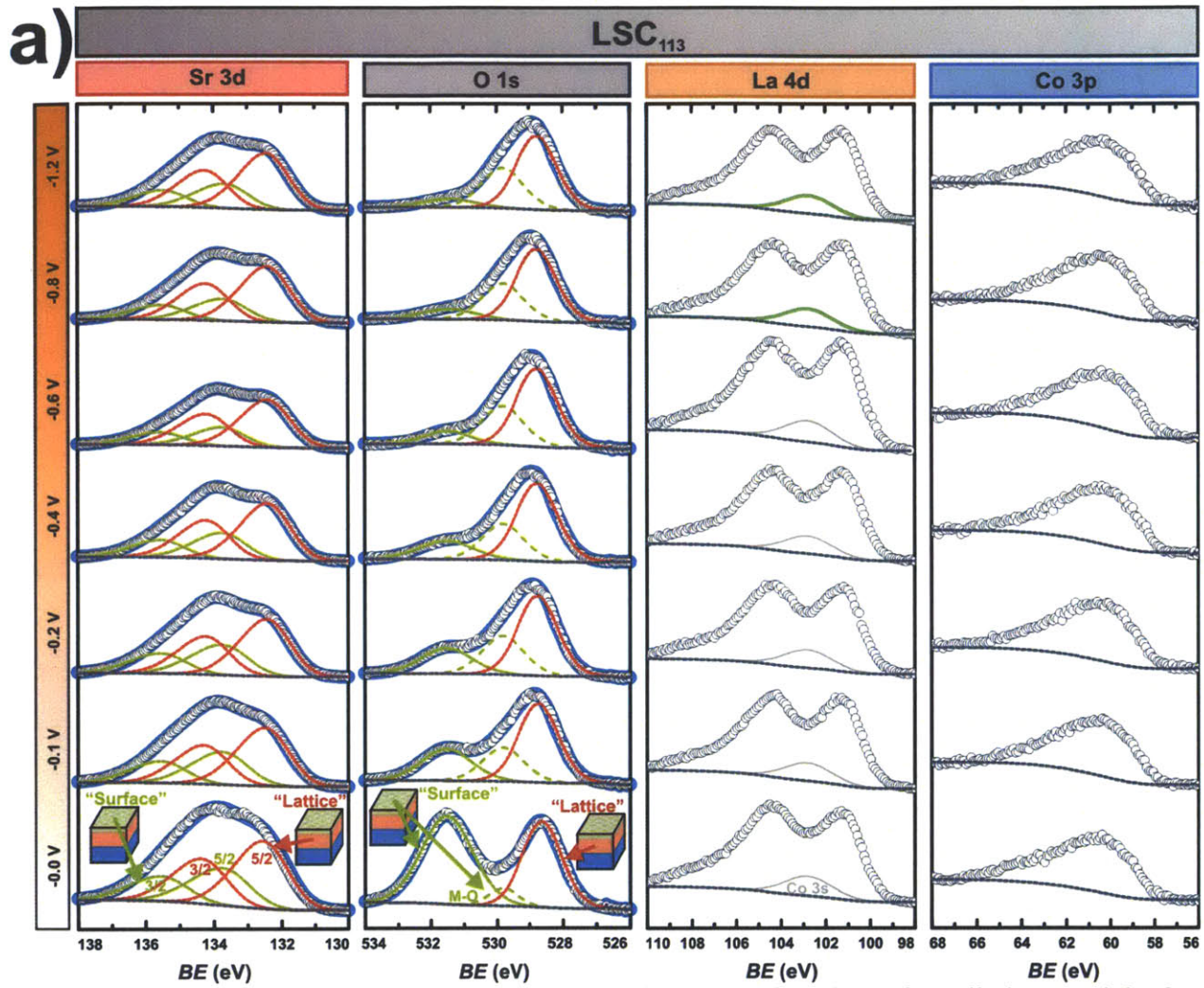

Figure S6-8a. *In situ* APXPS data of a LSC_{113} film as a function of applied potential after reaching 520 °C (**Figure S6-5a**). Sr 3d (E_{photon} = 390 eV), O 1s (E_{photon} = 690 eV), La 4d (E_{photon} = 390 eV) and Co 3p (E_{photon} = 390 eV) spectra at applied potentials of 0 V, −0.1 V, −0.2 V, −0.4 V, −0.8 V, and −1.2 V at a $p(O_2)$ of $1 \cdot 10^{-3}$ atm. The "lattice" component of the perovskite structure in the near-surface region is shown in red while the "surface" component for the secondary phases (including both surface components) is shown in green. White circles are for the measured data, blue lines indicate the sum of fits, and grey dotted lines correspond to the background.

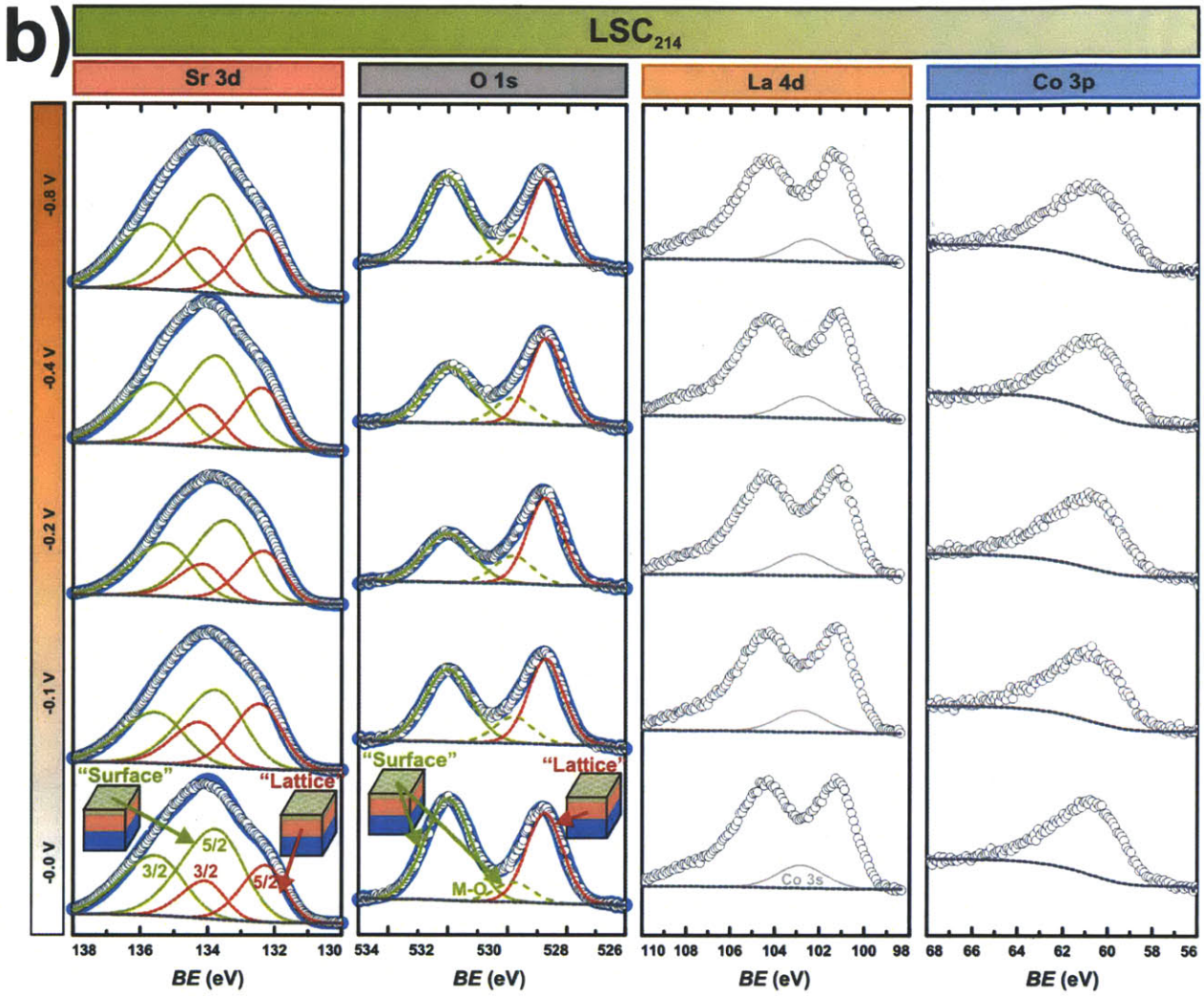

Figure S6-8b. *In situ* APXPS data of a LSC_{214} film as a function of applied potential after reaching 520 °C (**Figure S6-5b**). Sr 3d (E_{photon} = 390 eV), O 1s (E_{photon} = 690 eV), La 4d (E_{photon} = 390 eV) and Co 3p (E_{photon} = 390 eV) spectra at applied potentials of 0 V, −0.1 V, −0.2 V, −0.4 V, and −0.8 V at a $p(O_2)$ of $1 \cdot 10^{-3}$ atm. The "lattice" component of the perovskite structure in the near-surface region is shown in red while the "surface" component for the secondary phases (including both surface components) is shown in green. White circles are for the measured data, blue lines indicate the sum of fits, and grey dotted lines correspond to the background.

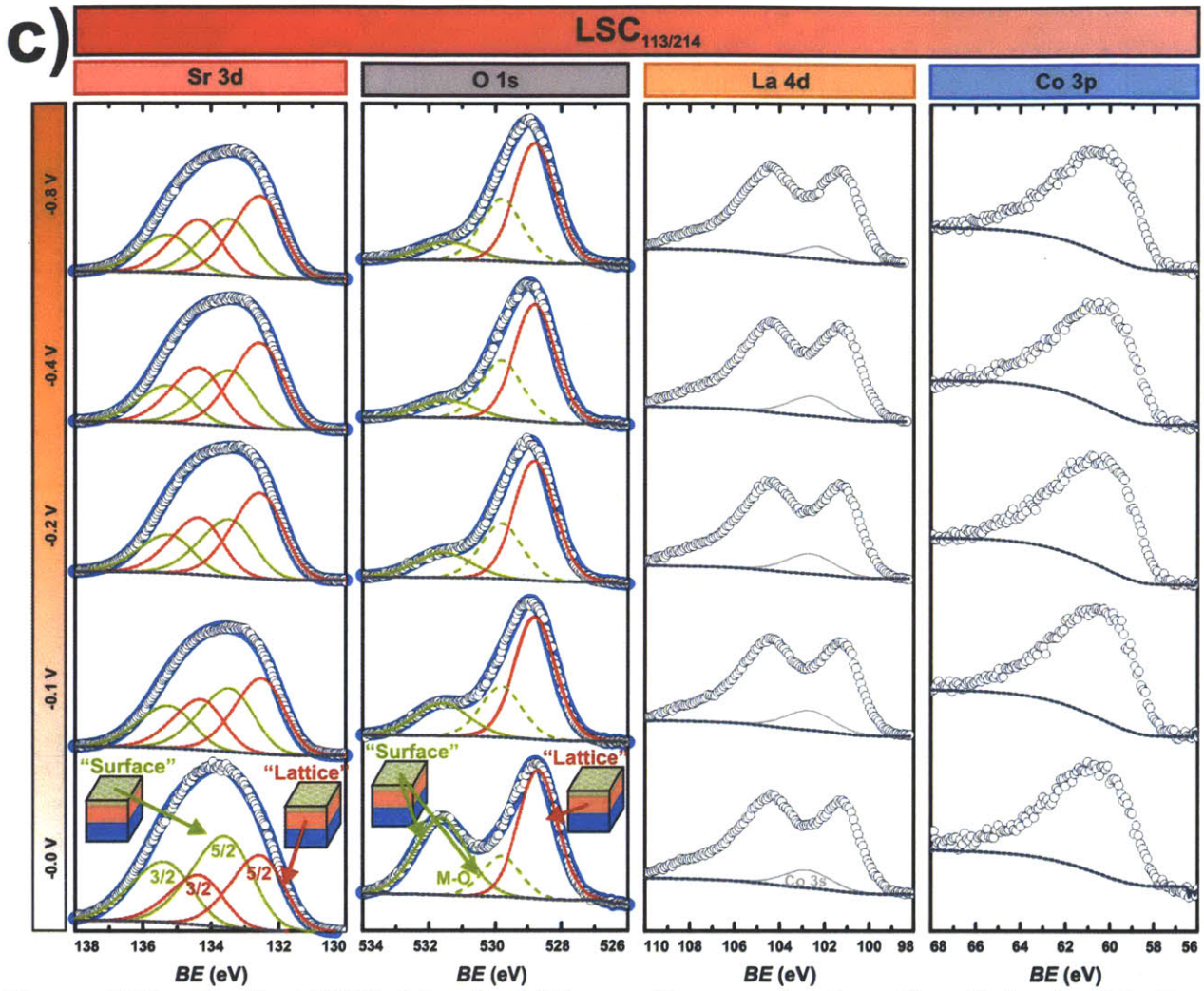

Figure S6-8c. *In situ* APXPS data of a $LSC_{113/214}$ film as a function of applied potential after reaching 520 °C (**Figure S6-5c**). Sr 3d (E_{photon} = 390 eV), O 1s (E_{photon} = 690 eV), La 4d (E_{photon} = 390 eV) and Co 3p (E_{photon} = 390 eV) spectra at applied potentials of 0 V, −0.1 V, −0.2 V, −0.4 V, and −0.8 V at a $p(O_2)$ of $1 \cdot 10^{-3}$ atm. The "lattice" component of the perovskite structure in the near-surface region is shown in red while the "surface" component for the secondary phases (including both surface components) is shown in green. White circles are for the measured data, blue lines indicate the sum of fits, and grey dotted lines correspond to the background.

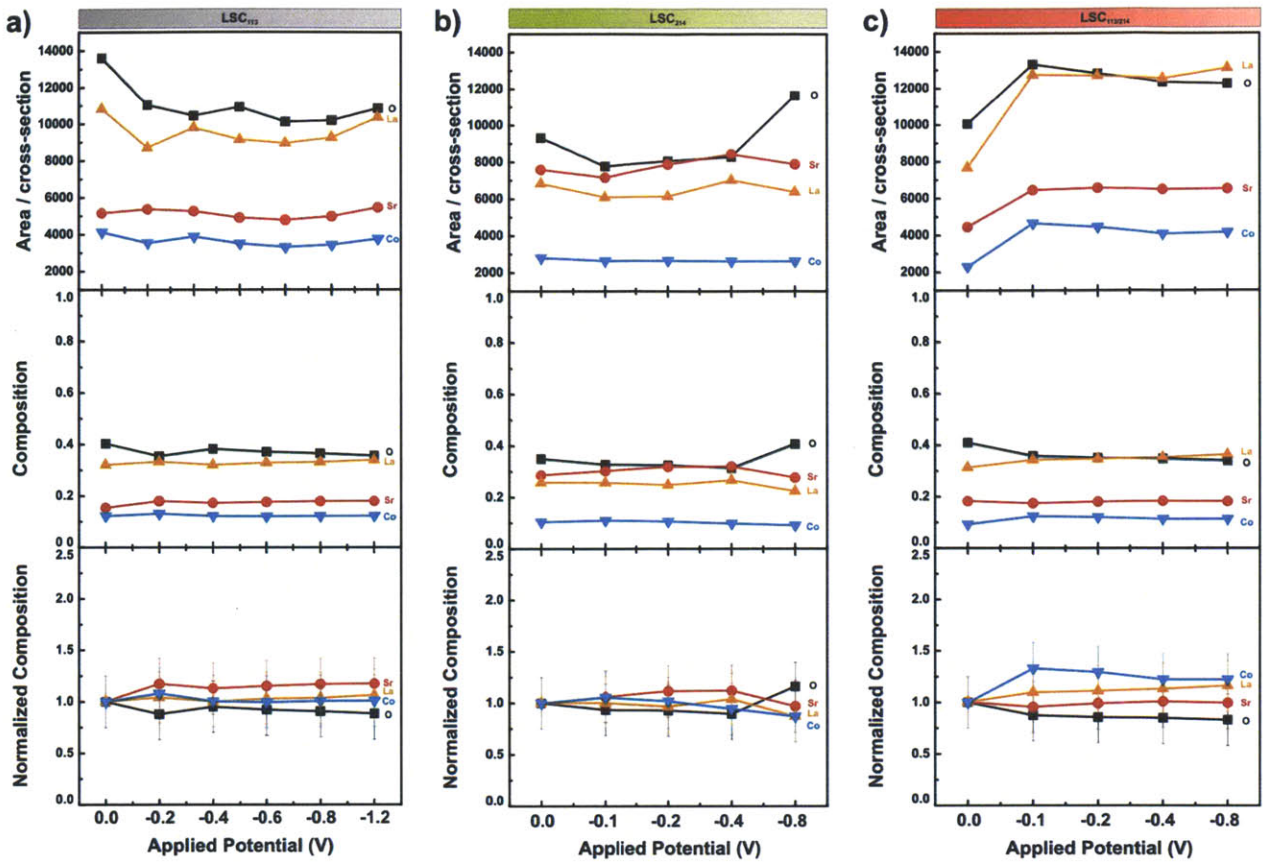

Figure S6-9. The changes in the **a)** LSC_{113} **b)** LSC_{214} and **c)** $LSC_{113/214}$ films as a function of applied potential (from spectra shown in **Figure S6-8**), (top) is the raw area intensities for La 4d, Sr 3d, Co 3p, and O 1s divided by their respective photo-ionization cross sections; (middle) the cross-section normalized intensity values are divided by the sum of all elemental values at each temperature, creating an effective concentration; (bottom) the concentration values for each element are normalized to the first condition, at 520 °C and $p(O_2)$ $1 \cdot 10^{-3}$ atm.

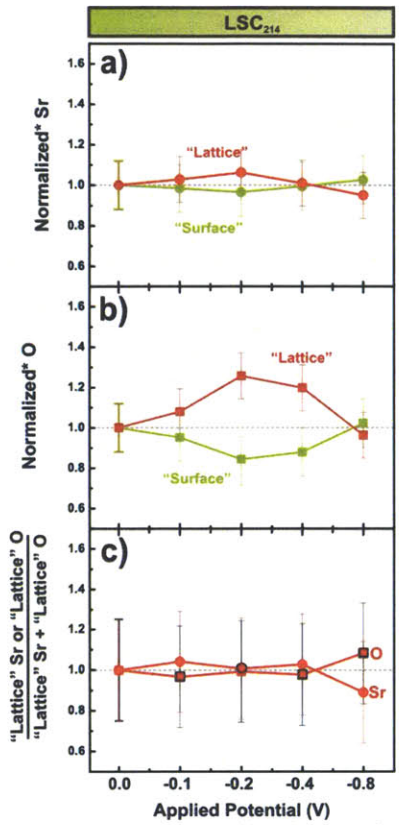

Figure S6-10. LSC_{214} changes in the relative contributions of "lattice" and "surface" to the total (**a**) Sr 3d, (**b**) O 1s cross-section-normalized intensity (lattice: red, surface green). (**c**) "Lattice" Sr enrichment in the near-surface region (determined by the cross-section-normalized "lattice" intensity of Sr 3d or O 1s was divided by the combined Sr and O "lattice" cross-section-normalized intensities) as a function of applied potential and referenced to the initial 0 V applied potential values, at 520 °C and $p(O_2)$ $1 \cdot 10^{-3}$ atm.

6.5 References

1. Adler, S. B. *Chemical Reviews* **2004**, *104*, 4791.

2. Adler, S. B.; Chen, X. Y.; Wilson, J. R. *Journal of Catalysis* **2007**, *245*, 91.

3. Lee, Y. L.; Kleis, J.; Rossmeisl, J.; Morgan, D. *Phys Rev B* **2009**, *80*, 224101.

4. Tarancon, A.; Burriel, M.; Santiso, J.; Skinner, S. J.; Kilner, J. A. *Journal of Materials Chemistry* **2010**, *20*, 3799.

5. Baumann, F. S.; Fleig, J.; Konuma, M.; Starke, U.; Habermeier, H. U.; Maier, J. *Journal of the Electrochemical Society* **2005**, *152*, A2074.

6. Crumlin, E. J.; Mutoro, E.; Ahn, S.-J.; la O', G. J.; Leonard, D. N.; Borisevich, A.; Biegalski, M. D.; Christen, H. M.; Shao-Horn, Y. *J. Phys. Chem. Lett.* **2010**, *1*, 3149.

7. Korte, C.; Schichtel, N.; Hesse, D.; Janek, J. *Mon. Chem.* **2009**, *140*, 1069.

8. Mutoro, E.; Crumlin, E. J.; Biegalski, M. D.; Christen, H. M.; Shao-Horn, Y. *Energy Environ. Sci.* **2011**, *4*, 3689.

9. Mutoro, E.; Crumlin, E. J.; P√∂pke, H.; Luerssen, B.; Amati, M.; Abyaneh, M. K.; Biegalski, M. D.; Christen, H. M.; Gregoratti, L.; Janek, J. r.; Shao-Horn, Y. *The Journal of Physical Chemistry Letters* **2012**, *3*, 40

10. Sase, M.; Hermes, F.; Yashiro, K.; Sato, K.; Mizusaki, J.; Kawada, T.; Sakai, N.; Yokokawa, H. *Journal of the Electrochemical Society* **2008**, *155*, B793.

11. Sase, M.; Yashiro, K.; Sato, K.; Mizusaki, J.; Kawada, T.; Sakai, N.; Yamaji, K.; Horita, T.; Yokokawa, H. *Solid State Ionics* **2008**, *178*, 1843.

12. Schichtel, N.; Korte, C.; Hesse, D.; Janek, J. *Physical Chemistry Chemical Physics* **2009**, *11*, 3043.

13. Yashiro, K.; Nakamura, T.; Sase, M.; Hermes, F.; Sato, K.; Kawada, T.; Mizusaki, J. *Electrochemical and Solid State Letters* **2009**, *12*, B135.

14. Misture, S. T. *Journal of Electroceramics* **2006**, *16*, 167.

15. Ovenstone, J.; White, J. S.; Misture, S. T. *Journal of Power Sources* **2008**, *181*, 56.

16. Crumlin, E. J.; Mutoro, E.; Liu, Z.; Grass, M. E.; Biegalski, M. D.; Lee, Y.-L.; Morgan, D.; Christen, H. M.; Bluhm, H.; Shao-Horn, Y. *Energy & Environmental Science* **2012**, *5*, 6081.

17. Luerssen, B.; Mutoro, E.; Fischer, H.; Gunther, S.; Imbihl, R.; Janek, J. *Angewandte Chemie-International Edition* **2006**, *45*, 1473.

18. Marsi, M.; Casalis, L.; Gregoratti, L.; Gunther, S.; Kolmakov, A.; Kovac, J.; Lonza, D.; Kiskinova, M. *Journal of Electron Spectroscopy and Related Phenomena* **1997**, *84*, 73.

19. Lee, A. F.; Wilson, K.; Lambert, R. M.; Goldoni, A.; Baraldi, A.; Paolucci, G. *Journal of Physical Chemistry B* **2000**, *104*, 11729.

20. Lizzit, S.; Baraldi, A. *Catalysis Today* **2010**, *154*, 68.

21. Bluhm, H.; Havecker, M.; Knop-Gericke, A.; Kleimenov, E.; Schlogl, R.; Teschner, D.; Bukhtiyarov, V. I.; Ogletree, D. F.; Salmeron, M. *J. Phys. Chem. B* **2004**, *108*, 14340.

22. Tao, F.; Dag, S.; Wang, L.-W.; Liu, Z.; Butcher, D. R.; Bluhm, H.; Salmeron, M.; Somorjai, G. A. *Science* **2010**, *327*, 850.

23. Tao, F.; Grass, M. E.; Zhang, Y.; Butcher, D. R.; Renzas, J. R.; Liu, Z.; Chung, J. Y.; Mun, B. S.; Salmeron, M.; Somorjai, G. A. *Science* **2008**, *322*, 932.

24. Whaley, J. A.; McDaniel, A. H.; El Gabaly, F.; Farrow, R. L.; Grass, M. E.; Hussain, Z.; Liu, Z.; Linne, M. A.; Bluhm, H.; McCarty, K. F. *Rev. Sci. Instrum.* **2010**, *81*, 086104.

25. Zhang, C.; Grass, M. E.; McDaniel, A. H.; DeCaluwe, S. C.; El Gabaly, F.; Liu, Z.; McCarty, K. F.; Farrow, R. L.; Linne, M. A.; Hussain, Z.; Jackson, G. S.; Bluhm, H.; Eichhorn, B. W. *Nature Mat.* **2010**, *9*, 944.

26. Howng, W.; Thorn, R. *Chem. Phys. Lett.* **1978**, *56*, 463.

27. Howng, W. Y.; Thorn, R. J. *J. Phys. Chem. Solids* **1980**, *41*, 75.

28. McIntyre, N. S.; Cook, M. G. *Anal. Chem.* **1975**, *47*, 2208.

29. van der Heide, P. A. W. *Surf Interface Anal* **2002**, *33*, 414.

30. Vasquez, R. P. *J. Electron Spectros.* **1991**, *56*, 217.

31. Uwamino, Y.; Ishizuka, T.; Yamatera, H. *J. Electron Spectros.* **1984**, *34*, 67.

32. Galenda, A.; Natile, M. M.; Krishnan, V.; Bertagnolli, H.; Glisenti, A. *Chem. Mat.* **2007**, *19*, 2796.

33. la O', G. J.; Ahn, S. J.; Crumlin, E.; Orikasa, Y.; Biegalski, M. D.; Christen, H. M.; Shao-Horn, Y. *Angew Chem Int Edit* **2010**, *49*, 5344.

34. Chen, X.; Yu, J.; Adler, S. B. *Chem. Mat.* **2005**, *17*, 4537.

35. Kawada, T.; Suzuki, J.; Sase, M.; Kaimai, A.; Yashiro, K.; Nigara, Y.; Mizusaki, J.; Kawamura, K.; Yugami, H. *J. Electrochem. Soc.* **2002**, *149*, E252.

36. Mizusaki, J.; Mima, Y.; Yamauchi, S.; Fueki, K.; Tagawa, H. *Journal of Solid State Chemistry* **1989**, *80*, 102.

37. Bishop, S. R.; Tuller, H. L.; Kuru, Y.; Yildiz, B. *Journal of the European Ceramic Society* **2011**, *31*, 2351.

38. Morin, F.; Trudel, G.; Denos, Y. *Solid State Ionics* **1997**, *96*, 129.

39. Petrov, A. N.; Cherepanov, V. A.; Kononchuk, O. F.; Gavrilova, L. Y. *J. Solid State Chem.* **1990**, *87*, 69.

40. Gadre, M. J.; Lee, Y.-L.; Morgan, D. *Physical Chemistry Chemical Physics* **2012**, *14*, 2606.

41. Christen, H. M.; Specht, E. D.; Silliman, S. S.; Harshavardhan, K. S. *Physical Review B* **2003**, *68*, 4.

Chapter 7. Discussion into Possible Mechanism Governing Oxygen Reduction Enhancement

7.1 Discussion

Currently there is no clear indication what property is truly responsible for $LSC_{113/214}$'s enhanced activity with respect to LSC_{113} and LSC_{214}, however this section will provide some hypothetical discussions evaluating possible mechanisms governing the enhanced activity. The previous sections have shown that all of the bare and decorated LSC films appear to be dissociation adsorption limited from the surface exchange coefficients $p(O_2)$ dependence.[1,2] Looking for a property to differentiate the activity, it is reasonable to consider the activation energy (E_a). A change in activation energy of the oxygen surface exchange could be responsible for the significant changes in activity. To evaluate the activation energy, one must consider the Arrhenius relationship below, where R_o is the initial resistance, R_g is the universal gas constant, and T is the temperature.

$$R = R_o \exp\left(\frac{-E_a}{R_g T}\right)$$

From this equation for E_a to make a unique contribution in revealing a property within the mechanism, R_o at a given temperature for LSC_{113} and $LSC_{113/214}$ should theoretically be the same, thus allowing a different E_a to be the root cause for the activity to diverge with changes in temperature. When considering E_a's for a wide range of mixed ionic and electronic conducting oxide materials over a wide temperature range,[3] **Figure 7-1** clearly shows that activity ranges over 2 – 3 orders of magnitude between 600 – 750 °C, while there are very little changes in the activation energy 1.3 – 1.8 eV.[3] Additionally, there are no clear systematic trends relating E_a and activity.[3] Therefore it is not clear that activation energy can be a clear and unique property governing the reaction mechanisms across a wide range of cathode oxide materials.

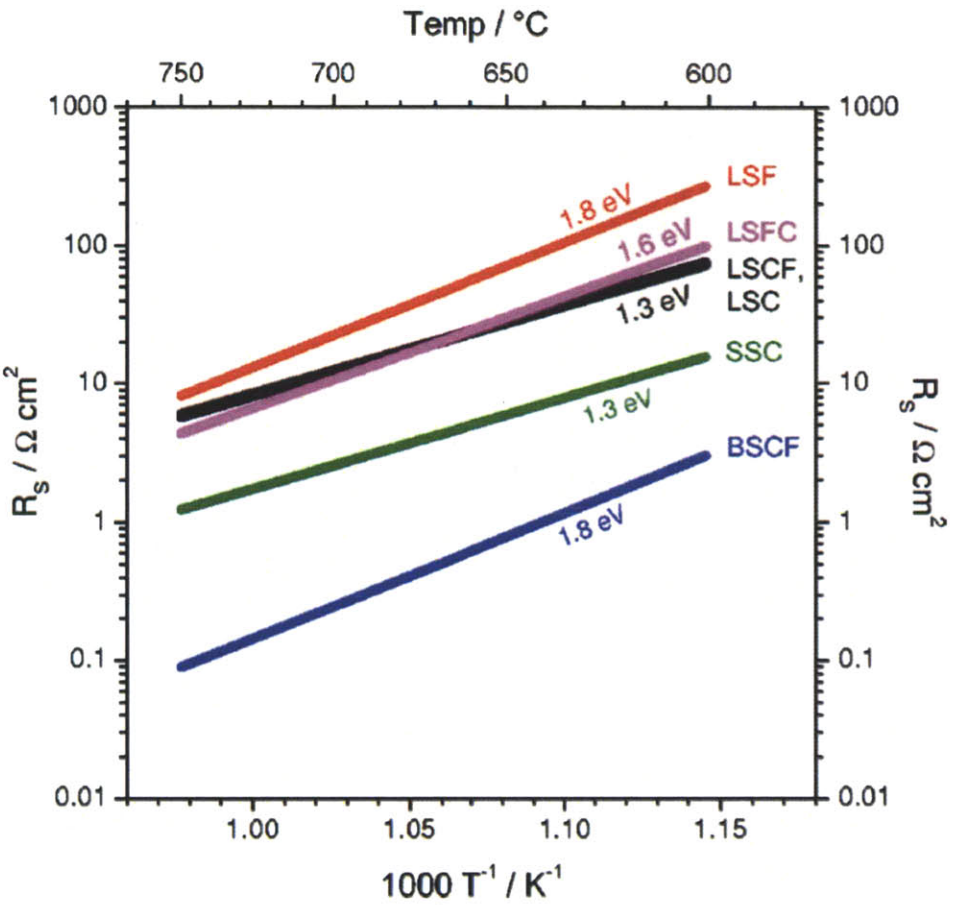

Figure 7-1. Reproduction of Baumann et al.[3], temperature dependence of the surface resistance R_s for six different compositions. Each one of the graphs is based on the average absolute R_s value determined at 750 °C as well as the average activation energy of this quantity obtained from temperature dependent measurements between 600 °C and 750 °C on at least two samples per composition.[3]

A more detailed hypothesis for connecting activation energy to activity is proposed by Jung et al,[4] where they observed a close correlation between E_a and $E_c - E_f$ (band gap, where E_c is the edge of conduction band and E_f is the Fermi level) on $SrTi_{1-x}Fe_xO_{3-\delta}$ (STF, where x represents the fraction of Fe and δ the oxygen nonstoichiometry) as shown in **Figure 7-2**.[4] This is an interesting concept, however it requires that the material possesses an energy bang gap at operating conditions. Scanning tunneling spectroscopy of LSC_{113}, both strained compressively and tensile, at elevated temperatures above 300 °C appeared to be semi-metallic and did not reveal a band gap which was only observed at lower temperatures **Figure 7-3**.[5] Additionally, from valence band data collected on our LSC_{113}, LSC_{214}, and $LSC_{113/214}$ thin films at 520 °C and $p(O_2)$ of 10^{-3} atm,

we do not observe any shifting in the Fermi edge away from 0 eV; thus confirming metallic like properties (**Figure 7-4**). However, this does suggest that an important property responsible enhanced reaction mechanism may lie within the electronic structure of the material. To probe this concept further, Lee et al[6] hypothesize the O *p*-band center position may be responsible for the enhanced activity.[6] Using DFT calculations they show a strong correlation between oxygen reduction reaction activity and the O *p*-band center position for a wide range of oxide materials, as shown in **Figure 7-5**.[6] This is an interesting theory, however we are unable to experimentally observe the O 2p band, and need to rely on DFT simulations which are currently being pursued for the materials discussed in this work. Initially we can look at the collected valence band data (**Figure 7-4**) and its challenging to see any clear differences between LSC_{113} and $LSC_{113/214}$ confirming the challenges to obtain experimental validation for this hypothesis, but it is one we should continue to consider.

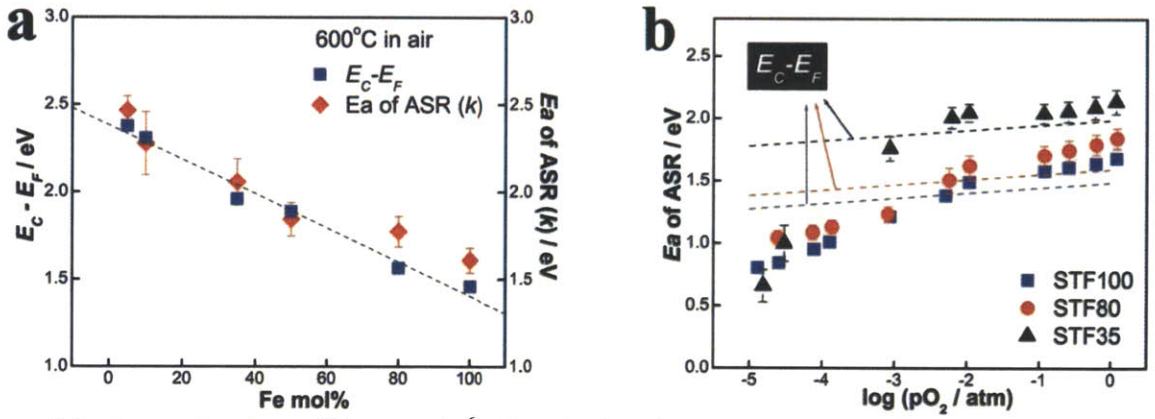

Figure 7-2. Reproduction of Lee et al.,[6] (a) calculated E_c-E_c (left axis and activation energy of R_{STF} (or k) measured by EIS (right axis) as a function of Fe composition at 600 °C in air. (b) Activation energy of R_{STF} (or k) as a function of $p(O_2)$ at 600 °C for STF35, 80, and 100. The corresponding E_c-E_f values (dashed lines) are also included for comparison.

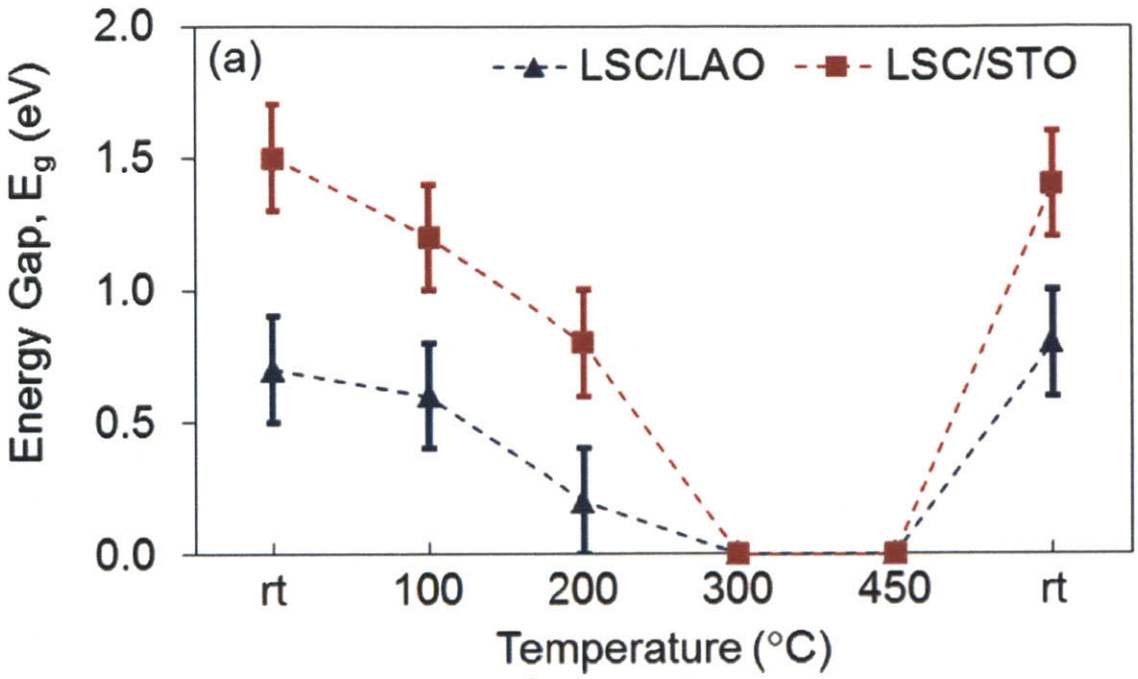

Figure 7-3. Reproduction of Cai et al.,[5] energy gap measured by scanning tunneling spectroscopy for tensile strained LSC/$SrTiO_3$ (STO) and compressively strained LSC/$LaAlO_3$ (LAO) surface as a function of temperature from room temperature (rt) to 450 °C and back to rt. The dashed connecting lines are a guide for the eye.

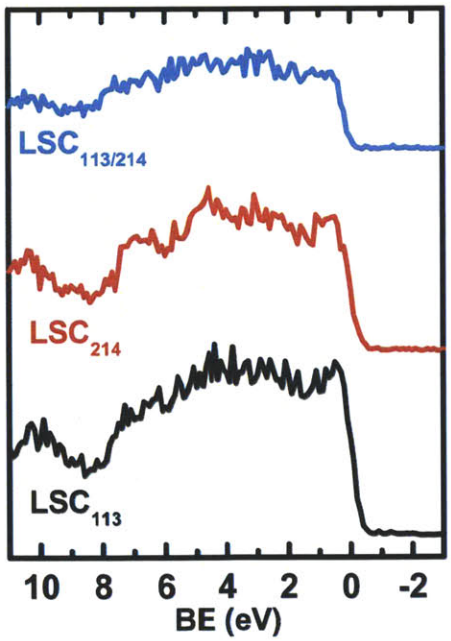

Figure 7-4. Valence band spectra for LSC_{113}, LSC_{214}, $LSC_{113/214}$ epitaxial thin films at 520 °C, $p(O_2)$ $1 \cdot 10^{-3}$ atm.

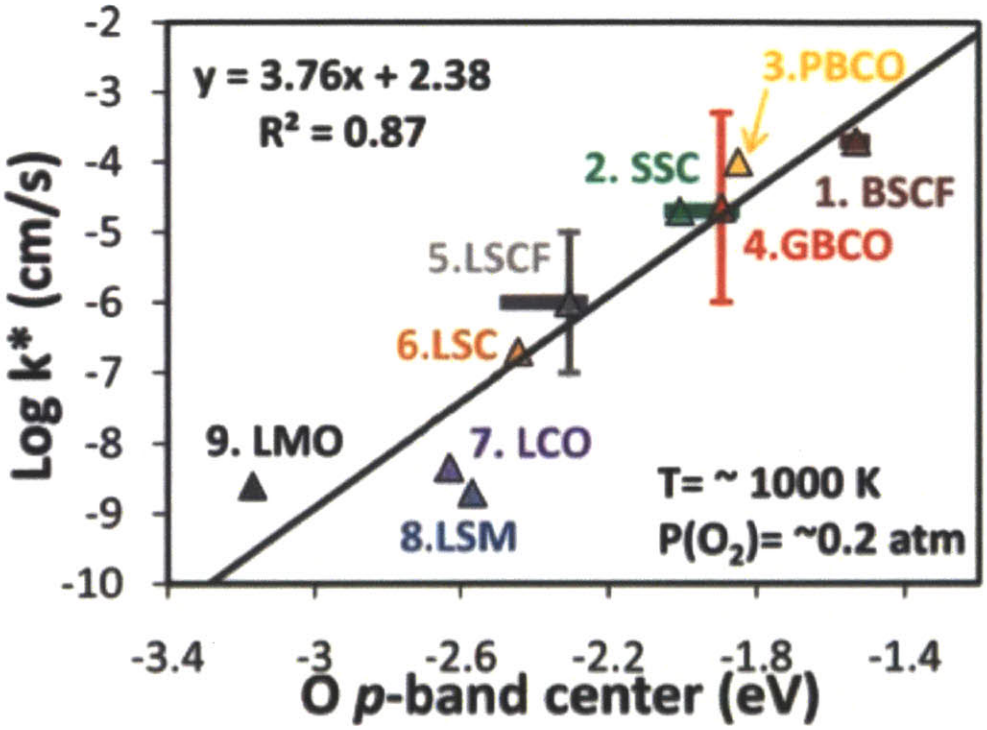

Figure 7-5. Reproduction of Lee et al.,[6] Experimental surface exchange coefficients (k^*s) measured under $p(O_2)$ = 0.2~1.0 bar at T ~ 1000 K vs. the calculated bulk O *p*-band center of perovskites: 1.$Ba_{0.5}Sr_{0.5}Co_{0.75}Fe_{0.25}O_3$ (BSCF), 2.$Sm_{0.5}Sr_{0.5}CoO_3$ (SSC), 3. $PrBaCo_2O_6$ (PBCO), 4.$GdBaCo_2O_6$ (GBCO), 5.$La_{0.625}Sr_{0.375}Co_{0.25}Fe_{0.75}O_3$ (LSCF), 6.$La_{0.75}Sr_{0.25}CoO_3$ (LSC), 7.$LaCoO_3$ (LCO), 8. $La_{0.75}Sr_{0.25}MnO_3$ (LSM), and 9.$LaMnO_3$ (LMO). Values with vertical errors bars are the average of multiple data values with an error bar equal to the standard deviation in the mean. The range of the calculated O p-band centers for different SQS for the disordered BSCF, SSC, and LSCF structures are represented with horizontal bars, and the data points are calculated using Boltzmann factor weighted averages at 1000 K of the SQS energies.

Taking a slightly different approach to attempt to explain the origins for the enhanced activity, I will deconstruct the surface exchange coefficients (k^q, shown below) properties to isolate the key parameters responsible.

$$k^q = \frac{k_B T}{4e^2 R c_o}$$

(with k_b: Boltzmann constant, e: electron charge, T: absolute temperature, R: area specific resistance, c_o: total concentration of lattice oxygen).

$$R = \frac{1}{2\pi f C}$$

Where R can be related to f: frequency and C: specific capacitance defined below

$$C = \frac{4F^2 L}{V_m\left(a_x + \frac{3R_g T}{\delta(3-\delta)}\right)}$$

Where F: Faraday constant, L: thickness of electrode, V_m: molar volume of electrode, a_x: thermodynamic non-ideality factor, δ: oxygen nonstoichiometry, R_g: universal gas constant, and T: absolute temperature.

Combining C into R, we obtain (note, that highlighted in **Red** are the variables that are not constants or fixed based on geometric constraints).

$$R = \frac{\boldsymbol{V_m}\left(\boldsymbol{a_x} + \frac{3RT}{\boldsymbol{\delta}(3-\boldsymbol{\delta})}\right)}{2\pi \boldsymbol{f}(4F^2 L)}$$

Using initial values for our LSC_{113} material as listed below, we can then evaluate the R as a function of the variables that can be changed to determine the most sensitive parameters and which may be most likely responsible for the enhanced activity of $LSC_{113/214}$.

$L = 8.5\ 10^{-6}$ cm

$T = 823$ K

$V_m = 33.66\ \text{cm}^3\ \text{mol}^{-1}$

$a_x = 10^6\ \text{J mol}^{-1}$

$\delta = 0.008$

$f = 0.04$ Hz

From this deconstruction shown in **Figure 7-6** we see how the area specific resistance changes as a function of V_m, a_x, δ, f. We see that even in the extreme values of V_m, a_x, and δ we can only modify the area specific resistance within an order of magnitude. Combining changes in several of these parameters at once will magnify the improvements, however the parameter that can

provide clearest enhancement across many orders of magnitude is the frequency. In fact, if we consider LSC_{113} and $LSC_{113/214}$ there were no clear differences in both a_x, and δ from our EIS measurements[1,2]; and most likely small if any changes to V_m are possible between these films. However, there was a 2 – 3 order of magnitude difference in the EIS peak frequency for the surface oxygen exchange. Therefore, the changes that are occurring do not seem to be dependent upon these other bulk properties, but within one that can modify the exchange rate frequency. This brings us back to properties within the electronic structure governing the oxygen bonding energy, cobalt's valence state, or the oxides surface geometry that can govern the reactions turn over frequency which future studies will continue to investigate.

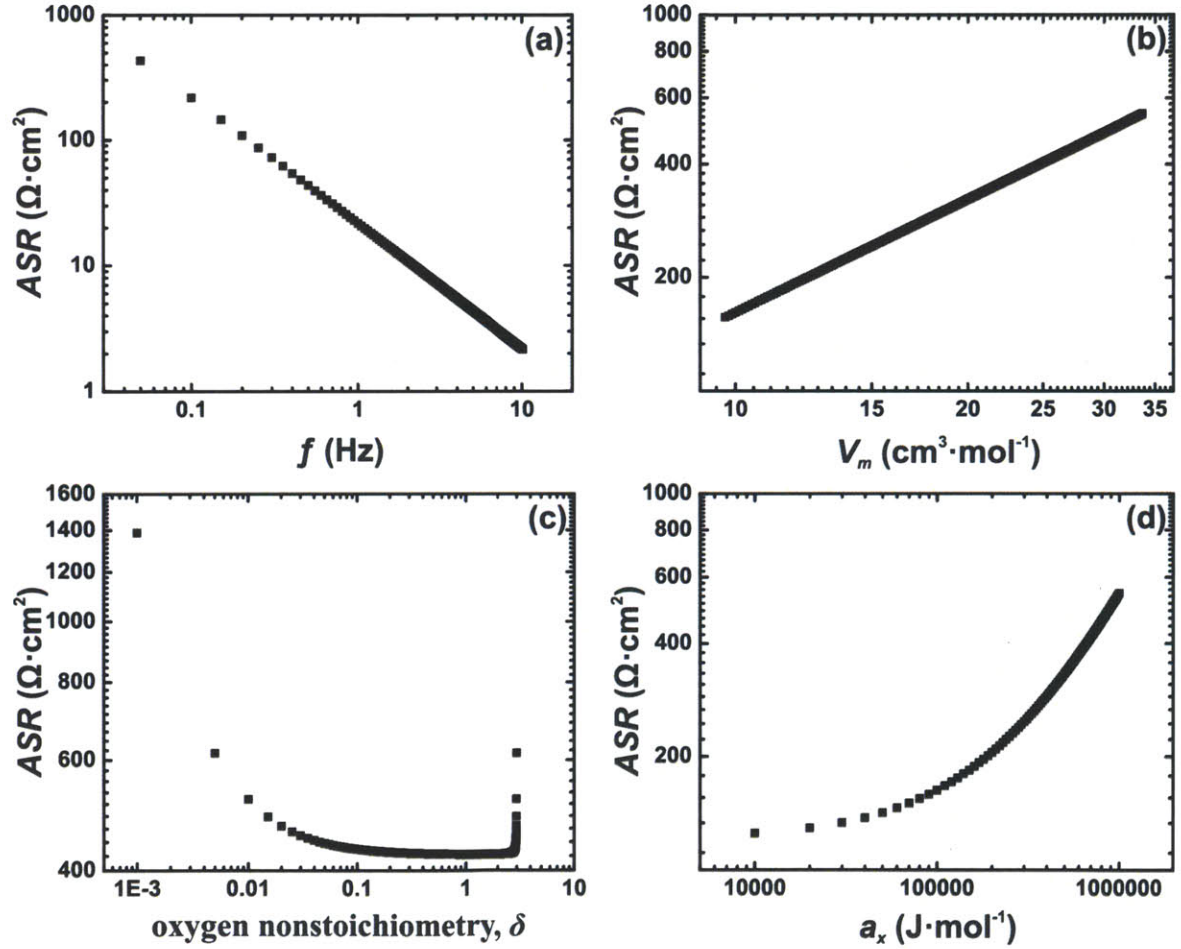

Figure 7-6. Area specific resistance versus a) f, b) V_m, c) δ, and d) a_x for LSC113 with L = 8.5 10^{-6} cm, T = 823 K, V_m = 33.66 cm^3 mol^{-1}, a_x = 10^6 J mol^{-1}, δ = 0.008, f= 0.04 Hz.

7.2 References

1. Crumlin, E. J.; Ahn, S.-J.; Lee, D.; Mutoro, E.; Biegalski, M. D.; Christen, H. M.; Shao-Horn, Y. *Journal of the Electrochemical Society***2012**, (Accepted).
2. Crumlin, E. J.; Mutoro, E.; Ahn, S.-J.; la O', G. J.; Leonard, D. N.; Borisevich, A.; Biegalski, M. D.; Christen, H. M.; Shao-Horn, Y. *The Journal of Physical Chemistry Letters***2010**, *1*, 3149
3. Baumann, F. S.; Fleig, J.; Cristiani, G.; Stuhlhofer, B.; Habermeier, H. U.; Maier, J. *Journal of the Electrochemical Society***2007**, *154*, B931.
4. Jung, W.; Tuller, H. L. *Advanced Energy Materials***2011**, *1*, 1184.
5. Cai, Z. H.; Kuru, Y.; Han, J. W.; Chen, Y.; Yildiz, B. *Journal of the American Chemical Society***2011**, *133*, 17696.
6. Lee, Y.-L.; Kleis, J.; Rossmeisl, J.; Shao-Horn, Y.; Morgan, D. *Energy & Environmental Science***2011**, *4*, 3966.

Chapter 8. Conclusions and Perspectives

8.1 Conclusions

The primary focus of the work presented in this thesis was to develop and improve our understanding of enhanced ORR active materials for SOFC. Bare epitaxial LSC80-20_{113} and LSC_{214}-decorated LSC80-20_{113} films were the foundation of this work, demonstrating ORR activity enhancement up to ~1-3 orders of magnitude on the LSC80-$20_{113/214}$ heterostructured thin films.[1] By probing microelectrodes of different diameters, it became possible to isolate and confirm[2-4] that the interfacial LSC80-$20_{113/214}$ regions are responsible for the observed ORR enhancement, and that the oxygen vacancy concentration of the entire film and a disordered interfacial $LSC_{113/214}$ structure are not attributed to the observed changes.[1]

In an attempt to further enhance ORR activity, Sr substitution was increased to 40%, thus creating epitaxial LSC60-40_{113} films. Interestingly, epitaxial LSC60-40_{113} thin films ORR activity was similar to both bulk LSC60-40_{113} and epitaxial LSC80-20_{113} films previously studied.[1, 5, 6] When LSC60-40_{113} is decorated with LSC_{214} the enhancement is similar to that reported for LSC_{214}-decorated LSC80-20_{113},[1, 6] and posses very comparable surface oxygen exchange kinetics. Moreover, these LSC_{214}-decorated LSC60-40_{113} films have the area specific resistance approaching ~0.45 Ωcm^2 at 1 atm and 550 °C,[1, 6] which are among the lowest reported to date.[7] This work can exclude the enhancement in ORR kinetics from being attributed to changes in the oxygen vacancy concentration of the entire films and film strains measured at room temperature, and support that continued attention be placed on the interfacial $LSC_{113/214}$ regions which are believed to be responsible for the observed ORR enhancement.[1, 6]

In situ characterizations are the forefront of our field providing unprecedented information into how a material changes at or near operating conditions. This work utilized *in situ* HRXRD and APXPS to enhance our understanding of how epitaxial LSC80-20_{113} thin films and bulk pellets structural and surface composition change at elevated temperatures and near ambient partial pressures. This work revealed that at 520 °C and a $p(O_2)$ of $1 \cdot 10^{-3}$ atm the film surface reduces its coverage of surface secondary phases and Sr increases within the near-surface perovskite region ("lattice") while the pellet surface has no appreciable change in surface

secondary phaes or "lattice" Sr enrichment. These differences between film and pellet surfaces can explain the enhanced activity of the epitaxial LSC80-20_{113} film for oxygen electrocatalysis relative to LSC80-20_{113} powder[1, 5, 8] where the Sr enrichment in the perovskite structure in the near-surface region can increase the activity as it is well known that increasing Sr in bulk $La_{1-x}Sr_xCoO_{3-\delta}$ perovskite materials leads to higher ORR activity.[9]

The final study made in this thesis probes epitaxial LSC80-20_{113} thin films upon thermally cycling (from 220 °C to 520 °C at a $p(O_2)$ of $1 \cdot 10^{-3}$ atm) and observe a small amount of reversible Sr surface enrichment and dilution under temperature cycling, preceded by a significant irreversible Sr enrichment in the "lattice" upon the initial temperature increase. Furthermore, using *in situ* APXPS to directly compare the surface composition of LSC80-20_{113}, LSC_{214}, and LSC80-$20_{113/214}$ films as a function of temperature and applied potential, we observe Sr concentration increases on the surface and within the "lattice" of the LSC80-$20_{113/214}$ film, while bare LSC80-20_{113} shows the opposite effect under applied potentials and LSC_{214} is essentially uninfluenced. We believe the heterostructured interface between LSC_{214}-decorated LSC80-20_{113} plays a significant role in enriching Sr near the surface,[10] resulting in the enhanced current exchange density[11] and previously reported surface exchange coefficients.[1] In addition, we observe for the first time that LSC80-20_{113} undergoes a reversible phase transition from a perovskite structure to vacancy-ordered/brownmillerite phase upon cathodic electrochemical polarization at 550 °C at a $p(O_2)$ of 1 atm. This work highlights the importance of *in situ* characterization and, more importantly, furthers our understanding of the role surface modification of perovskites has on surface composition, providing insight into the parameters governing activity which will be used for the development of highly active catalysts.

8.2 Recommendations for Future Work.

I must admit, as proud as I am of this work, these studies only add several more pieces of insight into an ever growing puzzle for high temperature solid oxide fuel cells with enhanced electrodes and understanding the mechanism governing their properties. Therefore I would like to offer some thoughts and suggestions for future work to continue efforts towards solving this puzzle, include:

-The working mechanism driving the 3-order of magnitude enhancement in ORR activity for $LSC_{113/214}$ still remains elusive. Additional modeling, such as those conducted by Morgan et al.,[10] and experimentation probing the interface properties responsible for the enhanced activity need to be continued. Once this interface mechanism is completely understood, one could utilize the discovered working principles to create new heterostructures with even more enhanced activity.

-Since it is very challenging to directly resolve the phenomena responsible for the enhanced behavior at the heterostructured interfaces, I would also recommend continuing indirect pursuits by changing the oxide material that is decorating LSC_{113}, such as other ABO_3 ($LaMnO_3$, $LaFeO_3$, etc) and A_2BO_4 (La_2NiO_4, Pr_2NiO_4, etc). One can even envision utilizing completely different elements and oxide structures, however due to the vast amount of potential combinations one must be diligent and develop a sound hypothesis before proceeding otherwise will be overwhelmed with costly and time consuming combinatory studies. Because of the vast quantity of options available this does bring forth great opportunities for computational methods to provide significant impact in this field of research, by quickly screening a wide range of heterostructured interfaces, to unravel the governing mechanisms, which can then be experimentally validated.

-Regarding *in situ* characterization of LSC_{113} and or $LSC_{113/214}$ materials, it would be of great interest to gain more information about the cobalt ions valance state from the Co 2p spectra. The studies presented in this work, were unable to probe the Co 2p spectra due to insufficient photon-flux at the high kinetic energies required to probe Co 2p spectra during these experiments. With the repairs/upgrades to ALS and the implementation of APXPS at other beamlines around the world one will be able to observe Co 2p spectra as a function of temperature, oxygen partial pressure, and applied potentials, which could be very beneficial in unraveling the working mechanism governing the observed enhanced activities.

-This work has demonstrated that oxide surface elemental composition can be very different from the bulk pellets and may change under various operating conditions invalidating the assumption that the surface of an oxide resembles the bulk unless experimentally proven.

Therefore, many more materials should be characterized using *in situ* techniques to understand what the true surface properties are and how they may vary from their bulk properties.

-Lastly, as I am a large proponent for *in situ* characterization, I would like to see this technique applied to many more chemical and electrochemical systems. I believe the findings from these techniques will become increasingly more important as they are more widely adopted and available for researchers around the world.

8.3 References

1. E. J. Crumlin, E. Mutoro, S.-J. Ahn, G. J. la O', D. N. Leonard, A. Borisevich, M. D. Biegalski, H. M. Christen and Y. Shao-Horn, *The Journal of Physical Chemistry Letters*, 2010, **1**, 3149 - 3155.
2. M. Sase, F. Hermes, K. Yashiro, K. Sato, J. Mizusaki, T. Kawada, N. Sakai and H. Yokokawa, *Journal of the Electrochemical Society*, 2008, **155**, B793-B797.
3. M. Sase, K. Yashiro, K. Sato, J. Mizusaki, T. Kawada, N. Sakai, K. Yamaji, T. Horita and H. Yokokawa, *Solid State Ionics*, 2008, **178**, 1843-1852.
4. K. Yashiro, T. Nakamura, M. Sase, F. Hermes, K. Sato, T. Kawada and J. Mizusaki, *Electrochemical and Solid State Letters*, 2009, **12**, B135-B137.
5. G. J. la O, A. Sung-Jin, C. Ethan, O. Yuki, D. B. Michael, M. C. Hans and S.-H. Yang, *Angewandte Chemie International Edition*, 2010, **49**, 3.
6. E. J. Crumlin, S.-J. Ahn, D. Lee, E. Mutoro, M. D. Biegalski, H. M. Christen and Y. Shao-Horn, *Journal of the Electrochemical Society*, 2012, (Accepted).
7. Z. P. Shao and S. M. Haile, *Nature*, 2004, **431**, 170-173.
8. E. Mutoro, E. J. Crumlin, M. D. Biegalski, H. M. Christen and Y. Shao-Horn, *Energy Environ. Sci.*, 2011, **4**, 3689-3696
9. T. Kawada, J. Suzuki, M. Sase, A. Kaimai, K. Yashiro, Y. Nigara, J. Mizusaki, K. Kawamura and H. Yugami, *J. Electrochem. Soc.*, 2002, **149**, E252-E259.
10. M. J. Gadre, Y.-L. Lee and D. Morgan, *Physical Chemistry Chemical Physics*, 2012, **14**, 2606-2616.
11. E. J. Crumlin, E. Mutoro, Z. Liu, M. D. Biegalski, W. T. Hong, H. M. Christen, H. Bluhm and Y. Shao-Horn, *(In Preparation)*, 2012.